

University of Warwick institutional repository: <http://go.warwick.ac.uk/wrap>

A Thesis Submitted for the Degree of PhD at the University of Warwick

<http://go.warwick.ac.uk/wrap/38432>

This thesis is made available online and is protected by original copyright.

Please scroll down to view the document itself.

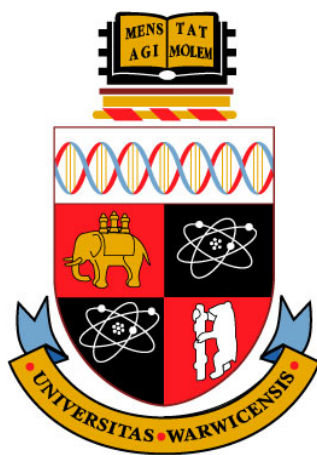
Please refer to the repository record for this item for information to help you to cite it. Our policy information is available from the repository home page.

Interface modification in organic and hybrid photovoltaics

A thesis submitted for the degree of
Doctor of Philosophy
at The University of Warwick

by
Stefan Schumann

Supervised by Prof. Tim S. Jones
Department of Chemistry
The University of Warwick, Coventry



March 2011

Abstract

With the growing importance of organic photovoltaics (OPVs) as an attractive, low cost and sustainable energy source the field has been investigated intensively, showing high potential for commercialisation. To further improve device performance, different routes of development have been explored targeting interfaces that play a crucial role in device performance including the donor (D)/acceptor (A) and electrode/photoactive layer interfaces, as well as incorporation of new materials.

Vertical co-deposition of water-soluble small molecule copper(II) phthalocyanine-tetrasulfonic acid tetrasodium salt (TSCuPc) and polymeric sodium poly[2-(3-thienyl)ethoxy-4-butylsulfonate] (PTEBS) with polystyrene (PS) nanospheres to template, followed by solvent vapour sphere removal, is shown as an excellent method to generate three-dimensionally ordered macroporous large area thin films of sub-100 nm pore size. After a subsequent infiltration by the electron acceptor phenyl-C₆₁-butyric acid methyl ester (PCBM), three-dimensionally (3D) interdigitated D-A composite structures are generated which are further implemented in complete OPV devices. PTEBS based 3D nanostructured D-A composite devices reached a comparable performance to planar reference devices but did not show the expected photocurrent improvement. This is most likely due to the complexity of this multistep fabrication method and the large probability of impurities in the films. However, it demonstrates a new approach towards nanoengineered 3D interdigitated organic D-A composite OPV devices.

For this templating technique monodisperse sub-100 nm PS nanospheres were synthesised by radical initiated surfactant-free emulsion polymerisation controlling different parameters with particular focus on styrene-4-sulfonic acid sodium salt (NaSS) co-monomer concentration. Furthermore, planar heterojunction OPV devices from TSCuPc and PTEBS were studied in detail and optimised for further understanding of the 3D D-A composite devices.

A substantial increase in device performance and operational stability in solution processed inverted bulk heterojunction (BHJ) OPVs is demonstrated by introducing a zinc oxide (ZnO) or titanium oxide (TiO_x) interlayer between the electron collecting bottom electrode and the photoactive blend of poly(3-hexylthiophene) (P3HT) and PCBM. The introduction of transition metal oxide (TMO) interlayers resulted in a remarkable increase in power conversion efficiency (*PCE*) with a maximum value of 4.91 %. The structure and morphology of the dense, planar ZnO layers was controlled either by electrodeposition or spray pyrolysis techniques.

Organic/inorganic hybrid OPVs combine the advantages of both types of semiconductors and offer an alternative to replace fullerene based electron acceptor materials. The small molecule organic semiconductor, boron subphthalocyanine chloride (SubPc), is a promising donor material for fabrication of inverted planar hybrid solar devices using TiO_x as the electron acceptor. The TiO_x /SubPc cells demonstrate performance characteristics comparable to the best-reported polymer/ TiO_x hybrid cells. A relatively high photocurrent and a maximum external quantum efficiency (*EQE*) of 20 % lead to a *PCE* of 0.4 % under AM1.5 solar illumination.

Table of contents

Abstract.....	ii
Table of contents	iv
Declaration.....	vii
Acknowledgements	viii
List of publications and presentations	ix
List of abbreviations	xi
List of symbols and notations.....	xiii
List of compounds	xv
Chapter 1: Introduction	1
1.1 General overview	1
1.1.1 The need for PVs	1
1.1.2 Background to PVs	2
1.1.3 Development of OPVs	4
1.2 Semiconductor and device theory	6
1.2.1 Condensed matter.....	7
1.2.2 Principle of operation.....	10
1.3 Materials and properties	17
1.3.1 Electron donor materials	18
1.3.2 Electron acceptor materials.....	21
1.3.3 Interlayer and electrode materials	23
1.4 Device interface modification and nanostructuring	25
1.4.1 D/A interface modification	25
1.4.2 TMO interlayers.....	29
1.4.3 Hybrid OPVs.....	31
1.5 Project motivation and thesis outline	32
Chapter 2: Experimental and analysis.....	35
2.1 Thin film and device fabrication	35
2.1.1 Material purification	35
2.1.2 Substrate cleaning	37
2.1.3 Solution processed thin films.....	37
2.1.4 Organic molecular beam deposition (OMBD).....	40
2.2 Thin film analysis.....	46
2.2.1 Atomic force microscopy (AFM)	47
2.2.2 Electron microscopy (EM).....	49
2.2.3 Electronic absorption spectroscopy	55
2.2.4 X-ray diffraction	56
2.3 PV device analysis	58
2.3.1 The sun and solar simulation	59
2.3.2 <i>J-V</i> characteristics	61
2.3.3 External quantum efficiency (EQE) measurement	65
Chapter 3: Nanosphere synthesis	68

3.1	Introduction	68
3.1.1	Definitions.....	68
3.1.2	Emulsion polymerisation	69
3.1.3	Dynamic light scattering (DLS).....	72
3.1.4	Aim	73
3.2	Experimental	74
3.2.1	Nanosphere synthesis.....	74
3.2.2	Sphere size characterisation and solid content measurement	77
3.3	Results	78
3.3.1	Nanosphere synthesis in the round-bottom flask	78
3.3.2	Reactor based nanosphere synthesis	82
3.4	Conclusion.....	87
Chapter 4: Planar heterojunction devices		89
4.1	Introduction	89
4.1.1	Solution processed TSCuPc.....	89
4.1.2	Solution processed PTEBS	90
4.1.3	Aim	91
4.2	Experimental	92
4.3	Results	93
4.3.1	TSCuPc thin film based OPV devices	93
4.3.2	PTEBS thin film based OPV devices.....	101
4.3.3	Device stability	108
4.3.4	Film surface treatment	109
4.4	Conclusion.....	111
Chapter 5: 3D interdigitated organic D-A composite structures and OPV devices		114
5.1	Introduction	114
5.1.1	Background.....	114
5.1.2	Colloidal crystals and templating.....	115
5.1.3	Nanosphere self-assembly	116
5.1.4	Organic 3D open-cellular and composite nanostructures	119
5.1.5	3D nanostructured composite OPV devices	120
5.1.6	Aim	122
5.2	Experimental	123
5.2.1	Open-cellular organic thin films	123
5.2.2	Fabrication of 3D nanostructured composite devices.....	125
5.3	Results	126
5.3.1	Open-cellular organic semiconductor thin films.....	126
5.3.2	D-A 3D nanostructured composite OPV devices	134
5.4	Conclusions	141
Chapter 6: Electrode modification through TMO interlayers		144
6.1	Introduction	144
6.1.1	Background of TMO interlayers in OPVs	144
6.1.2	Aim	147
6.2	Experimental	147
6.2.1	TMO interlayer preparation and characterisation.....	147
6.2.2	OPV device fabrication and assessment	148

6.3	Results	149
6.3.1	Transmission	149
6.3.2	Morphology.....	149
6.3.3	XRD	151
6.3.4	OPV device performance.....	153
6.3.5	Conclusions.....	164
Chapter 7:	Planar inorganic/organic hybrid devices	166
7.1	Introduction	166
7.1.1	Background of TMO/organic hybrid OPVs.....	166
7.1.2	Aim	167
7.2	Experimental	168
7.3	Results and discussion.....	168
7.3.1	Electronic absorption and transmission	168
7.3.2	Morphology.....	169
7.3.3	OPV device performance.....	171
7.3.4	<i>EQE</i> and device structure comparison.....	176
7.3.5	Device stability	178
7.4	Conclusion.....	181
Chapter 8:	Conclusions and further work	183
8.1	Conclusions	183
8.1.1	Nanosphere synthesis.....	183
8.1.2	Planar heterojunction devices	184
8.1.3	3D interdigitated organic D-A composite structures and OPV devices ...	185
8.1.4	Transition metal oxide (TMO) interlayers.....	186
8.1.5	Planar inorganic/organic hybrid devices.....	187
8.2	Further work.....	188
References	190

Declaration

The work presented in this thesis has been conducted by myself at the Department of Chemistry at The University of Warwick in Coventry except the following experiments in Chapter 6. All zinc oxide thin films were deposited and characterised by Dr. Benoit Illy at the Department of Materials at Imperial College London, including X-ray diffraction and light transmission studies. The transmission electron microscopy cross-section images of complete photovoltaic devices, fabricated by focused ion beam/scanning electron microscopy in Chapter 6 were also prepared and taken by Dr. Illy. Part of this work was supervised by Prof. David McComb who is also at the Department of Materials at Imperial College London. I confirm that none of the work included has previously been submitted for a higher degree.

Parts of the work have been patented, published in scientific journals and were presented at meetings with BP Solar as well as at conferences.

Acknowledgements

Firstly, I would like to thank my supervisor Professor Tim Jones for his support and guidance through my PhD. Tim gave me the great opportunity to conduct research in a scientific area, which had fascinated me already for a long time during my undergraduate studies. I hope with this project, I was able to make a contribution towards the big dream of human kind to exploit the sun's enormous energy potential to realise a sustainable future energy supply. At the same time, I am grateful to the Department of Chemistry at The University of Warwick for providing such excellent research facilities as well as a stimulating atmosphere and my industrial sponsor BP Solar for their funding.

The person, I would like to thank in particular for his great help, support and advice, is my post-doc Dr. Paul Sullivan. Thanks also go to Dr. Raffaello da Campo, who was involved in all the work conducted in collaboration with Imperial College London. It should not be forgotten all the help, support and fruitful discussions, but also great tea breaks I had with all the other members of my research group: Ian Hancox, Virendra Chauhan, Nicola Beaumont, Tom Howells, Luke Rochford, Edd New and Dr. Junliang Yang.

Here in our department, I would like to thank Dr. Ross Hatton as well as Dr. Stefan Bon and their research groups for a great collaboration and valuable inputs. Thanks also go to Steve York and Richard Beanland in the electron microscopy group in Physics for all their time for training and help.

At Imperial College London great thanks go to Dr. Benoit Illy, Dr. Amy Cruickshank, Dr. Mary Ryan, Prof. David McComb and Dr. Jason Riley at the London Centre of Nanotechnology (LCN) for the close collaboration and supply of zinc oxide (ZnO) substrates as well as Dr. Martyn McLachlan and now Dr. Sarah Berhanu for their help and inputs on the nanosphere project.

Last but not least I thank Sabine and my whole family, but also my close friends Bodo and Nici for their endless support, although they were quite far away. Finally, the biggest thanks go to my girlfriend and closest friend Vicky for all her support.

List of publications and presentations

Publications:

- **S. Schumann**, S. A. F. Bon, R. A. Hatton and T. S. Jones, *Open-cellular organic semiconductor thin films by vertical co-deposition using sub-100 nm nanosphere templates*, Chemical Communications, 2009, 6478-6480.
- **S. Schumann**, R. Da Campo, B. N. Illy, A. C. Cruickshank, M. A. McLachlan, M. P. Ryan, D. J. Riley, D. W. McComb and T. S. Jones, *Inverted organic photovoltaic devices with high efficiency and stability based on metal oxide charge extraction layers*, Journal of Materials Chemistry, 2011, 21, 2381-2386.
- **S. Schumann**, R. A. Hatton and T. S. Jones, *Organic Photovoltaic Devices Based on Water-Soluble Copper Phthalocyanine*, Journal of Physical Chemistry C, 2011, 10.1021/jp109544m.
- B. N. Illy, A. C. Cruickshank, **S. Schumann**, R. Da Campo, T. S. Jones, S. Heutz, M. A. McLachlan, D. W. McComb, D. J. Riley and M. P. Ryan, *Electrodeposition of ZnO layers with controllable thickness and orientation and their applications as electron extracting interlayer in organic photovoltaics*, Journal of Materials Chemistry, submitted.
- A. C. Cruickshank, S. E. R. Tay, B. N. Illy, R. Da Campo, **S. Schumann**, T. S. Jones, S. Heutz, M. A. McLachlan, D. W. McComb, D. J. Riley and M. P. Ryan, *Electrodeposition of Nanostructured ZnO Films onto Organic Thin Films*, Chemistry of Materials, submitted.
- **S. Schumann**, C. Dearden, T. Howells, R. Pitt, R. Da Campo, P. Sullivan and T. S. Jones, *Hybrid organic-inorganic solar devices based on the small molecule organic semiconductor boron subphthalocyanine chloride*, to be submitted.
- **S. Schumann**, R. A. Hatton and T. S. Jones, *Organic photovoltaic devices based on water-soluble polythiophene*, to be submitted.
- **S. Schumann**, R. A. Hatton and T. S. Jones, *3D nanostructured donor-acceptor composite organic photovoltaic devices by colloidal templating*, to be submitted.

Patents:

- **S. Schumann**, R. A. Hatton, T. S. Jones, *Templating films*, GB090840.5, 2010 PCT filed.

Presentations:

- BP Solar industrial sponsor meetings, Imperial College London, 2007-2010
- Excitonic solar cells 2009, University of Warwick, August 2008, Poster
- Postgraduate Research Symposium 2009, University of Warwick, June 2009, Poster
- BP Solar OPV workshop, Washington DC, Dulles (USA), July 2009, Talk
- IUPAC Congress, Glasgow, August 2009, Talk
- MRS Fall 2009, Boston (USA), December 2009, Talk
- CMMP 2009, University of Warwick, December 2009, Poster
- Postgraduate Research Symposium 2010, University of Warwick, June 2010, Talk
First prize
- Bristol Nanoscience Symposium 2010, University of Bristol, September 2010, Poster
- Research Council UK, University of Oxford, October 2010, Poster
- MRS Fall 2010, Boston (USA), December 2010, Poster

List of abbreviations

3DOM	Three-dimensionally ordered macroporous solids
(A)/D	(Acceptor)/donor
AFM	Atomic force microscopy
AM	Air mass
AO	Atomic orbital
BE	Binding energy
BHJ	Bulk heterojunction
BSE	Backscattered electrons
CB	Conduction band
(D)/A	(Donor)/acceptor
DLS	Dynamic light scattering
DSSC	Dye-sensitised solar cell
ED	Electrodeposition
EM	Electron microscopy
FEG	Field emission gun
(O)FET	(Organic) field effect transistor
FIB	Focused ion beam
HOMO	Highest occupied molecular orbital
HV	High vacuum
(N)IR	(Near) infrared light
(O)LED	(Organic) light emitting diode
LUMO	Lowest unoccupied molecular orbital
MIS	Metal-insulator-semiconductor
MO	Molecular orbital
NSL	Nanosphere lithography
OMBD	Organic molecular beam deposition
PBG	Photonic bandgap
PDI	Polydispersity index

(O)PV	(Organic) photovoltaic
QCM	Quartz crystal microbalance
RH	Relative humidity
SAM	Self-assembled monolayer
SE	Secondary electrons
SEM	Scanning electron microscopy
SP	Spray pyrolysis
SPM	Scanning probe microscopy
STM	Scanning tunnelling microscopy
UV	Ultraviolet light
VB	Valence band
vdW	Van der Waals
vis	Visible light
XRD	X-ray diffraction

List of symbols and notations

ϕ	Workfunction
\AA	Angstrom (1 \AA = 0.1 nm)
$BE_{(exc.,gem.)}$	Exciton binding energy, geminate pair binding energy
c	Concentration
d	Actual film thickness
d_{hkl}	Lattice plane spacing or interplanar spacing of plane (hkl)
D	Diffusion coefficient
ε	Dielectric constant
$E_{(F)}$	(Fermi) energy
E_G	Energy bandgap
$E_{(EA,IP)}$	Electron affinity, ionisation potential
E_{Vac}	Vacuum energy level
EQE	External quantum efficiency
$f(E)$	Fermi-Dirac distribution
$F_{(hd,ic)}$	Hydrodynamic force, immersion capillary force
FF	Fill factor
(hkl)	Miller indices
$IPCE$	Incident photon conversion efficiency
Φ_{AM}	Incident angle (sun light)
$J_{(dark,ph)}$	Dark current density, photo current density
$J_{(SC)}$	(Short-circuit) current density
J_{mp}	Current density at maximum power point
$J-V$	Current density-voltage
λ	Wavelength
L_D	Exciton diffusion length
$\eta_{(abs,ed,ct,cc)}$	Quantum efficiency of photon absorption and exciton formation, exciton diffusion, charge transfer, charge collection
P_{inc}	Incident radiation power density

P_{mp}	Operational maximum power output
PCE	Power conversion efficiency
$r_{(B,C)}$	Bohr radius, Coulomb radius
$R_{(l,s,sh)}$	Load resistance, series resistance, shunt resistance
R_q	Surface roughness parameter
s	Step edge thickness, actual film thickness
$S_{(0,1)}$	First singlet ground state, excited state
θ	Angle of incidence (XRD)
T	Temperature
$T(\lambda)$	Transmission
$TC_{(hkl)}$	Texture coefficient of (hkl)
τ	Life time
$V_{(OC)}$	(Open-circuit) voltage
V_{mp}	Voltage at maximum power point

Structure notation

$A(m)/B(n)$	Layer of compound A with the actual thickness m in brackets covered by a layer of compound B with an actual thickness n
$A:B$	Blend of compound A with compound B
$A-B$	Ordered composite structure of compound A and B

List of compounds

AMPAD	2,2'-azobis(2-methylpropion amidine) dihydrochloride
BCP	2,9-dimethyl-4,7-diphenyl-1,10-phenantroline (bathocuproine)
C ₆₀	Buckminster fullerene
CuPc	Copper phthalocyanine
H ₂ Pc	Metal-free phthalocyanine
ITO	Indium-tin oxide
KPS	Potassium persulfate (K ₂ S ₂ O ₈)
MEH-PPV	Poly(2-methoxy-5-(2'-ethyl-hexyloxy)-p-phenylene vinylene)
MoO _x	Molybdenum oxide
MWCNT	Multiwall carbon nanotube
NaSS	Styrene-4-sulfonic acid sodium salt
NH ₃	Ammonia
P3HT	Poly(3-hexylthiophene)
(M)Pc	(Metal) phthalocyanine
PCBM	Phenyl-C ₆₁ -butyric acid methyl ester
PEDOT:PSS	Poly(3,4-ethylenedioxythiophene) poly(styrene sulfonate)
PPV	Poly(phenylene)vinylene
PS	Polystyrene
PTEBS	Sodium poly[2-(3-thienyl)ethoxy-4-butylsulfonate]
SDS	Sodium dodecyl sulphate
SubPc	Boron subphthalocyanine chloride
TCO	Transparent conducting oxide
THF	Tetrahydrofuran
TiO _(x/2)	Titanium oxide, titanium dioxide
TMO	Transition metal oxide
TSCuPc	3,4',4'',4'''-copper phthalocyanine-tetrasulfonic acid tetrasodium salt
WO _x	Tungsten oxide
ZnO	Zinc oxide

Chapter 1: Introduction

In this chapter a general overview is given of the need of photovoltaic (PV) and organic photovoltaic (OPV) devices in particular, including the background and challenges. The general theory and concepts of semiconductors and devices are also explained. Furthermore, the materials used and their properties are explained in detail. Another section covers the concept of interface modification including template assisted nanostructuring, the use of electrode interlayers and hybrid device structures. The chapter is closed with an outline of the project motivation and the thesis content.

1.1 General overview

This section covers the world's energy challenge and how PVs, and more specifically OPVs, can contribute to a sustainable solution. In a general background section the different types of PVs are broadly explained dividing them into three technology generations, with OPVs being the least advanced. More details on OPV development and its challenges are revealed in the last section.

1.1.1 The need for PVs

With increasing world population and growing industrial use a steep increase in global energy demand is unavoidable. Conventional energy sources, including fossil fuels such as oil, gas and coal are limited in supply, and the predicted production peak is likely to be reached soon. With combustion based energy supply come two of the biggest threats to human and animal health: air pollution and greenhouse gases associated with global warming.^[1] Emitted carbon dioxide (CO₂) is a greenhouse gas and one of the main contributors to global warming, which has already led to a rise of the earth's global mean surface temperature by 0.6 °C during the twentieth century.^[2]

To meet the increasing energy demand, but also to work towards clean, renewable, emission-free energy supply, new alternative and sustainable energy sources

are required including hydro, wind, wave, tidal, biomass, geothermal and solar power.^[3, 4] Most of these technologies are either directly or indirectly fuelled by the sun, which is the only non-polluting renewable energy source available to mankind on a sufficient scale to cover present and future demand. PV devices offer an amazing potential to harvest and convert solar power into electricity due to their great flexibility and compatibility for powering portable devices and local grids to the attachment to buildings, modern transport vehicles, including solar cars, boats and even airplanes, but also applications in space technology.^[5]

The current challenge is to overcome the high energy input and fabrication cost involved in the production of PV devices. OPVs offer the potential of a new low-cost renewable solar PV technology which could potentially lead to such a large-scale application.^[6]

1.1.2 Background to PVs

Edmund Bequerel discovered the photovoltaic effect in 1839, but it took a further 100 years until the first successful PV devices were developed. After the discovery and development of p-n junction doping in crystalline silicon and progress in the fabrication of high quality silicon wafers in the 1950s, this technology rapidly developed into a relatively efficient, commercialised energy source.^[7] With silicon solar technology based on doped group IV semiconductors the first generation of PVs was born with two more generations to follow.

Conventional inorganic solar panels for terrestrial use are based on mono- or poly-crystalline p-n doped silicon with efficiencies of up to 25 %, ^[8] but latest technologies have already passed this limit (see Figure 1.1)^[9]. Crystalline silicon cells require a high energy input for large-scale production with high fabrication costs. Amorphous silicon with much lower fabrication cost can also be employed but leads to a lower cell efficiency of ~10 %. ^[8]

Second generation cells were developed shortly after the first, employing element combinations from groups III and V, e.g. gallium arsenide (GaAs) and indium phosphide (InP), or II and VI, e.g. cadmium sulphide (CdS) and cadmium telluride (CdTe), enabling

the growth of thin inorganic films which can be tailored in absorption behaviour to the solar spectrum.^[10] High efficiencies have been reached with multijunction III-V cells with around 36 %.^[8] Major drawbacks are the low abundance and high toxicity of certain elements used in the cells.

The latest generation of PVs are organic and organic/inorganic hybrid PVs which rely on stable exciton formation and efficient exciton diffusion. The cells usually employ at least one organic electron donor material in the form of a dye or chromophore thin film to harvest sun light. In most types of OPVs an organic compound is also employed as an electron acceptor material. All organic compounds consist mainly of the elements carbon, nitrogen, oxygen and hydrogen with variations of metals in complexes and other elements. The main advantages of this emerging generation are the use of low-cost compounds and fabrication technology, as well as favourable properties such as flexibility, non-toxic materials and low overall weight.^[11]

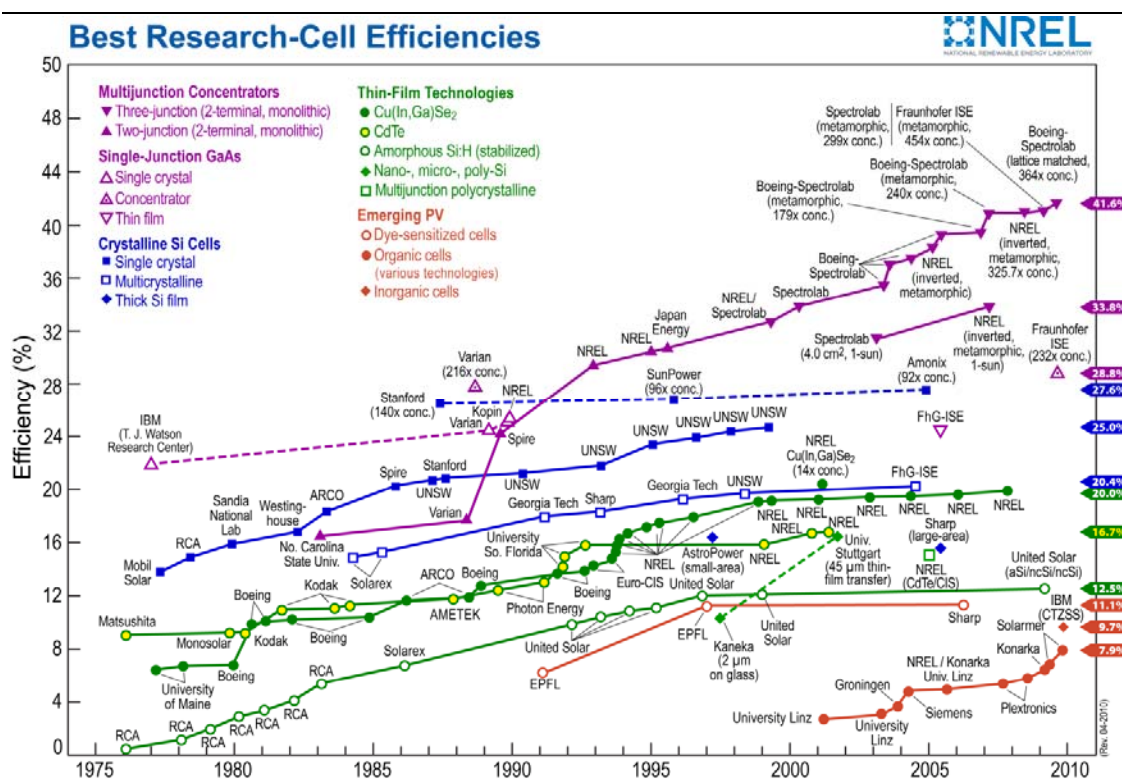


Figure 1.1 Development of PV devices including OPVs quoting the efficiencies for different technologies from 1976 until 2010.^[9]

Excitonic solar cells or OPVs can be divided into three main categories: dye-sensitised solar cells (DSSC), OPVs based on either small molecules or polymers, and hybrid organic/inorganic OPVs. The development of most PV technologies is summarised in Figure 1.1.^[9]

DSSCs were initially invented in 1991 by O'Regan and Graetzel and reached an early record of 12 % power conversion efficiency (*PCE*).^[12] The concept is based on a photo-electrochemical PV cell with a dye as a photon acceptor and electron donor, titanium dioxide (TiO₂) as an electron acceptor and an electrolyte to enable redox chemistry and charge transfer between the photo-sites and the electrode.^[13, 14] All other solid state OPVs are explained in detail in the following sections.

1.1.3 Development of OPVs

Early organic solar cells were based on small molecule single layer structures. These devices were made by deposition of conjugated molecules such as phthalocyanines or porphyrins as thin film layers of thicknesses around 100 nm sandwiched between two electrodes.^[15] Exciton dissociation in such Schottky cells is based on either defects and traps within the organic film or dissociation in the thin depletion region close to the electrode which makes such a device very inefficient. The first major advance was the substitution of one metal electrode by a metal oxide coated electrode providing an electrode workfunction difference. This type of PV cell is known as a metal-insulator-semiconductor (MIS) device.^[16] An important step was made by Tang in 1986 who established a new solar cell structure by using an organic/organic heterojunction.^[17] By employing two organic semiconductors, copper phthalocyanine (CuPc) as an electron donor and a perylene derivative, 3,4,9,10-perylenetetracarboxylic bis-benzimidazole (PTCBI), as an electron acceptor with different energy level offsets, significantly improved exciton separation at the electron donor/acceptor (D/A) interface was achieved. The cell efficiency was also improved due to both better separation of electron and hole transport in the appropriate films and less charge recombination in the two different materials. A further improvement was the use of Buckminster fullerene (C₆₀) in organic

solar cells, a material which was discovered by Kroto *et al.* in 1985.^[18] C₆₀ makes an ideal electron acceptor and provides a relatively large exciton diffusion length, L_D .^[19]

By employing C₆₀ in a heterojunction device architecture, the organic solar device performance increased significantly. In the last few years, devices employing vacuum deposited small molecules, such as phthalocyanines, subphthalocyanines, anthracenes and oligothiophenes reached device efficiencies of up to 5.2 %.^[20-23]

One of the crucial efficiency limiting factors in OPVs is the relatively short L_D in the range of a few tens of nanometres in polycrystalline organic semiconductors as photo-generated excitons have to reach the heterojunction interface for efficient exciton dissociation before recombining.^[24-26] A more detailed description can be found in Section 1.2.2. Therefore, a main part of organic heterojunction device performance optimisation is to find a compromise of the film thickness required for maximum absorbance and the limited L_D for efficient exciton dissociation.^[26, 27] This problem is also the main limiting factor of simple planar bilayer OPV devices.

By stacking two or more cells with the same or complementary optical band gaps in a tandem arrangement equipped with just a thin recombination layer, the layer thickness in the individual cells can be kept thin to match L_D with increased light absorption in the additional layers. The series connection of the cells leads to an increase in open-circuit voltage (V_{OC}).^[28, 29] Therefore, the efficiency can be significantly improved as demonstrated for small molecules by Cheyns *et al.* with 5.2 %^[30] and Heliatek with 8.3 %, ^[31] as well as for polymer/fullerene systems by Sista *et al* with 5.8%^[32] and by Kim *et al.* with 6.5 %^[33] reported for all-solution processed tandem devices.

Another way to improve the device current density is intermixing of the donor and acceptor material to minimise the exciton pathway. In 1995 the first intermixed bulk heterojunction (BHJ) OPV device was fabricated by Heeger *et al.* by spin-coating a solution mixture of an electron donor polymer and electron acceptor fullerene derivative.^[34] The main advantage of this type of cell is that spontaneous phase segregation takes place between the electron donor (polymer) and electron acceptor (fullerene derivative), which leads to the formation of nanoscale domains.^[35-38] This phenomenon enhances the capability of creating an increased heterojunction interfacial

area allowing higher charge separation efficiency with extremely fast electron transfer from the donor to the acceptor.^[39] This resulted in a very rapid development in BHJ OPV technology with the photoactive blend of poly(3-hexylthiophene) (P3HT) and phenyl-C₆₁-butyric acid methyl ester (PCBM) being the most studied system.^[40-42] Polymer design has recently been directed at increasing V_{OC} through intelligent tuning of the energy level difference between the highest occupied molecular orbital (HOMO) energy of the electron donor and the lowest unoccupied molecular orbital (LUMO) energy of the electron acceptor, whilst also optimising light absorption across the solar spectrum.^[43-45] This development has resulted in $PCEs$ as high as 7.4 %.^[46]

A different approach to solve the L_D problem was a D/A mixed layer system fabricated by co-deposition with organic molecular beam deposition (OMBD), providing an interpenetrating D/A interface. This was first introduced by Hiramoto,^[47] with Sullivan and Heutz *et al.* undertaking further investigations with particular focus on mixed layer compositions in the CuPc/C₆₀ system.^[48, 49] Very high device performance efficiencies of 5 % were later reported by Xue *et al.* using this approach.^[50]

Despite the overall performance improvement in both BHJ and mixed layer structures through enhanced exciton diffusion efficiency, charge transport is compromised due to the random nature of these mixed structures.^[26] To overcome this problem a more controlled interpenetrating D/A composite structure is required that has the advantages of mixed layers, but with well structured charge transport paths. OPV device limitations and new approaches to tackle this issue are discussed in detail in section 1.4.

Although good progress has been made in recent years, OPVs are at the moment still not able to compete with inorganic PVs in their PCE . However, despite this lower efficiency, the cheaper materials and lower manufacturing costs could make them competitive in the near future, with good market potential.^[51]

1.2 Semiconductor and device theory

All types of PVs are based on the combination of different semiconductors and metals. Semiconductors can be of inorganic or organic nature, but are classified and

defined the same way using similar concepts and conventions. In order to understand organic/organic and organic/inorganic heterojunctions, so called hybrid heterojunctions, as well as the resulting OPV devices, semiconductor theory and its implementation in OPVs is explained in the following sections.^[52, 53]

1.2.1 Condensed matter

One atom ($N=1$) consists of atomic orbitals (AO)s with discrete energy levels, only (1s) AOs in the case of hydrogen ($1s^1$) and helium ($1s^2$), but multiple AOs for all other elements. The AOs are populated by paired electrons of opposite spin up to the chemically active valence level which also allows partially filled orbitals (Figure 1.2). When two atoms ($N=2$) with unpaired valence electrons in their AOs are brought in close proximity, they can form bonds and create a molecule. The bonds are based on orbital energy splitting leading to a deeper lying, energetically favourable bonding and a higher energy, unfavourable, anti-bonding molecular orbital (MO) of discrete energies. The resulting MOs are slightly higher and lower in energy than the original AOs. The energetically deeper set of MOs is evenly populated with paired electrons establishing the bond. The higher lying anti-bonding set of MOs is empty. When larger numbers of atoms are combined ($N=\text{large}$) as found in atomic clusters, multiple splitting with high MO densities at discrete energy levels are established. This eventually leads to the formation of continuous bands when a large number is arranged in an ordered crystal. For inorganic materials the highest occupied band is called the valence band (VB) and the lowest unoccupied band is called the conduction band (CB). Similarly, for organic materials the relevant bands, mainly based on extended conjugated systems, are also referred to as MOs, i.e. highest occupied molecular orbital (HOMO) and lowest unoccupied molecular orbital (LUMO). Depending on the energy band distribution, which is defined by the density of states, bands continuously overlap to form a metal or are separated by a band gap, E_G , to form a semiconductor or insulator. Semiconductors have a small E_G of up to about 4 eV. If E_G exceeds 4 eV, it is usually defined as an insulator. Metals are always conducting due to an excess of delocalised valence electrons which also define the metallic bonding. Semiconductors are insulating at 0 K, but gain conductivity with

increased temperature due the population of the CB by thermally excited electrons ($E_G < k_B T$). This creates vacancies, positively charged holes, in the VB. For insulators the band gap is too large to be overcome by thermal excitation making charge flow impossible.

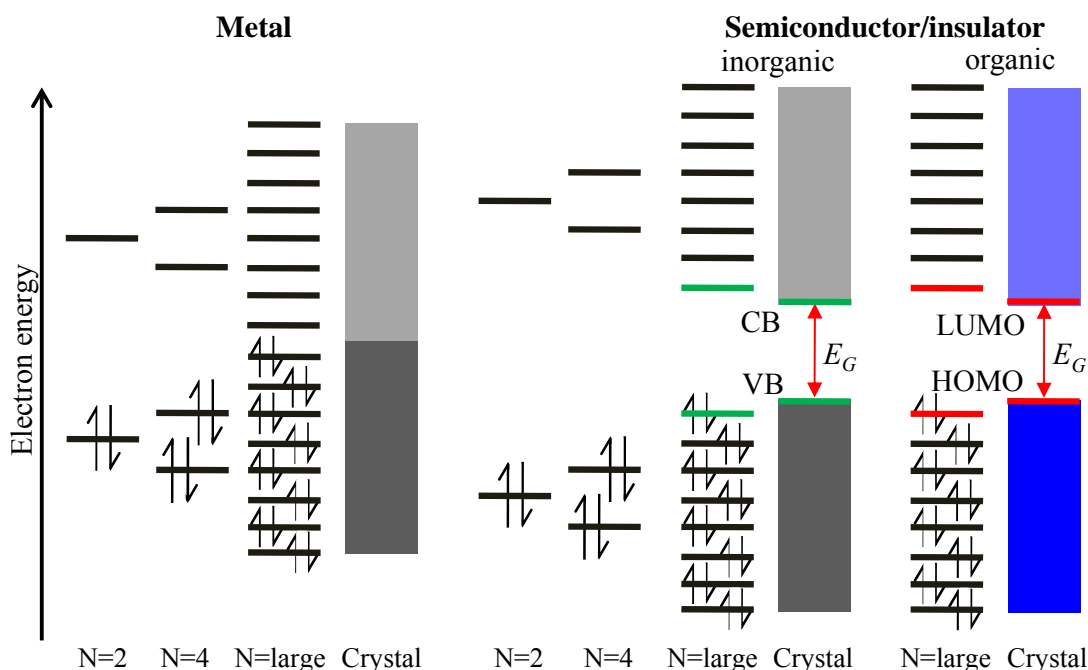


Figure 1.2 As the number of atoms, N , increases towards a cluster and then a crystal, the AOs split first into discrete, later merged multiple energy levels and finally form bands. In a metal the bonding and anti-bonding bands are overlapping. In a semiconductor or insulator of organic or inorganic nature, the bands or MOs are separated by an energy bandgap, E_G .

As shown in Figure 1.3 the CB edge energy level of a semiconductor is defined by the electron affinity (E_{EA}) of the material measured from the vacuum level (E_{Vac}). E_{EA} is defined as the least amount of energy needed to remove an electron from a singly charged negative ion or from the solid to the vacuum level. In other words, it describes how easy an electron can be accepted by the solid. E_{Vac} is the energy level at which an electron from the solid is far enough away such that it does not experience any interaction forces from the solid. The VB edge is defined by the ionisation potential (E_{IP}), also measured from the vacuum level. E_{IP} is the least energy required to remove an electron from an atom or molecule in its electronically neutral ground-state.

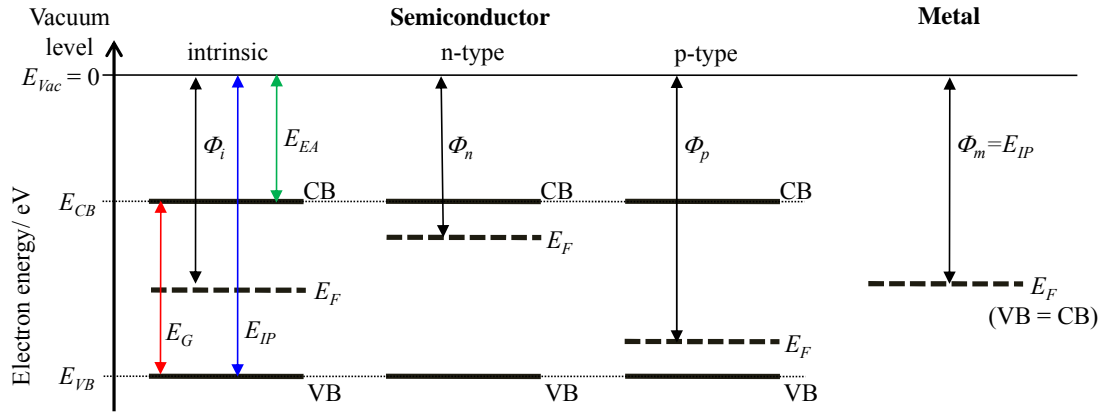


Figure 1.3 Band profiles of a metal and different types of semiconductors: intrinsic, n-type and p-type.

The likelihood of an electron being found in a certain level with energy E , is defined by the Fermi-Dirac probability distribution function, $f(E)$, shown in Equation 1.1,

$$f(E) = \frac{1}{e^{\frac{E-E_F}{k_B T}} + 1} \quad \text{Equ. 1.1}$$

where k_B is Boltzmann's constant, E_F is the Fermi energy or Fermi level, and T is the temperature. E_F is the theoretical energy level at which the population probability of an electron is 0.5. This is of special importance for both metals and semiconductors and plays a major role in further semiconductor classification. Another important material parameter linked to E_F is the workfunction ϕ_w , which is defined as the potential required to remove the least bound electron (Equation 1.2).

$$\phi_w = (E_{vac} - E_F) \quad \text{Equ. 1.2}$$

For metals E_F defines the band edge of the VB and CB due to band overlap and the workfunction of the metal, ϕ_m , is equal to E_{IP} .

Semiconductors can be divided into two classes; intrinsic and extrinsic semiconductors (see Figure 1.3). Extrinsic semiconductors can further be split into n-type and p-type. Intrinsic semiconductors are assumed to be perfect crystals without any defects or impurities. At equilibrium, the E_F is situated exactly midway between the VB

and CB in an inorganic semiconductor and between the HOMO and LUMO in an organic semiconductor with a workfunction ϕ_i . All organic semiconductors if not doped in any way are considered to be intrinsic semiconductors. n-type semiconductors are semiconductors doped with impurities which provide additional valence electrons to the host material. These impurities establish occupied energy levels close to the CB which also acts as an electron donor level. As a consequence, E_F is shifted between these induced electron donor energy levels and the CB. Equally, when an intrinsic semiconductor is doped with hole-rich and therefore electron accepting impurities, an acceptor energy level is established close to the VB with E_F being situated in between. The workfunction of an n-type semiconductor (ϕ_n) is lower and the workfunction of a p-type semiconductor (ϕ_p) is higher than the ϕ_i of its equivalent undoped intrinsic semiconductor.

1.2.2 Principle of operation

A typical heterojunction bilayer OPV device with its energy level schematic in open circuit condition can be seen in Figure 1.4a. The basic principles of operation of a D/A heterojunction OPV device, the conversion of solar energy into electrical energy, can be divided into four steps: light absorption and exciton formation (η_{abs}), exciton diffusion (η_{ed}), charge transfer (η_{ct}) and charge collection (η_{cc}). These processes are shown in the schematic of a closed circuit OPV device in Figure 1.4b.^[26, 54, 55] The short-circuit current (J_{SC}) of an OPV device depends on these four individual processes.

The external quantum efficiency (EQE) characterises the number of collected charges per incident photon which can be expressed as the product of the quantum efficiencies of all the processes involved (see Equation 1.3).^[56]

$$EQE = \eta_{abs}\eta_{ed}\eta_{ct}\eta_{cc} \quad (\text{Equ. 1.3})$$

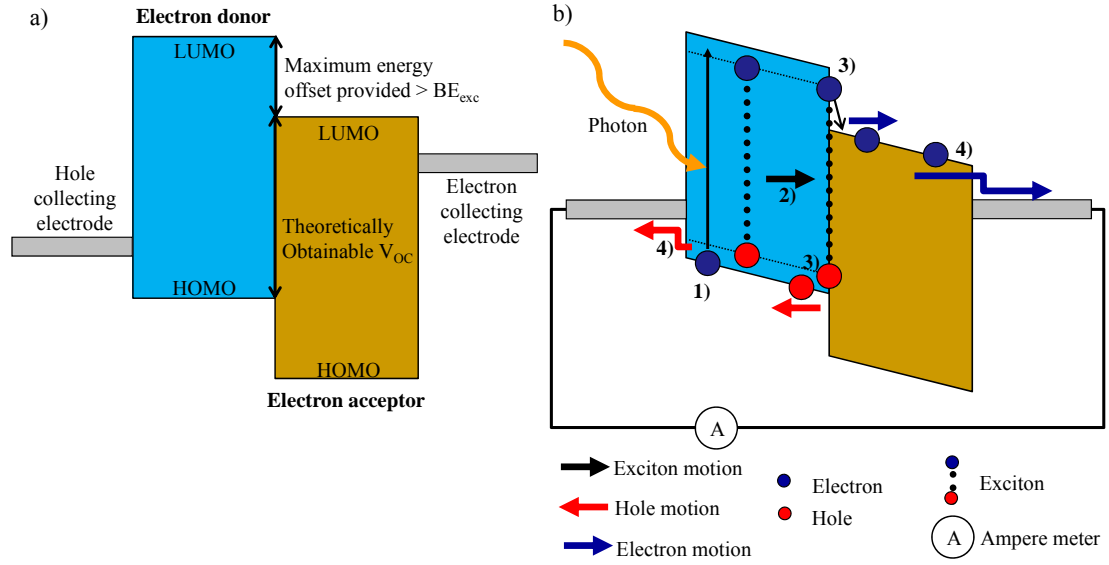
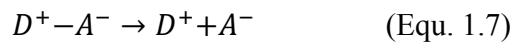
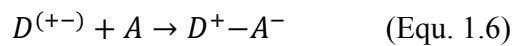


Figure 1.4 Schematic of an OPV heterojunction device in a) open and b) closed circuit condition. b) Basic principle of operation of a D/A heterojunction OPV device: 1) light absorption and exciton formation η_{abs} , 2) exciton diffusion η_{ed} , 3) exciton dissociation (charge transfer) η_{cts} , and 4) charge collection η_{cc} . (see also Equation 1.3 as well as 1.4 to 1.7)

Firstly, an incident photon promotes excitation of an electron from the electronic singlet ground state, S_0 , of a donor (D) to the first electronic singlet excited state, S_1 (D^*) (Equation 1.4). The resulting electron-hole pair relaxes from the excited state to the Coulombically stabilised exciton (D^{+-}) with a binding energy, BE_{exc} (Equation 1.5). After exciton diffusion to an appropriate interface with an acceptor (A) the exciton dissociates into separate charge carriers (D^+) and (A^-) on either side of the heterojunction (Equation 1.6). The charge carriers are still bound with Coulombic attraction across the interface, resulting in a geminate pair (D^+A^-). After overcoming the geminate pair binding energy, BE_{gem} , the pair splits into free charge carriers (Equation 1.7).



In all four stages recombination to S_0 can occur, including internal conversion, as well as exciton, geminate pair and bimolecular recombination.^[57, 58] Any recombination during the process, before the free charges are collected at either electrode, are counted as losses which reduce the *EQE* and have direct impact on the current output and overall efficiency achievement.^[59]

1.2.2.1 Absorption

Conjugated small molecules and polymers have the ability to absorb light from the visible range of the solar spectrum. The absorption bands are usually intense due to a good wavefunction overlap of the electronic ground state and lowest excited state. The transitions can also be influenced by morphology and molecular stacking.^[54] When a photoactive donor molecule absorbs a photon of a discrete energy $h\nu$, an electron is excited from the HOMO to the LUMO leaving a positively charged hole in the HOMO. This excited state relaxes immediately into an energetically more favourable bound excited state stabilised by Coulombic attraction of the oppositely charged species. Such an electron-hole pair is called an exciton and is neutral in electric charge. The efficiency of this step is referred as η_{abs} and it has significant importance for the operation of an OPV device.^[60]

1.2.2.2 Excitons

Depending on the nature of the photoactive material, the magnitude of BE_{exc} through Coulombic stabilisation can vary from a few meV in inorganic semiconductors up to a few tenths of an eV for organic semiconductors. BE_{exc} is mainly defined by the dielectric constant ϵ of the material.^[61-63] Typically, inorganic semiconductors have a high $\epsilon > 10$ which leads to a low $BE_{\text{exc}} = 5-27$ meV, enabling facile exciton dissociation even at room temperature. For organic semiconductors with low ϵ ($\sim 3-4$) the BE_{exc} can take values between 0.2 and 1.4 eV, but is typically around 0.3-0.6 eV.^[64, 65]

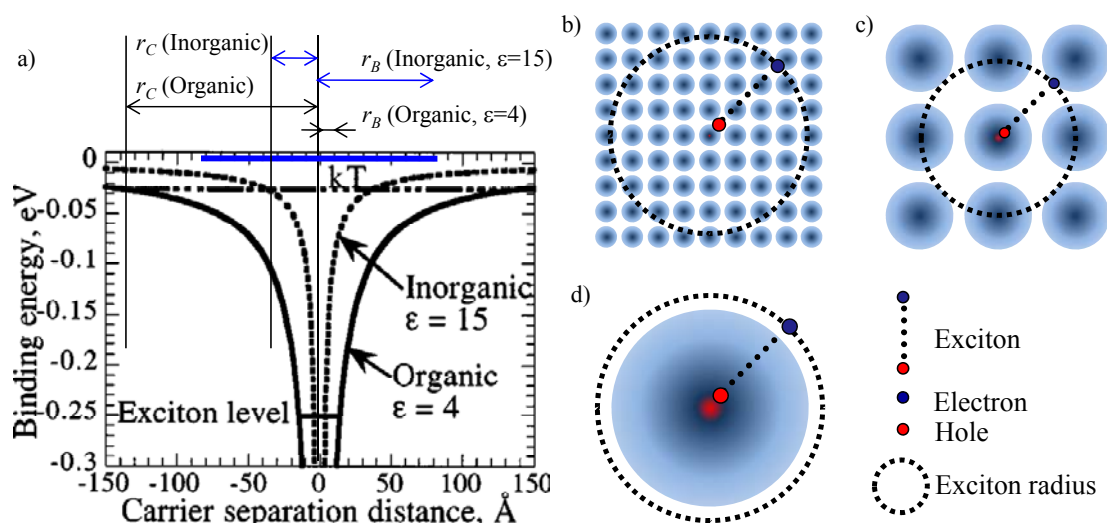


Figure 1.5 a) Binding energy diagram of a typical organic ($\epsilon=4$) and inorganic ($\epsilon=15$) semiconductor comparing the Bohr radius r_B and Coulomb radius r_C (adapted from Hanna *et al.*).^[61] The three different types of excitons include b) Mott-Wannier, c) charge-transfer and d) Frenkel exciton.

The type of exciton can be characterised by the factor, γ , which is defined by the ratio of the Coulomb potential radius, r_C , and the spatial dimensions of an exciton approximated by Bohr radius, r_B (Figure 1.5a).^[66] In an inorganic semiconductor, γ is <1 since $r_B \gg r_C$. The strong interatomic electronic interactions of covalently bound inorganic atoms allow a large r_B leading to delocalised charges. This type of exciton is called a Mott-Wannier exciton (see Figure 1.5b).^[66] The other extreme is a tightly bound Frenkel exciton found in organic semiconductors, and small molecular semiconductors in particular, with $\gamma > 1$ and $r_B < r_C$ due to spatial restriction of the exciton wave function to one molecule (Figure 1.5d). Semiconducting polymers form charge-transfer excitons which are an intermediate between the other two types. (Figure 1.5c).^[60]

1.2.2.3 Exciton diffusion

Excitons are mobile electrostatically neutral species, which can diffuse through a material via an energy transfer process that is not influenced by electric fields. Due to the low exciton density generated, the diffusion process is not driven by a density gradient. The idea of a random hopping process between molecules, domains and whole crystals is well established as the main exciton diffusion mechanism. Generally, the diffusion

process is measured by the material specific exciton diffusion length L_D , which is a function of the diffusion coefficient D and average lifetime τ as can be seen in Equation 1.8. τ is defined as the average duration from exciton formation to its recombination, which is typically of the order of nanoseconds.^[11]

$$L_D = \sqrt{D\tau} \quad (\text{Equ. 1.8})$$

Typically, L_D in organic semiconductors is far below 100 nm and quoted values can vary considerably. L_D for CuPc has been reported between 10 nm and 68 nm,^[24, 26] for C₆₀ around 40 nm,^[26] SubPc between 8 and 28 nm,^[67, 68] and pentacene around 65 nm.^[25] For polymeric semiconductors L_D is even lower, typically <10 nm.^[69] The diffusion process can be greatly hindered by early recombination at grain boundaries, defects and trap sites. Exciton diffusion to an appropriate heterojunction interface is crucial for efficient exciton dissociation before recombination. This highlights the dilemma of desired thick films for high absorption and preferred thin films for efficient exciton diffusion asking for new solutions based on interface nanostructuring (see section 1.4.1). The quantum efficiency of exciton diffusion to an interface is denoted as η_{ed} .

1.2.2.4 Exciton dissociation

To split an exciton successfully into two free charges the initially gained stabilisation energy of BE_{exc} in strongly bound Frenkel excitons has to be overcome. Unlike inorganic semiconductors, excitons in organic semiconductors are unable to gain the BE_{exc} equivalent from thermal energy at room temperature, which is roughly 25 meV. However, the binding energy can be overcome by the favourable energy offset of at least BE_{exc} at a D/A heterojunction to build an attractive energy pathway to enhance exciton dissociation, the development of which proved one of the biggest breakthroughs in OPV design. For a donor exciton the energy difference between the donor-LUMO and the acceptor-LUMO has to be greater than BE_{exc} to allow a favourable path for electron transport. Accordingly, for an acceptor exciton the energy difference between the acceptor-HOMO and the donor-HOMO has to be greater than BE_{exc} to allow a favourable path for hole transport.^[27] Charge transfer during dissociation is a very quick process

which only takes a few hundred femtoseconds or less.^[70, 71] The dissociation process is much quicker than any other competing process. This leads to a quantum efficiency η_{ct} of almost 100 %.^[26, 72] The charges of the split exciton then rearrange at the D/A interface to a Coulombically bound geminate pair.^[73] The geminate binding energy BE_{gem} is high due to the low dielectric constant.^[74, 75] Geminate pair splitting is mainly performed by the electric build-in field of the device.^[54, 56] To a first approximation the maximum obtainable V_{OC} of a specific D/A compound pair is defined by the energy level difference between the HOMO energy level of the electron donor and the LUMO energy level of the electron acceptor, also referred to as the effective band gap or interface gap, with reductions accounting for BE_{gem} and band bending.^[69, 76-78]

1.2.2.5 Charge transport and collection

The free charges after exciton and geminate dissociation have to be transported to the electrodes and then collected leading to a current flow in an external circuit. In an OPV device holes are conducted by the electron donor material to the hole collecting electrode and electrons are conducted by the electron acceptor material to the electron collecting electrode. The charge collection quantum efficiency η_{cc} depends strongly on carrier mobility. Charge mobility through an organic semiconducting material is mainly determined by the crystalline structure of the material. High charge mobilities can be found in monocrystalline covalently bound inorganic materials where long range crystalline order allows suitable charge transport pathways. However, organic semiconductors show weaker intermolecular bonding including van der Waals and π - π interactions. They tend to be polycrystalline or even amorphous, and hence have much lower charge carrier mobility based on charge carrier hopping between adjacent molecules and domains.^[55] Depending on the morphology and crystalline structure of an organic semiconductor film the mobility varies over several orders of magnitude from 10^{-6} - 10^{-3} $\text{cm}^2\text{V}^{-1}\text{s}^{-1}$ for disordered amorphous films to more than 1 $\text{cm}^2\text{V}^{-1}\text{s}^{-1}$ for ordered crystalline materials.^[58] Trap and defect sites can also impede charge transport and slow them down, which significantly lowers charge mobility. Furthermore, imbalanced charge mobility of holes and electrons in a device leads to charge build-up in specific layers and disturbs the build-in field.^[79]

Once the charges reach the organic/electrode interface charge injection into the electrode can take place. The work function of the contacts should align with the relevant energetic MO or band of the organic (HOMO/LUMO) or inorganic (VB/CB) material, otherwise energy barriers can hinder charge transfer. In an ideal case there is perfect alignment with no barrier; an ohmic contact.^[80] To obtain good contact energy level alignments with the limited selection of electrode materials available, electrode modification using self-assembled monolayers (SAM)s and different substrate treatments have been employed with great success.^[81-83] Recently, metal oxide interlayers have also been employed between the electrode and photoactive layers to form intermediate, energetically well-aligned charge selective contacts with high charge specific mobility.^[84, 85]

Depending on the type of device, fabrication methods and materials, the role of the specific charge collecting electrodes is interchangeable. Most OPV devices found in the literature follow the regular D/A device architecture with the transparent bottom electrode being the hole collection point and the top metal electrode being the electron collection electrode (see Figure 1.6a). In an acceptor/donor (A/D) inverted device architecture, the specific charge collecting electrodes are on opposite sides (see Figure 1.6b), giving advantages in certain systems such as vertical phase separation properties in BHJ OPVs and improved stability through decoupling of the active device layer from ITO.^[86, 87]

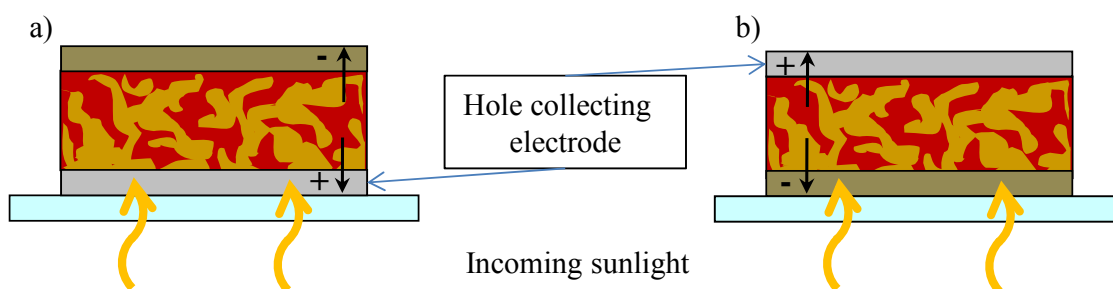


Figure 1.6 Schematic of a) a regular and b) an inverted OPV device architecture with specific charge collecting electrodes on opposite sides.

1.3 Materials and properties

In OPV heterojunctions the semiconductor with the HOMO and LUMO energy level lying closer to the vacuum level and therefore with lower E_{IP} and E_{EA} is always referred to as the electron donor material. The other semiconductor, with the HOMO and LUMO or VB and CB energy level lying further away from the vacuum level, and therefore with a higher E_{IP} and E_{EA} , is referred to as the electron acceptor. Typical donor materials are small molecules such as phthalocyanines or polymers such as polythiophenes. Possible acceptor materials can be either organic, e.g. fullerenes, or inorganic, e.g. transition metal oxides (TMO) in nature. Efficient devices are based on compatible D/A combinations with suitable energy level positions.

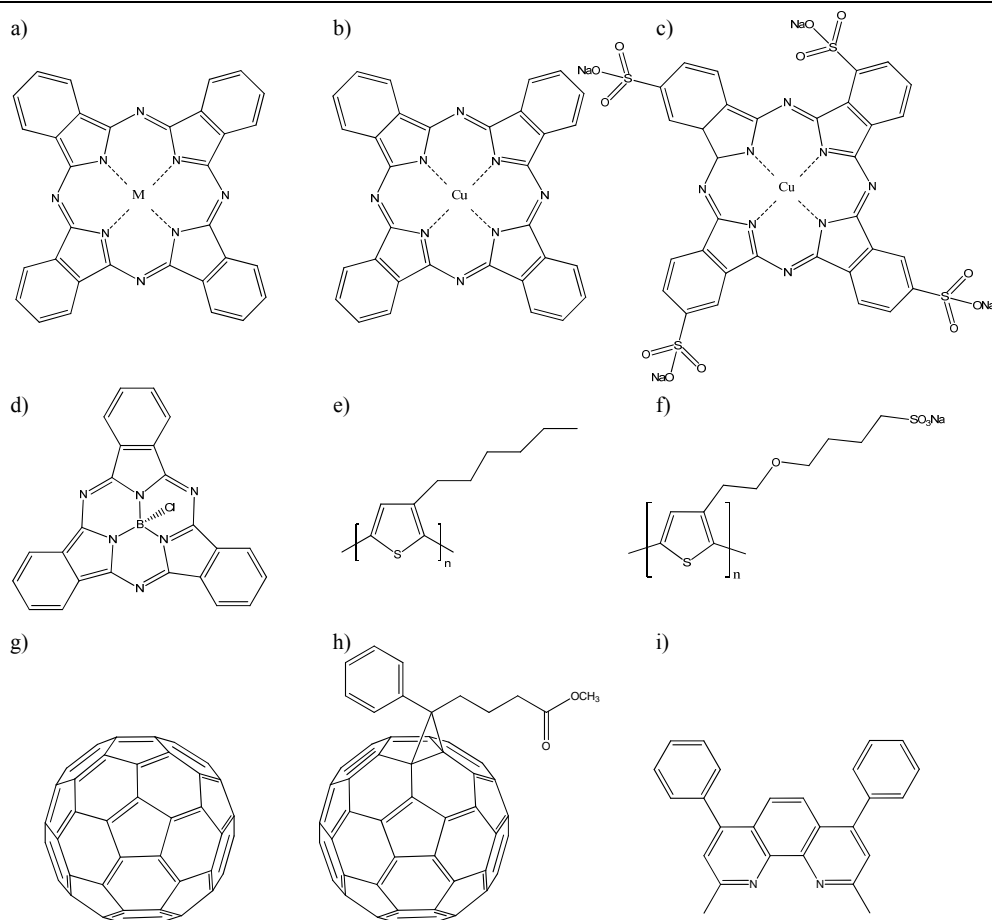


Figure 1.7 Molecular structures of organic semiconducting materials used in OPVs. a) to f) electron donor materials: a) MPc, b) CuPc, c) TSCuPc, d) SubPc, e) P3HT and f) PTEBS. g) and h) electron acceptor materials: g) C_{60} and h) PCBM. i) Exciton blocking material: BCP.

To achieve efficient charge extraction and minimal charge and exciton losses at the electrodes, electrode interlayers based on either TMOs or specific organic molecules are employed. Figure 1.7 introduces the molecular structure of all the organic materials used in further chapters.

1.3.1 Electron donor materials

1.3.1.1 Phthalocyanines

Since their discovery in 1934, phthalocyanines (Pcs) have been used as dyes in inks, and colouring for plastics and clothes (Figure 1.7a-c).^[88] More recently interest in this class of molecule has been in their use in organic electronics including organic field-effect transistors (OFET), sensing elements, organic light emitting diodes (OLED) and OPVs, which demonstrates the versatility of Pcs.^[26, 89-91]

Pcs are 18 π -electron heteroaromatics, derived from porphyrins, with a large π -system. These macrocycles, also defined as the phthalocyanato anion ($C_{32}H_{16}N_8^{2-}$), can act as a metal chelating ligand. The central ligand cavity can accommodate as many as 70 different metal ions and metal oxides (MPc), as well as hydrogen in the simple metal-free type (H_2Pc).^[92] Pcs prove to be chemically and thermally stable and can be vacuum deposited. In addition to the variety of metal centres, the molecules can be tuned in their solvent solubility as well as electronic and crystalline properties by substitution of the hydrogen groups at the outer ring. Halogenation, for example, shifts the HOMO and LUMO further away from E_{vac} due to the introduction of electron withdrawing groups making it a good electron acceptor.^[93] Substitution by ionic sodium sulfonic acid groups ($-SO_2Na$) drastically increases the solubility of otherwise poorly soluble Pcs in water.^[94]

Blue coloured CuPc and its derivative, 3,4',4'',4'''-copper(II) phthalocyanine-tetrasulfonic acid tetrasodium salt (TSCuPc), show good absorption in the range 550-700 nm. With a HOMO at -5.1 eV and the LUMO at -3.5 eV they exhibit suitable electron donor properties in combination with fullerenes for OPV devices.^[26]

Planar Pcs such as CuPc have the ability to undergo co-facial intermolecular stacking based on π - π system overlap of adjacent molecules. A typical molecular crystal structure adopted by CuPc and other planar phthalocyanines is the so-called herringbone

structure shown in Figure 1.8. In this structure the individual molecular stacks are arranged with a well-defined angle to each other. The crystal arrangement and morphology depends greatly on thermal treatment, type of substrate, underlying layer and the nature of any substituents, with bulky substituents leading to larger inter-stack separation.^[95, 96] Material properties such as charge mobility and exciton diffusion rely greatly on larger crystalline domains of higher order. In the case of charge mobility Pc thin films exhibit an anisotropic mobility with enhanced charge transport along the π - π stacking axis, which influences device behaviour.

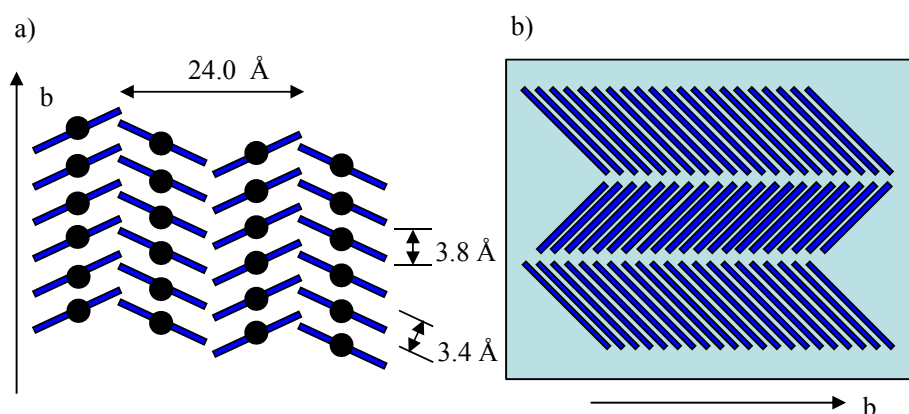


Figure 1.8 a) Crystal structure of CuPc in its α -phase. The Cu central atoms are highlighted by the black markers. b) CuPc crystal alignment on a weakly interacting flat substrate surface.

1.3.1.2 Subphthalocyanines

Subphthalocyanines (SubPcs), a different class of small molecule semiconductor derived from Pcs, were first synthesised in 1972 by Meller and Ossko in an attempt to synthesise boron phthalocyanines.^[97] Boron subphthalocyanine consists of only three N-fused diiminoisoindole rings arranged around the central B atom with a substituent, usually a halogen, bound directly to B at the axially accessible top site. The molecule adapts a non-planar, cone-shaped structure with a 14 π -electron system.^[98] Compared to Pcs, it was only possible to synthesise boron based subphthalocyanines. SubPcs have two target sites which can be substituted including the organic ligand ring and the open axial site directly bound to the B centre. SubPcs absorb visible light in the range of 500-650

nm. Unsubstituted boron subphthalocyanine chloride (SubPc – see Figure 1.7d) serves as an electron donor with a LUMO of -3.6 eV and a HOMO of -5.6 eV.^[99] If substituted on the ring with appropriate electron withdrawing groups such as halogens, SubPc derivatives can also act as an electron acceptor.^[100] The molecular arrangement in a thin film was found to be mainly amorphous due to the non-planar molecular structure and the sterically hindering axial substituent also leading to lower charge mobility compared to planar Pcs.^[54, 101] This also leads to pair formation through weak van der Waals interactions rather than efficient π - π stacking.^[98]

1.3.1.3 Polythiophenes

Conjugated polymers can undergo an efficient photoinduced charge transfer from the polymer to a fullerene which was discovered in 1992 by Sariciftci *et al.*^[39] Since then the field of semiconducting organic polymers has progressed dramatically with polythiophenes (PTs) and poly(phenylene vinylene) (PPV) being just two well-studied polymer groups out of many with versatile applications not just in OPVs, but also OLEDs, OFETs and other organic electronic applications.^[102, 103] Usually, such a polymer chain consists of a huge number of repeat units which create long π -conjugated sequences. The sequences are divided by chain twists and folds which interrupt the conjugated system. The π -conjugated system is formed by sp^2 -hybridised carbon atoms and is stretched along the polymer chain. The linear combination of the p_z -orbital wavefunctions adds up to an entire band-like π -MO with a broad energy level distribution.^[60] To avoid confusion with inorganic bandgap materials it will still be referred to as HOMO and LUMO.

To improve processability, polymers such as PTs and PPV were functionalised with alkyl and alkoxy side chains to make them more soluble. PTs consist of four carbon atoms and one sulphur atom per repeat unit. A well studied example of PT is P3HT (Figure 1.7e), which is functionalised with a hexyl side chain. Due to its low lying LUMO of about -3.0 eV to -3.3 eV and HOMO of -5.0 eV to -5.2 eV and with a broad absorption range from about 400-650 nm, it proved to be a suitable electron donor material.^[104, 105] Hole transport takes place through the conjugated polymer backbone but

also between chains. For highly regioregular P3HT the hole mobility was greatly improved to 5×10^{-2} - $10^{-1} \text{ cm}^2\text{V}^{-1}\text{s}^{-1}$.^[106] P3HT is very soluble in non-polar or weakly polar solvents such as toluene, chlorobenzene and dichlorobenzene and is mainly deposited as a blend with PCBM to form BHJ active layers, where it undergoes phase separation to form larger polymer domains during film formation. A different derivative is water-soluble sodium poly[2-(3-thienyl)ethoxy-4-butylsulfonate] (PTEBS – see Figure 1.7f) with methoxyalkyl sulfonate side chain group.^[107]

1.3.2 Electron acceptor materials

1.3.2.1 Fullerenes

Fullerene is an allotrope of carbon alongside diamond, graphite and amorphous carbon. Spherical fullerene was first discovered by Kroto, Curl and Smalley in 1985 which set the basis for a new class of materials with unique properties.^[18] The molecules were named after Buckminster Fuller due to close resemblance of the molecular structure to his futuristic architecture. The most common fullerene, C_{60} , is composed of 60 carbon atoms forming 12 pentagons and 20 hexagons. All carbon atoms are linked together, forming one double and two single bonds each leading to sp^2 hybridisation, which is shown in Figure 1.7g. Due to such an extended conjugated system, C_{60} is able to accept between 6 and 12 electrons, which makes it an ideal electron acceptor and explains its main application in OPV devices.^[19] With the sp^2 hybridisation of the entire C_{60} molecule a trigonal planar molecular geometry would be preferred. However, the strain induced by the curved surface forces the molecular geometry much closer to a tetrahedral one, as found in sp^3 configurations. As a result, reactions which saturate the surface, changing the hybridisation to sp^3 , lead to energetically more stable products, which explains the particularly high reactivity with oxygen. One of the characteristics of C_{60} is its photo-oxidation under intense light. As a consequence of this, trapped oxygen can cause an irreversible decrease in conductivity and defect induced recombination due to deep trap sites.^[108, 109] This leads to the idea of using more stable acceptor materials in hybrid OPV devices, where the C_{60} is replaced by transition metal oxides (TMOs) such as titanium oxide (TiO_x) and zinc oxide (ZnO) which demonstrate similar electron acceptor

characteristics. Recently, Yang *et al.* demonstrated the use of organic alternatives to C₆₀ based on F₁₆CuPc.^[110]

Delocalisation of π -electrons spread over the molecule surface lead to free rotation within all dimensions without a preferential orientation. Due to weak intermolecular interactions thin films are mainly amorphous with only few crystalline domains. C₆₀ thin films absorb light in two regions of the ultraviolet (UV)/visible (vis) spectrum: There is a broad band in the UV part in the range of 190 to 410 nm and a weak absorption in the visible part around 410 nm to 620 nm due to a forbidden transition.^[111, 112] With the HOMO at -6.1 eV and the LUMO at -4.5 eV as well as a high electron mobility of up to 1 cm²V⁻¹s⁻¹ (OFET) C₆₀ is suitable as an electron acceptor.^[113]

Despite its beneficial electronic properties, C₆₀ has a low solubility in most organic solvents and is therefore usually vacuum deposited for small molecule OPV devices. To increase its solubility, C₆₀ was functionalised with a butyric acid methyl ester group, also known as [6,6]-phenyl-C₆₁-butyric acid methyl ester or PCBM (Figure 1.7h). Due to the large increase in solubility, it found application in solution processed polymer/PCBM blend based BHJ OPV devices. In such blends phase separation occurs upon drying and annealing leading to distinct polymer and PCBM domains with a large active D/A interface, crucial for efficient BHJ OPV devices.

1.3.2.2 Transition metal oxides: ZnO and TiO_x

In order to replace less stable fullerenes with chemically and thermally more stable inert materials, organic/inorganic hybrid OPVs employ inorganic electron acceptor materials such as TiO_x and ZnO.^[114-116] Both TMOs are cheap alternatives, non-toxic and versatile in their applications. TiO_x and ZnO are II–VI inorganic semiconductors with a wide band gap of around 3.2 eV and 3.3 eV respectively.^[117] Due to their very high electron mobilities, which are orders of magnitude higher than for organic materials (1 cm²V⁻¹s⁻¹ for TiO_x and 205 cm²V⁻¹s⁻¹ for ZnO) and high electron affinity (-4.0 eV to -4.3 eV for TiO_x and -4.1 eV to -4.5 eV for ZnO), both materials are suitable electron acceptors.^[117] Additionally, TiO_x and ZnO are often employed as efficient electron extraction interlayers between the charge collecting electrode and the photoactive layers.^[86, 118, 119]

TiO_x and ZnO can be processed from solution either from nanoparticle suspension or precursor solution. This enables nanostructuring through templating as well as control over crystallinity and morphology to optimise structured D/A interfaces or electrode interlayers. As TiO_x is processed from a precursor and then converted to the oxide, the stoichiometry of Ti and O in the nanocrystalline film can vary and a proper TiO₂ anatase might not be obtained throughout the entire film.

ZnO is usually an n-type semiconductor due to the presence of defects such as oxygen vacancies and zinc interstitials. ZnO preferentially adopts the wurtzite crystal structure.^[115]

1.3.3 Interlayer and electrode materials

1.3.3.1 Charge extraction interlayers

Similar to the electron extraction layers based on TiO_x and ZnO, hole extraction interlayers can be employed to optimise the contact at the hole collecting electrode. The quoted VB and CB values for TMOs such as molybdenum oxide (MoO_x) and tungsten oxide (WO_x) differ by up to a few eV depending on the source and proposed underlying operation mechanism, which shows the need for further investigations. Earlier reports quoted the CB at -2.3 eV and -1.6 eV and the VB at -5.3 eV and -5.1 eV for MoO_x and WO_x respectively.^[120, 121] However, Kroeger *et al.* reported that MoO_x and WO_x had large workfunctions and are strongly n-type materials due to oxygen defects. For bulk material the CB was determined to be at -6.7 eV and -6.3 eV, the workfunction at -6.9 eV and -6.5 eV, and the VB at -9.7 eV and -9.7 eV respectively for MoO_x and WO_x.^[122] For TMO thin films of only a few nanometres in thickness, a strong induced dipole at the interface through charge transfer to the electrode results in a huge vacuum level shift. This leads to Fermi level pinning of the n-type TMOs to the electrode material. Additionally, band bending of the adjacent organic material layer towards the TMO occurs up to a few nanometres into the film which is caused by the induced interface dipole.^[123, 124]

Both materials are vacuum deposited but can show slight differences in stoichiometry to perfect MoO₃ and WO₃ after deposition and when in contact with ITO or a metal electrode.^[125] A slight lack of oxygen in MoO_x and WO_x is beneficial for efficient

charge transfer through created defect and gap states.^[126] MoO_x and WO_x are the most frequently employed metal oxide hole extraction interlayers in regular and inverted device architectures.

1.3.3.2 Exciton blocking layer: BCP

Thin films of bathocuproine, 2,9-dimethyl-4,7-diphenyl-1,10-phenanthroline (BCP), are almost transparent, and have been deposited on top of the acceptor layer in regular device architectures. The molecular structure is shown in Figure 1.7i. BCP has a large band gap of around 3.5 eV, which leads to the exciton blocking characteristic.^[127] Excitons diffusing towards the aluminium electrode cannot travel beyond the acceptor/BCP interface and are not directly quenched at the metal electrode which otherwise leads to a reduction in efficiency.^[128] BCP also acts as a sacrificial layer protecting the active organic layer from damage by hot deposited metal from the electrode deposition. Another role of BCP in a device is the built-in-field improvement leading to better diode behaviour of the device.^[129] Due to the large bandgap, electron transport through thin layers of BCP is assumed to occur via defect states, which are introduced by metal bombardment during the first few layers of electrode deposition.^[130]

1.3.3.3 Electrode materials: ITO and Al

Indium-tin oxide (ITO), the most common transparent conducting oxide (TCO), has most properties of a transparent metal and is widely used as the bottom electrode in OPVs and OLEDs. The high electrical conductivity of the normally insulating indium oxide arises from tin doping.^[131]

ITO is sputtered onto glass and can be chemically treated and modified prior to deposition. Due to its relatively high workfunction at around -4.7 eV, it is mainly employed as a hole acceptor from the HOMO of the donor compound, but can collect electrons in inverted device architectures.

As a top electrode, aluminium (Al) was chosen because of its relatively low workfunction at -4.3 eV for regular device architectures. The material is low in material cost, abundant and can be vacuum deposited. Other metals available with low work

functions are magnesium and calcium, but have the disadvantage of high chemical reactivity. Although in inverted devices top electrodes with high workfunctions, such as gold, are required, Al can still be used in combination with metal oxides, such as MoO_x and WO_x .^[125]

1.4 Device interface modification and nanostructuring

Despite great progress in recent years in OPV development, they still perform significantly lower in PCE and operational stability compared to inorganic PV technologies. In order to improve OPVs, crucial interfaces have been identified to have a large influence on device performance, in particular the D/A and electrode/photoactive layer interfaces. The interface structure and choice of material at these interfaces is critical.^[84, 85, 132-134] By developing new methods based on controlled nanoengineering to structure and optimise these interfaces, deeper understanding can be gained and device improvement can be achieved.

As shown in the principle of operation of a D/A heterojunction OPV device, the conversion efficiency of solar energy into electrical energy is greatly dependant on the four individual processes determining EQE and therefore J_{SC} . Different approaches are presented to contribute to a solution for improved OPV device performance: D/A interface nanostructuring, electrode contact interface modification by inserting TMO interlayers, and organic/inorganic D/A hybrid OPVs as an alternative approach to fullerene based acceptor materials.

1.4.1 D/A interface modification

1.4.1.1 Background and development of interface nanostructuring

Light absorption and exciton formation η_{abs} can be enhanced by either improved material dependant spectral overlap with the solar spectrum but also an increased film thickness. In order to perform exciton dissociation or charge transfer η_{ct} , the generated excitons need to reach a suitable heterojunction before recombination. This process is dominated and limited by the short L_D leading to a low exciton diffusion efficiency η_{ed} .

Therefore a compromise between the film thickness for maximum absorbance and the limited L_D for efficient exciton dissociation is essential for efficient photocurrent generation. This relationship defines the main limiting factor of planar bilayer OPV devices as shown in Figure 1.9a.^[26]

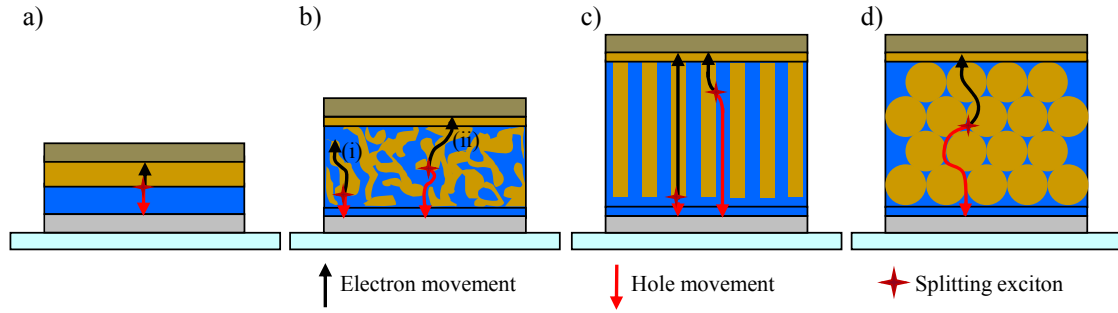


Figure 1.9 Schematic of different heterojunction OPV device architectures: a) bilayer, b) BHJ or mixed layer, c) and d) 3D nanocomposite devices. The black and red arrows indicate the traveling path of electrons and holes respectively. In b) (i) is a situation of a charge trapped in a dead end and (ii) shows successful charge transport to the collecting electrodes after exciton splitting.

To minimise the exciton diffusion paths and to generate a larger interface with increased total active layer thickness, D/A intermixed active layers were introduced, including solution-processed polymer/fullerene BHJ devices and vacuum co-deposited small molecules. In both cases charge transport pathways towards the charge collecting electrodes through randomly mixed layers are limited due to numerous isolated domains and cul-de-sacs in the D/A layer system resulting in charge trapping and recombination, as highlighted in Figure 1.9b. Despite the current density increase in both BHJ and mixed layer structures, there is an unavoidable trade-off between the improved η_{ed} and reduced η_{cc} .^[26, 135] By optimising the deposition conditions and by applying post-treatments such as temperature and solvent annealing a certain control over phase segregation and therefore the D/A interface order can be achieved.^[136, 137] A theoretical study by Yang *et al.* on photo-current generation in nanostructured OPVs revealed exactly the same trend. As the domain size of a D/A mixed layer was increased the specific interface area in a defined unit cell dropped resulting in an improved η_{cc} but reduced η_{ed} and a small, but still noticeable improvement in internal quantum efficiency (*IQE*).^[132]

To overcome this problem a more controlled three-dimensional (3D) highly interpenetrating D-A composite structure is required to exploit the advantages from BHJ and mixed layers, but with well structured charge transport paths.

Potential solutions for this complex problem are ordered organic nanostructures which would result in an increase in interface area, and therefore short exciton diffusion pathways, but also continuous charge transport pathways with increased film thickness and therefore improved absorbance.

An ideal solution is a finger-shaped interdigitated D-A device architecture with a small diameter to meet the L_D criterium.^[138, 139] Such structures have been realised in hybrid devices from vertically aligned metal oxide nanorods, but the devices showed only slight device current improvement.^[140-142] Another promising attempt by Haberkorn *et al.* is the template-assisted fabrication of free-standing nanorod arrays of a hole-conducting crosslinked triphenylamine derivative.^[143] A new route to achieve such ordered D/A interface patterning on a length scale of a few tens of nanometres in domain size is the use of self-assembled block copolymers facilitating donor and acceptor domains in the same chain. This route is complex from a synthetic and self-assembly point of view and remains very challenging.^[144] However, such a finger-shaped interpenetrating D/A system is not easy to realise on a sub-100 nm scale for purely organic OPVs (Figure 1.9c).

Close approximations to interpenetrating nanostructured interfaces have been produced by nanosphere lithography (NSL).^[145] NSL has been used to generate nanosphere templated 2D nanocomposite organic thin film structures based on a nanoparticle monolayer mask as a template, which consists of 2D-ordered nanosphere arrays. However, the interface area would be greatly compromised compared to any mixed or BHJ interface.

To take this development one step further template assisted three-dimensionally ordered macroporous solids (3DOM) and open-cellular thin films of the appropriate organic semiconductor could form the desired controlled matrix for ordered highly interpenetrating D-A composite systems, as demonstrated in Figure 1.9d. A synthetic opal structure from self-assembled polystyrene nanospheres, fabricated by sedimentation, spin-coating or controlled vertical drying, can serve as the initial template. The

fabrication process of 3DOM thin films typically involves three separate steps: (i) self-assembly of colloidal spheres or droplets into supra-structures; (ii) infiltration of the interstitial spaces with an application-specific material; and (iii) template removal. In certain cases the first two steps are combined into a single co-deposition procedure. The nanosphere templating process is widely applicable to inorganic materials including metal oxides and metals but proves to be very challenging for organic semiconductors.^[146] Further details are revealed in Chapter 5.

1.4.1.2 Concept and fabrication strategies

3D nanosphere templating involves numerous steps and processes to obtain the highly interpenetrating D/A composite structure: 1) convective self-assembly of polystyrene colloids to form the template structure, 2) infiltration of the nanosphere domains with appropriate donor material, which can be combined to a direct co-deposition, 3) colloid removal step, 4) second infiltration of the inverse structure with acceptor material, and 5) deposition of buffer layer and vacuum deposition of the covering top electrodes. The schematic of nanosphere templating for a complete nanocomposite device is shown in Figure 1.10.

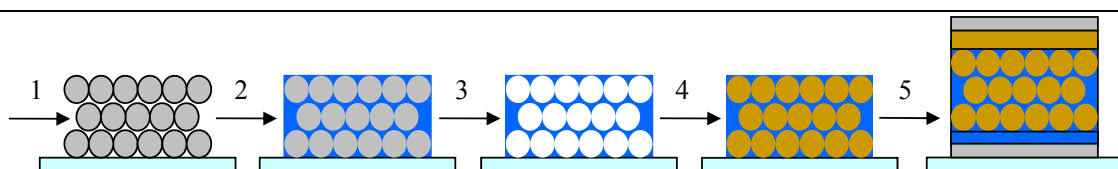


Figure 1.10 Schematic of fabrication method: 1) Self-assembly of polystyrene colloids, 2) infiltration of nanosphere domains with appropriate donor material, 3) colloid removal, 4) infiltration of inverse structure with acceptor material, 5) device fabrication using 3D nanosphere templating combined with organic molecular beam deposition. 1) and 2) can be combined to a co-deposition step.

In this unique approach to template organic semiconducting materials the templating material is sacrificial, which explains the choice of polystyrene (PS). The system is based on a two-phase system starting with water as a solvent and dispersion medium for PS and the water-soluble donor materials (PTEBS and TSCuPc). The removal process of the PS template by using non-polar solvents is selective leaving the

inverse opal structure made of donor material unchanged. The second infiltration of the acceptor material has to be performed from a non-polar solvent to prevent the remaining structure from damage or even complete dissolution. In this delicate approach it is of great importance to create a clean D/A interface avoiding any residues from the performed process steps and more importantly from the template. PS is a very good insulator and a thin film could already ruin the device without being detected. Other sources of residues are soaps which are added to stabilise the nanospheres during and after synthesis. Soaps and other additives are also the reason why all nanospheres were synthesised in house to control all parameters and compounds involved in the synthesis.

Co-deposition was developed to target very small sphere sizes down to 50 nm in diameter in order to match L_D , and is completely new to the field. The templating approach can also be used to template TiO_x and ZnO for nanostructured electrodes or hybrid devices.

1.4.2 TMO interlayers

Ideally, the photoactive layer consisting of donor and acceptor materials is sandwiched between two appropriate ohmic contacts to avoid any energetic barrier for efficient charge extraction. Enhanced selective charge extraction can be achieved by introducing TMOs between electrodes and the photoactive layer. Also the device stability can be improved by metal oxide encapsulation.^[84, 85]

TMOs such as MoO_x , nickel oxide (NiO), WO_x and vanadium oxide (V_2O_x) serve as hole extraction layers on the hole collecting electrode side.^[120, 121, 147] The concept of hole extracting layers has only recently been established resulting in significant device performance improvement, but there is still a lot of debate about the correct operation mechanism.^[85, 122] Good performance can only be achieved with very thin layers of a few nanometres in thickness without compromising charge transport and energy level alignment.^[121, 148] The materials are mainly vacuum deposited or sputtered which also limits the control over surface morphology, crystallinity and potential surface nanostructuring for advanced electrode modification.

Metal carbonates and TMOs including cesium carbonate (Cs_2CO_3), but mainly TiO_x and ZnO , work as electron extraction layers on the opposite electrode side following the same concept.^[104, 118, 119] For electron conducting materials such as PCBM a very close energy level alignment between the TMO CB and the PCBM LUMO can be achieved forming an ohmic-like contact.^[85] TiO_x and ZnO are both n-type materials, transparent in the visible range and are not limited to thin layers due to their exceptionally high electron mobility. Solution processing of TMOs enables nanostructuring through templating, thicker spacer layers for improved optical interference, as well as generally good control over crystallinity and morphology to optimise structured D/A interfaces or electrode interlayers (see Chapter 2).^[149, 150]

Hole and electron extracting TMO interlayers also have the general effect of improving the homogeneity of conductivity and workfunction. Additionally, when employed on one electrode or even as a sandwich structure from both sides operational device stability is greatly improved by preventing direct electrode contact which can lead to chemical and physical reactions.^[85, 124]

Investigations into different thin film structures from selected deposition methods of ZnO , such as spray pyrolysis and controlled electrodeposition are the target of the investigation in this thesis. The focus is on the ITO/TMO interface as well as the TMO/blend interface. TiO_x from sol-gel process are also employed to compare the systems. This should serve to develop a deeper understanding of the structure/function relationship between film morphology, crystallinity and device performance but also to optimise OPV device performance. In order to be able to compare the different systems to each other, and also work in the literature, the well known D/A BHJ system based on P3HT/PCBM was chosen.

Additionally, the system is used to develop the less commonly used inverted device architecture, which will then also be applied to hybrid devices. Hole and electron selective extracting TMO interlayers define the polarity of a device and are therefore crucial for device structures based on BHJs which can be operated as both regular and inverted device architectures. ITO and Al electrodes can be employed in both cases with the ability of collecting both types of charges.^[84, 85] More details on previous development and achievements are given in Chapter 6.

1.4.3 Hybrid OPVs

Fullerene replacement by inorganic semiconductors such as TiO_x and ZnO with high electron mobility and potential for nanostructuring demonstrates a promising concept for hybrid OPVs.^[117, 151, 152] Organic/inorganic hybrids have the advantage of combining highly absorbing organic donor materials with chemically and thermally stable, robust and cheap inorganic electron acceptor materials to produce thin film hybrid OPV devices. TMOs also provide a controlled interface with suitable energy levels to act as an electron acceptor with appropriate donor materials.

TiO_x and occasionally ZnO are employed in DSSCs.^[152] In contrast to DSSCs, D/A heterojunction hybrid OPVs employ the organic donor material not just as a sensitizer but also as charge transport material. Hybrid devices are much thinner than DSSCs, not exceeding 100 nm.

ZnO and TiO_x have a favourable energy band alignment with commonly used polymeric organic donor materials such as P3HT and poly(2-methoxy-5-(2'-ethyl-hexyloxy)-p-phenylene vinylene) (MEH-PPV). For both planar bilayer and nanostructured hybrid TMO/polymer devices, *PCE* is primarily limited by the low J_{SC} due to poor photocurrent generation with the vast majority of reported devices not exceeding a *PCE* of 0.5 %.^[153, 154] Due to the variety of processes from solution which can be used to deposit TMOs, surface nanostructuring through specific growth or templating is favourable. A lot of work has been carried out on the formation and implementation of TMO nanorods and other surface area increasing “pseudo 2D” structures. Most structures were implemented in polymer hybrids showing an increase in performance mainly due to a higher J_{SC} based on the larger active surface area.^[140, 142] The best devices with a *PCE* of up to 2 % are P3HT/ ZnO nanoparticle blends forming BHJ-like interconnected photoactive layers.^[155] More efficient polymer hybrid devices of up to 2.8 % are based on semiconductors including cadmium sulphide (CdS), cadmium selenide (CdSe) and copper indium selenide (CuInSe_2) which contribute significantly to J_{SC} but are either toxic or not abundant compounds.^[117]

Hybrid OPVs also provide a promising alternative system to apply the nanosphere templating approach for highly interpenetrating D/A interfaces based on a more stable TMO open-cellular thin film structure. The fabrication method is based on a sol-gel process followed by a simple calcination step to remove the template. By heat treatment of up to 450 °C very clean inorganic interfaces can be produced.

First a model system based on planar TMOs needs to be developed evaluating the use of different organic donor materials including polymeric and small molecule semiconductors which are employed in inverted device architectures. The system then serves as a basis for a possible expansion to 3D ordered highly interpenetrating D/A hybrid composite devices.

1.5 Project motivation and thesis outline

The focus of this work is on controlled interface engineering and modification for *PCE* and operational stability improvement by targeting two of the critical material interfaces in OPV devices: the photoactive D/A interface and the electrode/photoactive layer interface. Generally, this can be achieved by good control over device structure and morphology as well as energy level alignment through nanoengineering of organic/organic and organic/inorganic interfaces. In this case, D/A interface modification is performed through development of template assisted nanostructuring. The electrode interface is modified by the controlled insertion of TMO interlayers. Furthermore, the development of a deeper understanding of the structure/function relationship is crucial. In a further step some of the concepts are then applied to organic/inorganic hybrid heterojunction OPVs in order to work towards a new type of OPV device combining the advantages of both, organic and inorganic semiconductors, including increased charge mobility and chemical stability. The rest of this thesis is organised as follows below.

Chapter 2 covers all experimental and analysis techniques used in this thesis including thin film and OPV device fabrication as well as analysis. Current-voltage (*J-V*) characterisation of OPV devices is discussed in an individual section.

The focus of Chapter 3 is on the synthesis of small monodisperse polystyrene nanospheres. This includes approaches to surfactant-free radical initiated emulsion

polymerisation aiming for small nanospheres, <100 nm in diameter. The particle radius should ideally match L_D which proves to be very challenging. Particle characterisation includes dynamic light scattering and electron microscopy.

The fabrication of 3D interdigitated D-A composite structures in Chapter 5 requires selected D/A material combinations. For template penetration and co-deposition water-soluble donor materials such as polymeric PTEBS and low molecular weight TSCuPc were chosen. These materials are not well studied in OPV devices processed from aqueous solution. To gain deeper understanding of the $J-V$ behaviour of the new materials bilayer device studies were performed in Chapter 4. The findings help to interpret measurements on the more complex 3D D-A composite structures.

Chapter 5 covers colloidal thin film self-assembly from co-deposition of spheres and appropriate donor material to large ordered templated domains. The complete fabrication of 3D interpenetrating D-A composite structures and devices based on TSCuPc and PTEBS in combination with PCBM and C_{60} are demonstrated. The steps include co-deposition from vertical self-assembly, selective sphere removal in a solvent vapour treatment step, second infiltration with an appropriate acceptor material and final electrode deposition. This chapter demonstrates the new approach of nanoengineering to fabricate controlled interpenetrating D-A composite device structures highlighting the strengths of the technique but also the challenges.

The focus in Chapter 6 then switches to the electrode/photoactive interface where TMOs such as ZnO and TiO_x are employed as charge selective electron extraction layers to improve charge extraction but also to enable electrode nanostructuring and inverted device architectures. Interlayers from different deposition techniques including sol-gel, spray pyrolysis and electrodeposition are compared and optimised in an inverted device architecture using P3HT/PCBM BHJ devices as a model system.

Chapter 7 deals with organic/inorganic hybrid OPVs with the TMOs from Chapter 6 employed as the electron acceptor material in inverted device architectures. Apart from the polymeric donor P3HT, a new device concept based on small molecules such as SubPc is successfully demonstrated proving a working concept towards 3D nanostructured hybrid devices.

In Chapter 8 the conclusions of all chapters are brought together and summarised. Furthermore, possible directions for future work on the different concepts are outlined and discussed.

Chapter 2: Experimental and analysis

This chapter describes the different experimental steps and methods used for thin film deposition and OPV fabrication, including solution processes and vacuum deposition of organic and inorganic compounds. In the second part, different thin film analysis techniques are introduced and explained. A final section on OPV device characterisation and data analysis is included, which also discusses the necessary theory for better understanding. Nanosphere synthesis and templating are covered in the individual chapters.

2.1 Thin film and device fabrication

In this experimental section substrate preparation and material purification are explained, followed by thin film preparation and OPV device fabrication. Thin film preparation includes solution processes such as spin-coating, electrodeposition, sol-gel processes and spray pyrolysis. This section also introduces vacuum deposition of organic and inorganic materials leading from the basic concepts of single layer deposition to complete OPV device fabrication.

2.1.1 Material purification

Although the used materials were bought with very high purity, further purification of organic materials such as C₆₀ (Nano-C, Inc., 99.5%), CuPc (Aldrich, 97 %) and SubPc (Sigma-Aldrich, 85%) was important for a high device performance and is especially required in OMBD. Longer exposure to air and moisture could change its quality, forming unwanted oxidised derivatives which can result in a lower OPV device performance.^[156] Therefore thermal gradient sublimation was used for material purification.

The unpurified material is heated under high vacuum at around 10⁻⁵ mbar at the bottom of a glass tube until it sublimates. The glass tube lies in an outer quartz tube, which

closes the system to hold the high vacuum. Sublimed material condenses in the cooler part of the tube. A temperature gradient separates the volatile impurities from the purified material which has the highest sublimation temperature with the specific vacuum. Non-volatile impurities with too high sublimation temperatures stay unmoved at the end of the tube (see Figure 2.1). The sublimed pure material is harvested by breaking the inner glass tube after the complete purification cycle. Typical sublimation temperatures and conditions are listed in Table 2.1.

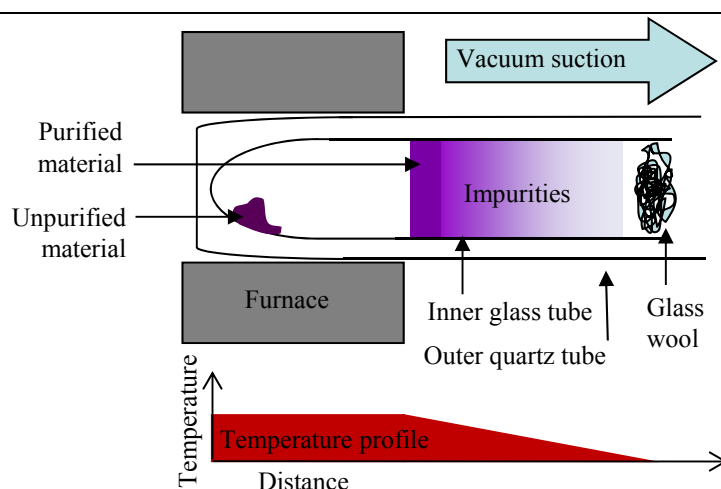


Figure 2.1 Schematic of the thermal gradient sublimation setup.

Table 2.1 Sublimation conditions for different organic small molecule compounds in thermal gradient sublimation.

Compound	Temperature [°C]	Time [min]	Heating rate [°C min ⁻¹]	Cycles
C ₆₀	480	600	1.0	1
CuPc	430	600	1.2	1
SubPc	320	600	1.0	1

All other materials were used as delivered including PC₆₀BM (Solenne, >99.5 %), P3HT (Rieke, >98 % regioregular, MW = 55-60 k), PTEBS (American Dye Source, Inc., MW = 100-1000 k), TSCuPc (Sigma-Aldrich, 85 %) and the TMOs, MoO₃ (Aldrich,

99.99%) and WO_3 (Aldrich, >99.9 %). For these compounds sublimation purification is not suitable due to their non-volatile nature.

2.1.2 Substrate cleaning

Unless stated otherwise, all thin films and devices were deposited onto either ITO-coated glass with a sheet resistance of $<15 \Omega \text{ sq}^{-1}$ (100-130 nm, Psiotec Ltd.), glass substrates or quartz substrates (Newcastle Optical Engineering, Ltd.) of various dimensions. A clean ITO surface is important to have a high electric conductivity and a homogenous workfunction. The following cleaning process was applied for all ITO and quartz substrates: Sonication for 15 min in acetone, deionised water/Decon 90 (detergent) 70:30 mixture, deionised water and isopropyl alcohol, followed by drying with a nitrogen jet and UV irradiation generated ozone treatment for 20 minutes. The ITO substrates were delivered with a red protective photo-resist which can easily be removed with acetone. UV/ozone treatment improves substrate surface wettability and removes carbon residues prior to film deposition.^[83]

2.1.3 Solution processed thin films

2.1.3.1 Spin-coating

Spin-coating is a simple method for thin film fabrication from solution including materials such as small molecular compounds, polymers, metal oxides and nanoparticle dispersions. It is well established in the OPV community for polymer blend based solar device fabrication. Spin-coating is cost-effective on lab-scale production but is mostly replaced in a scaled-up process by spray or ink jet printing techniques.

As shown in Figure 2.2 the substrate is mounted on a rotating stage and held in place by vacuum suction. A small amount of solution is applied to the centre of the substrate surface. When spun, the centripetal acceleration spreads the solution evenly across the whole substrate. Excess solution, which is unable to bind sufficiently to the substrate surface, leaves the substrate across the edges. Once the process is complete, an evenly spun film of a defined thickness remains on the substrate surface. The main

parameter is the spin speed, which controls film thickness and uniformity. Solution concentration and choice of solvent are also important, because they define the viscosity and volatility of the solution. For P3HT/PCBM blends this is crucial as the drying process defines the phase separation of the blend.

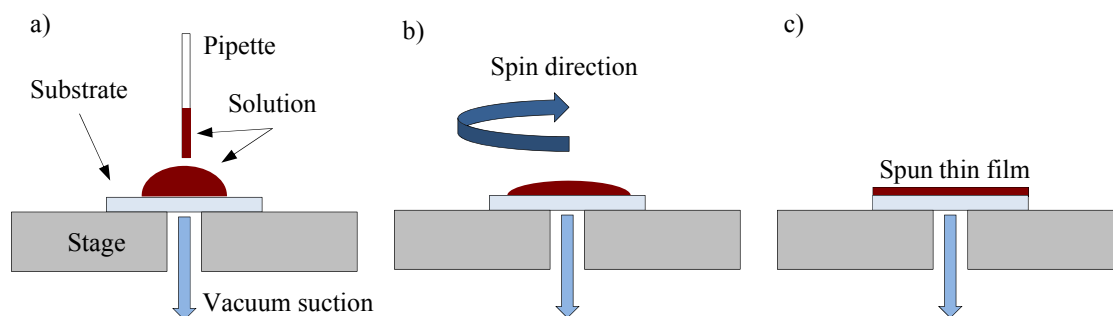


Figure 2.2 Schematic of the spin-coating process: a) dropping of the solution onto the target substrate, b) substrate spinning and c) the resulting spun thin film.

Spin-coating in air was used to produce thin films of TSCuPc, PTEBS and TiO_x . P3HT, PCBM and P3HT/PCBM blends were spun under N_2 atmosphere from 1,2-dichlorobenzene (Aldrich, 99%, anhydrous), employing a Laurell Technologies Corporation spin coater.

2.1.3.2 Sol-gel process

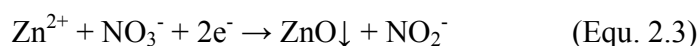
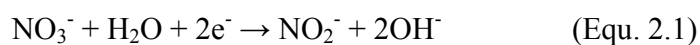
Sol-gel process is a common fabrication technique for metal oxide and ceramic thin films including TiO_x .^[114] Typical precursors for the solution process are metal salts or metal organic compounds such as metal alkoxides. Sol deposition is carried out by either dip-coating or spin-coating. The transition process from liquid sol to viscous or solid gel is mainly based on precursor hydrolysis and polymerisation forming metal-oxygen-metal chains and polymeric networks. In a calcination step with O_2 in excess the polymeric structure is then driven towards a higher oxygen content as needed for a proper metal oxide with the correct metal-to-oxygen stoichiometric ratios.

The process was used for thin film fabrication of TiO_x in Chapter 6 and 7. The precursor solution was based on a mixture of isopropanol (Fisher Scientific, HPLC

grade), titanium (IV) isopropoxide ($\text{Ti}[\text{OCH}(\text{CH}_3)_2]_4$, Sigma Aldrich, >98 %) and 2-amino ethanol ($\text{H}_2\text{N}(\text{CH}_2)_2\text{OH}$, Sigma Aldrich, >99 %) as a surfactant in a ratio of 20:1:0.5 by volume. The solution was degassed and stirred for 48 hours at room temperature prior to use.

2.1.3.3 Electrodeposition

Although electrodeposition (ED) from solution is well known as a thin film deposition technique for metals, it has only recently been adapted to deposit metal oxides, and ZnO in particular. Electrodeposition of ZnO is based on the reduction of oxygen or oxygen providing precursor compounds to electrochemically generate hydroxide (OH^-) *in-situ* at the working electrode. This leads to ZnO precipitation at the electrode and controlled thin film growth. Although zinc is already provided in the right oxidation state as Zn^{2+} in the bath solution from a zinc salt, the OH^- precursor feed remains challenging. O_2 ,^[157] hydrogen peroxide (H_2O_2)^[158] and nitrate (NO_3^-)^[159] are all candidate compounds. Due to a rather low O_2 solubility in aqueous solution and H_2O_2 instability limiting the film growth rate and control, NO_3^- was chosen as the precursor. NO_3^- ions are very soluble in aqueous solution and high film growth rates can be achieved. The process is split into two steps: NO_3^- is reduced to nitrite (NO_2^-) and OH^- in the presence of H_2O (Equation 2.1); OH^- then immediately reacts to form H_2O again and ZnO which precipitates and deposits the film (Equation 2.2). The overall reaction is summarised in Equation 2.3.^[160]



Electrodeposited ZnO films were prepared in a three-electrode set up consisting of an ITO working electrode, a Ag/AgCl/KCl (3.5M) reference electrode and a platinum mesh counter electrode. Electrodeposition was carried out potentiostatically using a computer-controlled potentiostat by applying a potential vs. the Ag/AgCl electrode in a heated deposition bath containing the zinc nitrate ($\text{Zn}(\text{NO}_3)_2$, Aldrich, ≥ 99.0 %)

precursor. Precursor concentration and pH were varied for different depositions.^[161] The films produced are discussed in further detail in Chapter 6.

2.1.3.4 Spray pyrolysis

Unlike other thin film preparation methods, spray pyrolysis (SP) is fairly cost effective, simple in application, scalable and ideal for metal oxide thin film deposition.^[162] Similar to sol-gel and electrodeposition the technique is based on a solution process involving a metal organic precursor or metal salt, which is converted to the final metal oxide upon heat and O₂ exposure. Typically, the precursor solution is sprayed by a gas jet onto a heated substrate. Primarily, the solution concentration and spray deposition time determine the film thickness, where temperature determines the film morphology and crystallinity. By influencing the O₂ exposure the stoichiometric ratio between metal content and oxygen can be controlled.

The ZnO thin films presented in Chapter 6 and 7 were deposited onto heated ITO substrates from a solution of zinc acetate (Zn(ac)₂, Aldrich, 99.99%) dissolved in methanol. Thin film preparation was completed by an annealing step in air for full conversion from Zn(ac)₂ to ZnO.

2.1.4 Organic molecular beam deposition (OMBD)

2.1.4.1 Principles of OMBD

OMBD is a vapour deposition technique performed under high vacuum (HV) and is based on molecule sublimation.^[163, 164] It is a typical and popular deposition technique for sublimable small molecule organic semiconductors with low solubility. The technique enables molecular thin film growth with a very precise thickness control down to sub-monolayer film thickness, i.e. sub-nanometre scale, and equivalent deposition rate control. The HV environment also provides very clean growth conditions, which proves to be vital for thin film OPV device and organic electronic technology.

OMBD of an appropriate organic compound is performed at a vacuum chamber base pressure of $<10^{-7}$ mbar. The organic compound, after purification by gradient sublimation (see section 2.1.1), is heated in an inert boron nitride crucible by a

temperature-controlled Knudsen cell (K-cell), as shown in Figure 2.3. The K-cell is heated by resistive heating with a range from about 50 to 500 °C and is monitored by a thermocouple. Based on the Knudsen effusion effect the organic compound is heated until it reaches the vapour pressure, which is required for the material to escape through the aperture provided to form a molecular beam.^[165] For a consistent molecular beam the K-cell temperature is above the minimum sublimation temperature and well below the decomposition temperature of the compound.

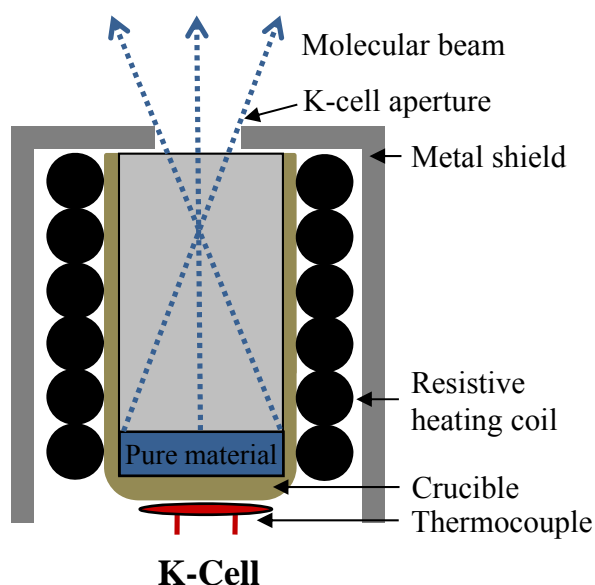


Figure 2.3 Schematic of a K-cell in detail.

The molecular beam formed is directed onto the cleaned substrates placed in the path of the beam. Molecules in the beam are then deposited onto the substrate surface and form a thin film caused by adsorption. The deposition rate is controlled by the K-cell temperature and is monitored *in-situ* together with the film thickness by quartz crystal microbalances (QCM) placed in the path of the beam. The precise film thickness is controlled by a beam shutter which acts as an “on/off” switch. The monitored thickness on the QCM has to be calibrated to the real thickness due to differences in film density and precise geometry inside the chamber. Film thickness monitoring based on QCMs and

ex-situ film thickness calibration by AFM step edge analysis is discussed in more detail in the following sections, 2.1.4.5 and 2.1.4.6.

2.1.4.2 OMBD chamber and thin film growth

A Kurt J. Lesker Spectros vacuum deposition system was used for the growth of all thin films and devices (see Figure 2.4).

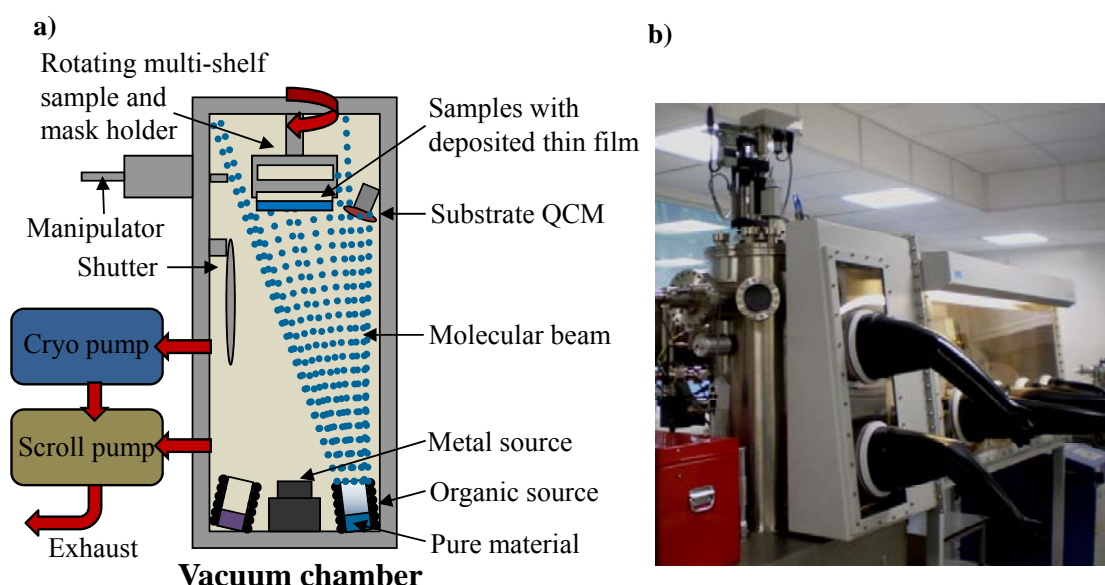


Figure 2.4 a) Schematic and b) photograph of the OMBD vacuum chamber.

The HV in the chamber is reached and maintained through a two-stage pump system. In a first stage rough vacuum is achieved with a scroll pump. In a second stage a cryogenic pump (Cryo Torr) reduces the inner chamber pressure to the operative base pressure of $<10^{-7}$ mbar. The growth chamber is equipped with six paired organic and three metal deposition sources, which are monitored by three QCMs close to the sources and one QCM next to the substrates. In addition to single organic source operation, two of them can be individually controlled at the same time for co-deposition growth. One main shutter close to the substrates blanks the beam when not in deposition mode. The temperature of the K-cells is monitored by a Eurotherm 2408. The QCMs, Eurotherms,

shutter and vacuum pumps are all linked to a computer which runs the device controlling and monitoring software.

The entire layer structure of a device can be grown in one cycle without breaking the HV by using the shutter and the multi-shelf sample and mask holder operated manually from outside by a manipulator. The sample holder can be rotated during growth to enable more homogeneous deposition. Samples and compounds were all loaded through a sliding door at ambient pressure under N₂ atmosphere kept by the surrounding glovebox. All devices were handled in the glovebox before and after deposition due to oxygen and moisture sensitivity. The glovebox was always kept at <1 ppm O₂ and H₂O.

Typical deposition rates for organic compounds were around 1 Å s⁻¹. Different organic materials have been deposited under base vacuum pressure at their specific evaporation temperature: C₆₀ at around 400 °C, CuPc at around 340 °C, SubPc at around 200 °C and BCP at around 150 °C. Freshly refilled crucibles were always out-gassed prior film deposition.

2.1.4.3 Deposition of metal oxide thin films

Although metal oxides such as MoO_x and WO_x are chemically very different to organic small molecules, the vacuum deposition technique can still be applied to deposit very thin homogenous films. When vacuum deposited, it is assumed that metal oxides do not form a molecular beam but rather a material beam of small oxide clusters. Metal oxides were deposited from a thermal metal source due to higher heat requirement. Low deposition rates of 0.05-0.10 Å s⁻¹ were applied to avoid damage of organic pre-deposited layers. MoO_x and WO_x were deposited as purchased. The metal oxides required an extended out-gassing step prior to film deposition, which can be seen as an *in-situ* material purification.

2.1.4.4 Deposition of metal electrodes

The top metal electrode, in this case Al, was deposited from a high temperature metal source. The metal source consists of a larger more robust heater. In order to reach the high evaporation temperatures required for Al the entire source holder acts as a

resistive heater passing through large currents at low voltage. A small Al pellet of very high purity is placed in a boron nitride crucible and heated to the required evaporation temperature. Attention must be paid at the beginning of the metal deposition, because the first few angstroms of hot deposited metal can damage the previously grown organic layer. Therefore, for the first 200 Å a low deposition rate of approximately 0.2 Å s^{-1} was applied. Later, the rate was increased to between 1 Å s^{-1} and 2 Å s^{-1} . Typically, an Al electrode thickness of about 1000 Å was deposited. To define the electrode shape and area for further J - V analysis different customised electrode shadow masks were used, as shown in Figure 2.5.

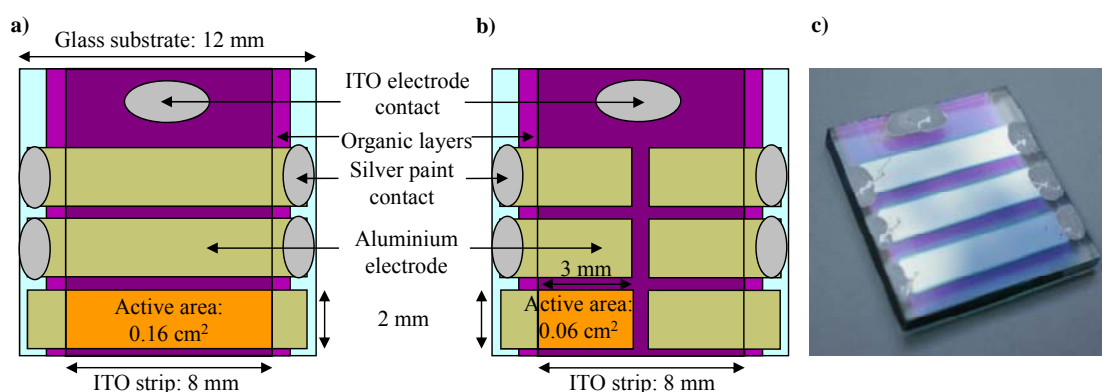


Figure 2.5 Schematic diagrams of a) a 3-pixel device with an active area of 0.16 cm^2 per pixel and b) a 6-pixel device with an active area of 0.06 cm^2 per pixel. c) Photograph of a complete 3-pixel device.

The device layouts used were either a 3-pixel device with an active area of 0.16 cm^2 per pixel (Figure 2.5a) or a 6-pixel device with an active area of 0.06 cm^2 per pixel (Figure 2.5b). In such a device the 8 mm wide ITO strip is completely covered by the deposited organic layers. The top metal electrodes were then vapour deposited onto the organic layers using one of the two masks. The second device contact to the ITO was fabricated by careful removal of all organic layers at the appropriate spot at the top end of the device. The ITO contact, as well as the ends of the Al electrodes on the glass substrate were enlarged with conductive silver paint for good contact in the device holder for J - V analysis.

2.1.4.5 Film thickness and rate monitoring

For organic semiconductor thin film growth and device fabrication, precise control over layer thickness and the linked deposition rate with sub-nanometre precision is of very high importance. Therefore, an *in-situ* measurement technique with the required sensitivity is needed enabling real-time monitoring during growth. The most convenient technique for such a measurement is a QCM, which is placed in the molecular beam path.^[165] The working principle of QCMs is based on the linear dependence of the change in mass per unit area to the change in quartz crystal oscillation frequency.^[166] As material is deposited by the beam onto the QCM, its mass changes due to the pseudo crystal extension and this is accompanied by a change in the oscillation frequency of the crystal. This change in frequency can be detected and related to a specific gain in mass per unit area and therefore deposited film thickness. This relationship is true under the assumption of the deposition of quartz onto a QCM but has to be scaled and calibrated for any other material. For an accurate thickness prediction of other materials a more complicated relationship has to be used. There are very few materials with complete parameter sets which predict bulk growth. Again, this can vary for thin film growth. For that reason an empirical tooling factor can be determined by relating the grown QCM film thickness to the actual film thickness. This sort of calibration works for most materials and simplifies the thickness monitoring process drastically without compromising the accuracy of the technique.

2.1.4.6 Film thickness calibration

A common and very accurate technique for thin film thickness calibration is step edge analysis by tapping mode atomic force microscopy (AFM). Step edges were produced by thin film deposition of the appropriate material onto a substrate with a specific QCM film thickness measured during the film growth process. The film was then carefully scratched with a sharp needle to generate a well defined step. The AFM scan is then performed across the edge revealing the height difference between the bare substrate and the film, as can be seen in Figure 2.6a. This actual film thickness, s , can be measured by either analysing single height profile cross-sections (Figure 2.6b) or by statistical height distribution analysis (Figure 2.6c), which proves to be more accurate as it averages

over the whole scanned area, filtering out edge and film defects. The ratio between s and the QCM film thickness is referred to as the tooling factor, which is material and deposition system specific. To gain more accuracy, this procedure was repeated at different sites of the substrate for one thickness and then extended to different thicknesses to create a tooling factor calibration line.

The example in Figure 2.6 shows a SubPc film with a thickness of 40 nm by QCM and with $s=28$ nm, resulting in a tooling factor of 0.70.

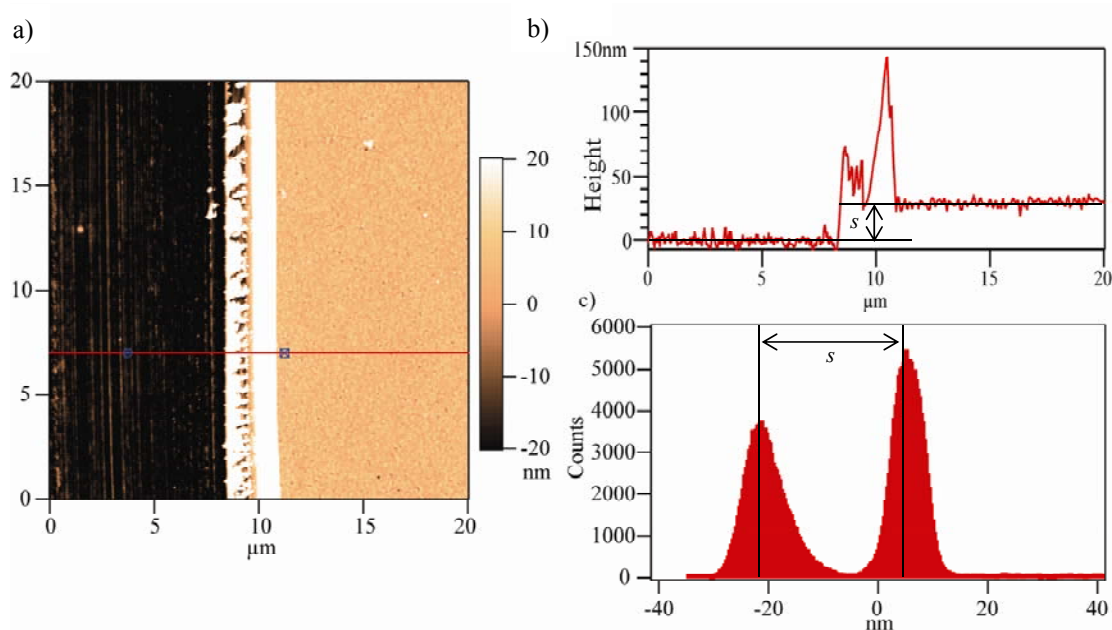


Figure 2.6 a) Step edge AFM image of a SubPc film with a grown QCM thickness of 40 nm. b) Cross-section height profile and c) statistical height distribution analysis show the actual film thickness s of 28 nm resulting in a tooling factor of 0.70.

2.2 Thin film analysis

Thin film analysis is an important part of OPV device fabrication and further understanding of the science behind it. The technology relies on high control over thin film thickness and morphology, but also defined layer interfaces. To monitor thin film deposition and to gain deeper understanding of thin film growth and structure/function relationship of morphology, crystallinity and interfaces, a complementary set of analysis

techniques is employed. For surface and near-surface analysis, AFM and scanning electron microscopy (SEM) are used with focused ion beam (FIB)/SEM and transmission electron microscopy (TEM) revealing more details of local structure further inside a sample. UV/vis electronic absorption spectroscopy and powder X-ray diffraction (XRD) are bulk material characterisation techniques probing electronic and crystal structure.

2.2.1 Atomic force microscopy (AFM)

With the invention of the scanning tunnelling microscope (STM) by Binnig and Rohrer in 1981,^[167] the first surface imaging technique of atomic resolution set the basis for a whole scanning probe microscope (SPM) family and nanotechnology as a new hot spot in science.^[168] The imaging capability of STM relies on an electrically biased, conductive scanning tip, which detects very low tunnelling currents from conducting or semiconducting samples with atomic spatial resolution.

In 1986, Binnig, Quate and Gerber extended the idea with the development of the AFM as an alternative to STM.^[169] AFM is also capable of scanning non-conducting surfaces with high spatial resolution on the nanometre scale to image surface structures and morphology. In contrast to STM, AFM is based on probing tip-sample surface interatomic force interactions when brought very close together.

When in close proximity to the surface the probing tip can experience attractive and repulsive forces depending on its distance to the surface.^[170, 171] Attractive forces are of longer range and include van der Waals (vdW) interactions, capillary forces, chemical forces and electrostatic attraction. Repulsive forces, such as hard sphere repulsion and electron-electron Coulomb repulsion are of much shorter range due to a high exponential decay law with increasing distance. The probing tip is attached to a cantilever (see Figure 2.7c), which acts as a spring with a well defined spring constant. Attractive forces bend the cantilever and the attached tip towards the surface and repulsive forces push it away. This attraction-repulsion force potential in conjunction with the classical Hooke's law describes the interaction behaviour and lateral movement of the tip, which leads to force and surface profile height measurements.

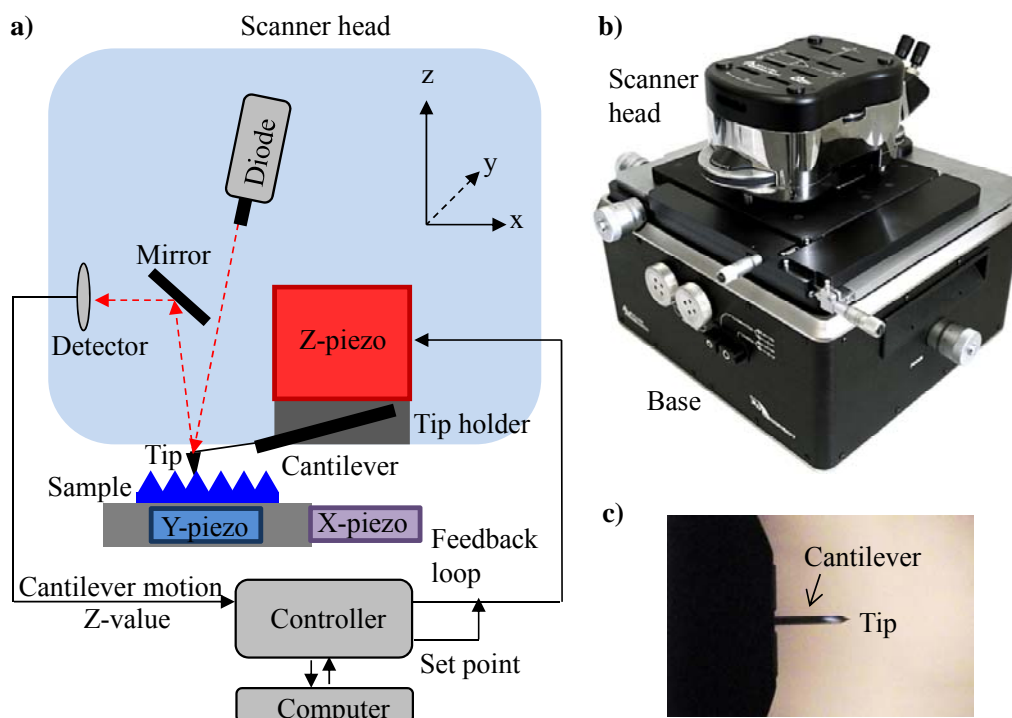


Figure 2.7 a) Schematic and b) photograph of an AFM. Photograph of c) an AFM tip. (The photographs in b) and c) were adapted from the MFP-3D Manual.)^[172]

The complete setup of an AFM by Asylum Research is shown schematically and as a photograph in Figure 2.7a and 2.7b respectively.^[172] Depending on the scanning mode the tip follows the surface contours either in contact with a constant force applied or in intermittent contact in tapping mode. A light beam is targeted onto the reflective backside of the tip and the resulting reflected beam is focused and positioned by a mirror for detection by the position sensitive photo-detector. The detector monitors the deflection of the tip, which is caused by surface–tip interactions. During a scan a feedback loop adjusts the tip height to maintain a constant amplitude or deflection, and therefore a measure of surface height is obtained. By scanning a local area a height profile can be determined by the computer software. The z-position of the tip is controlled by a piezo moving only along the z-axis with sub-nanometre precision. The tip holder, the deflection mirror and the photo-detector monitoring the tip position are all situated in the scanner head. The sample is mounted on a table with piezos moving it with nanometre precision along the x- and y-axis, placed in the base (see Figure 2.7b).

The two most common AFM scanning modes are contact mode and alternating contact (AC) or tapping mode. Contact mode is used for hard surfaces and conductive AFM. The tip is always kept in the repulsive force regime. It is referred to as being in contact to the surface with a constant force. Repulsive and attractive surface forces cause a bending of the cantilever with the feedback loop maintaining a constant cantilever deflection. This mode can damage soft surface structures such as thin film organic material layers. However, in tapping mode the tip is not constantly in contact to the surface. The cantilever is held very close but with a constant distance to the surface. It oscillates around its own resonance frequency and taps the surface gently during the scanning process. Interactions between the tip and the surface induce a slight change of the oscillation amplitude, which is restored by the feedback loop, and hence a height profile can be determined. Changes in phase and amplitude can give valuable information about the tip-surface interaction and add details to the pure topography based height image.

The surface topography of the samples was studied using an Asylum Research MFP-3D in tapping mode. Standard tapping mode tips (AC240TS) equipped with a silicon probe had a resonance frequency of 70 kHz and a tip radius of 9 nm. MFP-3D software based on Igor Pro was used for image reconstruction and analysis. The presented images have been line and plane filtered. By using the software, the surface roughness parameter, Rq , was determined. It is defined as the root mean square (RMS) of the sum over all N points for the surface height difference of each point Z_i and the average height Z_{avg} of the surface, as shown in Equation 2.4.

$$Rq = \left[\frac{1}{N} \sum_i^N (Z_i - Z_{avg})^2 \right]^{\frac{1}{2}} \quad (\text{Equ. 2.4})$$

2.2.2 Electron microscopy (EM)

2.2.2.1 Background and principles

In microscopy either a light or an electron beam is used to display an object as a larger image. The resolving power of a microscope is wavelength dependant, which is the

main factor limiting the optical microscope to a theoretically achievable resolution of about 150 nm, but normally around 500 nm. For much higher resolution, electron microscopy (EM) employs an electron beam with wavelengths between 0.001 nm and 0.01 nm. Depending on the acceleration voltage EMs are capable of reaching a resolution of 0.2 nm, which is in the range of atomic resolution.

There are two main types of EMs: the TEM and the SEM.^[173] All types of EMs consist of an electron gun, electromagnetic lenses and various sorts of detectors. EM has to be conducted under HV due to strong electron scattering of the beam under gas atmosphere. Electron beam sources can be either thermionic guns or field-emission guns (FEGs). Thermionic guns are based on a resistively heated filament made of tungsten or lanthanum hexaboride (LaB_6) which emits electrons towards an anode when heated to very high temperatures. By comparison, in a FEG electrons are extracted by a very high electric field from a sharp tungsten tip resulting in improved brightness. A first anode extracts the electrons from the target at low kV which are then accelerated down the column by an acceleration anode at high voltages of a few tens of kV.

Electrons can interact with the specimen in different ways creating various types of signals, including electron scattering and secondary effects. A summary of the important effects can be seen in Figure 2.8a.

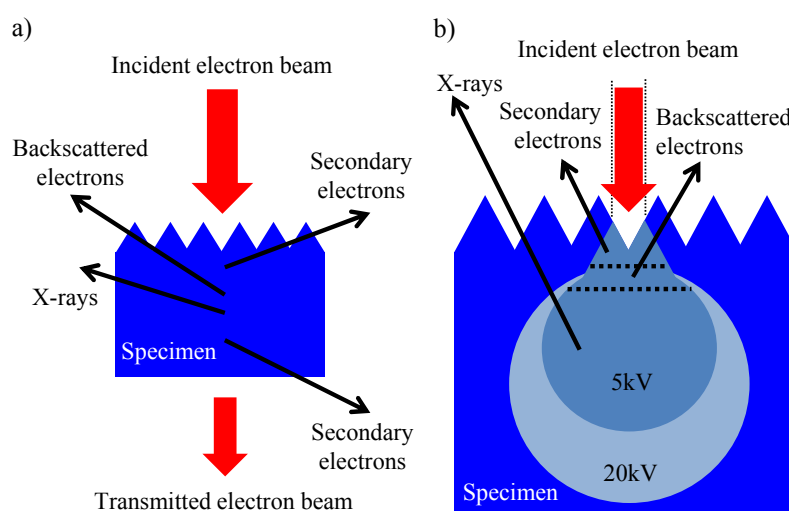


Figure 2.8 a) Summary of effects occurring from the interaction of a high energy primary electron beam with a specimen and b) the interaction volume of the specimen hit by an electron beam of lower and higher energy, including the specimen regions of specific signal occurrence from secondary effects.

Elastic electron scattering is based on the Coulombic interaction, i.e. attraction and repulsion of the beam or primary electron and the specimen atom, including nucleus and surrounding electrons. During the scattering process no kinetic energy of a primary electron gets lost. Deflection depends on the atomic number of the scattering atom and constitutes the key mechanism for electron diffraction. In an inelastic scattering process the primary electron loses kinetic energy due to interaction with the scattering atom, including the generation of backscattered electrons (BSEs) and energy absorption processes leading to secondary effects.

During specimen penetration the majority of primary electrons come to a stop within the interaction volume and generate either heat within the specimen, or initiate secondary effects in different parts of the volume which are then detectable from the outside, as shown in Figure 2.8b. Other secondary effects include secondary electrons (SE) with a lower energy of <50 eV and X-ray emission caused by relaxation of outer shell electrons which replace knocked out inner shell electrons.

2.2.2.2 Transmission electron microscopy (TEM)

In most TEMs a thermionic gun is used to generate an electron beam with an acceleration potential of between 80 and 200 kV. The beam is sent down a HV column in a vertical alignment passing two condenser lens systems, which control the beam spot size as well as the intensity on the specimen. The beam then interacts with the specimen leading to the scattered, transmitted electron beam which can be evaluated in either imaging or diffraction mode. In order to pass the specimen thickness with a certain beam intensity, the specimen has to be very thin, only a few hundred nanometres. In bright field imaging the image contrast is called mass-thickness contrast. With increasing specimen thickness, but also higher atomic number of the material, more scattering occurs resulting in darker image spots. TEM can also be seen as a bulk analysis of the internal structure of thin specimens. Generally, the sample is mounted on a support grid with a circular area of 3 mm in diameter. The transmitted electron beam then passes through the objective lens forming the intermediate image, which is then magnified by the intermediate lens and projected onto the screen. A TEM in imaging mode can be seen in Figure 2.9.

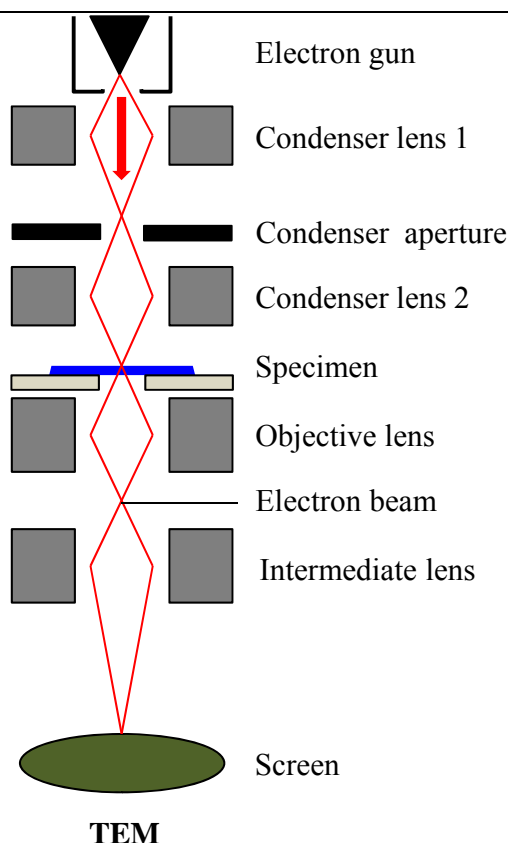


Figure 2.9 Schematic of a TEM in imaging mode.

In this project a JEOL 2000 FX TEM was used to image synthesised nanospheres <100 nm in diameter (see Chapter 3). A JEOL 2010 TEM was employed to image cross-section slices of ZnO modified polymer blend OPV devices (see Chapter 6) produced by FIB milling (done at Imperial by Dr. Benoit Illy). Typically, acceleration voltages of 150-200 kV were used in imaging mode. The samples were mounted on Formvar coated copper grids with mesh 200.

2.2.2.3 Scanning electron microscopy (SEM)

SEM is a surface or near-surface probing technique based on a specimen scanning electron beam of typically between 1 kV and 25 kV, much lower than for a TEM. The electron beam is generated either by a FEG or thermionically using a tungsten filament. The electrons are accelerated down the high vacuum column passing through a condenser

and then an objective lens, where the condenser lens first de-magnifies the beam the way that a very small beam spot of only 2-10 nm in diameter reaches the specimen. The objective lens then helps to focus the beam onto the specimen. In order to generate a complete image of a few micrometre height and width, computer controlled scan coils control the exact x-y beam position and raster the specimen surface systematically. The received intensity signals are collected by the computer. Specific software then reconstructs the 2D image. In Figure 2.10 a schematic of a SEM in imaging mode can be seen.

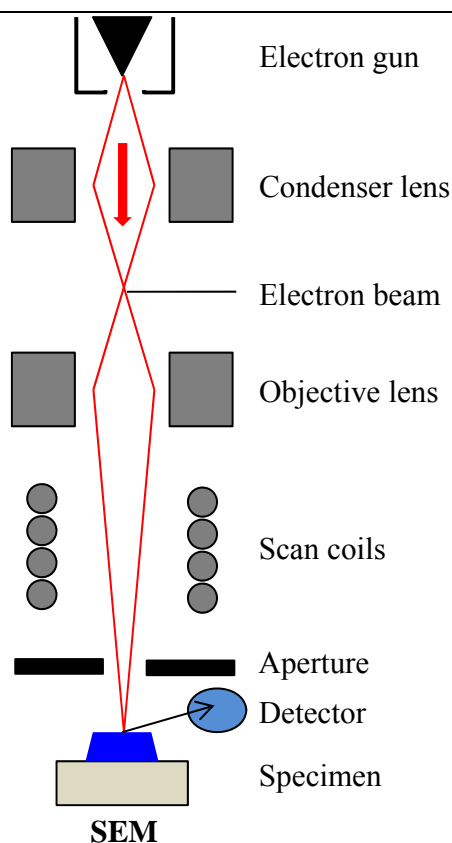


Figure 2.10 Schematic of a SEM in imaging mode.

When the electron beam interacts with the specimen various signals are emitted including BSEs, SEs and X-rays, which are then detected by the specific detector. For image interpretation it has to be taken into account that the interaction volume can penetrate the specimen as far as a few micrometres. The penetration volume and depth

scale with increased acceleration voltage (see Figure 2.8b). Common imaging modes use SEs which originate from the low surface, are abundant and give the best spatial resolution. However, SEs are low in energy and have to be accelerated by an applied electric field in order to generate a signal in an SE detector. High resolution SEMs are equipped with a through-the-lens detector which can detect both, SEs and BSEs. For semiconducting or insulating specimens a few nanometres thick charge conducting coating is applied and connected to ground in order to avoid surface charging which can disturb the beam and the signal. Possible coating materials are sputtered metals such as Au or Pt, but also arc-deposited carbon, where Pt and carbon give the smoothest coating.

In this project a FEG-SEM, Zeiss Supra 55VP and a FEG-SEM Gemini 1525 were used for various types of samples including PS spheres, self-assembled PS nanosphere thin films, open-cellular films, as well as different types of thin films and cross-sections (see Chapter 3, 5, 6). The samples were mostly coated with carbon or Pt and mounted on aluminium stubs by conductive silver paint or carbon tape. Typical imaging voltages were between 1 kV and 20 kV.

2.2.2.4 Focused ion beam (FIB)

FIB microscopy is based on the same principles as SEM but instead of an electron gun it is equipped with a field emission ion gun. A field emission ion gun works the same way as an ordinary FEG employing gallium as an ion source. Molten gallium forms a very fine tip from which Ga^+ ions can be extracted and accelerated with a few tens of kVs down the vacuum column. This focused ion beam is only a few nanometres in diameter and enables precise imaging based on the same signal effects as in SEM, including BSEs, SEs and X-rays. More importantly, FIB is also capable of ion milling or cutting very thin cross-section membranes for TEM. Imaging is performed with a fine ion beam and milling with a coarse ion beam. Both modes are referred to as sputtering because the beam is destructive, but also re-deposits material. When the specimen is bombarded with heavy Ga^+ ions of high kinetic energy, specimen atoms are ejected upon ion collision leading to controlled material removal. Furthermore, by using metal-organic or carbon containing gas, the ion beam can deposit fine metal and carbon films prior to cutting and protect the surface of the section of interest. Some draw-backs are the slow material

removal rate and the danger of sample material amorphisation at the cutting edge effecting TEM analysis, i.e. crystallinity. Most FIB microscopes are combined FIB/SEM instruments to allow destruction-free imaging by the electron beam and to enable FIB/SEM tomography. For the ZnO/blend device cross-sections in Chapter 6 a FEI FIB200-SIMS equipped with a FEG was used to produce the TEM sample membranes.

2.2.3 Electronic absorption spectroscopy

With electronic absorption spectroscopy the intrinsic properties of the compounds used in thin film technology and OPVs can be accessed including general light absorption and transmission behaviour, but also the electronic structure, vibronic behaviour and optical bandgaps. When an incoming photon of a discrete wavelength, and therefore energy, interacts with matter, excitation between two states of exactly this energy difference in the material can occur, i.e. photon absorption. Depending on the wavelength of the incoming light, either electronic, vibrational or rotational transitions are stimulated. Electronic transitions are mainly caused by higher energy electro-magnetic waves or photons of the UV/vis spectrum. Fine excitations of vibrational and rotational transitions are initiated by near-infrared (NIR) to infrared (IR) irradiation and microwaves respectively.

The photon absorption process of a sample is wavelength dependant and can be quantified directly by the ratio of the incident light intensity $I_0(\lambda)$ to the remaining light intensity $I(\lambda)$ leaving the sample, i.e the transmission, $T(\lambda)$. The Beer-Lambert law describes the logarithmic dependence of $T(\lambda)$ to the product of the molar absorptivity $\varepsilon(\lambda)$ of the compound, the penetration path l and the concentration c in solution as shown in Equation 2.5,

$$T(\lambda) = \frac{I}{I_0} = 10^{-\varepsilon(\lambda)lc} = 10^{-\alpha(\lambda)L} \quad (\text{Equ. 2.5})$$

For thin films the law is modified by adapting the exponent to the concept of thin film solids. Concentration of solids is defined by the product of relative molecular mass and the density of the solid. Absorptivity $\alpha(\lambda)$ is the combination of the concentration of

the solid and its molar absorption coefficient. L is still the penetration path, but also represents film thickness.

Absorption follows the same law and can be modified in the same way as for solid thin films in transmission. It scales linearly with the product of $\varepsilon(\lambda)$, l and c as well as $\alpha(\lambda)$ and L in solution and for solid thin films respectively, as shown in Equation 2.6.

$$A = \log \left(\frac{I_0}{I} \right) = \varepsilon(\lambda)lc = \alpha(\lambda)L \quad (\text{Equ. 2.6})$$

For compounds used in OPVs the absorption behaviour of the materials in the UV and visible part of the spectrum is of particular interest because electronic excitation leads to exciton generation and it is the part of the solar spectrum with the highest irradiation intensity.

In this thesis a Bentham spectrophotometer was used for transmission measurements on ZnO thin films in Chapter 6. A Perkin-Elmer Lambda 25 spectrometer was used for all other absorption and transmission measurements. All measurements were carried out in the range 200 nm to 900 nm. Thin films were measured on either quartz, glass or ITO substrates and solutions were measured in quartz cuvettes, with the appropriate background correction applied.

2.2.4 X-ray diffraction

2.2.4.1 Crystal theory

A crystal is defined by its smallest repetitive building block called a unit cell. A unit cell consists of a defined number of arranged motifs, including ions, atoms or molecules, which form repetitive patterns or a crystal lattice. The shape and size of such a unit cell is defined by six lattice constants consisting of three vectors a , b and c and the three angles α , β , and γ between the vectors. The vectors also define the crystallographic axis. Despite the variety of different combinations of the six constants, the number of possible lattices is reduced to 14 Bravais lattices. Crystal planes connecting arrays of motifs are indexed by Miller indices (hkl), which are the reciprocal distances of the

intercept of the crystal plane and the crystallographic axis. Therefore, plane (hkl) intersects with the crystallographic axis with distances of $1/h$, $1/k$ and $1/l$ respectively. The interplanar distance of two parallel planes with the same index is referred to as lattice plane spacing or interplanar spacing, d_{hkl} .

2.2.4.2 Diffraction theory

Similar to light diffraction with an optical grating, diffraction can be observed on crystal lattices acting as such a grating, if the probing wavelength matches the interplanar distance. In crystals this distance is in the regime of only a few angstroms. This condition can be satisfied by electromagnetic waves in the X-ray spectrum and led to X-ray diffraction, which is one of the most common characterisation techniques of crystalline solids.

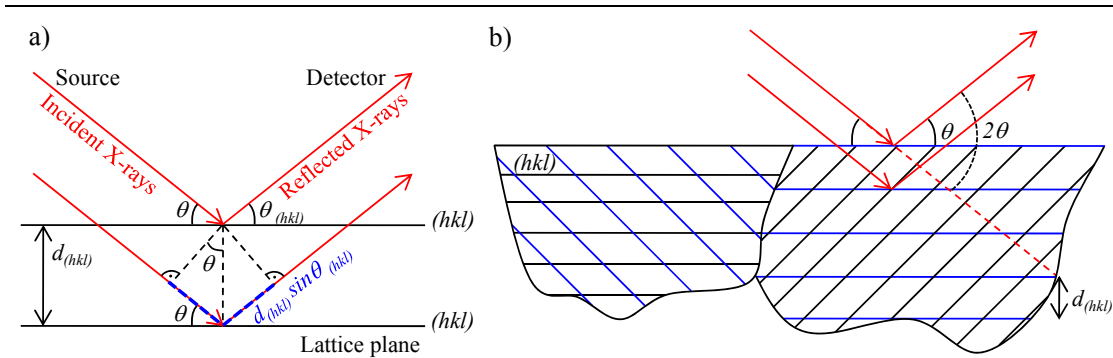


Figure 2.11 a) Bragg diffraction on adjacent (hkl) lattice planes and b) powder diffraction with diffraction occurring from the blue planes.

As shown in Figure 2.11a, incident X-ray beams penetrate the sample with an angle θ and are reflected by parallel crystal planes with an interplanar spacing, d_{hkl} . Constructive interference through diffraction occurs if the two parallel waves of the same wavelength are reflected by two parallel planes in such a way that they leave the sample in phase again. This condition is satisfied, if the wave reflected by a deeper plane travels a multiple of its wavelength, which is described by Bragg's law in Equation 2.7,

$$2d_{hkl} \sin \theta = n\lambda \quad (\text{Equ. 2.7})$$

where n is an integer and λ is the wavelength. By varying θ the exact condition for the strongest reflection can be found.

2.2.4.3 Powder diffraction

Powder X-ray diffraction is used for any polycrystalline sample consisting of domains of randomly oriented crystals, including powders and thin films. By varying the angle θ of the incident beam from a monochromatic X-ray source and the detector simultaneously, the sample can be screened for different (hkl) planes with appropriate interplanar distances, which is also known as the θ - 2θ technique. When the Bragg conditions at a certain angle θ are satisfied, a peak of high intensity appears in the angle resolved diffraction pattern for the specific (hkl) plane in a crystal grain. With changing θ diffraction will occur from different planes leading to a complete diffraction pattern (Figure 2.11b). A completely mixed powder shows strong diffraction at all angles. However, for thin films powder XRD shows only diffraction of planes parallel to the substrate which enables the determination of a preferential orientation of crystals in a film when compared to the signal intensity of a perfectly random powder.

A common X-ray source is the Cu K α emission with a wavelength of 1.542 Å. For XRD scans a Philips PANalytical X'Pert PRO MPD diffractometer with Cu K α radiation and a Ni filter was used.

2.3 PV device analysis

J - V analysis of OPV devices under light irradiation is a vital part of solar device characterisation because it gives details of the general device behaviour and performance, including the mostly cited PCE . OPV device analysis typically includes J - V curves under dark and light conditions as well as wavelength resolved scans to determine the EQE .^[52, 53]

2.3.1 The sun and solar simulation

The spectrum of our sun can be closest described by blackbody radiation, which was mathematically formulated by Planck in 1900. A blackbody is an ideal absorber and emitter of electro-magnetic radiation. When it is heated the blackbody starts to emit electro-magnetic radiation. The spectral emission shape can be described by the Planck distribution, which is wavelength and temperature dependent (see Equation 2.8).^[174]

$$E(\lambda, T) = \frac{2\pi hc^2}{\lambda^5 \left(e^{\frac{hc}{\lambda kT}} - 1 \right)} \quad (\text{Equ. 2.8})$$

In Equation 2.8, $E(\lambda, T)$ is the spectral emissive power, λ is the wavelength, h is Planck's constant, k is Boltzmann's constant, c the speed of light and T the blackbody temperature. As the temperature increases, the emission spectrum changes shape and shows a more pronounced maximum with a long tail towards longer wavelengths and drastically increased emission intensity at shorter wavelengths, as seen in Figure 2.12a.

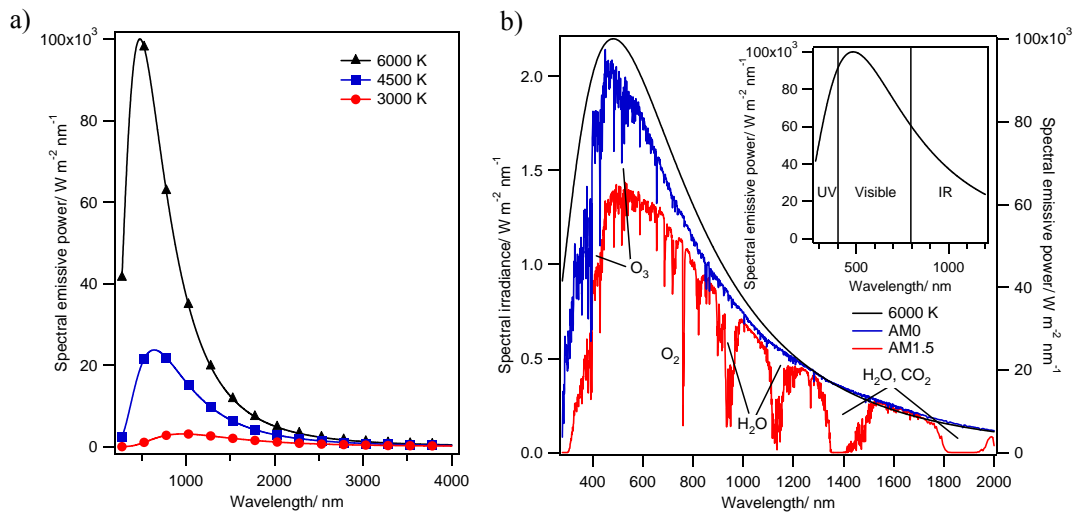


Figure 2.12 a) Black body emission at different temperatures: 3000 K, 4500 K and 6000 K. b) Solar irradiation spectra of AM0 and AM1.5 in comparison to an ideal black body emission at 6000 K, which matches the solar spectrum closely. Specific absorption windows reducing the incoming solar irradiance are labelled. The inset shows the spectral coverage of a 6000 K black body emission with the highest emission power in the visible range of the solar spectrum.

Our sun is a giant glowing sphere of heated gas, with a surface temperature of close to 6000 K, fuelled by nuclear fusion. The sun's spectral irradiation as observed from our planet matches the 6000 K blackbody radiation closely as shown in Figure 2.12b, but it also makes it very difficult to simulate a spectrum for such high temperatures. The inset in Figure 2.12b also shows that the highest spectral emission is found in the visible part of the spectrum which is very important to be aware of for PV engineering towards efficient PV cells.

To reach the earth's surface the sun light has to travel through the earth's gas atmosphere, where light absorption and scattering reduces irradiation intensity and leads to a characteristic spectrum. Typical solar spectrum features on earth originate from light absorption by water, O₂, CO₂ and O₃ as shown in Figure 2.12b.^[174] The irradiation intensity and spectrum are dependent on the distance travelled through the atmosphere and therefore the incident angle, φ_{AM} (see Figure 2.13). This angle dependence is measured in air mass (AM) and can be described by Equation 2.9.

$$AM = \frac{1}{\cos \varphi_{AM}} \quad (\text{Equ. 2.9})$$

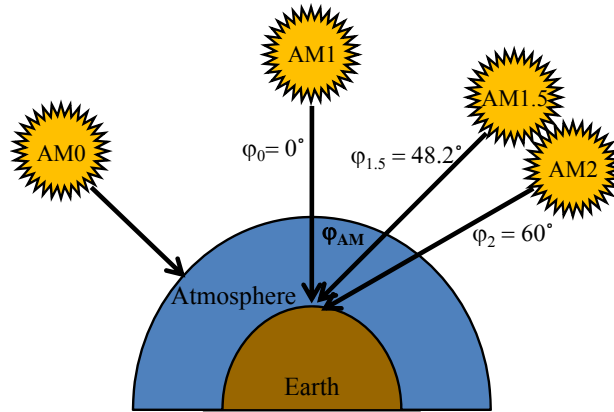


Figure 2.13 Angle dependence of AM for φ_{AM} between incoming sun light and surface of the earth calculated at one surface point. AM0 is measured just outside the atmosphere with no atmosphere present.

The extra-terrestrial irradiation intensity spectrum, AM0, is measured outside the atmosphere giving a light intensity of 135 mW cm⁻² and does not show any gas absorption features (see Figure 2.12b). AM1 is defined by the sun position at $\varphi_0 = 0^\circ$ (sun

overhead) with an AM of 1. For AM1.5 and AM2 the angles are $\phi_{1.5} = 48.2^\circ$ and $\phi_2 = 60^\circ$ respectively. With a reduced light intensity of 100 mW cm^{-2} the AM1.5G spectrum is accepted as the PV device testing standard. The global spectrum, G, is a combination of direct and diffuse sunlight, where the diffuse light accounts for light reaching the earth which has been scattered by clouds and the atmosphere.

For reliable PV device testing solar irradiation of AM1.5G was simulated with a Newport Oriel solar simulator with a xenon arc lamp as a light source. An AM1.5G spectral filter was employed to match the solar spectrum as closely as possible. The light intensity was set to 1 sun (100 mW/cm^2) using neutral density filters and was measured with a Fraunhofer calibrated PVM 482 photodiode with a KG-5 filter. By combining different neutral density filters the beam intensity could be tuned from 10 to about 400 mW cm^{-2} for extended light intensity measurements.^[175]

2.3.2 *J-V* characteristics

2.3.2.1 Plots and parameters

An important part of the OPV device characterisation is the measurement of *J-V* behaviour in the dark as well as under illumination. Figure 2.14a shows these *J-V* curves for both types of device architectures, regular and inverted, with charge collection at opposite electrodes resulting in point symmetric curve plots (centred at 0 V and 0 mA cm^{-2}). The *J-V* measurement involves a device current scan under an applied bias ranging from a negative to a positive voltage (typically from -1 V to +1 V). Scanned under dark condition, an asymmetric diode-like *J-V* curve is recorded. The ideal characteristic diode current curve of the dark current, J_{dark} , shows no current flow under negative bias and an exponentially growing current under forward bias once the built-in voltage of the diode is exceeded. Under illumination the *J-V* curve shows an offset to J_{dark} , known as the photocurrent, J_{ph} . This gain in current is the crucial part in OPV devices, where incoming light is transformed into electric current. Important values such as J_{SC} and V_{OC} are measured in the fourth quadrant of the *J-V* plot for regular and in the second quadrant for inverted OPV devices, where the bias is scanned the other way around.

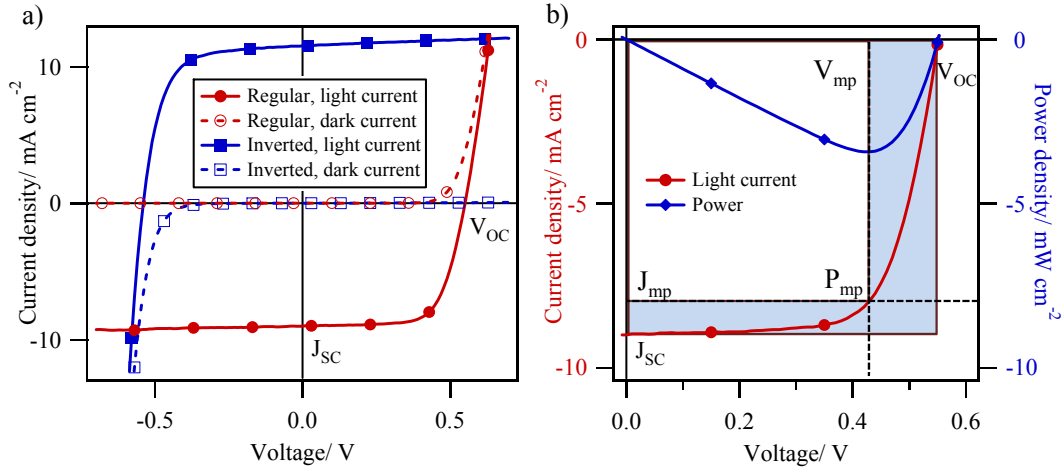


Figure 2.14 a) J - V plot of currents in a regular and an inverted device architecture under light and dark condition. b) Power density plot of a regular device explaining the FF of a PV device.

OPV heterojunction diodes are assumed to be non-ideal diodes due to material and fabrication process related defects causing current leakage, pin-holes, shorts and poor contacts, which lead to non-ideal series resistance (R_s , ideal = 0 Ω) and shunt resistance (R_{sh} , ideal = ∞).^[52] The most widely accepted diode model to describe the J - V behaviour of an OPV device is the generalised Shockley equation (see Equation 2.10).^[56]

$$J(V) = \frac{R_{sh}}{R_s + R_{sh}} \left[J_s \left(e^{\frac{q(V - J R_s)}{n k_b T}} - 1 \right) + \frac{V}{R_{sh}} \right] - J_{ph} \quad (\text{Equ. 2.10})$$

where $J(V)$ is the voltage dependant device current density, V is the voltage, J_s is the reverse saturation current density and n the diode ideality factor. An electric circuit equivalent can be seen in Figure 2.15.

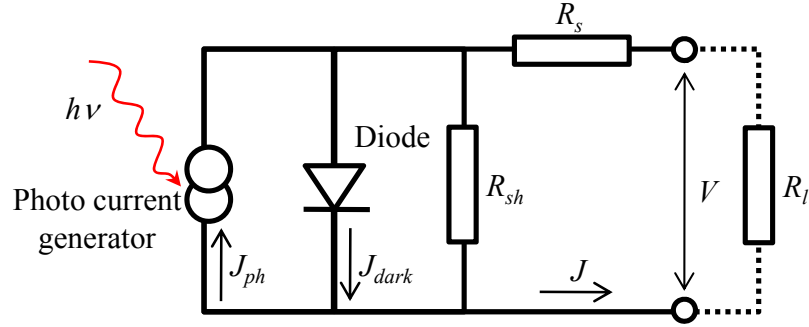


Figure 2.15 Schematic of a circuit equivalent to a PV device including resistances (R_s and R_{sh}) and load resistance (R_L).

From the J - V behaviour in the dark and under illumination the important OPV device characterising parameters can be directly read out or indirectly determined, including V_{OC} , J_{SC} , fill factor (FF), PCE , operational maximum power output (P_{mp}), R_s , R_{sh} , J_s and n .

V_{OC} is the maximum device voltage achievable across a device at open circuit, i.e. the load resistance, R_L being infinitely high in the outer circuit and at internal charge equilibrium. On a J - V curve V_{OC} can be found at the voltage intercept where $J(V)=0$ (see Figure 2.14b). The voltage obtained from a device in operation under closed circuit condition and under load is always smaller than V_{OC} .

J_{SC} states the maximum achievable net current density in an OPV device at $V=0$ and $R_L=0$, i.e. under short circuit condition. It is the sum of all the collected current from contributing photoactive layers in a device and is therefore heavily dependent on η_{abs} , η_{ed} , η_{ct} and η_{cc} .

P_{mp} is reached when the product of V and $J(V)$ is maximised, defined as current density at maximum power point (J_{mp}) and voltage at maximum power point (V_{mp}) respectively, where $J_{mp} < J_{SC}$ and $V_{mp} < V_{OC}$ applies (Equation 2.11). It defines the operational maximum power output of an OPV device, but also determines the area of the smaller square area needed to define the FF (see Figure 2.14b).

$$P_{mp} = V_{mp}J_{pm} = V_{OC}J_{SC}FF \quad (\text{Equ. 2.11})$$

FF is determined by the ratio of the operational maximum power output of an OPV, P_{mp} , and the maximum achievable power output defined by the product of J_{SC} and V_{OC} demonstrated in Equation 2.12 and Figure 2.14b.

$$FF = \frac{V_{mp}J_{mp}}{V_{OC}J_{SC}} = \frac{P_{mp}}{V_{OC}J_{SC}} \quad (\text{Equ. 2.12})$$

The FF is always <1 . It indicates how closely a measured diode curve matches the ideal and most efficient square shape and is therefore used to find the PCE of a device. Factors limiting the FF include both resistances.

One of the most important parameters of OPVs is the PCE , which is defined as the ratio of P_{mp} and the incident radiation power density (P_{inc}) shown in Equation 2.13. The PCE is the overall conversion efficiency of all incoming light into electrical current.

$$PCE = \eta_{eff} = \frac{P_{mp}}{P_{inc}} = \frac{V_{OC}J_{SC}FF}{P_{inc}} \quad (\text{Equ. 2.13})$$

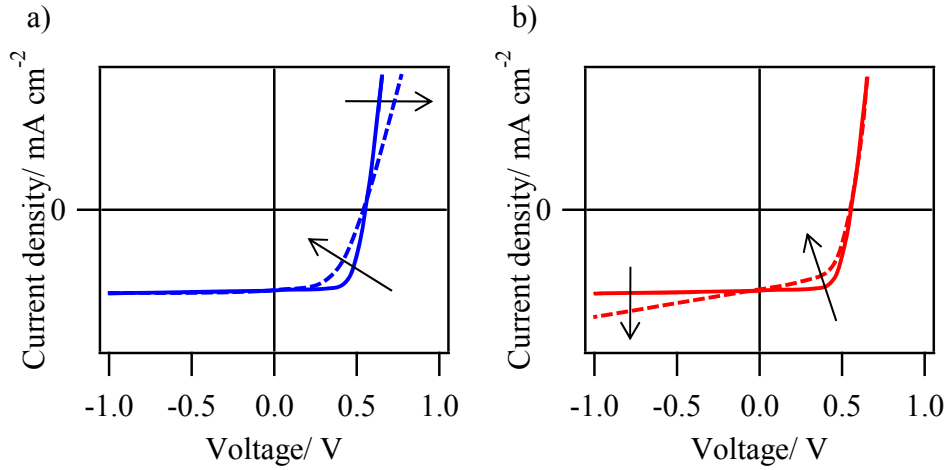


Figure 2.16 Effect of resistances on J - V curve shape including a) R_s and b) R_{sh} . The arrows indicate the trend of change in curve shape with a) increasing R_s and b) decreasing R_{sh} reducing the FF in both cases.

Resistances such as R_s and R_{sh} reduce the FF and therefore the PCE of an OPV device due to various loss mechanisms (see Figure 2.16). In an ideal device circuit R_s is considered to be zero and R_{sh} to be infinite. With increasing R_s and decreasing R_{sh} the

power output of the circuit is reduced. The main loss mechanisms causing an increase in R_s are based on the resistivity of the materials and layers across the cell as well as resistive contacts. R_{sh} originates in current leakage through the cell caused by pinholes, film defects and leaky contacts.

In this thesis J - V measurements were recorded with a computer controlled Keithley 2400 source-meter. Attached to both device electrodes a voltage is applied to the device with scans being carried out from -1 V to +1 V for regular and +1 V to -1 V for inverted devices. This measurement was firstly conducted under dark and afterwards under illuminated conditions. The device connected in the sample holder is positioned in the centre of the calibrated light beam. The measured data are collected by a computer running custom LabView software. All devices were tested in a sealed sample holder under nitrogen atmosphere unless otherwise stated.

2.3.3 External quantum efficiency (EQE) measurement

To obtain a better understanding of the photocurrent contribution from the individual compounds employed in OPV devices, the EQE or incident photon conversion efficiency ($IPCE$) can be used to determine their spectral response. For most materials a close correlation of the absorption spectrum and the spectral photocurrent response is expected due to exciton formation at the specific wavelength. For devices with several photoactive compounds the device EQE reflects the individual photocurrent contributions. Furthermore, the measurement reveals more information about the exciton diffusion and the charge collection behaviour of a device. EQE or $IPCE$ is defined as the photocurrent response of the OPV device to the incident monochromatic light and defines the ratio of the number of charges collected in an external circuit per incident photon. It can also be seen as the ratio of the monochromatic $J_{SC(device)}(\lambda)$ to the theoretical maximum photocurrent at a particular wavelength as shown in Equation 2.14,

$$EQE(\lambda) = IPCE(\lambda) = \frac{J_{SC(device)}(\lambda)}{qN(\lambda)} = \frac{J_{SC(device)}(\lambda)}{qS(\lambda)} \frac{hc}{\lambda} \quad (\text{Equ. 2.14})$$

where $N(\lambda)$ is the monochromatic incident photon flux density, q is the elementary charge, $S(\lambda)$ is the spectral irradiance of the incident light, h is Planck's constant, c is the speed of light and λ is the wavelength of the incident photon.^[56] In reverse, $J_{SC(device)}$ can be estimated by integrating the product of the measured $IPCE(\lambda)$ and $S(\lambda)$ over the whole irradiation spectrum as demonstrated in Equation 2.15.

$$J_{SC(device)} = \int_{\lambda_1}^{\lambda_2} \frac{q\lambda}{hc} IPCE_{(device)}(\lambda) S(\lambda) d\lambda \quad (\text{Equ. 2.15})$$

Experimentally the $IPCE_{(device)}$ is calculated by direct comparison of the measured $J_{SC(device)}$ to a reference photodiode (silicon solar cell) with a known $IPCE_{(ref)}$ and measured $J_{SC(ref)}$ using the following Equation 2.16:

$$\frac{IPCE_{(device)}(\lambda)}{IPCE_{(ref)}(\lambda)} = \frac{J_{SC(device)}(\lambda)}{J_{SC(ref)}(\lambda)} \quad (\text{Equ. 2.16})$$

EQE example spectra of the spectral current and response of a TiO_x /SubPc device and the reference silicon photodiode as well as the estimated current of the TiO_x /SubPc device are shown in Figure 2.17.

The measurement setup used was based on a Sciencetech solar simulator with a xenon arc lamp as a white light source and a computer controlled PTI monochromator. The monochromatic light intensity was calibrated with a Si photodiode (818UV, Newport) as a reference cell. The current measurement was performed with a current-voltage amplifier (Femto DHPCA-100) and lock-in amplifier (Stanford Research SR 830 DSP). After an initial reference scan, the device was scanned over the same wavelength range, typically between 350 and 800 nm. In order to match the active device area either a masking system or an area correction factor was applied.

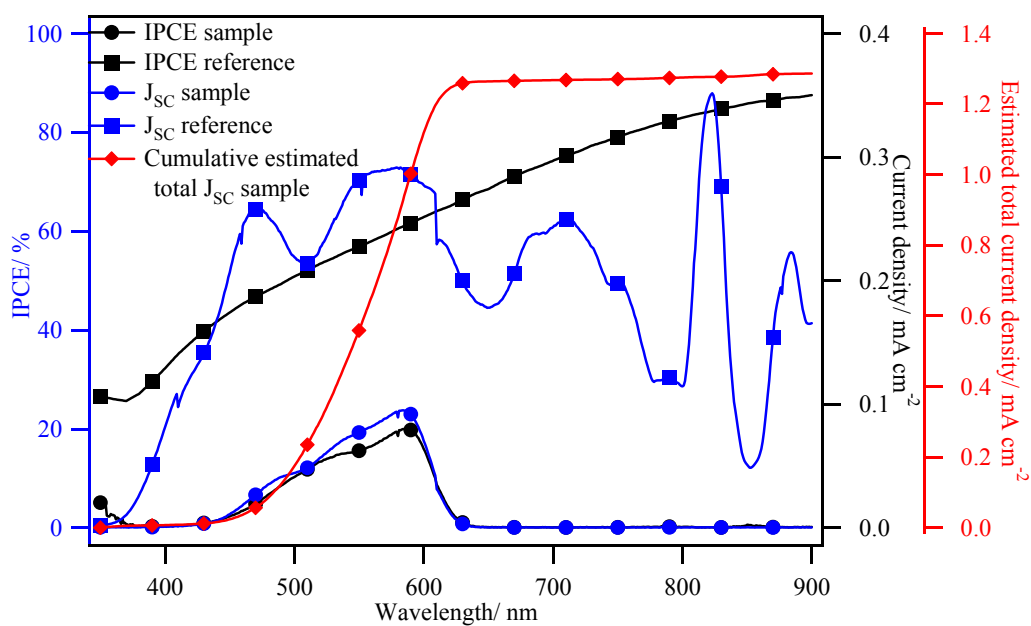


Figure 2.17 *EQE* example spectra showing the spectral current and response of a $\text{TiO}_x/\text{SubPc}$ device and the reference silicon photodiode as well as the estimated current of the $\text{TiO}_x/\text{SubPc}$ device.

Chapter 3: Nanosphere synthesis

This chapter covers the synthesis of PS nanospheres with small diameter, i.e. <100 nm, and good monodispersity which are then used for nanosphere templating in Chapter 5.

A variety of different PS nanoparticles are available commercially, but most of these latexes contain surfactants used for emulsion polymerisation. Surfactants can greatly influence sphere self-assembly and packing behaviour with significant impact on the subsequent formation of colloidal crystals, 3DOM structures and composite OPV devices.

For PS nanoparticles of small diameters synthesised by radical initiated emulsion polymerisation, soaps are needed as particle stabilisers. Purification through dialysis to remove surfactants is not efficient for the small, but expensive batches which are available commercially. Surfactant-free emulsion polymerisation of small <100 nm particles is very challenging, but needed for OPV templating application.

3.1 Introduction

3.1.1 Definitions

Colloids are defined as a two-phase system of a dispersed phase and a continuous phase, where the dispersed phase is homogeneously mixed into the continuous phase.^[176] In the case of two immiscible liquids it is called an emulsion. A dispersed solid in a liquid is defined as a heterogeneous suspension for particles typically >1 μm and a dispersion or sol for particles <1 μm . Suspensions can gradually phase separate due to sedimentation by gravitational forces. Colloids in dispersions are small enough to be dominated by their thermal energy or Brownian motion, which balances gravitational forces and keeps them dispersed. Polymer dispersions in particular are also referred to as latex. If the size distribution of the particles in a latex is very narrow the particles are monodisperse which is indicated by the polydispersity index (PDI).

3.1.2 Emulsion polymerisation

3.1.2.1 Surfactant assisted emulsion polymerisation

One of the most common and suitable techniques to synthesise polymer nanospheres is radical initiated emulsion polymerisation as it offers good control over polydispersity and size with the potential to generate sub-100 nm nanospheres.^[177-179] Latex synthesis is based on a heterogeneous reaction using a monomer, surfactant, an initiator and a dispersion medium, such as water. A typical surfactant used for a variety of polymer emulsion polymerisations is sodium dodecyl sulphate (SDS).^[180, 181]

In the case of PS synthesis, styrene is dispersed in a water phase. In a first step, the surfactant emulsifies parts of the monomer by micelle formation. The micelles are then infiltrated by the monomer. Free radicals are formed in the heating step by initiator decomposition based on single bond homolysis. The radical attacks a dissolved monomer and initiates a chain reaction leading to oligomers in the water phase. In a next step the still reactive oligomers enter the bigger monomer-swollen micelles and continue the polymerisation eventually forming a colloidal sphere. The terminal active centres are fed by dissolved monomer from the aqueous phase until either all the monomer is used or the radical site becomes quenched in one of the possible side reactions.^[182, 183] Typical initiators are anionic persulfates such as potassium persulfate (KPS) and cationic 2,2'-azobis(2-methylpropion amidine) dihydrochloride (AMPAD). The surfactant and the charged remains of the initiator on the particle surface lead to colloidal sphere stabilisation in the dispersion. The molecular structure of the different compounds and product can be seen in Figure 3.1.

In the case of nanosphere templating in OPVs, surfactants have the ability to form a residue film on the templated organic interface after organic solvent treatment. A clean D/A interface is vital for efficient OPV device operation, hence a remaining surfactant film can severely disturb device operation. Although dialysis removes residues, surfactant and unreacted monomer in the latex, it may cause sphere instability and particle agglomeration. Also, surfactants and residues can disturb sphere self-assembly leading to blockage of the voids in between the particles. Complete removal of surfactants and reaction residues is very difficult to achieve.^[184]

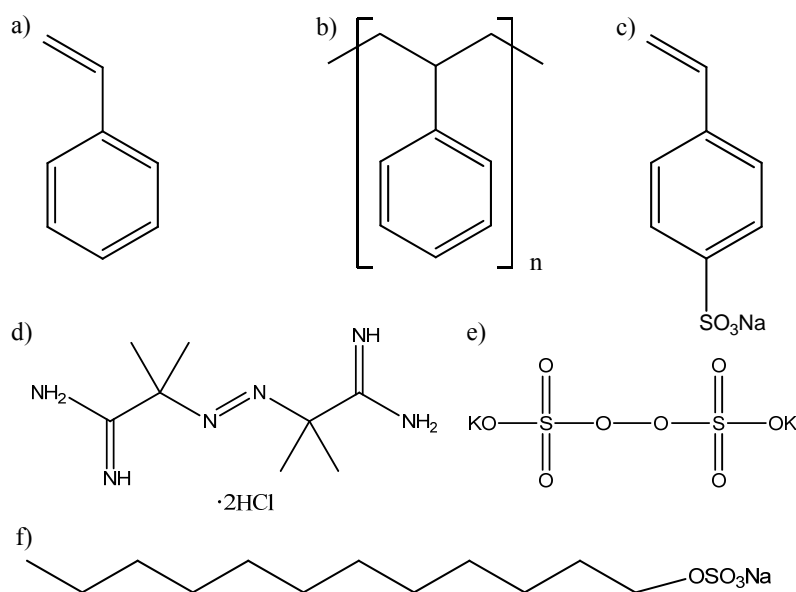


Figure 3.1 Molecular structures of compounds used in emulsion polymerisation: a) styrene, b) PS, c) NaSS, d) AMPAD, e) KPS, f) SDS.

3.1.2.2 Surfactant-free emulsion polymerisation

To produce ‘cleaner’ polymer nanospheres, surfactant-free radical initiated emulsion polymerisation was developed, using just monomer, a dispersion medium, and the initiator.^[185, 186] Surfactant-free emulsion polymerisation typically leads to particles with diameters in the range 200 nm to 1000 nm which are stabilised by their ionic surface charge.^[187] Smaller particles are hard to achieve due to the absence of additional particle stabilising surfactant.

The reaction mechanism is similar to a general emulsion polymerisation with the main difference of micelle formation by preformed oligomers. Oligomers are short polymer chains generated in the first polymerisation step. They are similar in structure and function to surfactants consisting of a long hydrophobic tail which assembles inside the micelle, and an ionic head which faces the aqueous phase providing sphere stability. After micelle formation by assembled oligomers, monomer and primary radicals diffuse into the micelles and polymerise. With continuous sphere growth, the particle surface charge decreases leading to instability. To regain stability particles coagulate benefiting from the favourable surface-to-volume growth dependence as observed for regular

emulsion polymerisation. By fusing two or more particles the new particle gains in surface charge density. The charged surface groups prevent the nanospheres from aggregation through vdW attraction using electrostatic repulsion to keep the particles dispersed. The charged spheres form an electrical double layer to maintain charge neutrality in close proximity of the particles in solution.

To form colloidal crystals with long range order the polydispersity of nanospheres has to be in the range of 4-8 % in diameter distribution, which correlates with a PDI of <0.05 .^[188, 189] In surfactant-free emulsion polymerisation nanosphere synthesis there are many parameters which determine particle size and polydispersity. Some of the parameters interfere with each other making precise size control very difficult. Size control of small particles <100 nm is particularly challenging.^[190]

Amongst the parameters affecting the nanosphere size in a synthesis are reaction temperature, stirring speed, as well as monomer, initiator and additive concentrations.

With a temperature above 60 °C the initiator decomposition rate is high enough to be eliminated as the reaction rate limiting factor, which otherwise can lead to uneven particle growth with a large size distribution. With increased initiator decomposition rate more nuclei are formed which therefore reduces the average sphere size. A higher monomer concentration ultimately leads to a higher solid content, but also increases the particle size due to larger nuclei and more monomer per nuclei.^[191] The initiator concentration defines the number of seed nuclei provided for particle growth, but also sets the concentration of micelle forming oligomers. Hence, an increase in initiator concentration with all other parameters kept constant causes a decrease in particle size but is also linked to a higher PDI due to secondary nucleation.^[186] However, with increasing initiator concentration the ionic strength of the solution increases and thins the vital electrical double-layer which prevents the particles from coagulation during the growth process. This effect leads to an increase in particle size and also polydispersity. In the literature both processes were observed.^[186, 191, 192]

To synthesise small nanospheres, styrene-4-sulfonic acid sodium salt (NaSS) can be added in low quantities as a monomer building block.^[190] NaSS is based on a styrene monomer which is functionalised with a sulfonic acid substituent for increased surface charge in anionic systems. The molecular structure of NaSS is shown in Figure 3.1.

Unlike surfactants, NaSS copolymerises with styrene and adds charged functional groups to the otherwise hydrophobic polymer chain and therefore increases the surface charge. With even small concentrations of NaSS the particle size was significantly reduced due to promoted nucleation but also the additional surface charges.^[193] Xue *et al.* achieved particle sizes of about 40 nm with NaSS and a continuous monomer feed.^[194] NaSS helps to form smaller particle sizes but can also lead to high polydispersity. Similar to an increased initiator concentration, the ionic strength of the solution can be raised with added NaSS and can therefore cause particle coagulation and larger particle sizes. Therefore, a balance between low particle diameter, latex stability and acceptable polydispersity has to be found.

The entire synthesis is very oxygen sensitive due to initiator quenching, which explains why the synthesis is performed under N₂. However, oxygen can also be used to quench the polymerisation in an early stage, when the particle size is still small. By not allowing full conversion the solid content is assumed to be very low and purification needs much more care due to vast amounts of remaining monomer.

3.1.3 Dynamic light scattering (DLS)

Dynamic light scattering is a commonly used technique to determine the diameter of nanospheres in dispersion.^[195] Compared to other techniques such as EM, DLS is very quick and reliable if the particle size distribution in the sample dispersion is close to monodisperse. Particle size determination by DLS does not require sophisticated sample preparation and is well established in the field.

The measurement is based on the evaluation of the Brownian motion driven particle diffusion. The particle size can be determined from the diffusion coefficient, D , by using the Stokes-Einstein equation (Equation 3.1),

$$d(H) = \frac{k_B T}{3\pi\eta D} \quad (\text{Equ. 3.1})$$

where $d(H)$ is the hydrodynamic diameter of the particle, k_B is Boltzmann's constant, T is the absolute temperature and η is the viscosity. The measurement setup

includes a laser light source, a sample holder accommodating the cuvette and a photomultiplier as a detector. Measurement control and data analysis are performed by computer-assisted Malvern software. The incoming laser beam is scattered by the nanoparticles in dispersion generating a scattering pattern, which is detected at a set angle by the detector. As the nanoparticles diffuse randomly, the light scattering pattern and intensity change over time and are monitored. The signal correlation is of short life time and decays very quickly depending on the particle size. By using a correlation function the decay can be fitted to extract D and therefore $d(H)$. Smaller particles diffuse quicker than larger ones and show faster correlation function decay. The PDI in DLS is derived from the slope of the decay fit and is specifically used for sphere diameter characterisation differing from the polydispersity index definition of polymers defined by molecular mass distribution. PDI values are typically much smaller than 1. Values lower than 0.05 are regarded as monodisperse, i.e. a very narrow size distribution. Care has to be taken with non-spherical or aggregated particles as their diameter might be overestimated by the measurement. The hydrodynamic diameter $d(H)$ is slightly larger than the diameter of the sole dry particle, because it includes the electrical double layer.

To compare different types of synthesis and to screen specific synthesis parameters, DLS is a good technique for particle characterisation to determine the average hydrodynamic diameter (Z-average diameter) and PDI of a latex compared to EM. Dynamic light scattering measurements in this chapter were performed on a Malvern Instruments Zetasizer 3000HSA and a Malvern Zetasizer Nano in aqueous dispersion.

3.1.4 Aim

Small monodisperse PS nanoparticles, ideally <100 nm, from surfactant-free emulsion polymerisation need to be synthesised to achieve nanosphere templating on L_D scale. In a first approach certain synthesis parameters are screened in experiments in a round-bottom flask. In a second step the synthesis is conducted in a jacketed reactor with focus on the influence of NaSS concentration to systematically study size and polydispersity behaviour. The particle sizes were initially in the range 100 nm to 300 nm with further improvements made to achieve diameters <100 nm.

3.2 Experimental

3.2.1 Nanosphere synthesis

The general procedure of emulsion polymerisation in either a round-bottle flask or a reactor involved a degassing phase, polymerisation initiation and conversion.^[196, 197]

First the monomer styrene (Fluka, purum, monomer, $\geq 99\%$ (GC), 0.005 % 4-tert-butylcatechol) and the required volume of deionised, prior degassed water were poured together in the reaction vessel. Depending on the type of synthesis other additives including surfactant SDS (BDH Laboratory supplies), co-monomer NaSS (Aldrich, technical, $\geq 90\%$) and pH buffer sodium hydrogen carbonate (NaHCO_3) (Aldrich, $> 99.5\%$) were added. The vessel was then sealed with septums to provide a closed system and the solution was degassed by excess N_2 injection below the solution surface through an inserted needle for about 30 minutes under constant stirring. After completion of the degassing stage the reaction solution was heated up to $70\text{ }^\circ\text{C}$ followed by initiator injection from a syringe. The initiator was pre-dissolved in a few millilitres of distilled water. The nitrogen syringe was then withdrawn above solution level. In these experiments two radical generating initiators of opposite charge were used, anionic KPS ($\text{K}_2\text{S}_2\text{O}_8$, Aldrich, 99 %) and cationic AMPAD (Aldrich, 97%). A first indicator of a working initiator is the change in appearance of the dispersion from transparent to opaque white. This change is due to particle formation of $<50\text{ nm}$ in diameter which happens within the first 20 minutes to one hour. The reaction was stirred for at least 4 hours to reach full conversion. After cooling to room temperature the nanosphere dispersion was filled into dialysis tube membranes (Sigma-Aldrich, Dialysis Tubing, Cellulose membrane, 33 mm diameter). The latex was dialysed against distilled water for up to two weeks. For efficient monomer and additive removal the water was changed daily. Upon completion the product was stored in air-tight bottles in the dark.

3.2.1.1 Round-bottom flask

In the first experiments a 250 mL round-bottom flask with a magnetic stirrer bar and an oil bath heater was employed for PS nanospheres synthesis. In these experiments

different compounds and parameters for radical initiated emulsion polymerisation of monodisperse nanospheres were screened. The temperature was monitored by a temperature probe immersed in the oil bath and controlled by a temperature controller linked to the hot plate. The stirring speed during the reaction was held at ca. 200-300 rpm. A total of five reaction recipes were screened in this way.

In reaction 1 (R1) to 3 (R3), deionised water (90 mL), styrene (10.0 g, 0.10 mol) and KPS initiator (0.05 g - 0.10 g, 0.2×10^{-3} mol - 0.4×10^{-3} mol) were used (see Table 3.1). To reduce the particle size and to probe the potential of a surfactant, SDS (0.50 g, 1.7×10^{-3} mol) was added in (R3).

Table 3.1 Summary of the experimental parameters of synthesis (R1) to (R3) using KPS with different synthesis conditions. The synthesis was carried out in a round-bottom flask.

React.	H ₂ O	Styrene	KPS	NaSS	SDS
	[mL]	[mol L ⁻¹]	[10^{-3} mol L ⁻¹]	[10^{-3} mol L ⁻¹]	[10^{-3} mol L ⁻¹]
(R1)	90	1.07 (10.0 g)	2.1 (0.05 g)	5.4 (0.10 g)	Surfactant-free
(R2)	90	1.07 (10.0 g)	4.1 (0.10 g)	5.4 (0.10 g)	Surfactant-free
(R3)	90	1.07 (10.0 g)	2.1 (0.05 g)	5.4 (0.10 g)	19.3 (0.50 g)

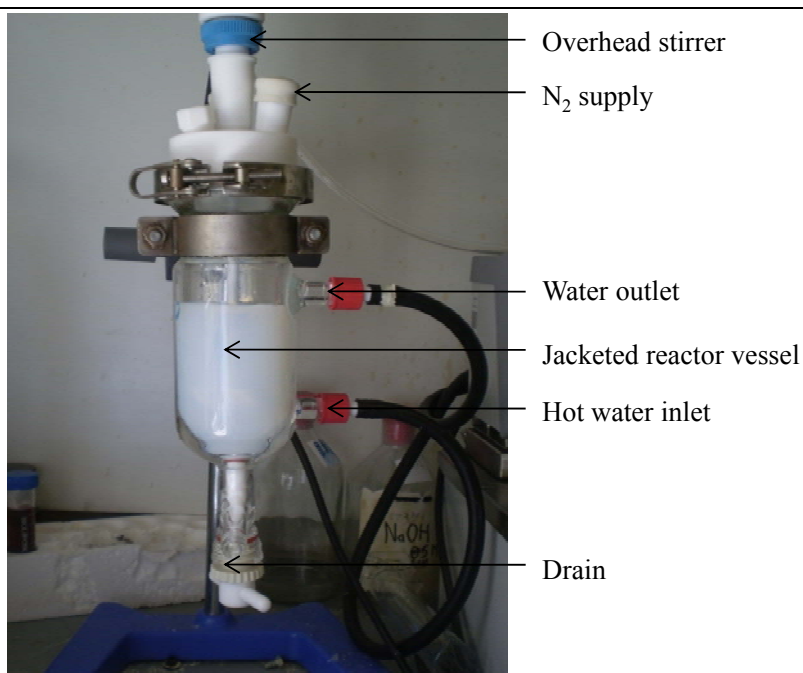
In reaction 4 (R4) and 5 (R5), deionised water (100 mL), styrene (1.0 g, 0.01 mol) and AMPAD (0.16 g, 0.6×10^{-3} mol) were used. A technique to reduce the particle size involves reaction quenching by sudden O₂ injection, and is used in (R5). The exact details for each reaction are summarised in Table 3.2.

Table 3.2 Summary of the experimental parameters of synthesis (R4) and (R5) using AMPAD with different synthesis conditions. The experiments were carried out in a round-bottom flask.

React.	H ₂ O [mL]	Styrene [mol L ⁻¹]	AMPAD [10 ⁻³ mol L ⁻¹]	Quenching
(R4)	100	0.10 (1.0 g)	5.9 (0.16 g)	-
(R5)	100	0.10 (1.0 g)	5.9 (0.16 g)	O ₂

3.2.1.2 Reactor

In later experiments a 250 mL reactor with an overhead four-blade stirrer and a water heater aggregate (HAAKE K41) has been used to allow better control over parameters such as temperature and stirring compared to synthesis in the round-bottom flask. The reactor setup is shown in Figure 3.2. Typical stirring speeds were between 250 and 350 rpm.

**Figure 3.2** Photograph of the reactor setup for emulsion polymerisation of PS latex.

In reaction 6 (R6) to 8 (R8) deionised water (180 mL), styrene (2.0 g – 10.0 g, 0.02 mol - 0.10 mol), AMPAD (0.10 g - 0.30 g, 0.4×10^{-3} mol - 1.1×10^{-3} mol) or KPS (0.05 g, 0.2×10^{-3} mol) with NaSS (0.10 g, 0.5×10^{-3} mol) were used to study full conversion emulsion polymerisation with an anionic and a cationic initiator in a reactor. In experiments 9 (R9) to 19 (R19) deionised water (180 mL), styrene (20.0 g, 0.19 mol), KPS (0.10 g, 0.4×10^{-3} mol), NaHCO_3 (0.10 g, 1.2×10^{-3} mol) and NaSS (≤ 0.40 g, $\leq 1.9 \times 10^{-3}$ mol) were used to study full conversion emulsion polymerisation. In this set of experiments all parameters were kept constant only varying the concentration of NaSS to regulate particle size and PDI. These experiments were all based on the anionic initiator KPS. The details for each reaction (R6) to (R19) are listed in Table 3.3.

Table 3.3 Summary of the experimental parameters of synthesis (R6) to (R8) using AMPAD and KPS as well as (R9) to (R19) using KPS with varying NaSS concentration. All reactions were carried out in a reactor.

React.	H ₂ O	Styrene	AMPAD	KPS	NaSS
	[mL]	[mol L ⁻¹]	[10^{-3} mol L ⁻¹]	[10^{-3} mol L ⁻¹]	[10^{-3} mol L ⁻¹]
(R6)	180	0.53 (10.0 g)	2.0 (0.10 g)	-	-
(R7)	180	0.11 (2.0 g)	6.1 (0.30 g)	-	-
(R8)	180	0.53 (10.0 g)	-	1.0 (0.05 g)	2.7 (0.10 g)
(R9)	180	1.07 (20.0 g)	-	2.1 (0.10 g)	0.0 (0.00 g)
to (R19)					to 10.8 (0.40 g)

3.2.2 Sphere size characterisation and solid content measurement

Dynamic light scattering (DLS)

The nanosphere dispersion was analysed after dialysis with DLS to determine the Z-average diameter and PDI. The dispersion was either used as synthesised or slightly diluted to satisfy the scattering conditions. Sample dispersions were analysed in disposable plastic cuvettes at 25 °C after at least 10 minutes of temperature equilibration.

Typically, data acquisition times of 20 seconds per measurement with 10 measurements per run, averaged over 10 runs, were used to determine particle diameter and PDI.

Electron microscopy (EM)

For selected latexes additional size analysis by TEM or SEM was carried out to determine the sphere diameter of the dry particles, which is slightly lower than the average diameter determined by DLS. An average number of at least 30 particles were measured for each reaction using the software Image Tool 3.00.

Solid content measurement

The determination of solid content mass fraction of a latex was performed gravimetrically. A measured amount of dispersion was weighed on a metal tray with a defined mass and put in an incubator over night to evaporate the solvent. By weighing the tray again with just the remaining dry solid content, the solid mass fraction can be calculated.

3.3 Results

3.3.1 Nanosphere synthesis in the round-bottom flask

The first PS emulsion polymerisation experiments (R1) to (R5) were all carried out in a round-bottom flask following a modified recipe published by Tauer *et al.* and McLachlan *et al.*^[196, 197] The recipe was adapted for the synthesis of PS nanospheres of <100 nm in diameter using both initiators.

(R1) and (R2) used the same conditions for surfactant-free emulsion polymerisation with only a change in KPS initiator concentration between $2.1 \times 10^{-3} \text{ mol L}^{-1}$ and $4.1 \times 10^{-3} \text{ mol L}^{-1}$ (0.05 g – 0.10 g, $2.1 \times 10^{-3} \text{ mol}$ - $4.1 \times 10^{-3} \text{ mol}$). The increase in KPS concentration results in a slightly larger particle diameter and PDI, increasing from 100 nm and a PDI of 0.010 in (R1) to 118 nm and a PDI of 0.052 in (R2) (see Table 3.4). For both reactions the nanospheres are reasonably monodisperse and can be used for colloidal crystal growth. With increasing initiator amount more micelle forming

oligomers and nuclei are created. If the monomer concentration is kept constant more spheres with smaller diameter should be created. However, the regulation of the sphere size via increased initiator concentration is not the most reliable parameter in a round-bottom flask synthesis due to temperature and stirring inhomogeneity and hence the expected trend is not seen.

Table 3.4 Summary of the experimental data of synthesis (R1) to (R3) using KPS as well as (R4) and (R5) using AMPAD. The reactions were carried out in a round-bottom flask. Sizes and polydispersity were all measured by DLS after dialysis.

React.	Initiator [10 ⁻³ mol L ⁻¹]	Treatment	Z-average diameter [nm]	PDI	Weight percentage [%]
(R1)	2.1 (KPS)		100	0.010	6.0
(R2)	4.1 (KPS)		118	0.052	7.5
(R3)	2.1 (KPS)	SDS	44	0.149	9.6
(R4)	5.9 (AMPAD)		82	0.058	0.3
(R5)	5.9 (AMPAD)	O ₂ quenched	61	0.086	<0.1

To achieve particle sizes of <<100 nm SDS was added as a surfactant in (R3) using the same conditions as for (R1) to compare it as a reference system. The addition surfactant SDS with a concentration of $19.3 \times 10^{-3} \text{ mol L}^{-1}$ showed a large effect with a decreased particle diameter of ca. 44 nm, but a very high polydispersity, PDI = 0.149. Figure 3.3 shows SEM images of PS nanospheres of (a) 100 nm (R1) and (b) 44 nm (R3) particle diameters. With all other parameters kept constant the difference of a surfactant-free reaction (R1) and SDS containing (R3) is clearly visible in sphere size and polydispersity, but also particle shape. The nanoparticles in (R1) appear to be spherical and uniform in size. However, the particles in (R3) do not all show a typical spherical shape and the sphere boundaries are not well defined. This clustering effect could be due to the remaining surfactant which acts as a glue and fuses the particles together leaving no interstitial vacancies between the particles.

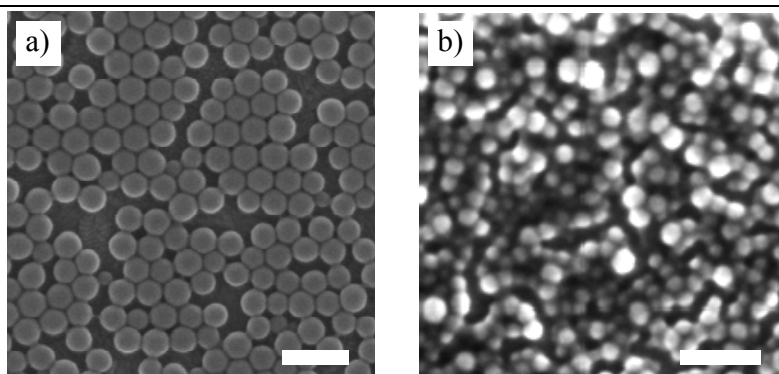


Figure 3.3 SEM images of PS nanospheres of a) 100 nm (R1) and b) 44 nm (R3) in diameter using KPS as the initiator. The difference of a surfactant-free reaction (R1) and SDS containing (R3) is clearly visible in sphere size and polydispersity, but also particle shape. Despite dialysis the remaining surfactant glues the particles together to form clusters. The scale bar is 200 nm.

In contrast to surfactant-free emulsion polymerisation, SDS pre-forms micelles in water due to its ionic molecular architecture, i.e. a polar head and apolar tail. This leads to a different reaction mechanism with the initiator being primarily responsible for nuclei formation. The micelles also help to stabilise PS particles of critically small sizes to form spherical shapes in water without collapsing. Such low particle diameters as achieved in (R3) would be desirable for nanosphere templating in composite OPVs. However, the very high polydispersity and the sphere clustering makes the latex unsuitable for colloidal crystal growth.

Reaction (R1) to (R3) resulted in small spheres of around 100 nm or less in diameter from a full conversion reaction. For all anionic particles based on KPS as the initiator, NaSS was added in small concentrations as an anionic co-monomer to increase the surface charge of formed particles. This leads to further particle stabilisation in aqueous solution. For cationic particles based on AMPAD an equivalent functionalised co-monomer is not commercially available and has to be synthesised which limits its use for the synthesis of small <100 nm particles.

In surfactant-free emulsion polymerisations (R4) and (R5) the cationic initiator, AMPAD, was used functionalising the surface of the particles with positively charged terminal groups. Both reactions were run under the same conditions with a low styrene concentration of only 0.10 mol L^{-1} (1.0 g, 0.10 mol) in deionised water (100 mL). (R4) was run until full conversion was achieved which led to nanospheres of 82 nm in

diameter and a PDI of 0.058 (Table 3.4). Such a PDI indicates a larger size distribution but is still acceptable for further templating applications. To reduce the particle diameter further without the help of surfactants such as SDS an alternative attempt was based on radical quenching with O₂.

In (R5) the same conditions were applied as for (R4) except the reaction was quenched by O₂ injection at a specific point of conversion during the reaction process with immediate arrest of the particle growth. The quenching step was conducted after a slight change in appearance of the solution from transparent to slightly opaque white which indicates that the particle growth process reached a sphere size of about 50 nm in diameter. The quenching in (R5) led to almost monodisperse particles with a PDI of 0.086 and a diameter of 61 nm. Although the particles are not classified as monodisperse anymore the polydispersity is still acceptable for further templating applications employing such small particles (Table 3.4).

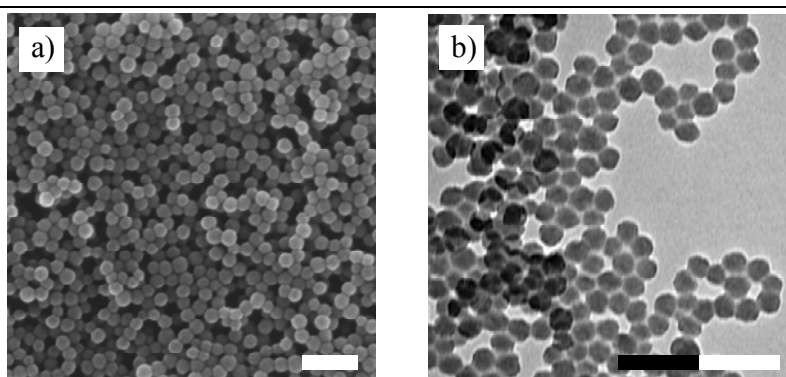


Figure 3.4 Images of PS nanospheres of O₂ quenched (R5) obtained by a) SEM and b) TEM. The scale bar is 200 nm.

As can be seen in the SEM and TEM images in Figure 3.4 the particles do not cluster as seen for SDS based particles from (R3). The nanoparticles are not entirely spherical in shape which can lead to an overestimation of the diameter measured by DLS. A more reliable size measurement was carried out by TEM resulting in an average diameter of 35 nm for the dry particle with a relative standard deviation of 9.9 %.

However, by using reaction quenching rather than full conversion at already low styrene concentrations, (R5) did result in very low solid content and therefore weight

percentage. The latex also requires very thorough dialysis to clean the dispersion from remaining monomer, which is very challenging with simple dialysis tubes. Another concern is the particle stability because the reaction was quenched in a non-equilibrium state compared to full conversion reactions which can lead to particle coagulation. Furthermore, a size determination at the point of change in appearance only by eye is not precise enough to obtain good reproducibility for such small particles. To synthesise small nanoparticles of a particular size using the quenching approach it would be desirable to predict the particle size at each state of the synthesis for more accurate reaction quenching. Tauer *et al.* used *in-situ* measurements including specific conductivity as well as transparency in combination with the corresponding calibrated sphere size to track the particle size development during emulsion polymerisation which could help to find a more systematic approach.^[197]

One of the main problems with round-bottom flask based synthesis is the consistency of temperature and inhomogeneous stirring. As the reaction temperature is measured in the oil bath and heat is applied from the hotplate, the temperature in the round-bottom flask can fluctuate easily by a few degrees. Furthermore, a temperature gradient of up to 10 °C below the required 70 °C was measured inside the flask with the coldest point in the centre of the reaction vessel. Such a gradient can cause differences in reaction kinetics and initiator activation which can cause batch-to-batch variations in sphere size and polydispersity. This temperature gradient is partly caused by the indirect heat monitoring but also insufficient stirring capability which results in limited reproducibility and consequently led to reactor based PS emulsion polymerisation.

3.3.2 Reactor based nanosphere synthesis

Surfactant-free emulsion polymerisation in a reactor equipped with a temperature controlled water jacket and an overhead stirrer allows better control and homogeneity of the reaction temperature and stirring.

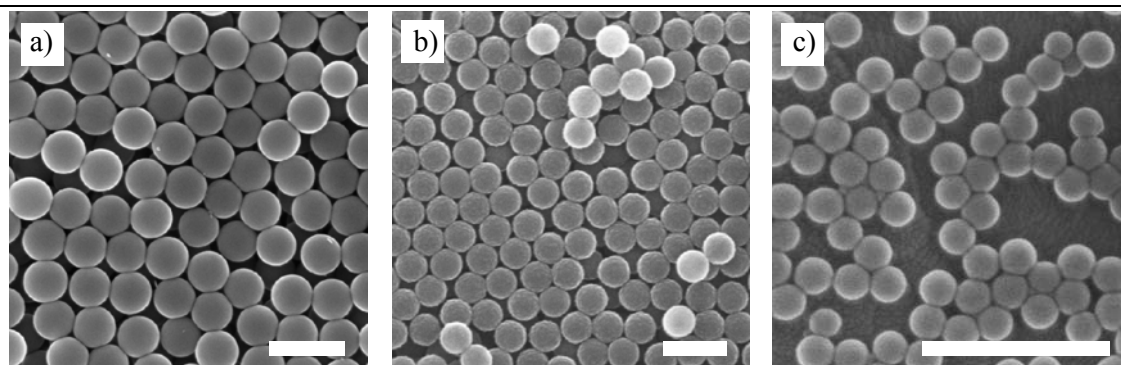


Figure 3.5 SEM images of PS nanospheres of a) 298 nm (R6), b) 253 nm (R7) and c) 115 nm (R8), in diameter using AMPAD in (R6) and (R7) or KPS in (R8) as the initiator. The reduction in concentration of styrene from 0.53 mol L^{-1} (10.0 g) to 0.11 mol L^{-1} (2.0 g) and an increase of the concentration of the initiator from (R6) to (R7) showed only a slight decrease in diameter. In (R8) the same compound quantities as in (R1) are used with a lower styrene concentration resulting in a comparable particle diameter and PDI. The scale bar is 500 nm.

Figure 3.5 shows SEM images of PS nanospheres of reactor based surfactant-free emulsion polymerisations (R6) to (R8) using AMPAD in (R6) and (R7) and KPS in (R8). (R6) and (R7) resulted in particle diameters of 298 nm and 253 nm and a PDI of 0.013 and 0.045 respectively. With the aim to synthesise smaller particles the concentration of styrene in the reaction was reduced from 0.53 mol L^{-1} (10.0 g, 0.10 mol) to 0.11 mol L^{-1} (2.0 g, 0.02 mol) and the initiator concentration was increased from $2.0 \times 10^{-3} \text{ mol L}^{-1}$ (0.10 g, $0.4 \times 10^{-3} \text{ mol}$) to $6.1 \times 10^{-3} \text{ mol L}^{-1}$ (0.30 g, $1.1 \times 10^{-3} \text{ mol}$) from (R6) to (R7). The change of parameters led to a decrease in diameter by 45 nm which follows the expected trend of styrene and initiator concentration changes. When compared to the round-bottom flask reaction (R4) with similar conditions (R7) shows drastically increased particle size from 82 nm to 253 nm instead of the expected slight reduction. This also gives an indication of how different the two reactor systems are which makes cross-comparison between round-bottom flask and reactor very difficult.

Reaction (R8) uses the same quantities as (R1) in the reactor with a lower styrene concentration resulting in a latex of very monodisperse particles with a diameter of 115 nm and a PDI of 0.014. This is the same particle diameter as achieved in (R1) but with a slightly lower polydispersity. Due to a favourable particle size and PDI the latex of (R8) is very suitable for further use in colloidal crystal growth. The data of (R6) to (R8)

including type of initiator, average particle diameter, PDI and weight percentage are summarised in Table 3.5.

Table 3.5 Summary of the experimental data of synthesis (R6) and (R7) using AMPAD and (R8) using KPS. The reactions were carried out in a reactor. Sizes and polydispersity were all measured by DLS after dialysis.

React.	Initiator [10^{-3} mol L $^{-1}$]	Z-average diameter [nm]	PDI	Weight percentage [%]
(R6)	2.0 (AMPAD)	298	0.013	3.9
(R7)	6.1 (AMPAD)	253	0.045	0.6
(R8)	1.0 (KPS)	115	0.014	2.2

Table 3.6 shows the different nanosphere characteristics of latexes (R1), (R5) and (R8) determined by DLS and EM which were selected for further use in nanosphere templating in Chapter 5. The main difference between the two measurement techniques is the slight change in sphere diameter. The average diameter of the dry particles determined by EM is always smaller than the Z-average diameter from DLS due to the additional electrical double layer. With smaller nanospheres the particle stabilising charge density on the particle surfaces increases leading to a thicker double layer and a larger diameter difference.

Table 3.6 Summary of the different nanosphere characteristics from (R1), (R5) and (R8) comparing the size measurements obtained by DLS and EM.

Reaction	Average diam. (dry) [nm]	Standard deviation (dry) [nm]	Relative standard deviation (dry) [%]	Z-average diameter (DLS) [nm]	PDI
(R1)	78	4.6	5.9	100	0.010
(R5)	35	3.5	9.9	61	0.086
(R8)	96	5.0	5.2	115	0.014

For surfactant-free emulsion polymerisation the co-monomer NaSS is an important additive to achieve PS particle diameters of far less than 200 nm with anionic initiators. In reactor experiments (R9) to (R19) based on KPS, all parameters of the reaction were kept constant with only NaSS being varied from 0 to 2 weight percent of the monomer or 0 to $10.8 \times 10^{-3} \text{ mol L}^{-1}$ (0 g - 0.40 g, 0 mol - $1.9 \times 10^{-3} \text{ mol}$) in concentration to screen particle diameter development and PDI against increased NaSS concentration. With the set of experiments a reliable reaction system should be developed which allows the prediction of the particle size with known parameters. Moreover, it helps to determine the upper and lower particle size and polydispersity limits of the system. Figure 3.6 shows the data trend obtained from (R9) to (R19) of particle diameter and PDI against varying NaSS concentration. The complete summary of the experimental data of synthesis (R9) to (R19) can be found in Table 3.7.

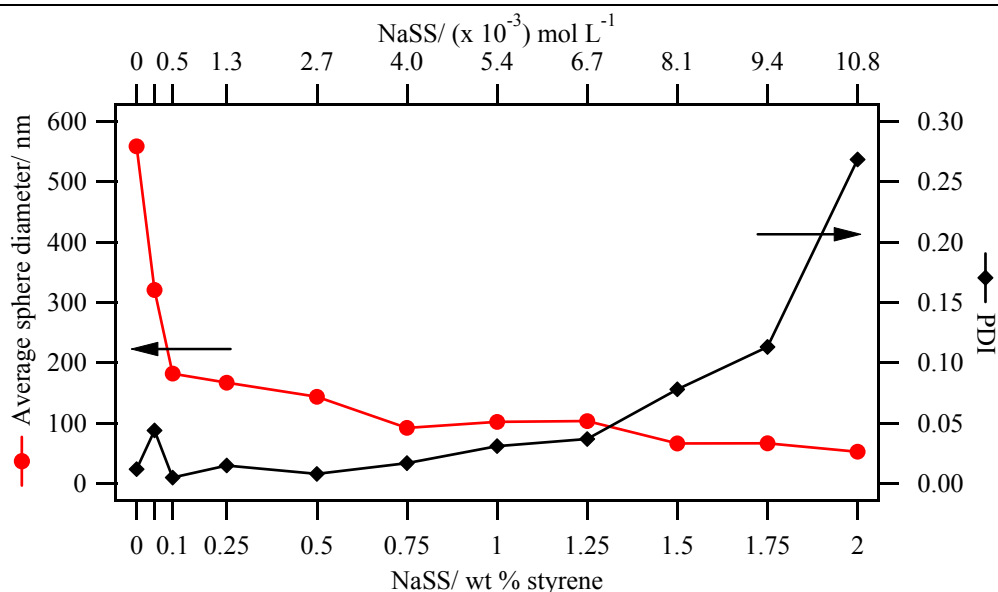


Figure 3.6 Plot of the average sphere diameter and the corresponding PDI against the amount of NaSS as a percentage of the styrene monomer weight.

Table 3.7 Summary of the experimental data of synthesis (R9) to (R19) using KPS with varying NaSS amounts as a percentage of the monomer amount. All reactions were carried out in a reactor. Sizes and polydispersity were all measured by DLS after dialysis.

React.	NaSS [10 ⁻³ mol L ⁻¹]	NaSS [wt % styrene]	Z-average diameter [nm]	PDI
(R9)	0.0 (0.00 g)	0.00	558	0.012
(R10)	0.3 (0.01 g)	0.05	320	0.044
(R11)	0.5 (0.02 g)	0.10	182	0.005
(R12)	1.3 (0.05 g)	0.25	167	0.015
(R13)	2.7 (0.10 g)	0.50	144	0.008
(R14)	4.0 (0.15 g)	0.75	92	0.017
(R15)	5.4 (0.20 g)	1.00	102	0.031
(R16)	6.7 (0.25 g)	1.25	104	0.037
(R17)	8.1 (0.30 g)	1.50	66	0.078
(R18)	9.4 (0.35 g)	1.75	67	0.113
(R19)	10.8 (0.40 g)	2.00	53	0.268

There are two clear opposite trends with increased NaSS concentration. The particle diameter first drops sharply from 558 nm in (R9) with no NaSS to 320 nm in (R10) and 182 nm in (R11) with 0.1 % NaSS. A further increase in NaSS concentration to 2.0 % in (R19) shows a steady decline in diameter to as small as 53 nm. Despite the high PDI, such low particle sizes are close to the reported diameter of 41 nm obtained by constant monomer feed.^[194] (R14) to (R16) with NaSS concentrations of 0.75 % to 1.25% show very little variation in size with all particle diameters remaining steady at around 100 nm but increased polydispersity with higher NaSS concentration. The PDI development with increasing NaSS concentration shows the opposite trend to the size development. Latexes from low NaSS concentrations of ~1.25 % (R16) have a PDI much lower than 0.05 which makes them monodisperse. From (R17) to (R19) the system

becomes very polydisperse with PDIs of up to 0.268. Both trends fit well with the expected behaviour and show clearly the limits of the system which fit to findings in the literature.^[198, 199] The experiments showed that the monodispersity of the latex up to NaSS concentrations of 1.25 % in (R16) is preserved. Other sources claim a NaSS concentration of $10 \times 10^{-3} \text{ mol L}^{-1}$ to be the limit for a PDI of <0.1 which is almost double the concentration of $6.7 \times 10^{-3} \text{ mol L}^{-1}$ (R16) found in the reactor experiments.^[186, 198] With increasing NaSS concentration the charge number on a polymer chain and therefore the water-solubility are increased. Consequently fewer chains are needed to stabilise a colloid in water. More particles can be formed and hence the sphere size is reduced.^[198] On the other hand polydispersity increases due to a higher ionic strength of the solution which leads to particle coagulation and therefore broadens the size distribution.

The method shows that surfactant-free emulsion polymerisation of PS in (R9) to (R16) with NaSS concentrations from 0 % to 1.25 % produce monodisperse latexes covering the particle diameter range of 558 nm to 92 nm which are suitable for further use in colloidal crystal growth. Latexes of smaller particle diameters show an increased polydispersity and are limited in use for high quality colloidal crystal growth but might well be suitable as an alternative porosity template.

3.4 Conclusion

Surfactant-free emulsion polymerisation is particularly challenging for the synthesis of monodisperse nanospheres with diameters of $<200 \text{ nm}$ due to the lack of the stabilising effect of surfactants. However, particles with diameters approaching the range of L_D without surfactants are needed for templating approaches suitable for OPV devices.

The PS nanosphere synthesis was based on radical initiated surfactant-free emulsion polymerisation. Synthesis was carried out in a round-bottom flask in the first experiments. The synthesis was then extended to a reactor which provides more control and consistency over reaction parameters such as stirring and temperature. It also allows larger batch volumes and higher percentages in solid content.

Reactions in the round-bottom flask with varying concentrations of styrene and both types of initiator, anionic KPS and cationic AMPAD, led to monodisperse latexes of ca. 80 nm to 120 nm in sphere diameter. An increase in initiator concentration of KPS did not lead to the expected decrease in particle size remaining close to 100 nm in diameter. The SDS surfactant based reference reaction showed a significant reduction in particle diameter to as low as 44 nm but suffered from high polydispersity and resulted in non-spherical particle clusters with no use for templating purposes. The O₂ quenched reaction showed a promising reduction in particle diameter from 82 nm at full conversion to 61 nm. Although the latex was almost monodisperse, the main disadvantages of this approach are latex purification, stability and very low solid content. Despite no differences in reaction mechanism between cationic and anionic initiators, there is no co-monomer such as NaSS for cationic AMPAD commercially available to improve the particle stability at reduced diameter which makes it less interesting as a reaction system for very small particles.

Reactor based reactions under similar conditions as used for the round-bottom flask led to much larger particles of 253 nm to 298 nm for AMPAD and similar particle diameters of around 100 nm but very monodisperse particles with KPS. This highlights how different the two reactor systems are which makes cross-comparison between round-bottom flask and reactor very difficult.

In a series of reactions varying only the NaSS co-monomer concentration two opposite trends were observed. With increasing NaSS concentration the particle diameter decreased and the PDI showed an increase following the expected trend behaviour which is also reported in the literature. Latexes with particle diameters from 550 nm down to about 90 nm were all monodisperse and suitable for colloidal crystal growth. The limit in NaSS weight percentage of the monomer for small and monodisperse nanospheres was found to be ≤ 1.25 %. Particles with diameters as small as 53 nm were achieved but show a much broader size distribution and are not suitable for high-quality colloidal crystal growth. Nevertheless, it could serve as a template for porous structures with pore diameters $\ll 100$ nm. The regulation of the NaSS concentration parameter in reactor based reactions proves to be the most promising method to achieve good control over nanosphere size and polydispersity producing latex suitable for templating purposes.

Chapter 4: Planar heterojunction devices

In this chapter planar heterojunction OPV devices employing aqueous solution processable small molecule TSCuPc and polymeric PTEBS in combination with C₆₀ have been fabricated and optimised. Only very few studies with these materials have been reported and more comprehensive studies are required to understand such water-soluble donor materials.

Thin films were studied in detail using UV/vis absorption spectroscopy, XRD and AFM. Combined with *J-V* analysis a deeper understanding of the relation between material characteristics, thin film morphology and the impact on OPV device behaviour is presented. Planar heterojunction devices of TSCuPc and PTEBS serve as model systems to understand and interpret the 3D interpenetrating nanostructured D-A composite thin films and devices in Chapter 5, where both donors are employed.

4.1 Introduction

4.1.1 Solution processed TSCuPc

The most common thin film deposition process for molecular semiconductors is HV OMBD, a thermal vapour-deposition technique, which enables highly reproducible thin film growth and complete device fabrication.^[48] The use of solution processed molecular semiconductors for OPV devices has received considerably less attention, despite the potential for cheaper device manufacture.^[200] In contrast to most solution processed molecular semiconductors, TSCuPc can be deposited from aqueous solution, which simplifies the device fabrication process and makes it potentially more economically as well as ecologically viable. The molecular structure of TSCuPc is shown in Figure 1.7c in Chapter 1. TSCuPc has also demonstrated potential for more general applications in organic electronics, with new thin film structures for electrode modification as well as templated porous and composite structures.^[201-203] In addition, water-soluble Pcs are non-toxic and find applications as photo-sensitisers in anti-cancer

drugs.^[204] Thin film fabrication of water-soluble Pcs has been demonstrated using a number of different techniques including spin-coating and Langmuir-Blodgett methods in order to obtain precise control over molecular stacking and film thickness.^[205, 206]

Hatton *et al.* successfully demonstrated an improvement in the performance of bulk heterojunction OPV devices through electrode modification by incorporating an interlayer of nanostructured TSCuPc-sensitised multiwall carbon nanotubes (MWCNTs) between the ITO substrate and the photoactive polymer:fullerene (P3HT:PCBM) blend.^[94, 201, 207] In this device the TSCuPc/MWCNT composite interlayer acts as a hole-extraction layer due to improved interfacial energy level alignment with the HOMO of P3HT. More recently, Bente *et al.* reported the fabrication of TSCuPc films from layer-by-layer deposition with a modified OPV device architecture, demonstrating a *PCE* of 0.01 %.^[208] Due to its relatively rare property of water-solubility TSCuPc has also found application in nanosphere templating as one of the few solvent compatible infiltration materials to generate porous large area organic semiconductor thin films with 400 nm down to sub-100 nm open-cellular 3D networks.^[202, 209] Complete D/A 3D composite structures have subsequently been fabricated by back-filling of porous thin films with an appropriate electron acceptor material.^[203, 210]

4.1.2 Solution processed PTEBS

Most polythiophenes are solution processed from environmentally damaging organic solvents such as chlorobenzene and toluene. The solubility of polymers such as polythiophenes, arises from the functionalisation through appropriate side chains. Usually, the films are cast from a blend of the polymer, P3HT being the most common, and the electron acceptor material, typically PCBM, forming efficient BHJ devices. One of the few exceptions is the water-soluble polythiophene PTEBS, which is functionalised with a methoxyalkyl sulfonate group for greatly enhanced water solubility.^[107] The molecular structure is shown in Figure 1.7f in Chapter 1. By using water as a solvent the device fabrication process is much more environmentally friendly and cost effective. Despite its obvious advantages very few studies have reported the use of this type of polythiophene.

Conjugated polymers functionalised with ionic side groups, also known as conjugated polyelectrolytes (CPE), have been employed as donor materials in conjunction with a water-soluble C_{60} derivative in controlled layer-by-layer deposited OPV devices, and show *PCEs* of up to 0.04 %.^[211]

The first devices employing the CPE based polythiophene PTEBS were polymer/ TiO_x hybrid devices with *PCEs* of up to about 0.1 % but very low photocurrents.^[212, 213] Miller *et al.* fabricated bilayer OPV devices from PTEBS and PTEBS/MWCNT composites with C_{60} as the electron acceptor. The use of PTEBS/MWCNT composite donor layers improved the *FF* and the *PCE* from 0.46 % to 0.55 % due to more favourable energy alignment and enhanced hole extraction.^[207, 214] Independently, Yang *et al.* reported *PCEs* of about 0.4 % for PTEBS/ C_{60} devices based on thick PTEBS layers of around 60 nm. Here the reported J_{SC} was below 1 mA cm⁻². Similar to TSCuPc, PTEBS is a potential electron donor material suitable for template infiltration from water to form open-cellular polymeric semiconductor thin films as well as whole D-A composite structures and OPV devices in a second fabrication stage.^[209]

4.1.3 Aim

For water-soluble TSCuPc and PTEBS, the dependence of solution concentration, film thickness, crystallinity and solar device performance were investigated to characterise and optimise the devices which are then used as model cells for D-A 3D-nanostructured composite devices in Chapter 5. The TSCuPc and PTEBS thin films are characterised by UV/vis absorption spectroscopy and AFM to develop a deeper understanding of the molecular arrangement and its impact on subsequent OPV device behaviour. Additionally, the films were taken through the fabrication steps used for nanosphere templating in order to understand the impact on OPV devices, including heat and solvent treatment (see also Chapter 5).

4.2 Experimental

OPV devices were fabricated on pre-cleaned ITO-coated glass substrates, which were treated in UV/ozone to remove contaminants and improve the wettability of the ITO prior to film deposition. TSCuPc was used as purchased without further purification. The solutions were prepared using deionised water (pH 7) and basic solutions (0.1 M NH_3 , pH 11) with the TSCuPc concentrations ranging from 5 mg mL^{-1} to 20 mg mL^{-1} . The solutions were stirred for 24 hours at 50 °C and then filtered (0.2 μm) before spin-coating at 2000 rpm for 1 minute in air under ambient conditions. PTEBS (MW = 100-1000 k) solutions with dye concentrations from 1 mg mL^{-1} to 15 mg mL^{-1} were prepared with ammonia solution (pH 11) to improve the polythiophene solubility in water. The solutions were stirred for 24 hours at 50 °C and then centrifuged at 10000 rpm to remove larger, undissolved particles before spin-coating at 1500 rpm for 2 minutes. The films were then dried for 30 minutes in air at room temperature, followed by 15 minutes at 100 °C under an inert atmosphere to remove any remaining water or ammonia.

The general bottom-up thin film device structure used on top of the ITO was PTEBS or TSCuPc as the electron donor material followed by C_{60} and BCP sandwiched by an Al top electrode. C_{60} , BCP and Al were deposited by OMBD. C_{60} and BCP films were grown with film thicknesses of 40 nm and 7 nm respectively, if not stated otherwise. In the reference device CuPc was vacuum deposited with a film thickness of 30 nm. Al electrodes with a film thickness of approximately 100 nm were deposited *in-situ* through a shadow mask defining the active area to 0.16 cm^2 . J - V measurements under light and dark conditions and EQE as well as thin film analysis involving UV/vis and AFM were carried out as described in detail in Chapter 2. Operational stability measurements for extended testing times of one hour of constant light exposure were carried out at 100 mW cm^{-2} for devices based on both TSCuPc and PTEBS.

TSCuPc and PTEBS films were also taken through the fabrication steps used for nanosphere templating in Chapter 5. The treatment of the planar thin films involves heat and moisture exposure for three days at 60 °C in an incubator followed by solvent treatment (THF) including either immersion or vapour exposure for 10 minutes and 20 minutes respectively.

4.3 Results

4.3.1 TSCuPc thin film based OPV devices

4.3.1.1 UV/vis absorption

Figure 4.1 shows normalised UV/vis absorption spectra of TSCuPc in neutral and basic solution as well as a thin film. Both solution spectra reveal an absorption band ranging from about 550 nm to 700 nm with a dominant maximum at 630 nm and a shoulder at 662 nm. The absorption spectrum for the spin-coated thin film is broader, and shows a blue-shifted maximum at 613 nm with an extended and less pronounced shoulder. Thin films from both solutions showed the same absorption spectra. This suggests that the peak at lower wavelengths corresponds to molecular aggregates, co-facially stacked dimers and oligomers, and the shoulder at higher wavelengths to monomers.^[201, 208] The extended tail for TSCuPc films >700 nm is probably attributed to light scattering due to the rough surface which is reflected in the high background intensity. The inset in Figure 4.1 shows a CuPc thin film and solution spectrum for comparison, with a distinct difference in the monomer to aggregate ratio.

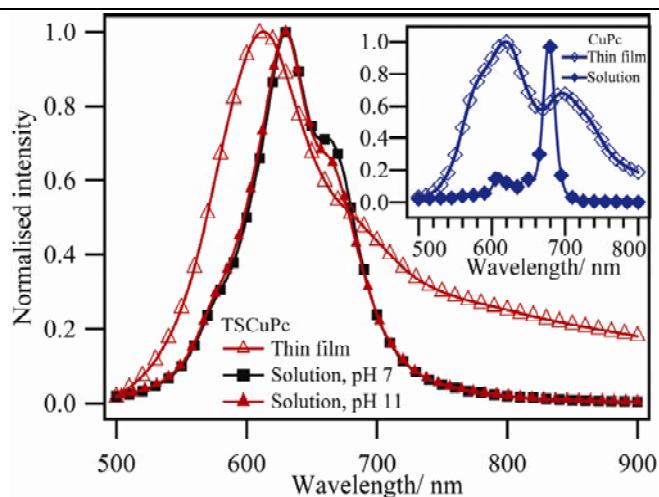


Figure 4.1 UV/vis absorption spectra of TSCuPc in pH neutral and basic solutions as well as the spin-coated thin film (pH 11). Inset: The solution and thin film spectra of CuPc as a comparison to highlight the different solution phase characteristics.

The CuPc spectra have a pronounced monomer peak in solution and a mixed distribution in the thin film dominated by aggregates similar in shape to TSCuPc.^[215] For TSCuPc the resemblance between the thin film and solution spectra in both shape and peak ratio is rather unexpected and the absence at higher wavelengths of a clear monomer peak in solution is very different to that seen for CuPc. The low proportion of monomer in solution and the pronounced absorption peak for aggregates indicate that TSCuPc does not entirely dissolve and forms a suspension containing partially dissolved TSCuPc nano-crystals and clusters.^[205, 206] This finding is further supported by the AFM data presented in the next sections. Further heat treatment, longer dissolution times and sonication did not change the TSCuPc solution spectrum.

4.3.1.2 Thin film morphology

AFM morphology studies of TSCuPc thin films spun from pH neutral and basic solution with dye concentrations of 10 mg mL⁻¹ and 20 mg mL⁻¹ are shown in Figure 4.2. The images reveal a mesh of long crystal-like features with no preferred orientation with complete coverage of the ITO substrate. With increasing TSCuPc concentration the crystal shape becomes more pronounced and the crystal feature length increases due to coalescence of several smaller crystal segments to one crystal unit indicating crystal ripening upon deposition. For both 10 mg mL⁻¹ solutions, at pH 7 and pH 11, the morphology is very similar with crystal features up to 500 nm long and about 50 nm wide forming a dense network (Figure 4.2a and 4.2b). The surface roughness parameter R_q of 2.4 - 2.5 nm indicates that the films are both smoother and very different in appearance than bare ITO, which has an R_q of 4.4 nm. The height cross-sections confirm the round and smooth crystal shapes embedded in the films. For films made from 20 mg mL⁻¹ TSCuPc, larger crystals of up to 1 μ m in length and 100 nm in width are observed with a difference in roughness and crystal appearance for the two different solutions used, pH 7 and pH 11 (Figure 4.2c and 4.2d). Processed from basic solution, R_q remains at 2.5 nm, but increases for pH 7 to 3.4 nm with even larger and better defined crystals based on a slightly lower solubility. Despite the presence of such pronounced crystals R_q is still low which can be explained by the deposition and infiltration of vacancies with well dissolved material. The large crystals found on the TSCuPc film surface are assumed to

be formed during the spin-coating and/or drying process from much smaller assembled crystals (<200 nm) which are present in solution after the filtration step.

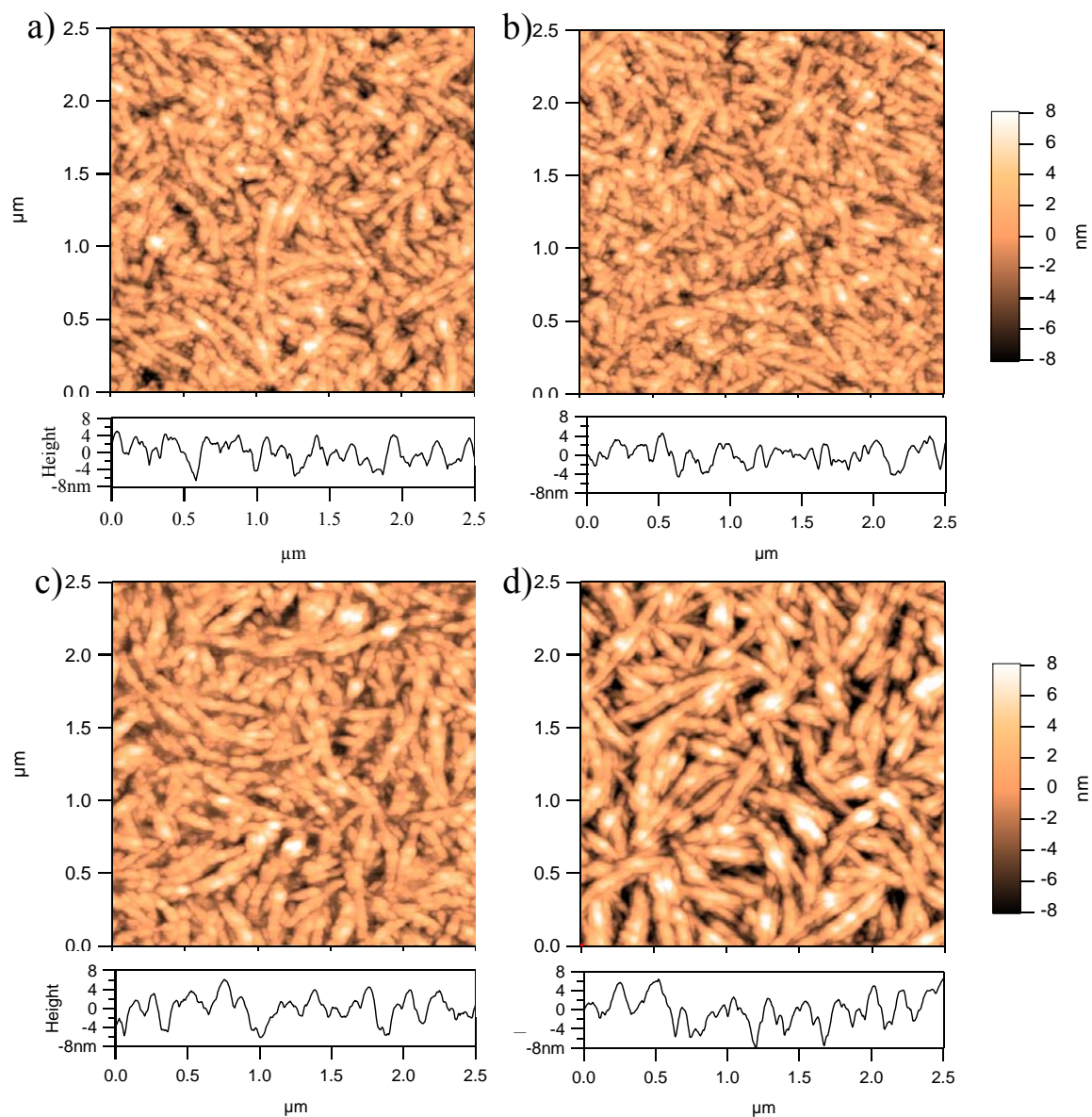


Figure 4.2 AFM images of spin-coated TSCuPc thin films on ITO, processed from water with concentrations of 10 mg mL^{-1} a) pH 11 (NH_3), b) pH 7 and 20 mg mL^{-1} c) pH 11 (NH_3), d) pH 7 with the corresponding height profiles shown below each image to highlight changes in crystal size and morphology.

4.3.1.3 *J-V* device characteristics

TSCuPc single layers were incorporated in complete OPV devices with a planar TSCuPc (d nm)/ C_{60} heterojunction structure, as shown schematically in Figure 4.3b. The devices fabricated varied in TSCuPc film thickness d and solvent pH: device (A) (8 nm, 5 mg mL⁻¹), (B1) (13 nm, 10 mg mL⁻¹), (C) (18 nm, 15 mg mL⁻¹) and (D) (30 nm, 20 mg mL⁻¹) from basic solution and device (E) (13 nm, 10 mg mL⁻¹) and (F) (30 nm, 20 mg mL⁻¹) from pH neutral solution. As the spin speed was set to 2000 rpm for all devices the film thickness was varied by changes in concentration. As a reference, device (N) was based on just ITO/ C_{60} (40 nm)/ BCP/ Al without a TSCuPc layer. Figure 4.3a shows the *J-V* curves of devices (A) to (D) and (N) under 1 sun illumination and the inset under dark conditions.

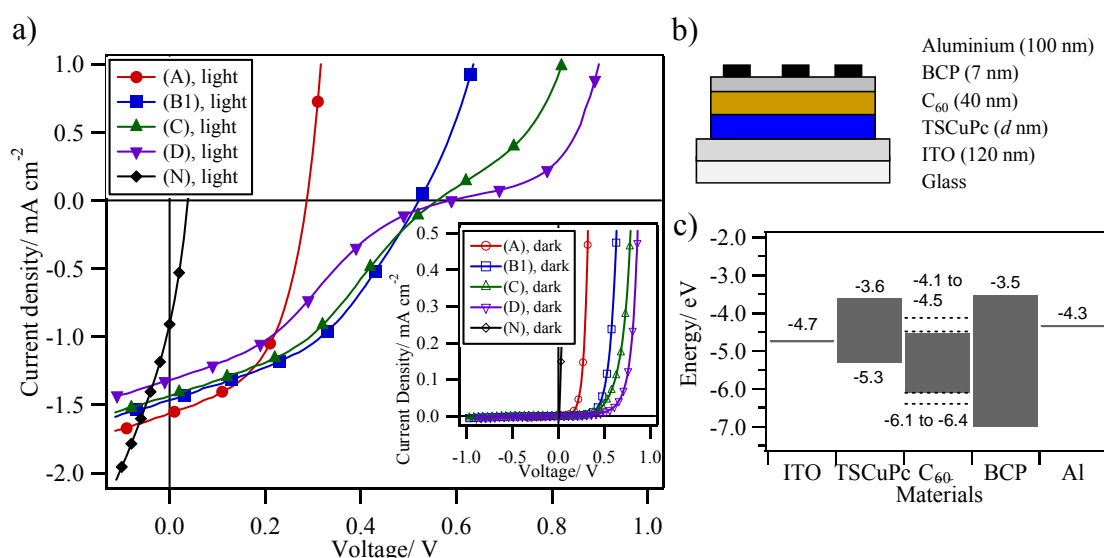


Figure 4.3 a) *J-V* curves under 1 sun illumination for devices (A) to (D) fabricated with varying TSCuPc concentration and film thickness and device (N) based on just C_{60} . The inset shows the *J-V* curves under dark conditions. b) Schematic OPV device architecture and c) electronic energy level diagram. The dotted lines in c) show the range of the values reported in the literature.

The V_{OC} increases significantly from the thinnest device (A) with 0.29 V to (B1) with 0.52 V and levels off towards (D) with 0.59 V, the thickest TSCuPc layer ($d = 30$ nm). The J_{SC} and the FF show the opposite trend. J_{SC} and FF start at 1.56 mA cm⁻² and 0.50 for device (A) and decrease steadily with increased TSCuPc film thickness to 1.32

mA cm^{-2} and 0.28 respectively for device (D). The *PCE* starts at 0.23 % for device (A), reaches a maximum of 0.32 % for device (B1), 0.30 % for device (C) and then decreases to 0.23 % for device (D). These trends are shown in Figure 4.4a and the complete set of values is summarized in Table 4.1. Devices processed at pH 7 show a similar trend but demonstrate a generally lower overall performance. Device (E) exhibited a V_{OC} of 0.44 V, a J_{SC} of 1.48 mA cm^{-2} , a *FF* of 0.42 and a *PCE* of 0.28 %. Device (F) produced a V_{OC} of 0.44 V, a J_{SC} of 1.19 mA cm^{-2} , a *FF* of 0.27 and a *PCE* of 0.14 %. The reference device (N) based on just C_{60} gave a V_{OC} of only 0.04 V, a J_{SC} of 0.91 mA cm^{-2} , a *FF* of 0.30 and a *PCE* of 0.01 %.

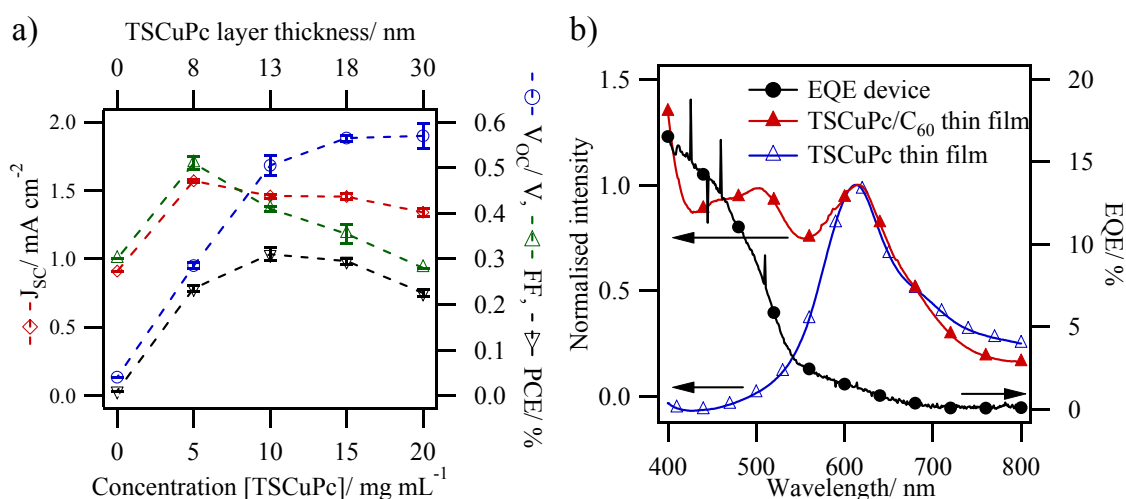


Figure 4.4 a) Summary of performance parameters for devices (A) to (D) and reference (N), including J_{SC} , V_{OC} , *FF* and *PCE*, with varying TSCuPc concentration (pH 11) and film thickness d . The reproducibility of the experiments is reflected in the error bars. b) Comparison of the *EQE* of device (B1) with the UV/vis absorption spectra of the appropriate TSCuPc/ C_{60} bilayer and just TSCuPc thin films.

Table 4.1 Summary of device characteristics for OPVs based on an ITO/ TSCuPc (d nm)/ C_{60} (40 nm)/ BCP (7 nm)/ Al structure with varying TSCuPc thickness d . Devices (A) to (D) were fabricated at pH 11; devices (E) and (F) were fabricated at pH 7. Reference devices (N) and (O) are based on an ITO/ C_{60} (40 nm)/ BCP (7 nm)/ Al structure without TSCuPc and an ITO/ CuPc (30 nm)/ C_{60} (40 nm)/ BCP (7 nm)/ Al respectively.

Device	TSCuPc Thickness [nm]	V_{OC} [V]	J_{SC} [mA cm ⁻²]	FF	PCE [%]
(A)	8 (pH 11)	0.29	1.56	0.50	0.23
(B1)	13	0.52	1.47	0.41	0.32
(C)	18	0.56	1.44	0.37	0.30
(D)	30	0.59	1.32	0.28	0.23
(E)	13 (pH 7)	0.44	1.48	0.42	0.28
(F)	30	0.44	1.19	0.27	0.14
(N)		0.04	0.91	0.30	0.01
(O)		0.48	3.57	0.55	1.00

The best V_{OC} obtained for the TSCuPc/ C_{60} devices is 0.11 V to 0.13 V higher than typically achieved for standard CuPc/ C_{60} devices with 0.46 V reported in the literature and 0.48 V achieved by the CuPc reference device (O).^[216] The gain in V_{OC} can be explained by the increased ionisation potential of the donor material caused by the presence of the electron withdrawing sulfonic acid groups. The HOMO of TSCuPc lies at -5.3 eV, which is 0.2 eV deeper than the HOMO of CuPc (-5.1 eV) (Figure 4.3c).^[94]

For very thin TSCuPc layers the substrate coverage is probably not uniform due to the crystalline network, and C_{60} can contact through to the ITO forming a by-pass which causes a loss in voltage due to the lack of an energetically suitable organic heterojunction. The extreme case of V_{OC} loss is demonstrated in device (N) based on just C_{60} without a D/A heterojunction interface. The J_{SC} decreases slightly with thicker TSCuPc layers from 1.56 mA cm⁻² for device (A) to 1.32 mA cm⁻² for device (B1). In general, the film thicknesses of the photoactive layers are a compromise between absorption and the limited L_D of organic semiconductors. For thicker films η_{ed} decreases

and R_S increases. Although an increase in J_{SC} with increasing thickness for such thin layers of only 8 nm is expected based on the higher absorbance, the slightly decreased J_{SC} values suggest that a trade-off in the photocurrent generation limit is already reached for device (A). The J_{SC} maximum at 8 nm TSCuPc thickness may correlate with a short estimated L_D for this material. Although L_D of vapour deposited CuPc is reported to be between 10 nm and 68 nm, it is almost certainly much lower for TSCuPc because of the increased interplanar spacing with the bulky substituent groups and different less homogenous film morphology. This is likely to have a detrimental influence on L_D as well as charge mobility as a result of the increased separation between the molecular stacks and leads to a lower J_{SC} .^[24, 26, 217] This is supported by the findings reported by Terao *et al.* where J_{SC} shows a linear correlation with the hole mobility and an estimated correlation with L_D of the metal phthalocyanines tested.^[218] It is clear that in thicker layers the additional absorbed light does not lead to a higher J_{SC} and more importantly, a thicker TSCuPc layer increases the charge collection pathway which is coupled to increased resistive current losses.

In contrast to CuPc, solution processed TSCuPc films are made of randomly oriented nanocrystals with a high density of grain boundaries, as seen in the UV/vis and AFM studies reported earlier, which can act as exciton quenching sites. Originating from the solution process from water in air the thin films also contain more impurities, residues and counter ions which act as additional exciton quenchers and trap sites, influencing both the bulk and interface properties. Possible residues in the donor film are traces of oxygen and trapped water.

Surprisingly, the *EQE* measurements of device (B1), shown in Figure 4.4b, reveal a clear dominance of C₆₀ as the main contributor to the photocurrent with an *EQE* of above 15 % and almost no contribution from TSCuPc, as can be seen by comparison to the absorption spectrum. This finding is further confirmed by the relatively high J_{SC} of 0.91 mA cm⁻² obtained for the device based only on C₆₀ (N), providing about two thirds of the photocurrent without any D/A interface present. This leads to the conclusion that the main role of the TSCuPc layer is to provide a D/A heterojunction, with the relatively large V_{OC} obtained reflecting the interface gap arising from the energy difference between the donor HOMO and acceptor LUMO. Furthermore, this interface enables successful

charge transfer for excitons originating from the C_{60} . This is also consistent with the observation that increased layer thicknesses do not result in any further enhancements in photocurrent.

The main losses for devices fabricated with thicker TSCuPc layers are reflected in the reduced FF value, which also reflects an increased R_s . This device behaviour can be seen in the well pronounced kink or so called S-shaped $J-V$ curves under illumination (Fig. 4.3a) as the film thickness increases from device (A) to (D) indicating a charge extraction barrier which leads to charge accumulation. Imbalanced charge mobilities are also discussed as a cause for such a device curve shape. The less mobile charges, holes in TSCuPc, form a space charge layer in the device which leads to enhanced recombination and therefore a lower J_{SC} and FF .^[79]

The devices fabricated at pH 7 (E and F) showed a generally poorer performance when compared to those processed from basic solution, with the lower J_{SC} and V_{OC} values leading to a reduced PCE . As the film thicknesses of these devices are comparable to the ones spun from the same TSCuPc concentration at pH 11, the change in OPV performance is probably related to the change in morphology from smaller crystals, found for basic solution processed films, to larger ones (20 mg mL^{-1}) based on the different dissolution behaviour and film formation. The larger grain size for these devices with the elongated crystals aligning parallel to the substrate surface results in a rougher film with partly incomplete substrate coverage leading to a disturbed D/A interface and therefore a reduced J_{SC} and V_{OC} .

The PCE of 0.32 % for the optimised device (B1) with 13 nm TSCuPc thickness and processed from basic solution is much higher than any reported values in the literature for OPV devices fabricated with this material.^[208] This improvement in performance is related to the processing of the TSCuPc films as well as optimisation of the heterojunction device architecture. However, the improvement of V_{OC} through molecular orbital energy tuning and improvement of solubility by substitution with functional groups is a trade-off due to compensation by a shorter L_D and limited charge carrier transport of the material.

4.3.2 PTEBS thin film based OPV devices

4.3.2.1 UV/vis absorption

The UV/vis absorption spectra of PTEBS in basic solution and as a thin film, as well as P3HT as a well studied polythiophene comparison are shown in Figure 4.5. In both spectra the main absorption occurs in the wavelength range 350 nm to 550 nm with a maximum at 446 nm in solution and at 434 nm for the thin film. The broad peak appearance is based on a π - π^* electronic transition with no distinct features.^[214] The absorption range for such a conjugated polymer is mainly defined by the size of the conjugated system, i.e. chain sequences with an uninterrupted π -system. The solution spectra maximum of PTEBS and P3HT (see inset Figure 4.5) are both around 450 nm and very similar in shape. However, the solid film absorption maximum of P3HT is red shifted by about 100 nm, where the solid film spectrum of PTEBS remains at a similar position to its solution spectrum. The thin film peak of P3HT also consists of three distinguishable features, with the first two peaks at lower wavelengths originating from π - π^* transitions and the shoulder towards longer wavelengths from inter-chain interactions.^[219] P3HT forms microcrystalline regions of π -stacked polymer chains in one direction and lamellae structures of these interlocked side chains in the other direction giving an increase in charge carrier mobility.^[220] Both effects are enhanced with highly regioregular P3HT. Despite the same polythiophene backbone in PTEBS, neither a red shift nor such distinct features appear for the thin film. This remarkable difference is due to the strong influence of the different side chain properties. PTEBS has a charged functional group in the side chain surrounded by counter-ions, which can lead to a lower degree of ordered packing of the polymer backbone chains and side chains due to bulkiness, repulsive charges and packing disruption through counter-ions. The missing absorption shoulder at longer wavelengths might be explained by a lack of polymer crystal domains indicating the existence of mainly isolated poorly interacting single polymer chains. Furthermore, the bulky side chains can lead to a twisted polymer backbone and therefore shorter conjugated sequences of different lengths.^[221]

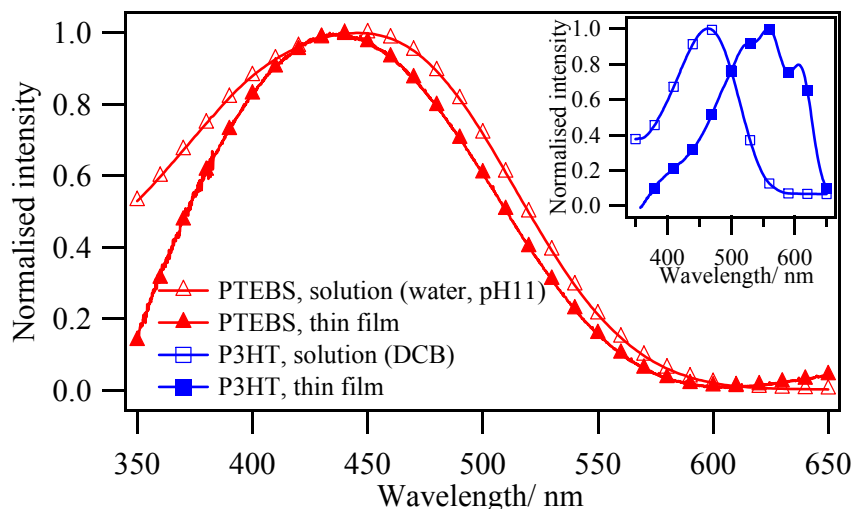


Figure 4.5 UV/vis absorption spectra of PTEBS in basic solution and as a spin-coated thin film. The inset shows the absorption spectra of P3HT in solution from dichlorobenzene (DCB) and a spin-coated thin film as a comparison.

4.3.2.2 Thin film morphology

Figure 4.6 shows AFM images of PTEBS thin films spun from different concentrations including the cross-sectional height profiles. The film morphology and roughness change drastically with increasing concentration from a rough surface and defined features for bare ITO to a much smoother film surface for a film spun from a 10 mg mL^{-1} solution. The R_q decreases from 4.4 nm for bare ITO to 3.9 nm for a film from 2.5 mg mL^{-1} , still showing the sharp features of the underlying ITO substrate, which hints towards incomplete surface coverage. For films prepared from 5 mg mL^{-1} and 10 mg mL^{-1} R_q steeply declines to 2.4-2.6 nm. The films show a smooth morphology with very little or no exposure of the underlying ITO features and uniform surface coverage.

During film formation the solution penetrates the featured substrate structure and fills vacancies before complete layers are formed. For high concentrations such as 10 mg mL^{-1} , material accumulation with thicker films appears as island formation in some areas of the surface, where other neighbouring areas seem to consist of thinner layers. This effect could be due to a washing and material transfer process during spin-coating. The film thickness for a 5 mg mL^{-1} film was found to be approximately 5 nm, 20 nm for 10 mg mL^{-1} and 28 nm for 15 mg mL^{-1} . Film thicknesses for thinner layers could not be

determined because of incomplete surface coverage and the limitation of the measurement.

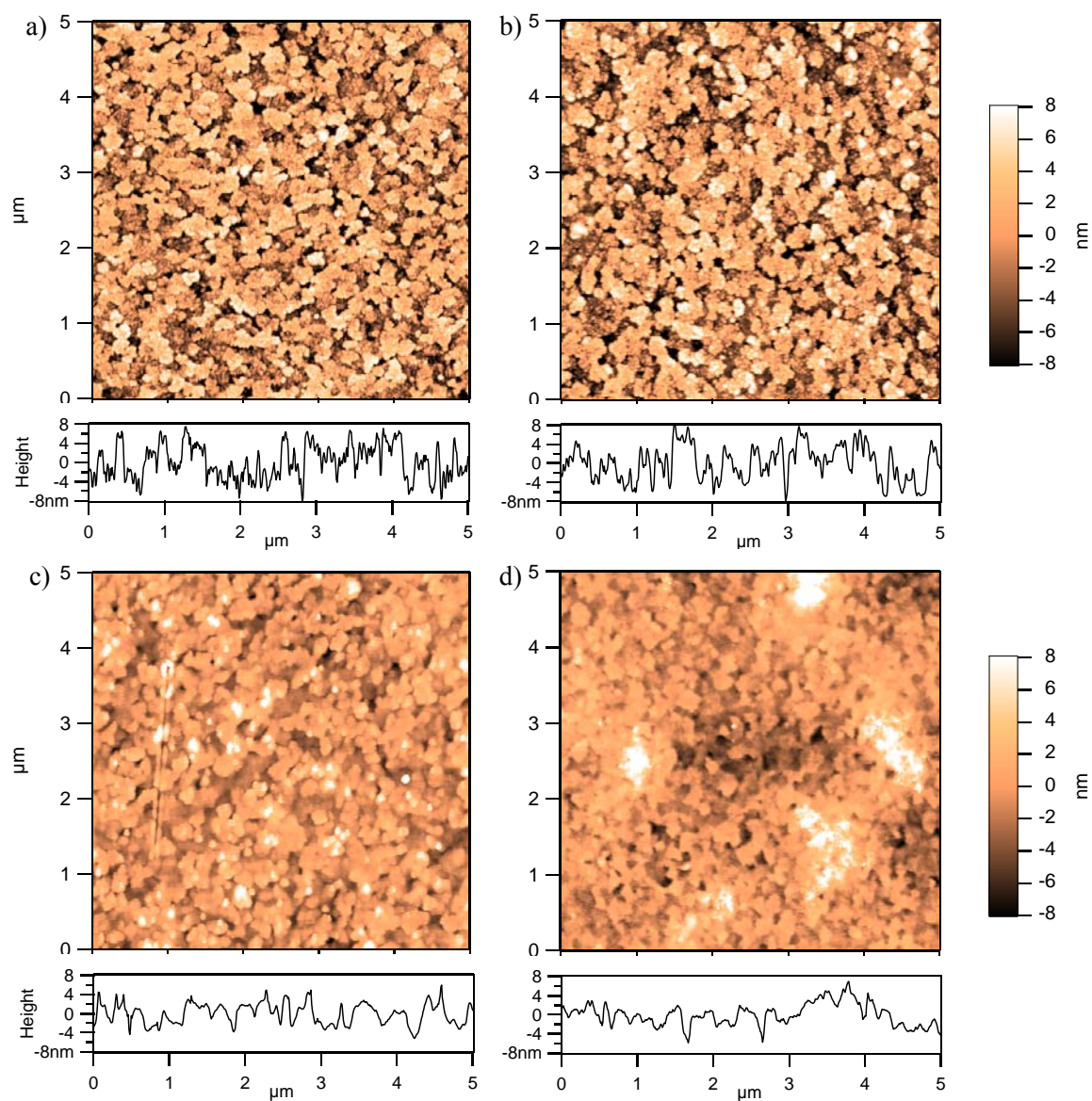


Figure 4.6 AFM images of spin coated PTEBS thin films on ITO substrates, processed from basic solution with different concentrations: a) bare ITO, b) 2.5 mg mL⁻¹, c) 5 mg mL⁻¹ and d) 10 mg mL⁻¹ with the corresponding height profiles shown below each image to highlight changes in surface roughness.

4.3.2.3 *J-V* device characteristics

Solution processed planar PTEBS donor layers of different concentrations c varying from 1 mg mL^{-1} to 15 mg mL^{-1} were used to fabricate complete OPV devices based on an ITO/ PTEBS ($c \text{ mg mL}^{-1}$)/ C_{60} (40 nm)/ BCP (7 nm)/ Al device structure (Figure 4.7b): device (G) (1 mg mL^{-1}), (H) (2.5 mg mL^{-1}), (I1) (5 nm , 5 mg mL^{-1}), (J) (7.5 mg mL^{-1}), (K) (20 nm , 10 mg mL^{-1}), (L) (12.5 mg mL^{-1}) and (M) (28 nm , 15 mg mL^{-1}). Figure 4.7a shows the *J-V* curves of devices (G) to (M) as well as the reference (N) under 1 sun illumination and under dark conditions (inset). The complete data set for all devices (G) to (M) can be found in Table 4.2.

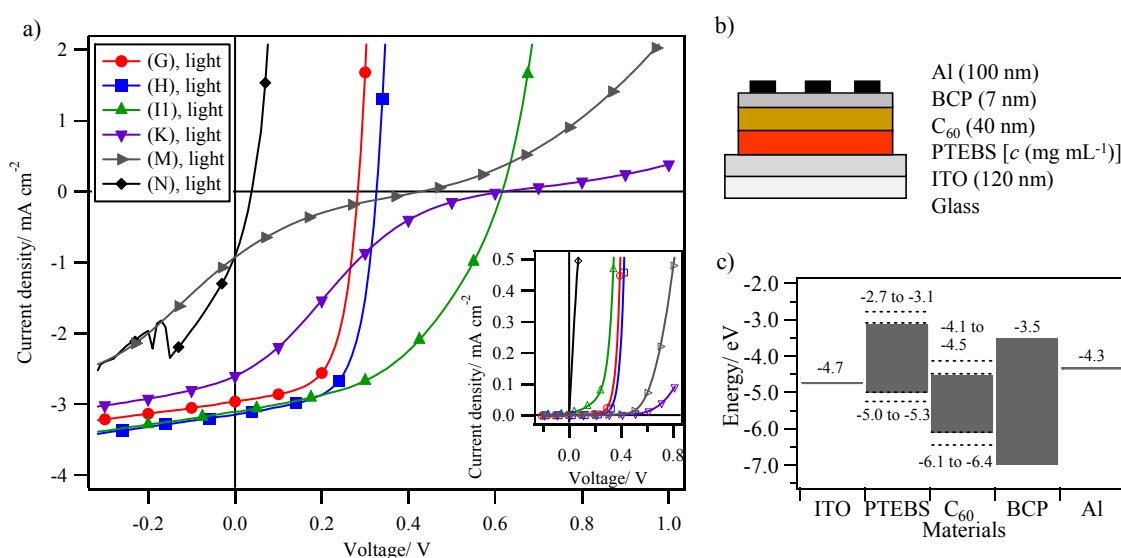


Figure 4.7 a) *J-V* curves under 1 sun illumination for devices (G) to (M) fabricated with varying PTEBS concentrations and reference device (N) based on just C_{60} . The inset shows the *J-V* curves under dark conditions. b) Schematic OPV device architecture and c) electronic energy level diagram. The dotted lines in c) show the range of the values reported in the literature.

Table 4.2 Summary of device characteristics for OPVs based on an ITO/ PTEBS (c mg mL⁻¹)/ C₆₀ (40 nm)/ BCP (7 nm)/ Al structure with varying PTEBS concentration c for devices (G) to (M). Reference device (N) is based on an ITO/ C₆₀ (40 nm)/ BCP (7 nm)/ Al structure without PTEBS.

Device	PTEBS [mg mL ⁻¹]	V_{OC} [V]	J_{SC} [mA cm ⁻²]	FF	PCE [%]
(G)	1	0.28	3.26	0.60	0.56
(H)	2.5	0.28	3.15	0.60	0.53
(I1)	5	0.52	3.12	0.50	0.81
(J)	7.5	0.56	3.11	0.35	0.57
(K)	10	0.58	2.54	0.19	0.28
(L)	12.5	0.57	1.80	0.14	0.14
(M)	15	0.41	0.84	0.16	0.06
(N)		0.04	0.91	0.30	0.01

For J_{SC} a trend was found showing a clear decrease with increasing PTEBS concentration. The trend starts with a shallow slope from 3.26 mA cm⁻² for device (G) to 3.11 mA cm⁻² for device (J) followed by a steep decrease for higher concentrations down to 0.84 mA cm⁻² for device (M). The V_{OC} follows the opposite trend starting low with 0.28 V for devices (G) and (H). Device (I1) shows a steep increase to 0.52 V with a slight improvement to 0.56 V for devices (J) and (K) and 0.57 V for device (L). Device (M) from the highest concentration marks a decline in V_{OC} to 0.41 V. Similar to J_{SC} , the FF starts at high values of 0.60 for devices (G) and (H). It then decreases to 0.50 for device (I1) followed by a steep decline to below 0.20 for devices (K) to (M). This results in an overall PCE trend from 0.56 % and 0.53 % for devices (G) and (H) to a performance maximum of 0.81 % for device (I1) with the highest PCE measured for this device being 0.90 %. This is almost double the efficiency of any other previously reported values.^[214, 221] For thicker devices the PCE decreases from 0.57 % for device (J) to 0.06 % for device (M). All trends are shown in Figure 4.8a.

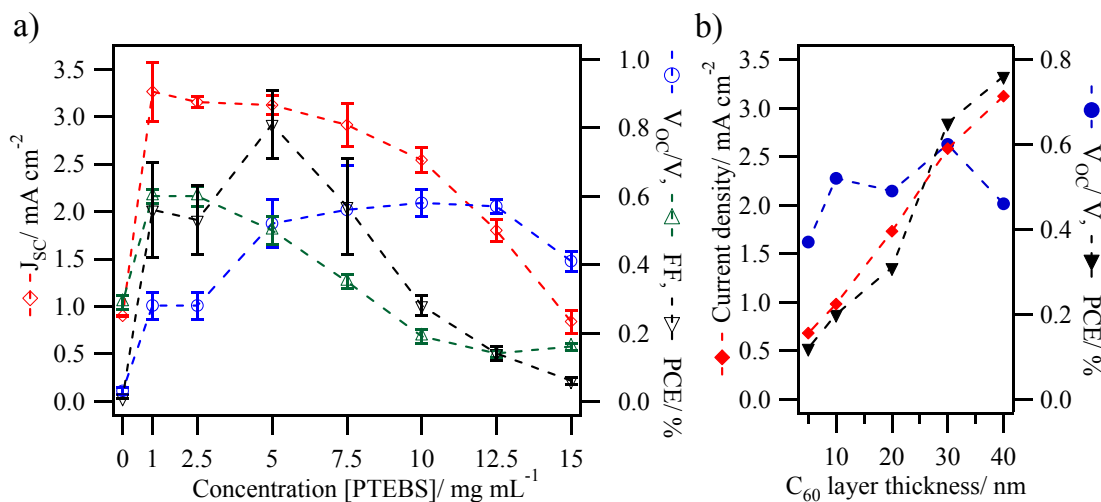


Figure 4.8 a) Summary of performance parameters for devices (G) to (N), including J_{SC} , V_{OC} , FF and PCE , with varying PTEBS concentration c . The reproducibility of the experiments is reflected in the error bars. b) Performance plot of device (I1) with varying C_{60} thickness from 5 nm to 40 nm showing the J_{SC} , V_{OC} and PCE values.

For low PTEBS concentrations of 1 mg mL⁻¹ in device (G) and 2.5 mg mL⁻¹ in device (H), the substrate coverage was found to be non-uniform and areas seemed to be very thinly or insufficiently covered, which was confirmed by AFM. However, the V_{OC} is reduced since parts of the cell are only based on a single layer of C_{60} which does not provide a defined D/A interface. The overall V_{OC} therefore originates from a combination of a C_{60} homojunction, as found in reference device (N) and a PTEBS/ C_{60} heterojunction. For thicker layers with complete surface coverage the V_{OC} saturates around 0.56 V, which is consistent with reported results of V_{OC} between 0.58 V and 0.65 V.^[214, 221] The V_{OC} found is reasonable based on the HOMO/LUMO energy values reported in the literature for PTEBS and C_{60} , as can be seen in the energy level diagram in Figure 4.7c.^[99, 212, 222] However, it is difficult to make a firm prediction of an exact value due to uncertainty in the energy level values measured by different groups.

Although an increase in J_{SC} with thicker donor layers up to a compromise thickness is expected, the trend found for PTEBS showed the highest J_{SC} for the thinnest PTEBS layers up to 5 nm with a clear decrease towards 28 nm. Therefore, a compromise between light absorption and L_D is found for devices (G) to (J). This behaviour leads to the hypothesis that L_D of solution processed PTEBS is in the range of less than 10 nm

which would be in good agreement with the exciton diffusion length of <10 nm reported for solution processable P3HT.

The main photocurrent contributor for this PTEBS/ C_{60} heterojunction device is C_{60} which was confirmed in an additional experiment varying the C_{60} thickness in a device (Figure 4.8b) as well as by *EQE* measurements (Figure 4.9). In this set of devices the layer thickness of C_{60} was varied from 5 nm to 40 nm on a 5 nm PTEBS layer as used in device (I1). J_{SC} increases linearly with thicker C_{60} layers without compromising either V_{OC} or FF , which is reflected in the close match of the trend by *PCE*. The same can be seen in the *EQE* spectra of devices (I1) and (K) (see Figure 4.9). Although the absorbance increases with a thicker PTEBS layer the *EQE* is reduced from around 22 % at 434 nm by about 5 % to an *EQE* of 17 % which shows that the additional PTEBS in the thicker layer has no overall beneficial contributing effect on the current. In both *EQE* spectra the C_{60} can be identified as the main photocurrent contributor from the comparison of the PTEBS and PTEBS/ C_{60} absorption spectra to the *EQE* spectra.

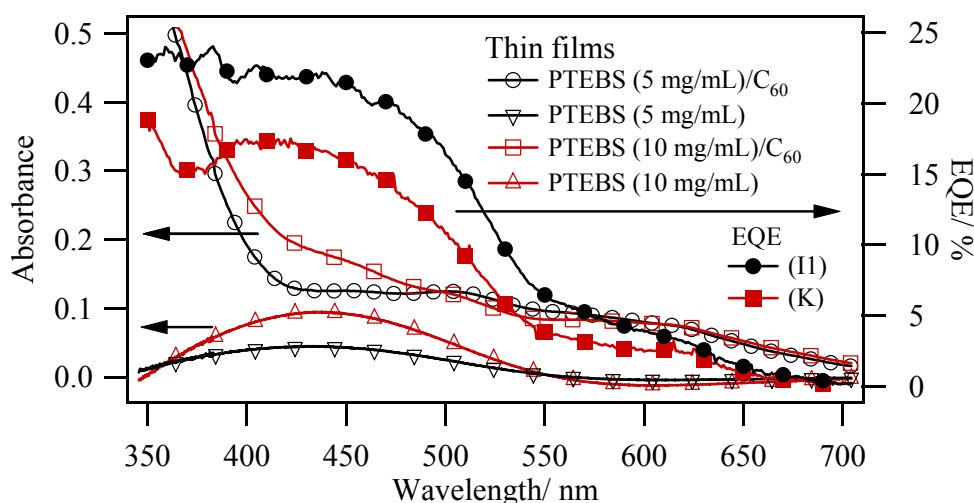


Figure 4.9 Comparison of the *EQE* spectra of devices (I1) and (K) with the UV/vis absorption spectra of the appropriate PTEBS/ C_{60} bilayer and PTEBS single layer thin films.

Nevertheless, the PTEBS proves to be vital in establishing an efficient heterojunction when compared to the C_{60} reference device (N). With thicker layers, R_s increases leading to a lower FF and significant performance loss. This behaviour of

increased R_s is clearly reflected in the S-shape of the J - V curve for large thicknesses in device (K) to (M) (Figure 4.7a). This increase in resistance could be due to the packing nature of this water-soluble polymer in which the side chains are equipped with a charged functional group, but also counter ions may remain in the film. Hole selective charge transport occurs mainly through the polythiophene backbone which is well known for P3HT. The transport along a chain could be reduced through a more twisted polymer backbone and therefore shorter conjugated sequences. Additionally, chain-to-chain charge transfer is hindered through the ionic functional groups of the side chains as well as their counter ions, which interrupt the vital chain interlink for higher order packing as known for P3HT.^[220] The same phenomenon affects L_D for this material. Similar to TSCuPc the S-shape of the J - V curves could also originate in imbalanced charge mobilities with less mobile holes in PTEBS forming a space charge in the device and causing the lower J_{SC} and FF .^[79]

4.3.3 Device stability

Operational stability measurements under continuous light exposure for 1 hour at 100 mW cm⁻² were carried out for a TSCuPc based device (B1) and a PTEBS based device (I1). The change in the key J - V parameters with time is shown in Figure 4.10.

Device (B1) shows an overall decrease in performance with a significant drop in V_{OC} of 24 % and a drop of PCE by 36 % within the first 10 minutes. The decreasing trend slows down towards 60 minutes with a total decrease in FF by 17 %, J_{SC} by 26 % and V_{OC} by as much as 43 % resulting in a reduction of the PCE by 65 %. Even more substantial degradation of the PTEBS based device (I1) is seen. The device shows an overall decrease in performance with a drop in FF by 13 %, in J_{SC} by 14 %, in V_{OC} by 38 %, and in PCE by a remarkable 54 % in the first 10 min of constant light exposure. Towards 60 min the degradation trend slows down with a total decrease in FF of 34 %, in J_{SC} by 43 % and in V_{OC} by as much as 79 % resulting in a dramatic reduction of PCE by 92 %. In both cases the drop in PCE is very large with V_{OC} being the main cause for the reduction, which hints towards unstable interfaces.

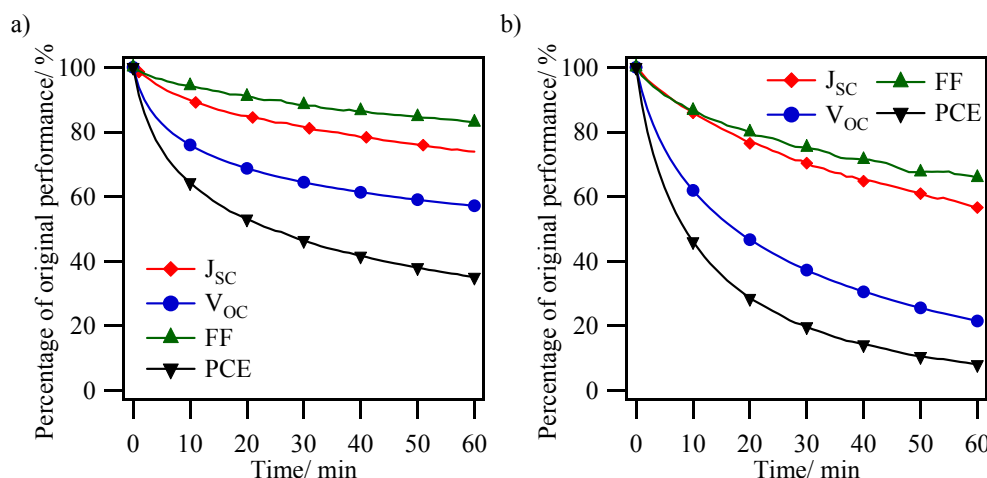


Figure 4.10 Plots of key device characteristics as a function of time during continuous light exposure for 1 hour at 100 mW cm^{-2} for devices a) (B1) based on TSCuPc and b) (I1) based on PTEBS.

A possible explanation for such a significant degradation could be trapped water and bound oxygen remaining within the donor film upon water based solution processing. During light exposure C_{60} , as well as the donor can undergo degrading photo-catalysed oxidation or photo-bleaching, including the donor/ C_{60} and electrode interfaces. The process continues further into the layer with extended exposure time. It is also known that oxygen can diffuse from ITO into the active layer where it leads to oxidation of the photoactive components.^[223-225] The oxidation process can be accelerated by illumination and ultimately leads to a reduced photocurrent, and charge transport reduction resulting in a lower FF and V_{OC} .^[224] The degradation effect was irreversible in the dark for both materials. To improve the stability of PTEBS and TSCuPc based devices hole extracting metal oxides such as MoO_x and WO_x could be inserted between ITO and the donor layer to prevent direct electrode contact and oxygen diffusion into the active layer from the bottom electrode.^[124, 148] However, the stability of the devices is still limited by the oxygen and water initially retained within the donor layers from the fabrication process.

4.3.4 Film surface treatment

PTEBS and TSCuPc are employed as donor materials in D-A 3D nanostructured composite devices (Chapter 5). In order to understand the impact of the fabrication steps

used for nanosphere templating on J - V behaviour, OPV device performance was investigated after different donor film treatments related to the process. This includes heat treatment as performed in the co-deposition process of donor material and PS followed by solvent exposure to THF which occurs during PS template removal.

Table 4.3 summarises the device performance of the untreated reference device (B1), device (B2) after heat and THF vapour treatment and device (B3) after heat and THF immersion treatment. For device (B2) the FF and J_{SC} improved by more than 10 % and V_{OC} decreased by about 24 % leading to no significant change in PCE . In THF the FF and J_{SC} improved by more than 7 % and 20 % respectively for device (B3). The V_{OC} decreased by about 59 % reducing the PCE to about half of the original performance. In all cases the FF and J_{SC} improved upon solvent treatment due to impurity and process residue removal. It has to be remarked that TSCuPc was used as purchased without further purification. Although the materials are fairly insoluble in THF, material removal upon solvent exposure can occur, leading to slightly thinner and sometimes incomplete substrate coverage which can result in J_{SC} changes and a reduction in V_{OC} as discussed in the earlier device section 4.3.1.3. Overall, vapour treatment seems to be the more gentle and beneficial surface treatment with immersion in solvent leading to greater film disruption.

Table 4.3 Summary of device characteristics for OPVs based on device (B1) with different heat and solvent treatments of the TSCuPc thin film prior to C_{60} deposition and device structure completion. The percentages in brackets state the change in performance compared to the untreated reference (B1).

Device	Treatment	V_{OC} [V]	J_{SC} [mA cm ⁻²]	FF	PCE [%]
(B1)	Untreated	0.52	1.47	0.41	0.32
(B2)	Heat, THF vapour, 20 min	0.40 (-24 %)	1.67 (+14 %)	0.48 (+16 %)	0.31 (-3 %)
(B3)	Heat, THF solution, 10 min	0.22 (-59 %)	1.57 (+7 %)	0.49 (+20 %)	0.16 (-49 %)

The same experiment was carried out for PTEBS and the results are summarised in Table 4.4 including the untreated reference device (I1), device (I2) after heat and THF

vapour treatment and device (I3) after heat and THF immersion treatment. Device (I2) shows only a slight reduction in V_{OC} by 6 % and almost no change in FF . The J_{SC} decreased by 27 % and the PCE by 34 %. The same trend was found for device (I3) in THF solution with a slight decrease in FF by 7 %, in J_{SC} by 18 % and in V_{OC} by 7 % respectively. In all cases the V_{OC} and FF remained fairly stable. J_{SC} was reduced in all cases. The very thin PTEBS layer (~ 5 nm) can easily be transformed upon solvent treatment with material removal being the most likely explanation.

Table 4.4 Summary of device characteristics for OPVs based on device (I1) with different heat and solvent treatments of the PTEBS thin film prior to C_{60} deposition and device structure completion. The percentages in brackets state the change in performance compared to the untreated reference (I1).

Device	Treatment	V_{OC} [V]	J_{SC} [mA cm ⁻²]	FF	PCE [%]
(I1)	Untreated	0.52	3.12	0.50	0.81
(I2)	Heat, THF vapour, 20 min	0.49 (-6 %)	2.27 (-27 %)	0.49 (-1 %)	0.54 (-34 %)
(I3)	Heat, THF solution, 10 min	0.48 (-7 %)	2.56 (-18 %)	0.47 (-7 %)	0.57 (-29 %)

4.4 Conclusion

The characteristics of water-soluble TSCuPc and PTEBS in solution, thin film and when incorporated as the donor layer in planar heterojunction OPV devices have been demonstrated.

TSCuPc solution consists of dissolved monomer and partially suspended nanocrystals resulting in dense and defined crystal networks on the substrate surface after spin-coating. For optimised devices a maximum PCE of 0.32 % was obtained. This PCE is to our knowledge the highest demonstrated for OPV cells based on water-soluble molecular semiconductors. The TSCuPc devices also showed an improved V_{OC} of up to 0.59 V, a 0.13 V improvement over standard CuPc/ C_{60} devices. Despite this V_{OC} , EQE measurements revealed a very low contribution to the photocurrent from the TSCuPc layer with the C_{60} acceptor being the main contributor. TSCuPc only serves as a

favourable interface for efficient exciton dissociation from the photoactive C₆₀ layer in the device. Devices fabricated with thicker TSCuPc layers suffer from several problems, including an increased R_S and imbalanced charge mobility causing S-shaped J - V curves under illumination, a short estimated L_D compared to CuPc, and grainy film morphology. The J_{SC} reduction with increasing film thickness over a range from 8 nm to 30 nm does not follow a steep decline as expected if the device was purely exciton diffusion length limited. The increase in R_S with thicker TSCuPc layers and the assumed imbalanced charge mobility induces a carrier extraction barrier due to poor hole conductivity. TSCuPc has almost no contribution to the photocurrent. Therefore, an increase in film thickness only inhibits carrier extraction and ultimately reduces FF and J_{SC} . The higher V_{OC} was achieved with the larger TSCuPc HOMO-LUMO band gap compared to CuPc. The advantages of higher V_{OC} and solubility in water through substitution by sulfonic acid functional groups are compromised by a lower charge mobility, shorter L_D and a lower FF . Devices from basic solution showed a generally higher performance than devices from pH neutral solution, which followed the same film thickness/performance trend.

Water-soluble PTEBS has a UV/vis absorption maximum in the lower wavelength part of the solar spectrum at around 434 nm with almost no change in solution and thin film spectra hinting towards a lack of vital inter-chain interlocking. The polymer forms smooth films on the substrate surface and adapts well to the underlying structure. For low concentrations of up to 2.5 mg mL⁻¹ the substrate surface coverage is incomplete leading to a reduced V_{OC} . Optimised devices with film thicknesses of about 5 nm achieved a PCE of up to 0.90 %, which is to our knowledge almost double the PCE of any previously reported devices based on this material and the highest reached for water-soluble polymeric semiconductors. Similar to TSCuPc, J_{SC} is mainly dominated by the C₆₀ contribution which was confirmed by J - V experiments with varying C₆₀ thickness and EQE . Thicker PTEBS layers are greatly compromised in performance by the L_D which is assumed to be shorter than 10 nm. Additionally, with thicker PTEBS films the increased R_S and the charge mobility imbalance with a low hole mobility in PTEBS lead to a reduction in FF and cause the pronounced S-shaped J - V curves. Both phenomena are

believed to be due to polymer disorder, which originate from the water-soluble charged functional groups on the polymer side chains.

Operational stability measurements showed a rather fast degradation process under illumination for both materials with remaining water and oxygen in the donor film layer from the fabrication process being the most likely cause. Film surface treatment following the templating process in Chapter 5 showed a reduction in performance for various reasons concerning the interface and thin film characteristics.

The main advantage of the organic semiconductors TSCuPc and PTEBS are the processability from aqueous solution, which demonstrates an important step towards greener, sustainable device fabrication. Furthermore, these materials offer a broad range of applications in organic electronics, including composite structures for electrode modification, templated porous structures and OPV devices.

Chapter 5: 3D interdigitated organic D-A composite structures and OPV devices

Vertical co-deposition of <100 nm PS nanosphere templates with water-soluble small molecule (TSCuPc) or polymeric semiconductors (PTEBS), followed by selective solvent vapour assisted sphere removal, is shown to be a good method for generating porous large area organic semiconductor thin films with sub-100 nm open-cellular networks. The open-cellular thin films were then used to fabricate complete organic D-A composite OPV devices which were characterised and compared to planar OPV devices.

5.1 Introduction

5.1.1 Background

In order to tackle the device performance limiting problem of the short L_D in organic semiconductors from an interface design point of view, a more controlled highly interpenetrating 3D D-A composite structure is required. Such an interdigitated structure allows to maximise the advantages from BHJ structures combined with continuous charge transport paths.

A promising approach is the development of 3DOM thin films of appropriate organic semiconductors which form the desired controlled matrix. Such a matrix is then employed to fabricate ordered highly interpenetrating D-A composite systems and subsequently OPV devices by using nanosphere templating.

3D nanosphere templating involves numerous steps and processes to obtain the highly interpenetrating D-A composite structure: 1) convective self-assembly of PS colloids to form the template structure; 2) infiltration of the nanosphere domains with appropriate donor material, which can be combined with step 1) by direct co-deposition; 3) colloid removal step; 4) second infiltration of the inverse structure with acceptor

material; and 5) implementation of the composite structures into complete OPV devices. All fabrication steps mentioned in this chapter follow the strategy and concepts described in section 1.4.1.

5.1.2 Colloidal crystals and templating

Self-assembly of colloidal spheres to highly ordered 2D and 3D thin film arrays, so called colloidal crystals, has been of great interest for a long time in materials and colloidal science due to numerous applications in photonics, lithography and templating.^[176] Highly ordered colloidal crystals, also known as opal structures, have a unique optical property called opalescence, which is based on the Bragg-Snell relationship leading to light diffraction by the two-phase crystal (high and low refractive index), which influences the propagation of light. This leads to light diffraction behaviour, with direct proportionality to the diffracted wavelength and lattice constant.^[226-228] This diffraction behaviour is used for photonic bandgap (PBG) materials and was first introduced in 1987 by Yablonovitch and John respectively.^[229, 230] The same phenomenon is responsible for the colourful appearance of the natural gemstone opal. Artificial opal structures of high quality are usually grown by nanosphere self-assembly from titania, silicon or polymer nanospheres and can even be deposited onto flexible substrates.^[228, 231, 232]

Moreover, the use of colloidal particles or emulsion droplets as templates to fabricate open-cellular or macroporous, often periodically structured materials, has proven to be widely applicable in areas as diverse as catalyst supports, insulating structures, absorbents, batteries, sensors as well as photonic and electronic devices.^[232-235]

2D arrays of self-assembled monolayers found great application in NSL acting as a mask for vapour deposited materials and semiconductors to nanostructure photoactive materials and electrodes.^[236, 237] 3D lattices have attracted a lot of attention as a template to form macroporous inverse opal structures of air spheres, with similar optical properties to an ordinary opal.^[238, 239] For metals, metal oxides, and inorganic semiconductors inverse opal structures were grown successfully due to the ease of complete template removal via calcination or solvent treatment.^[240-242] Especially for TMOs such as TiO_x

and ZnO grown from sol-gel processes or via electrodeposition, the fabrication process proves to be a promising templating technique to generate 3DOM structures and thin films which can find great application in composite organic-inorganic hybrid OPV and DSSC devices.^[243, 244] Due to the high sensitivity of most organic materials to heat and solvents, complete selective template removal is very challenging and explains why the nanosphere templating method is not well established for this specific material class. Only recently, nanosphere templating was applied for organic materials such as polymeric and small molecule organic semiconductors, which is discussed later in more detail in the specific section 5.1.4.^[133]

Inverse opals expose a huge surface area combined with an interconnected, well ordered, porous network not just suitable for DSSCs and novel composite structures for OPVs but also for catalysis and sensors.^[245, 246]

5.1.3 Nanosphere self-assembly

Nanosphere self-assembly to large 3D ordered arrays from dispersion is a self-organisation process driven or influenced by local interaction including Brownian motion, Van der Waals forces, electrostatic forces and capillary forces.^[247, 248] There is a range of different established techniques to grow ordered domains or colloidal crystals from latex including Langmuir-Blodgett deposition, spin-coating, doctor blading, sedimentation and centrifugation, filtering as well as vertical self-assembly.^[188, 233, 249, 250] In this work vertical self-assembly was chosen for nanosphere self-assembly due to the ease of film fabrication, relatively good control over layer thickness, scalability and suitability for substrates and materials employed in solar devices. Although highly ordered large crystal domains can be achieved, defect-free large area coverage is very challenging.

Vertical self-assembly

Vertical self-assembly is a controlled drying technique to grow photonic crystal-like arrays from nanospheres in dispersion. The substrate is almost vertically immersed in an aqueous dispersion of PS nanoparticles, wetting the substrate and forming a meniscus

at the liquid-substrate-air interface (see Figure 5.1). Solvent evaporation at the meniscus causes a convective flow of new dispersion towards the shallow part of the meniscus, where particle self-assembly takes place. Ideally, the particles form close-packed arrays, followed by the drying process.^[251-253] Different key parameters control the self assembly process including temperature, relative humidity, particle diameter and particle volume fraction.^[189, 196, 234] It is a very slow fabrication method, because it is based on controlled drying, which can take up to a few days.

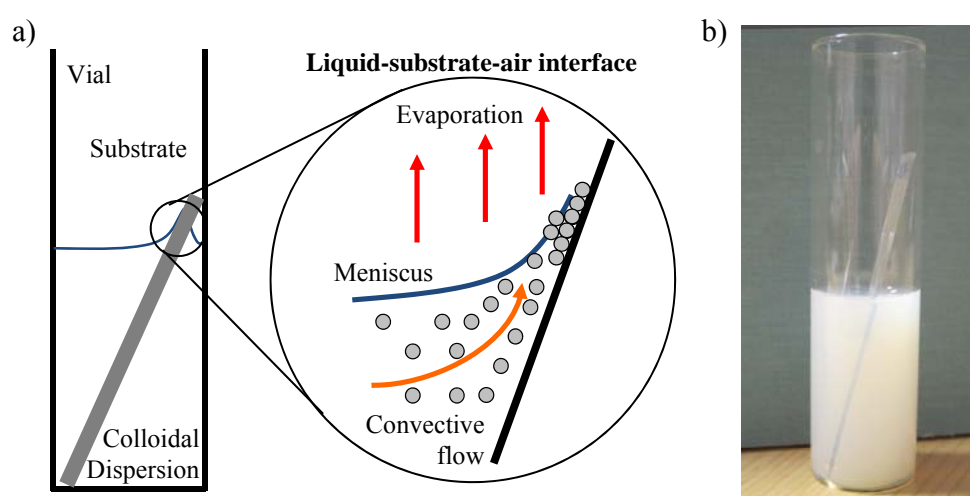


Figure 5.1 a) Schematic and b) photograph of convective self-assembly of PS colloids. Solvent evaporation above the meniscus drives a convective flow towards the shallow part at the interface where colloidal self-assembly takes place followed by the drying process.

Capillary forces are long-range forces which typically occur at triple interfaces, between liquid, gas and the sphere or more generally a capillary wall. Figure 5.2 shows the different types of self-assembly with the acting immersion capillary forces (F_{ic}) between just two particles and a liquid film bridge (Figure 5.2a) and for horizontal film formation on a substrate (Figure 5.2b).^[254] In a film formation process, such as convective self-assembly, strong hydrodynamic forces (F_{hd}) from solvent evaporation through the preformed lattice pull particles to the shallow end of the meniscus. F_{hd} act additionally to the present F_{ic} (Figure 5.2c). The generated hydrodynamic flux delivers dispersion towards the growth site to compensate evaporation losses. The monolayer and double layer of ordered spheres can be seen in Figure 5.2d. Typically, a face-centred

cubic close-packing is adopted, which is limited to a maximum of 74 % solid volume content under ideal sphere packing. 26 % of the film volume is formed by interconnected voids.^[248] These volume fractions also apply for inverse and composite structures.

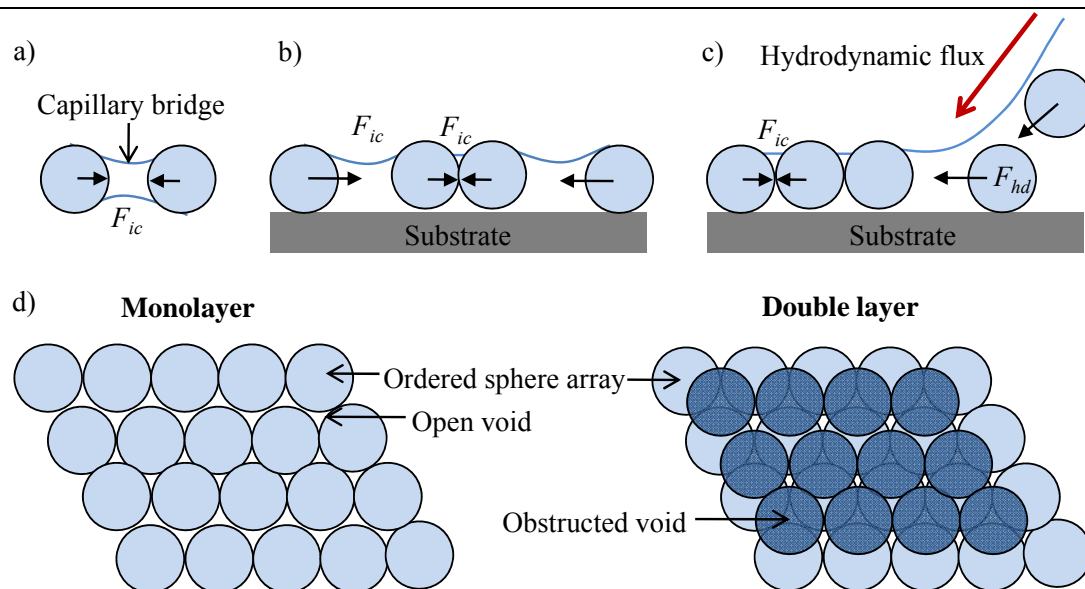


Figure 5.2 Particle self-assembly in solution is driven by capillary forces in a) a free film, b) a horizontal assembly and c) a convective self-assembly. d) Schematic of a monolayer (2D lattice) and a double layer (3D lattice) of close-packed nanospheres highlighting the voids created in between the spheres.

Co-deposition

In order to generate two-phase composite structures of spheres and a void filling compatible material, the voids can either be filled in a second infiltration step or can be directly fabricated by co-deposition of the two materials. Very little is reported about such a nanosphere co-deposition process.

Imhof and Pine reported the fabrication of emulsion droplet templated macroporous metal oxide materials through a sol-gel process.^[255] Similarly, Jonas *et al.* reported the fabrication of binary colloidal crystal arrays in which the interstitial spaces between the large colloidal crystal were filled with smaller particles.^[256] The fabrication of crack-free colloidal crystals using a modified vertical deposition of silica spheres and a silica precursor was also reported by Wang *et al.*^[257]

In the case of organic open-cellular structures for composite OPV devices a water-soluble organic semiconductor, i.e. PTEBS or TSCuPc, is required to be co-deposited with PS nanospheres from aqueous dispersion.

To date nothing has been reported in the literature on co-deposition of two organic materials and an organic semiconductor/PS composite in particular which gives this new approach its novelty.

Co-deposition offers a path to simplifying the process of two component film fabrication thereby increasing the viability of the sphere templating approach for a number of applications, in particular those involving organic semiconductor materials, e.g. for sensing and PVs.^[26, 258]

5.1.4 Organic 3D open-cellular and composite nanostructures

In these applications a large interface area, combined with a high degree of open-cellular interconnectivity is required, necessitating the use of ‘small’ template particles having dimensions <100 nm in order to match the L_D of the organic semiconductors employed. The open-cellular structures are generated by a selective sphere removal process.

The first organic semiconducting inverse opal structures were fabricated by Caruso and co-workers using electropolymerisation of pyrrole or thiophene to infiltrate the voids of PS colloidal crystals to form free-standing 3DOM thin films of polypyrrole or polythiophene.^[259] By using a similar approach inverse opal thin films of polyaniline were achieved.^[260]

McLachlan *et al.* first demonstrated the fabrication of 3DOM thin film structures using the small molecule organic semiconductor, TSCuPc, and colloidal crystals from vertical deposition with relatively large (250-400 nm diameter) template particles.^[202] In this approach the usual two-step process was employed instead of co-deposition. Selective template removal was achieved by solvent immersion. Based on the same approach with similar particle sizes, Berhanu *et al.* later demonstrated a complete D-A TSCuPc composite structure templated from similarly sized particles. This work included the additional second infiltration step using the solution processable electron acceptor

material PCBM to form complete D-A nanocomposite films.^[210] In a follow-up study the fully interconnected phases were analysed in detail and successfully confirmed by “pseudo tomography” using FIB/SEM, with TSCuPc-PCBM 3D nanocomposite images reconstructed from the cross-sectional cuts.^[203] The study confirmed a 2-3 times greater interfacial area to volume ratio compared to planar structures with the higher ratio for smaller sphere diameters. For particles with a diameter of 461 nm and 224 nm, volume ratios of 35.5:63.3 and 45.9:50.0 for TSCuPc:PCMB were determined respectively. These ratios differ from the theoretically expected value of 26:76 for TSCuPc:PCMB due to sphere shrinkage upon drying as well as film cracks and defects.

Although there have been very few reports of templating with particles of smaller sizes, this particular technique seems to be promising for particles and therefore pore diameters down to 100 nm, but will be very challenging for spheres small enough to match the short L_D of most organic semiconductors which can be as low as <10 nm. For templates smaller than 100 nm, material infiltration is very difficult due to the small voids, which leads to the development of template/donor material co-deposition to grow a complete composite layer.

5.1.5 3D nanostructured composite OPV devices

Although BHJ and mixed layer devices show a better overall device performance compared to planar heterojunction devices due to a higher J_{SC} , an even greater improvement in device performance can be expected using engineered nanostructured D-A composite devices with fully interconnecting phases. There have been many attempts to fabricate organic/organic and hybrid nanostructures as well as composites to aim for an increase in D/A interface area and the generation of small, but interconnected D-A domains.^[133, 261] However, most studies do not present the implementation of such structures into working OPV devices to produce a proof of concept.

TiO_x nanosphere and pore structures from nanosphere templating found great application in DSSCs, being used as an electrode structure as well as a light scattering layer.^[262] In DSSCs the TiO₂ porous electrode can be several μm thick and therefore does not require such a precise engineering and fabrication as the composite structures for

other OPV devices. Opal and inverse opal mesoporous structures offer a large surface area for dye-sensitisation coupled with good porosity for improved dye infiltration and efficient electrolyte diffusion as well as modification of absorption behaviour. Hence, a relative improvement in photocurrent performance compared to simply sintered randomly ordered TiO₂ nanoparticle clusters is expected.^[246, 263] In the case of ideal inverse opal crystals with a photonic stop band in the photoactive region of the dye, a reduction in current was seen. However an implementation of such a structure as a mirror layer improved the performance due to enhanced back reflection.^[264]

Nanostructured hybrid OPV devices with a controlled interdigitated A/D interface of predominantly TMO/polymer combinations are mainly based on vertically grown nanorods which show enhanced photocurrent with increased surface area.^[140-142] Other attempts to create porous thin films include block co-polymer templating of TiO_x where the photocurrent improvement is attributed to the engineered morphology.^[154, 265] Nanostructuring of hybrid OPVs, especially of TMO based devices, has a direct effect on the photocurrent as it allows thicker photoactive composite layers and enhances the photocurrent due to higher exciton generation from the sole current contributor. However, the use of template assisted TMO based opal or inverse opal structures for devices have not been reported.

Controlled nanostructuring of organic semiconductors is more complicated due to heat, solvent and chemical sensitivity leaving only few options. Snaith *et al.* fabricated interdigitated composite devices of hole-transporting polymer brushes of CdSe nanocrystal sensitised polyacrylate with high *EQEs*.^[266, 267] Another strategy for nanostructuring is mechanical nanoimprinting to fabricate isolated pillar features. A photocurrent improvement has been demonstrated for nanoimprinted pentacene in pentacene/C₆₀ devices and P3HT in hybrid P3HT/ZnO devices.^[268, 269] He *et al.* used the same approach for P3HT in polymer/polymer devices reaching a remarkable PCE of 1.9 %.^[270] Wiedemann *et al.* used a similar approach of P3HT nanoimprinting to generate an 80 nm periodicity of 40 nm wide pillars.^[271] The device was completed by a layer of PCBM creating a larger interfacial area, which led to a slightly higher *J_{SC}* of 0.13 mA cm⁻² and a PCE of 0.05 % compared to 0.09 mA cm⁻² and 0.03 % for a conventional planar bilayer device.

Most nanostructuring approaches of D/A interfaces show an improving effect on the device performance of such complicated interdigitated composite structures. This results in a proof of concept, but none of the device systems are able to compete close to state-of-the-art high efficiency OPVs. However, most methods are complex multistep fabrication processes in different environments which can be a source of film defects, surface and interface residues as well as material degradation caused by oxygen and moisture exposure. This makes new strategies very challenging. Quite often the improvement of device characteristics through nanostructure engineering is greatly compromised.^[132] From a device structure point of view, it has also been discussed that with increasing interface area in interdigitated composites a competing effect of higher recombination is expected.^[271] This phenomenon is predicted to have a particular impact when stepping up from pillar and rod based interpenetrating composites to 3D cage-like structures with partially opposing electrical fields which leads to less efficient charge separation due to enhanced geminate pair recombination.^[272]

5.1.6 Aim

By using nanosphere templating, organic D-A composite 3D interpenetrating nanostructured OPV devices with a large and controlled D/A interface are fabricated for improved photocurrent generation. The fabrication is a multistep process including template deposition, donor material infiltration, template removal and acceptor infiltration as well as completion of the composite OPV device.

Continuous, large area 3D open-cellular thin film structures are produced from vertical co-deposition of templating PS spheres of sub-100 nm diameter in conjunction with water-soluble small molecule (i.e. TSCuPc) or polymeric (i.e. PTEBS) organic semiconductors followed by subsequent solvent based template removal. This involves the development of the co-deposition process of colloidal dispersion and dissolved donor material using vertical self-assembly as well as efficient and selective template sphere removal. After re-infiltration by an appropriate acceptor material the composite structures are implemented in complete OPV devices and further characterised.

5.2 Experimental

5.2.1 Open-cellular organic thin films

Synthesis of the 3DOM inverse open-cellular structures from co-deposition is a two step process: (i) vertical or convective self-assembly of “small” PS spheres in the presence of the organic semiconductor fillers, to form thin periodic sheets; and (ii) removal of the PS nanosphere template.

Vertical self-assembly by co-deposition

PS sphere latexes with mean particle diameters of 96 nm, 78 nm and 35 nm were prepared with polydispersities of 0.010, 0.014 and 0.086 (5.2 %, 5.9 % and 9.9 % relative standard deviation) synthesised in (R8), (R1) and (R5) respectively from Chapter 3 (Table 5.1).

Table 5.1 Summary of the different nanosphere characteristics employed in vertical co-deposition from (R8), (R1) and (R5) (Chapter 3).

Average diam. (dry) [nm]	Standard deviation (dry) [nm]	Relative standard deviation (dry) [%]	Z-average diameter (DLS) [nm]	PDI	React. (Chapt. 3)
96	5.0	5.2	115	0.014	(R8)
78	4.6	5.9	100	0.010	(R1)
35	3.5	9.9	61	0.086	(R5)

Typically, 0.10-0.30 mL of latex was added to 15 mL of water (pH 11) containing 0.02-0.15 mg mL⁻¹ of pre-dissolved water-soluble polymeric semiconductor, PTEBS, or the molecular semiconductor, TSCuPc. The latex volume fractions were varied between 0.015 % and 0.080 %. In case of the very small particles of 35 nm in diameter latex volumes of up to 4 ml were added due to the very low initial solid content of nanospheres (<10⁻³ %) from the quenched reaction (R5). Composite films of close-packed, self-

assembled monodisperse PS spheres infilled with water-soluble organic semiconductors were fabricated in a single-step process (co-deposition). The growth was adapted to vertical self-assembly conditions reported by McLachlan *et al.*^[196, 202]

Ordered colloidal composite thin films were grown on either 12 x 75 mm glass slides (VWR International) or 12 x 36 mm ITO coated glass substrates, which were immersed in the appropriate colloidal dispersion in glass vials (Figure 5.1). All substrates were cleaned following the standard method. Glass substrates were used to optimise the growth parameters prior to ITO substrate use. Typical dispersion volumes were 15 mL in glass vials with dimensions of 25 mm in diameter and 100 mm in height. After immersing the substrate in a blend of colloidal dispersion and organic semiconductor, the structures were grown in a temperature-stable incubator at $60\text{ }^{\circ}\text{C} \pm 0.4^{\circ}\text{C}$ and a relative humidity (RH) <20 %. Under these growth conditions an empirical balance between solvent evaporation and particle sedimentation was found.^[189, 202] The temperature was monitored by either a digital thermometer or a data logger (Dickson, TM325) with remote probe for RH and temperature measurement. The samples were usually kept in the incubator for up to 3 days until the drying process was completed.

PS sphere template removal

The PS sphere templates were selectively removed from the composite structure by direct exposure of the sample to vapour from refluxing tetrahydrofurane (THF) for 20 to 30 minutes. For hot solvent vapour sphere removal a reflux apparatus was set up with a round-bottom flask as a solvent reservoir, a column and a water-cooled condenser with a sample holder placed in the vapour stream at the height of optimal solvent condensation. Penetration of pure solvent vapour into the composite thin film, condensation and dissolution of the PS spheres followed by gravity-induced draining of the polymer solution resulted in the formation of well-defined 3DOM organic thin films. This process is equivalent to continuous washing in high purity warm solvent, although it requires only a very small amount of solvent and the degree of template removal is simply a function of exposure time. After successful sphere removal the samples were dried for 10 minutes at $80\text{ }^{\circ}\text{C}$ under inert atmosphere to remove remaining solvents. The resulting 3DOM structures were analysed by SEM.

5.2.2 Fabrication of 3D nanostructured composite devices

For 3D interpenetrating nanostructured D-A composite OPV devices pre-fabricated open-cellular thin films of PTEBS and TSCuPc on ITO from different template sphere diameters were used. The second infiltration by the acceptor material was performed from solution with either PCBM or C₆₀ dissolved in 1,2-dichlorobenzene (5 to 20 mg mL⁻¹) under inert atmosphere. The acceptor material solutions were prepared and stirred under N₂ for at least 24 hours and filtered (0.2 µm) to prior use. The infiltration of the 3D open-cellular thin films was performed by different methods. A first method employed one simple dipping step in a dichlorobenzene solution of C₆₀ (20 mg mL⁻¹). A second method involved drop-casting (20 mg mL⁻¹ C₆₀ or 10 mg mL⁻¹ PCBM) with a penetration time of 2 minutes followed by spin-coating at 700 rpm. The third method was based on drop-casting of solution (5 mg mL⁻¹ PCBM) followed by controlled drying. After initial solvent evaporation at room temperature for 10 minutes the films were slowly heated up and dried at 120 °C for 20 minutes. In order to complete the device an additional C₆₀ buffer layer of 40 nm followed by a BCP layer of 7 nm and a thicker Al electrode of ca. 200 nm thickness were grown on top of the generated composite structures by vacuum deposition. Thick Al electrodes are deposited to flatten surface inhomogeneities to provide sufficient contact coverage. The device top contact area is 0.06 cm². Film and device analysis included *J-V* device characterisation as well as SEM for structure and morphology analysis.

In addition to the devices presented in Chapter 4, planar reference devices with solution processed acceptor layer were fabricated using optimised PTEBS (5 mg mL⁻¹) layers as a basis for C₆₀ and PCBM solution deposition. C₆₀ and PCBM solutions (20 mg mL⁻¹) were spin coated onto the pre-deposited PTEBS film at 2000 rpm for 2 minutes followed by drying at room temperature and elevated temperature of 120 °C for 20 minutes under inert atmosphere. The devices were completed by the vacuum deposition of 7 nm of BCP and Al. The fabrication of heat and solvent treated reference devices (I1) and (I2) it is reported in Chapter 4.

5.3 Results

5.3.1 Open-cellular organic semiconductor thin films

5.3.1.1 3D ordered donor-PS composite structures

Figure 5.3a shows photographs of typical PS-donor composite film samples as formed by vertical co-deposition. The composites are based on TSCuPc and PTEBS deposited onto glass and ITO substrates. In the close-up photograph in Figure 5.3b the three characteristic growth zones (I) to (III) can be seen following the film growth direction.

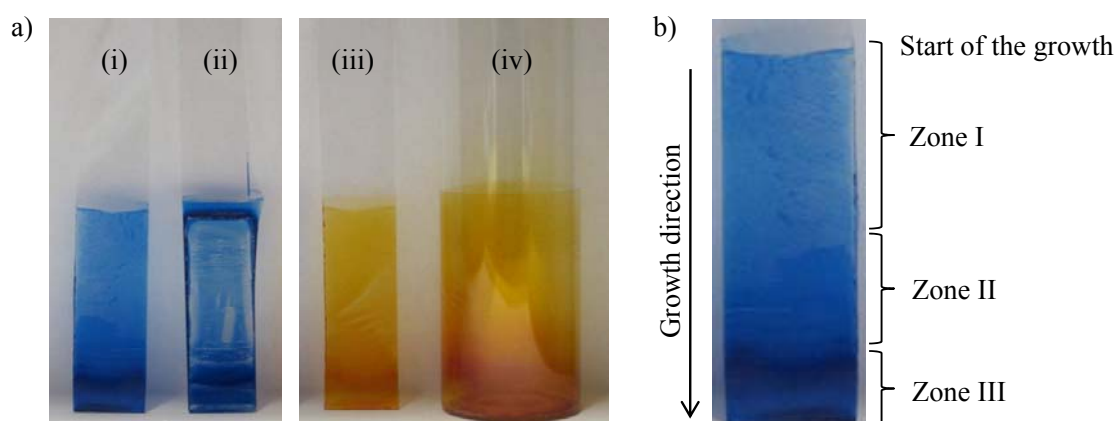


Figure 5.3 a) Photographs of PS-donor composite film samples deposited by vertical co-deposition: composites based on TSCuPc deposited onto (i) glass and (ii) ITO substrates as well as a composite based on PTEBS on glass (iii). (iv) The corresponding vial after a successful growth. b) Close-up photograph of a deposited film highlighting the film growth direction and the three characteristic growth zones (I) to (III).

Zone (I) shows the characteristic band formation perpendicular to the growth direction which is known as stick-slip. It occurs at low concentrations of the colloidal suspension and is caused by an imbalance of convective particle transport and surface tension forces.^[273] The band pattern is a sequence of deposited colloidal arrays of up to a few layers in thickness followed by a bare substrate section. This leads to incomplete substrate coverage and is therefore unsuitable for device fabrication. With reduced suspension volume due to evaporation and increased colloid concentration the distance between the bands shrinks and eventually leads to homogenous substrate coverage in

zone (II). This film section is more uniform in film thickness and reliable for device purposes. However, vertical film cracks along the growth direction break the film into domains. Zone (III) appears at the bottom of the substrate where high particle concentrations lead to less controlled, uneven and very thick films. In some cases the adhesion to the substrate is poor and parts of the film peel off in long flakes. Zone (III) is not suitable for further implementation in OPV devices. The length of the individual zones depends on the initial concentration leaving at least one 12 mm long section of zone (II) suitable for a 12 x 12 mm device substrate which was selected and cut after film deposition. Similar results were obtained for either type of substrate, i.e. glass and ITO, including growth zones length and sections.

Figure 5.4 shows SEM images of PS-TSCuPc composite films from co-deposition using 96 nm particles. On a macroscopic scale it can be seen that the composite films crack along the vertical growth direction with domain widths of up to a few tens of μm in width divided by 1-2 μm wide cracks (Fig. 5.4a). The cracks penetrate through the entire film thickness exposing the underlying substrate (Fig. 5.4b and inset). On a much smaller scale the domains consist of close-packed self-assembled nanospheres and TSCuPc filled interstitial voids forming a compact PS-TSCuPc composite structure (Fig. 5.4c). The sphere packing quality varies with local spots of good dense packing interrupted by assembly defects, unfilled voids and small cracks (Fig. 5.4d). The image of a cross-sectional view in Fig. 5.4e shows that such a packing with sufficient TSCuPc infiltration is also provided close to the substrate. These defects and deviation from ideal dense packing arise from the modified vertical self-assembly method using co-deposition. The filling material introduces larger distances between the assembling particle which weakens the capillary effect as well as F_{hd} and therefore reduces the packing order. Moreover, such an effect is enhanced with increasing polydispersity of the templating particles.

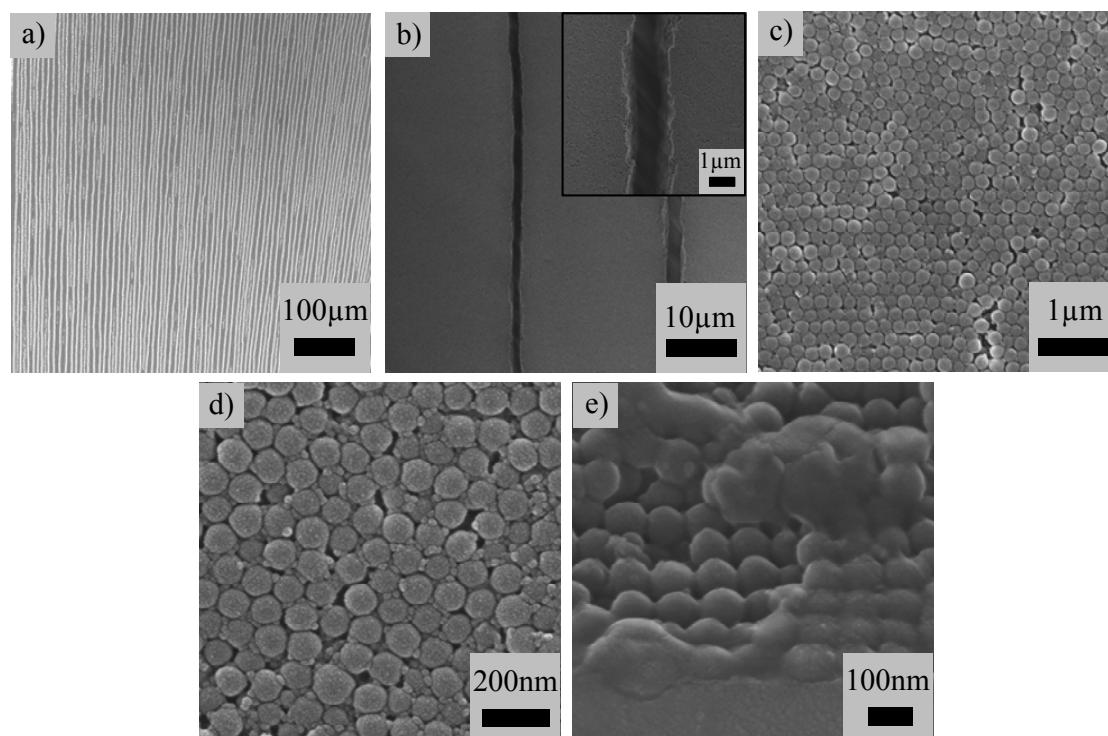


Figure 5.4 SEM images of TSCuPc-PS composite films from co-deposition of TSCuPc with 96 nm PS latex particles: (a-c) film domains divided by long parallel cracks cover large substrate areas (inset: close-up image of a typical film crack dividing two domains), d) and e) high-resolution images from top and cross-sectional view of close-packed domains showing the grade of infiltration between the spheres as well as packing and infiltration defects.

Figure 5.5 shows SEM images of PTEBS-PS co-deposited composite structures using 78 nm nanospheres. On a low magnification scale no film cracks appear for PTEBS which is a great advantage over the TSCuPc-PS composite films (Fig. 5.5a and b). At a higher magnification film defects such as short cracks and point defects are distributed across the film surface in between well ordered dense packed composite domains a few micrometres in size (Fig. 5.5c). The cracks are <200 nm in width, only a few layers deep and short in length (Fig. 5.5a). Despite these local cracks an interconnected network of domains is preserved without suffering isolation of large domains which ultimately leads to complications in device fabrication. Figures 5.5d-e show that the penetration and deposition of PTEBS between the spheres within the top layer is not entirely uniform leaving larger unfilled or only partially filled gaps. Furthermore, some clusters of spheres are packed very closely not allowing sufficient PTEBS penetration which hints towards a

pre-assembling of the cluster before the film formation process. The significantly reduced crack density with only local film defects is most likely caused by a different strain release mechanism compared to pure nanosphere colloidal crystals and the TSCuPc-PS composites.^[274] It is believed that the induced strain to the film during the drying process is reduced through co-deposition of the spheres with a donor. The donor reduces the capillary and hydrodynamic forces of the self-assembly by partially filling the capillary voids between adjacent particles which widens the capillary and prevents sphere shape deformation. Moreover, in this particular material combination of two polymers the elasticity of the polymer-PS composite structure does not allow strain build-up over larger areas leading to local release at weak defect points.

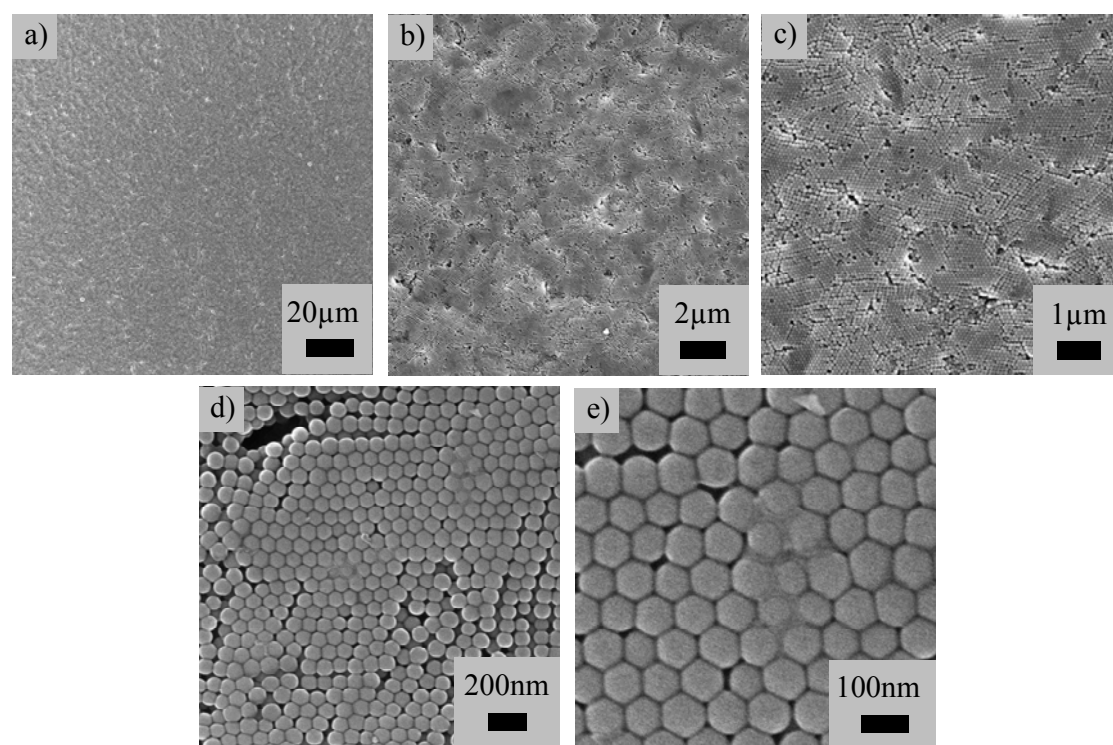


Figure 5.5 SEM images of PTEBS-PS composite films from co-deposition of PTEBS with 78 nm PS latex particles: (a-c) films of low defect density cover large substrate areas, d) and e) high-resolution images of close-packed domains showing grade of infiltration between the spheres as well as packing and infiltration defects.

5.3.1.2 3D open-cellular thin films

Figure 5.6 shows SEM images of the 3DOM films templated from close-packed arrays of 96 nm PS spheres using TSCuPc as the filling donor material. Uniform 3DOM domains of about 10-20 μm in width of the macroporous semiconductor films were obtained (Fig. 5.6a). The domains are divided by 1-2 μm wide cracks which follow the vertical film growth direction as can be seen in the figure inset. Compared to the clean cracks in the TSCuPc-PS composite films in Figure 5.4 the cracks after the solvent based sphere removal process are washed out and show fragment deposition of TSCuPc between adjacent 3DOM domains. Within the 3DOM domains the images show that an interconnected open-cellular structure was realised (Fig. 5.6b and c). Typically, in each cavity there are three pores visible, consistent with a close packed cavity array mirroring that of the template spheres. It can therefore be inferred that below the film surface each cavity is connected to all six adjacent cavities via a pore. Apart from major crack defects, the open-cellular structures show larger TSCuPc domains which can fill several sphere voids and disrupt the sphere packing (Fig. 5.6b). This suggests that these film defects are solution born and were not caused by the sphere removal process. The open-cellular structures show local dense-packing with good order surrounded by packing defects. The wall thickness of the TSCuPc scaffold varies significantly from as thin as 10 nm to about 50 nm which therefore defines the distance to the adjacent sphere or air sphere respectively leading to different pore sizes and numbers at the contact points.

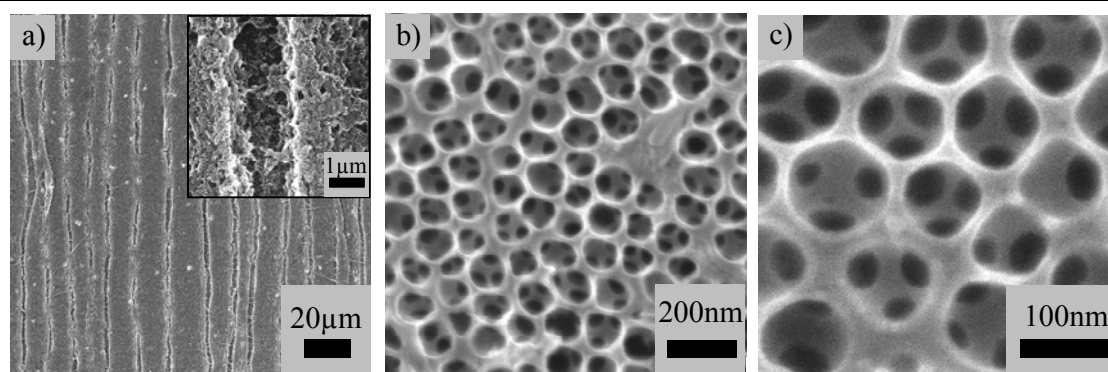


Figure 5.6 SEM images of template assisted 3D open-cellular thin films from co-deposition of TSCuPc with 96 nm PS latex particles: a) film of open-cellular TSCuPc domains divided by long parallel cracks cover large substrate areas, b) and c) providing a well-defined porous network. The inset in a) shows a close-up image of such a crack between two film domains.

In Figure 5.7 SEM images of the 3DOM films templated from close-packed arrays of 78 nm PS spheres using PTEBS are shown. Uniform crack-free domains of larger than $100 \times 100 \mu\text{m}$ of the macroporous semiconductor films can be seen (Fig. 5.7a and b). Figure 5.7c highlights the characteristic point defects of about 200-300 nm in diameter which are scattered across the film. The holes vary in depth from a surface defect up to a few layers deep. The defects are caused by clustered nanospheres which do not allow sufficient PTEBS deposition within the interstitial voids to form a robust scaffold. Subsequent sphere removal by solvent treatment washes out the entire cluster leaving behind the hole. Furthermore, it is assumed that the point defects replace large cracks as the strain release mechanism, dispersing the impact upon film drying and sphere shrinkage. The images in Figures 5.7d-e show that an interconnected open-cellular structure with good ordering over areas of a few μm^2 was realised for PTEBS.

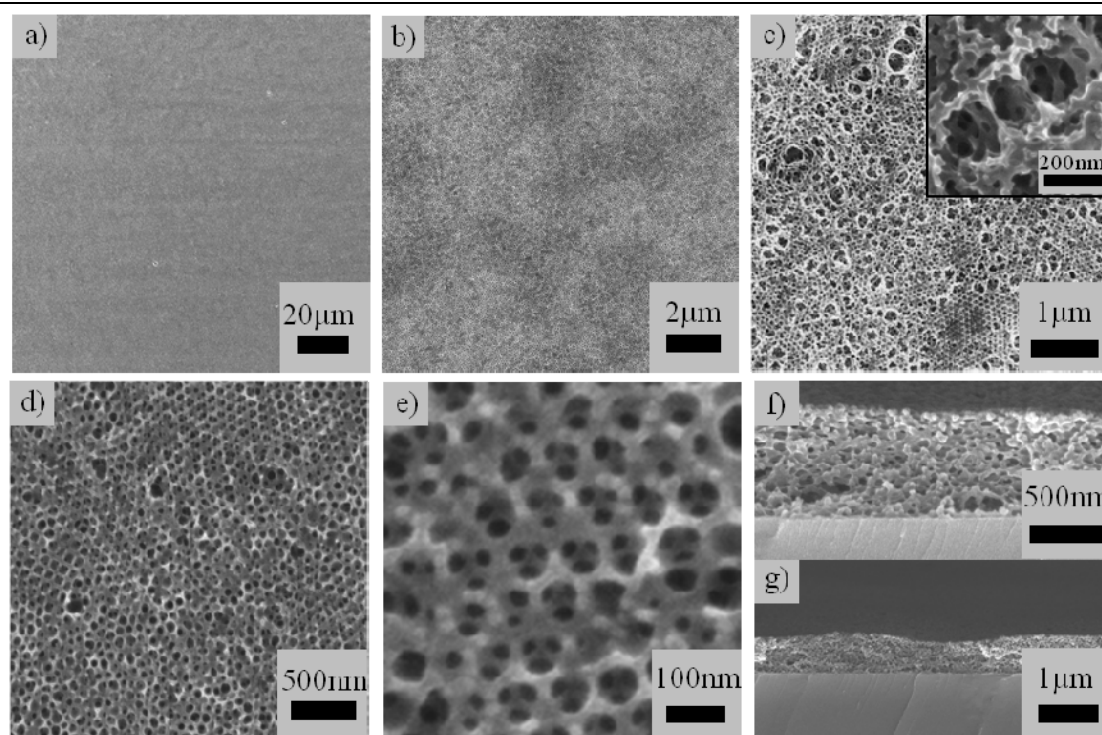


Figure 5.7 SEM images of template assisted 3D open-cellular thin films from co-deposition of PTEBS with 78 nm PS latex particles: a) and b) films of PTEBS with low defect density cover large substrate areas, c) containing some hole-like film defects (highlighted in the inset), d) and e) providing a well-defined porous network. f) and g) cross-sectional views of the 3D open-cellular thin films with some film thickness variations on a larger scale.

The air spheres are well connected to all six adjacent cavities via a pore. The wall thickness is <50 nm with average thicknesses between 20 nm and 30 nm. Cross-sectional images (Fig. 5.7f-g) reveal a porous network of less ordered and pronounced open-cellular structures than seen from the top view. Nevertheless, template removal proves to be successful all the way through the film to the substrate surface. The film thickness of the open-cellular films is consistent over a few micrometres in length but shows fluctuations on larger scales with typical average thicknesses ranging between about 300 nm to 1 μm depending on the section chosen of the zone (II). The variation within a short section of the film shows how difficult the thickness control of co-deposited films can be. Keeping the film thickness between 5 to 10 layers of spheres by latex volume fraction control enables the film fabrication of open-cellular films with sub-100 nm pore sizes with reasonable thicknesses and good substrate coverage.

In both cases, TSCuPc and PTEBS, the structure is not a perfect inverse opal since there are irregularities in the cavity shapes and separating wall thicknesses. This prevents the film structures from PBG effects which could reduce the penetration intensity of specific wavelengths. These departures from ideality can be attributed to a combination of the size distribution of the template spheres and relaxation of the organic semiconductor matrix upon template removal. It is important to note that during co-deposition the soluble filling material acts as a surfactant, modifying the inter-sphere interactions and capillary forces which drive PS sphere self-assembly. In some cases the presence of the filling material may destabilise the latex leading to random clustering and agglomeration of PS spheres.

The cracks observed for TSCuPc based open-cellular thin films are caused by drying-induced strain release through film cracking.^[189, 202, 274] Strain build-up within the film can originate from sphere shrinkage during the drying process.^[189] Although the colloidal crystal structure is reinforced by a TSCuPc scaffold the crystalline composite seems to be too brittle. In contrast to TSCuPc, the films formed from polymeric PTEBS do not crack which is most likely due to the co-deposition process coupled with an increased elasticity of the polymer which leads to local strain release. Local film weaknesses such as hole defects serve as a strain buffer and stretch to release the tension without long range impact (inset Fig. 5.7c). The combination of the co-deposition process

of nanospheres and a polymeric filling material gives this method the advantage of open-cellular film fabrication without film cracking.

The co-deposition strategy developed was also applied using PS spheres of 35 nm diameter to further increase the total surface area of the macroporous cellular structure upon sphere removal. Figure 5.8 shows examples of 3DOM films using PTEBS (a-c) and TSCuPc (d-e).

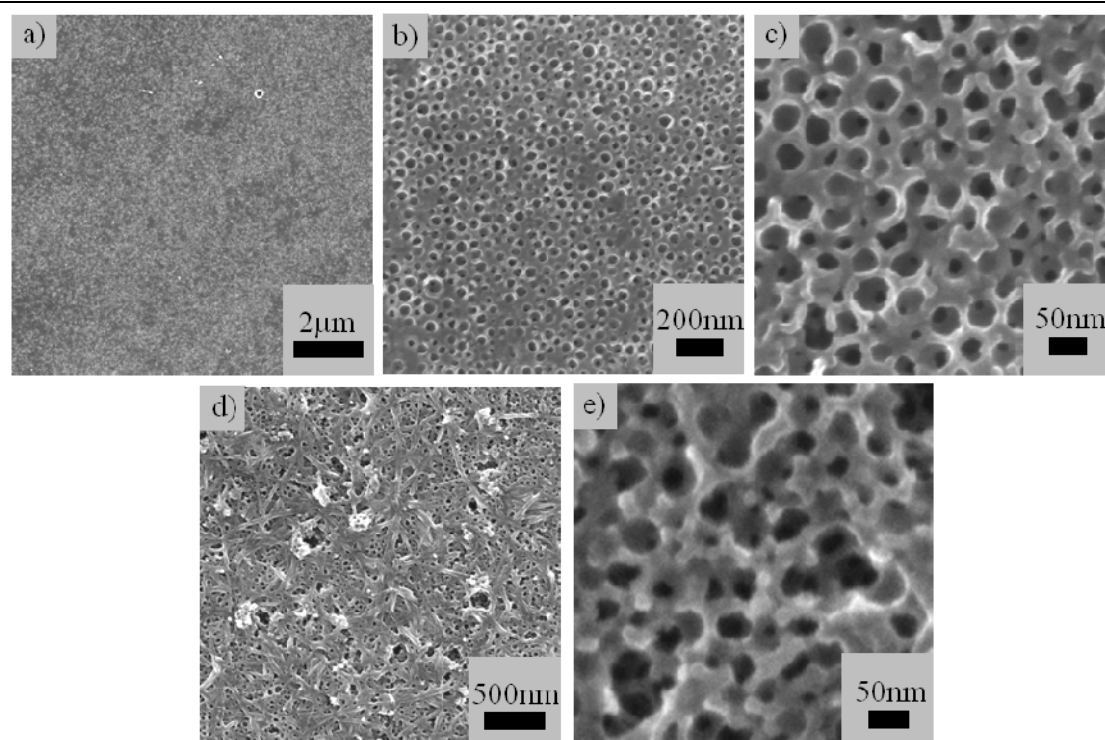


Figure 5.8 SEM images of 3DOM films of (a-c) PTEBS and (d-e) TSCuPc templated with 35 nm spheres from co-deposition. For very small pore sizes the porous structure is still present but less regular and defined.

The SEM images show the presence of porous structures. However, they are less regular and not as well defined as those templated using the larger PS spheres. Furthermore, in the open-cellular structure there are fewer pores between adjacent cavities, although sufficient to ensure continuous interconnectivity. Whilst PTEBS films showed a higher degree of regularity in their porous network than those fabricated from TSCuPc, both are much more defective than those fabricated using the larger spheres.

This can in part be ascribed to the broader sphere size distribution exceeding the threshold of 8 % for good colloidal crystal quality (9.9 % for 35 nm spheres; 5.2 % and 5.9 % for 96 nm and 78 nm spheres). However, for sub-100 nm nanospheres, the self-assembly driving capillary attraction energy decreases to a level comparable to the thermal energy of the particles, thus counteracting particle ordering.^[275] Since the latter operates to disrupt regular array formation the level of disorder in the films fabricated using 35 nm diameter spheres is to be expected. The films fabricated provided continuous interconnectivity through a few layers but were very thin, varied in thickness and did not provide uniform substrate coverage for device fabrication due to stick-slip. For these reasons open-cellular thin films from very small spheres <50 nm with naturally higher polydispersity were not used for further OPV device fabrication.

5.3.2 D-A 3D nanostructured composite OPV devices

5.3.2.1 3D nanostructured composite films and devices

In a further step the 3D open-cellular structures of PTEBS and TSCuPc templated from particles of 96 nm and 78 nm in diameter were infiltrated with acceptor materials such as C₆₀ and PCBM from solution. Although the solubility of C₆₀ in dichlorobenzene is not as high as for PCBM it was solution-processed in order to have a comparable component system as used in the planar reference devices in Chapter 4. Different infiltration techniques were employed to generate complete D-A composite thin films including simple dipping, solution drop-casting followed by spinning as well as drop-casting combined with controlled drying at elevated temperature. The infiltration methods were mainly studied on PTEBS films due to the better open-cellular thin film quality. For OPV device completion a 40 nm C₆₀ buffer layer followed by BCP and Al were deposited by vacuum evaporation. D-A composite structures from different infiltration methods as well as cross-sectional images of complete OPV devices from PTEBS are shown in Figure 5.9.

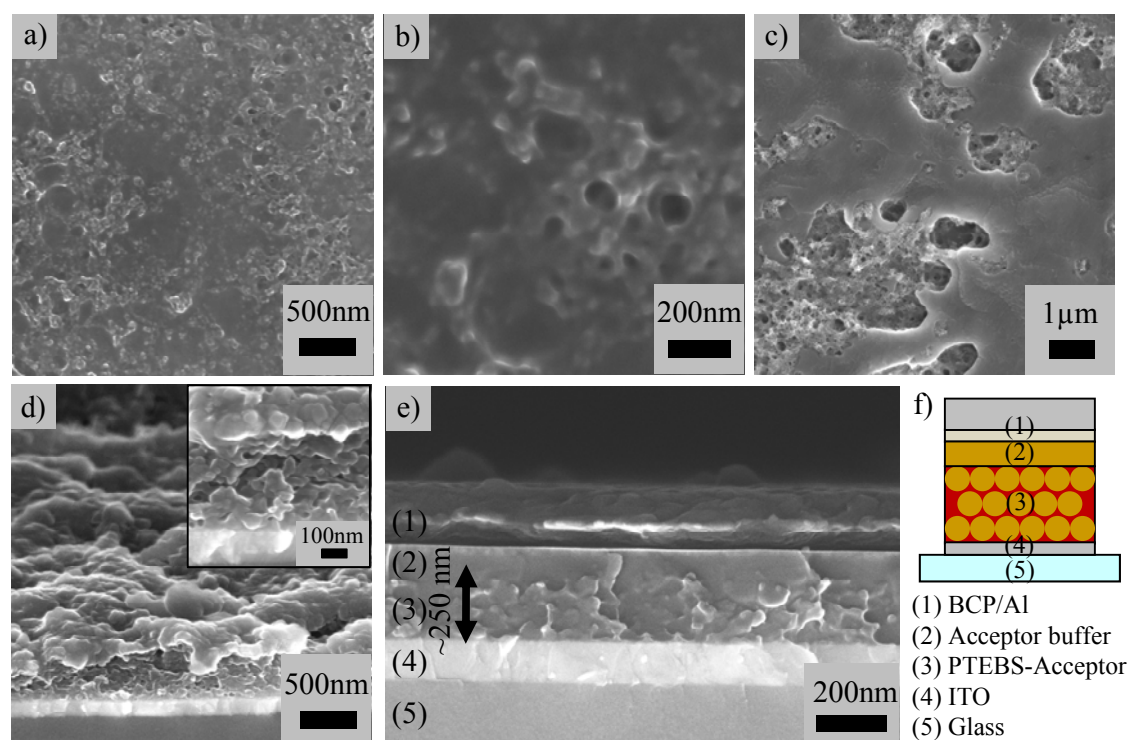


Figure 5.9 Top view SEM images of PTEBS- C_{60} and PTEBS-PCBM composite films fabricated by different infiltration methods: a) and b) drop-casting followed by spinning (C_{60}) and c) dipping (C_{60}). d) and e) show cross-sections of complete OPV devices with an integrated D-A (PTEBS-PCBM) composite structure from d) drop-casting followed by spinning and e) drop-casting followed by heat assisted drying respectively. The inset in d) shows the device structure in more detail. The arrow in e) indicates the thickness of the active D-A composite layer. f) Corresponding composite device schematic.

Drop-casting followed by spinning of PCBM or C_{60} solution resulted in film penetration with a smooth but not complete coverage as seen in Figures 5.9a-b. The films are not uniform as thicker layers are found covering cavities where at other places the underlying 3D scaffold is completely exposed. Although the spinning was introduced to rid excess solution and enhance solution spreading and penetration it mainly led to solution losses at exposed features which at some uneven spots cannot be compensated by the 40 nm C_{60} buffer layer. The cross-sectional image in Figure 5.9d demonstrates the surface roughness in a complete device resulting in a non-uniform electrode with disconnected or isolated contact areas. Simple dipping of 3D open-cellular films in acceptor solution resulted in very inhomogeneous surface coverage with little penetration of the deeper pores (Figure 5.9c). The deposition leaves large areas uncovered exposing the entire donor structure with other sections covered with a thick layer which leads to

very uneven and rough sample surfaces. In the case of dipping the penetration time is far too short to wet the surface and penetrate the porous structure, then not allowing trapped gas in the voids to escape. The third method based on drop-casting followed by controlled drying with subsequent drying at elevated temperature resulted in good pore infiltration through the entire film with a very uniform top layer. This can be seen in the cross-sectional image of the complete device in Figure 5.9e. This method allows the solution to slowly penetrate the film with some remaining solution on the top surface to form an even layer. This makes it the most promising method to realise such 3D interpenetrating nanocomposite layers.

It is assumed that the penetration of the porous film and especially smaller cavities is based on capillary effects which require longer exposure times. One of the main issues in the fabrication of such structures is the delicate combination of the materials: water-soluble hydrophilic donor scaffolds infiltrated by a hydrophobic acceptor solution. It is a requirement that the solvent does not dissolve the matrix which also makes it harder to penetrate small pores deep in the film. A possible explanation for the infiltration mechanism of the presented films could be that the low concentration acceptor solution based on dichlorobenzene partly dissolves a thin surface film of the scaffold to enhance its wettability, then enabling the infiltration of the pores through capillary forces.

5.3.2.2 *J-V* device characteristics

3D D-A composite structures of templated donor (PTEBS and TSCuPc) and infiltrated acceptor material (C_{60} and PCBM) were implemented in complete devices and tested under 1 sun illumination. The devices vary in template sphere size, the donor and acceptor material combination and the infiltration method. All D-A composite devices presented in this section employ the same device architecture: ITO/composite/ C_{60} (40 nm OMBD)/BCP (7 nm)/Al (see Figure 5.9f). The device parameters and performance characteristics are summarised in Table 5.2. Standard deviation is not given if the variation between the pixels within the devices and across devices was not representative due to shorts or variations of a few orders of magnitude. In such cases only the best working pixel is stated.

Table 5.2 Comparison of device performance data of D-A composite structures (A) to (F) as well as planar heterojunction reference devices (G), (H), (I1) and (I2) all based on PTEBS and TSCuPc as the donor in conjunction with C₆₀ and PCBM as the acceptor.

Device	V_{OC} [V]	J_{SC} [mA cm ⁻²]	FF	PCE [%]	Sphere diam. [nm]/ add. information
(A) PTEBS-C ₆₀ (dipped)	0.60	0.008	0.24	1.2×10^{-3}	78
(B) PTEBS-C ₆₀ (casted + spun)	0.07	0.007	0.25	1.2×10^{-4}	78
(C) TSCuPc-PCBM (casted + spun)	0.14	0.002	0.23	4.7×10^{-5}	96
(D) PTEBS-PCBM (casted + spun)	0.65	0.010	0.24	1.5×10^{-3}	78
(E) PTEBS-PCBM (casted + heated)	0.43 ± 0.05	0.444 ± 0.130	0.38 ± 0.03	0.07 ± 0.02	96
(F) PTEBS-PCBM (casted + heated)	0.55 ± 0.12	0.312 ± 0.061	0.38 ± 0.02	0.07 ± 0.02	78
(G) PTEBS/C ₆₀	0.38 ± 0.08	1.32 ± 0.01	0.43 ± 0.01	0.21 ± 0.05	Planar
(H) PTEBS/PCBM	0.44 ± 0.11	0.91 ± 0.05	0.35 ± 0.04	0.14 ± 0.05	Planar
(I1) PTEBS/C ₆₀ (untreated)	0.52 ± 0.07	3.12 ± 0.10	0.50 ± 0.04	0.81 ± 0.10	Planar, optimised
(I2) PTEBS/C ₆₀ (heat + THF treated)	0.49 ± 0.12	2.27 ± 0.36	0.49 ± 0.05	0.54 ± 0.16	Planar, treated

Both devices (A) and (B) are based on the same D-A composite device structure templated by 78 nm spheres only differing in the infiltration method with simple dipping for (A) and drop-casting followed by spinning for (B). Devices (A) and (B) exhibited a

V_{OC} of 0.60 V and 0.07 V, a J_{SC} of 0.008 mA cm⁻² and 0.007 mA cm⁻², a FF of 0.24 and 0.25 as a PCE of 1.2×10^{-3} % and 1.2×10^{-4} % respectively.

Device (C) and (D) were fabricated from drop-casting followed by spinning using PCBM. Device (C) uses TSCuPc as a donor templated from 96 nm spheres where device (D) was based on PTEBS templated from 78 nm spheres. Device (C) produced a V_{OC} of 0.14 V, a J_{SC} of 0.002 mA cm⁻², a FF of 0.23 and a PCE of 4.7×10^{-5} %. By contrast device (D) demonstrated a high V_{OC} of 0.65 V, a J_{SC} of 0.010 mA cm⁻², a FF of 0.24 and a PCE of 1.5×10^{-3} %.

The most successful devices (E) and (F) were based on PTEBS infiltrated by PCBM solution drop-casting combined with controlled drying at elevated temperature. Device (E) was templated from 96 nm and device (F) from 78 nm spheres resulting in a V_{OC} of 0.43 V and 0.55 V and a J_{SC} of 0.444 mA cm⁻² and 0.312 mA cm⁻² respectively, with the same FF of 0.38 and average PCE of 0.07 % for each which can be seen in Figure 5.10. The highest PCE achieved was 0.11 % for device (E) and 0.08 % for device (F). Both devices show a large standard deviation in V_{OC} and J_{SC} adding up to a deviation in the PCE of almost 30 %. A cross-sectional image of device (E) is shown in Figure 5.9e.

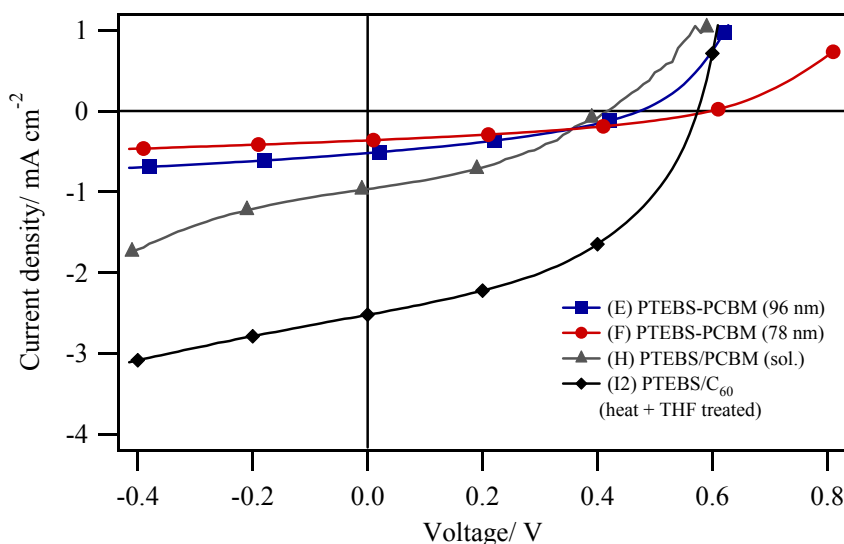


Figure 5.10 J - V curves of PTEBS-PCBM 3D composite devices (E) and (F) templated from spheres with 96 nm and 78 nm in diameter as well as planar reference devices (G), (H) and (I2).

Reference devices (G), (H), (I1) and (I2) are based on planar D/A heterojunction device architectures using different acceptor layers, solvent and vacuum deposition as well as solvent treatment (Figure 5.10): ITO/PTEBS (5 mg mL⁻¹)/acceptor/BCP (7 nm)/Al. In (G) and (H) a ~30 nm layer of either C₆₀ or PCBM is spin-coated from solution onto PTEBS in order to have a system closely comparable to solution processed D-A composite devices. The C₆₀ based device (G) showed a V_{OC} of 0.38 V with a large variation, a J_{SC} of 1.32 mA cm⁻², a FF of 0.43 and a PCE of 0.21 % with a relative standard deviation of 24 %. Device (H) employing PCBM exhibited a slightly higher V_{OC} of 0.44 V again with a large variation, a J_{SC} of 0.91 mA cm⁻², a FF of 0.35 and a PCE of 0.14 % with a relative standard deviation of 25 %. Reference devices based on vacuum deposited C₆₀ (I1) and (I2) are discussed in detail in Chapter 4.

For both D-A composite devices (A) and (B) the performance is very low with particular lack in J_{SC} . The open-cellular films were not sufficiently penetrated by the solution with either infiltration method leading to open voids and very uneven contact layers. Such J - V behaviour was expected from the composite film morphology revealed by SEM in Figure 5.9a-c. The low V_{OC} in (B) can be explained by the absence of a proper D/A heterojunction at exposed fractures of the PTEBS matrix, connecting bottom and top electrode through pinholes.

The very low OPV performance of TSCuPc device (C) was expected as the large film cracks of 1-2 μm in width (Fig. 5.6a) could not be sufficiently filled by the acceptor in the infiltration process. This leaves the top electrode scattered in small domains without interconnection and therefore no current collection which makes this approach unsuitable for TSCuPc based composite structures. The material could be a potential candidate if the film cracking during nanosphere self-assembly can be significantly reduced or eliminated as was achieved for polymeric PTEBS. PTEBS device (D) performed similarly to (A) and (B) with exactly the same low performance and low current hinting towards poor infiltration regardless of the acceptor material. The device also shows a very rough top layer making homogenous large area top contacts impossible (Fig. 5.9d). This leads to the conclusion that the choice of infiltration method is vital for a working D-A composite device and was not satisfied by infiltration methods such as drop-casting followed by spinning or dipping.

The best performance for 3D nanostructured D-A composite devices were achieved by PTEBS-PCBM devices (E) and (F) with significant improvement in J_{SC} and FF over all other D-A devices (A) to (D). (E) templated from 96 nm spheres and (F) templated from 78 nm spheres differ in V_{OC} and J_{SC} as well as highest achieved PCE . Device (E) with larger pore size and therefore larger PCBM domains reveals a ~40 % larger J_{SC} compared to device (F) which is probably based on the increased PCBM current contribution from the larger overall PCBM volume in the larger voids. The lower V_{OC} can partly be explained by direct PCBM domain contact in the composite matrix to the ITO bypassing the D/A interface. The larger pores and the absence of a PTEBS buffer layer enable such an unfavourable contact. For smaller pores as found in (F) the ITO coverage with PTEBS is better which prevents it from V_{OC} losses reaching higher values. Due to the special fabrication method involving water immersion and various solvent treatments a PTEBS (and TSCuPc or CuPc) buffer on the ITO is not possible which shows one of the limitation of this approach. With a FF of 0.38, both devices perform slightly higher than the reference (H) with a FF of 0.35 which indicates a good in-tact interpenetrating structure. The best PCE of 0.11 % for device (E) is in a comparable range to the reference device (H) with 0.14 % (optimised thin PTEBS layer) but reaches only about half of the J_{SC} which was the main target of improvement with such a templating attempt. Device (F) with even smaller domains does not show an increase in J_{SC} either. A possible explanation for the lower J_{SC} but better FF of the D-A composite devices compared to planar references could be the presence of larger PV inactive composite domains or areas in the device which do not contribute to the photocurrent, where other composite areas with well pronounced composite structures generate an increased photocurrent leading to an averaged lower J_{SC} . The influence of THF vapour exposure as well as heat in (I2) showed only a reduction in J_{SC} by 27 % compared to (I1) which is not seen as the main limiting factor. PS residues are assumed to be the greater problem for such delicate devices as there is no certain proof of their complete removal. Even very thin layers of PS can ruin the interface by covering it with an electrically insulating film.

In case of the presented PTEBS-PCBM and TSCuPc-PCBM composite devices from 96 nm and 78 nm spheres the L_D criteria of both materials sufficiently match the

structure dimensions which theoretically set the basis for higher J_{SC} s through improved exciton diffusion efficiency. The sphere radius (48 nm and 39 nm) matches the reported L_D of fullerenes of 40 nm.^[26] With a halved average wall thickness of 10-15 nm the PTEBS walls are on the higher limit of $L_D < 10$ nm (see Chapter 4) for an optimised cell. A more general problem of this particular templating approach is the limitation to only water-soluble donor materials, e.g. PTEBS and TSCuPc, due to the necessity of two completely different solvent systems required by the multistep fabrication process. As shown in Chapter 4 both donors are vital to establish a working heterojunction. However, TSCuPc does not and PTEBS does only very slightly contribute to the J_{SC} which differs from the characteristics defining an ideal OPV donor. It has also to be taken into account that 3D open-cellular or porous structures incorporate cage-like features. Such a structure might not be ideal from charge separation point as parts of the interface are inverted and opposing the built-in electric field. This leads to enhanced geminate pair recombination and therefore current loss.^[272]

Overall, it is assumed that the gained improvement of an engineered 3D interpenetrating D-A composite structure with increased active interface area is greatly compromised by the complexity and conditions of such a multistep fabrication process leading to film defects, residues and material exposure to air and water. Nevertheless, to our knowledge this novel approach to fabricate 3D ordered interpenetrating D-A composite structures and working OPV devices has not been reported in the literature and can serve as a model system towards a proof of concept.

5.4 Conclusions

In this study a new fabrication route for large surface area 3DOM organic thin films with a sub-100 nm open-cellular interconnected structure is presented. The films are achieved by co-deposition of the organic semiconductors and ‘small’ spherical PS particles, which is shown to be an efficient means of simultaneously assembling the PS spheres and infiltrating the interstitial vacancies. The method is demonstrated using both low molecular mass, i.e. TSCuPc, and high molecular mass, i.e. PTEBS, organic semiconductors thereby demonstrating the versatility of the approach. Moreover, by

using polymeric PTEBS as a filling material large area composite films of very low crack density were achieved. Subsequent template removal by hot solvent vapour treatment is shown to be an efficient technique of sphere removal generating 3D open-cellular organic semiconductor films of tunable pore size between 35-96 nm depending on the size of the PS latex spheres used. Despite minor defects and partially distorted packing order - particularly when using the smallest sphere templates - the resulting interconnected cellular networks of organic semiconductor provide an ideal platform for subsequent solution based infiltration of electron acceptor materials, such as PCBM and C₆₀ to form interpenetrating network nanocomposites. From the different infiltration methods tested, drop-casting followed by controlled drying at elevated temperature lead the best void infiltration and uniform surface coverage. In a further step TSCuPc and PTEBS based composites of 78 and 96 nm were implemented in complete OPV devices and tested at 1 sun illumination. Composite devices fabricated from TSCuPc resulted in a very low performance due to larger cracks in the composite films which could not be compensated by the infiltrated material. PTEBS-PCBM based composite devices with the best performing devices templated from 96 nm and 78 nm spheres reached a PCE of 0.11 % and 0.08 % respectively. Although a current increase due to improved exciton diffusion efficiency and maintained charge collection efficiency was expected, both devices showed a J_{SC} which was significantly lower than found for the solution processed reference device. However, a slightly higher FF in both composite devices indicated an in-tact composite structure for these much thicker layers suggesting that parts of the composite film might be inactive in current generation. There are various possible causes for such a current loss including defects, residues as well as variation in film quality and total thickness.

For such complicated devices it is assumed that the gained improvement of an engineered 3D interpenetrating D-A composite structure with increased active interface area tailored to L_D is greatly compromised by the complexity and conditions of such a multistep fabrication process. However, the presented approach to fabricate 3D ordered interpenetrating D-A composite structures and more importantly working OPV devices is a novel route. To our knowledge, no such devices have been reported in the literature. Despite the complexity of the multistep fabrication process and draw-backs in various

device and structure related areas the developed composite structures can be used as a model system towards a proof of principle.

Chapter 6: Electrode modification through TMO interlayers

In this chapter the influence of a TMO interlayer based on ZnO or TiO_x between the electron collecting bottom electrode and the photoactive blend of P3HT and PCBM in an inverted structure is investigated. The first part covers the TMO thin film deposition and characterisation including AFM, SEM, UV/vis absorption spectroscopy and XRD. The ZnO films were either deposited by electrodeposition or spray pyrolysis. The TiO_x thin films were fabricated from sol-gel process. In a second part the interlayers are studied in solution processed inverted BHJ OPV devices with focus on *J-V* characterisation as well as operational device stability measurement.

6.1 Introduction

6.1.1 Background of TMO interlayers in OPVs

To achieve even higher device efficiencies and to obtain increased shelf and operational stability the insertion of charge extraction and exciton blocking layers, as well as the use of new electrodes have been explored. Device design has focused on the use of hole-extracting TMO interlayers such as MoO_x, V₂O_x, NiO and WO_x, to either replace or cover the commonly used, but unstable poly(3,4-ethylenedioxythiophene) poly(styrene sulfonate) (PEDOT:PSS) layer.^[120, 121, 147, 276, 277] Hole-extracting TMOs have been employed in both the standard device architecture, with the ITO electrode collecting holes and the metal electrode collecting electrons, and more innovative inverted architectures with opposite charge collection (Figure 1.6a-b).^[104, 120] Despite its advantages of good hole conductivity, electron blocking behaviour and higher workfunction compared to ITO, long-term degradation of devices is at least partly caused by PEDOT:PSS due to reactions with oxygen and water as well as delamination.^[277, 278]

PEDOT:PSS can also be corrosive when solution-processed onto ITO substrates or when in contact with other metal electrodes due to the acidity of PSS, resulting in interface damage and device degradation.^[84, 125] Furthermore it reveals heterogeneous electronic properties across the film.^[276] Ideally, TMO interlayers should successfully prevent contact between the ITO or metal electrode and the active organic layer, thus reducing current leakage, as well as providing a more homogenous electrode conductivity and workfunction.^[131, 148] TMO insertion also allows a better energy level alignment of the donor HOMO energy level to the electrode workfunction via provided defect states for efficient charge extraction.^[124, 279] Moreover, TMOs can be deposited by vacuum or solution deposition which makes them easily processable and gives good control over film growth.

Applying the same interlayer concept to the opposite electrode, an electron-extracting and hole-blocking TMO buffer layer can be integrated using materials such as ZnO and TiO_x.^[118, 280] Such TMOs can be processed from solution using a number of different techniques, including sol-gel process, spray pyrolysis and electrodeposition.^[125, 162, 281-283] Furthermore, BCP can be replaced, which is involved in the performance degradation process of devices due to film re-crystallisation.^[284]

Only a limited number of studies have been conducted investigating this new class of materials as electron extraction layers in OPVs. One of the key challenges is the move to inverted device architectures since most TMO deposition techniques are performed on bare ITO substrates as they involve either high temperature annealing to improve crystallinity, e.g. sol-gel process or spray pyrolysis, or the use of conductive substrates, e.g. electrodeposition, to fabricate planar and nanostructured thin films. If the two types of charge extracting layers are combined in one device a very stable TMO/polymer blend/TMO sandwich structure can be realised with chemically inert TMO films around the delicate photoactive blend with greatly improved charge extraction.^[125] Additionally, when applied to inverted device architectures the favourable vertical phase separation of the photoactive blend seen in typical P3HT:PCBM systems with a higher concentration of the fullerene in the proximity of the electron extracting layer, is advantageous and results in better overall charge extraction, improved J_{SC} and larger FF .^[84, 285] Previous reports have involved the use of electrochemically grown ZnO

nanorods and corrugated ZnO nanoridges, resulting in *PCEs* of up to 4.0 %.^[150, 286] Recently, a *PCE* of 4.4 % has been demonstrated by integrating a cross-linked fullerene material layer between the ZnO and the blend layer of P3HT and PCBM (molecular structures see Figure 1.7), a remarkable result for an inverted BHJ device architecture.^[287] Similarly, inverted BHJ OPVs employing TiO_x from sol-gel process with either a PEDOT:PSS/Au, MoO_x /metal or WO_x /metal electrode show good performance of between 2.0 % and 4.1 % efficiency.^[86, 125, 288] Using TiO_x based inverted BHJ devices Tao *et al.* showed an independence of the workfunction of the top metal electrode in inverted architectures by introducing the MoO_x interlayer between the photoactive polymer blend and the metal electrode with similar device performance for Al, Ag and Au.^[125]

Electrodeposition of ZnO is shown to offer the highest control over the experimental parameters. It allows the creation of a broad variety of different morphologies, grades of crystallinity and structures, as well as nanostructuring and template assisted growth. The procedure is conducted at low temperature, leading to homogenous dense planar films with high film crystallinity and different preferential crystal orientation without thermal annealing and offers easy scalability to larger areas.^[115, 289] Electrodeposition also allows better control over impurities, defects, vacancies and stoichiometry, which all influence the photoconductive behaviour of ZnO.^[116, 290] Spray pyrolysis of ZnO is a widely used technique to produce wurtzite structures with the naturally grown polar (002) preferential lattice orientation but requires high temperatures of up to 500 °C which can be damaging for ITO.^[162] The technique is simple and suitable for scale-up in area, but restricted to planar film fabrication.

TiO_x thin films are mainly fabricated from sol-gel process which allows fabrication of very thin and dense films of tens of nanometres with good control over film thickness and roughness. Other deposition techniques such as electrodeposition, spray pyrolysis, sputtering and direct oxidation can be employed for TiO_x film fabrication but were rarely employed for OPVs.^[114, 291] In DSSCs, TiO_2 crystals are usually deposited from solution or as a paste by doctorblading and sintered to form meso-porous films of a few micrometres in thickness which is not suitable for BHJ OPVs. More details about TMO interlayers can be found in the introduction section 1.3.3 and 1.4.2.

6.1.2 Aim

The formation and properties of different types of ZnO and TiO_x interlayers are compared using UV/vis, AFM, SEM, XRD and TEM combined with FIB milling. Furthermore, the impact of the electron collecting TMO interlayers on OPV device behaviour when integrated into inverted BHJ P3HT:PCBM devices is assessed including *J-V* and operational stability measurements. In both cases a first step is the development of functional inverted device structures which include the introduction of hole collecting TMOs. For TiO_x the film deposition and thickness is optimised for inverted BHJ OPVs as a reference system. A more detailed study on the different ZnO interlayers is carried out to develop a deeper understanding of the structure/function relationship of crystal structure and orientation as well as film morphology for an optimised device performance.

6.2 Experimental

6.2.1 TMO interlayer preparation and characterisation

ITO-coated glass substrates used for ZnO deposition were ultra-sonicated for 10 minutes in acetone, methanol, 0.1 M sodium hydroxide aqueous solution and deionised water (18 MΩ cm, Onda Purite) prior to ZnO deposition. All other ITO-coated substrates were cleaned according to the method described in Chapter 2.

ZnO films prepared by spray pyrolysis (SP) were deposited onto ITO substrates at 400 °C from a solution of 0.2 M Zn(ac)₂ dissolved in methanol followed by an annealing step in air at 400 °C for 20 minutes. Electrodeposited (ED) ZnO films were prepared in a three-electrode set up consisting of an ITO working electrode, a Ag/AgCl/KCl (3.5M) reference electrode and a platinum mesh counter electrode. Electrodeposition was carried out potentiostatically by applying a potential of -1.3 V vs. the Ag/AgCl electrode. The deposition was halted after a charge of 0.15 C cm⁻² had been passed (8 seconds for a 1 cm² electrode). The deposition bath contained 0.1 M and 0.13 M Zn(NO₃)₂ for films A-

ED and B-ED respectively and was maintained at 85 °C. For B-ED the solution was kept at pH 2.5 by adding concentrated hydrochloric acid (also see section 2.1.3.3).

The TiO_x thin films were fabricated from a sol-gel process using the precursor solution described in section 2.1.3.2. The films were spin-coated with spin speeds between 1000 rpm and 5000 rpm in air followed by a multi-step drying and annealing procedure in air. The films were first dried at room temperature followed by a heating step with gradually increased temperature up to 200 °C over 1 hour, 1 hour at 200 °C and then 2 hours at 450 °C. All films were characterized by XRD, FE-SEM, TEM, AFM in AC mode, and UV/vis electronic absorption spectroscopy.

6.2.2 OPV device fabrication and assessment

The solution of P3HT (MW = 55-60 k) and PCBM was prepared via dissolution of 20 mg mL⁻¹ of each compound in 1,2-dichlorobenzene and was left stirring at 40 °C for at least 36 hours under inert atmosphere and filtered (0.2 µm) prior to spin-coating. The blend solution was spin-coated onto ITO, ITO/ZnO or ITO/TiO_x substrates for inverted, or onto ITO, ITO/WO_x or ITO/MoO_x substrates for regular, devices at 1000 rpm. This step was followed by drying for 45 min at room temperature and then annealing at 120 °C. The WO_x and MoO_x interlayers on ITO were predeposited with film thicknesses of 10 nm and 5 nm respectively. The film thickness of the blends was about 140 nm, measured by AFM on film step edges on ITO substrates. For the top contact of the inverted devices, WO_x and Al were deposited by thermal evaporation with film thicknesses of 10 nm and ~100 nm respectively. The top electrode of the regular devices was based on a 7 nm BCP layer followed by Al. The active area of the fabricated OPV devices is 0.06 cm². *J-V* measurements under illumination and under dark conditions were conducted as described in section 2.3. All devices were tested in a sealed sample holder under a N₂ atmosphere.

Device optimisation experiments were carried out for B-ED samples, including thicker polymer blend layers of ~173 nm deposited via spin-coating. Operational stability measurements for extended testing times of up to 40 hours of constant light exposure were carried out with a tungsten halogen lamp calibrated to 100 mW cm⁻².

6.3 Results

6.3.1 Transmission

Transmission spectra of ITO, ITO/TiO_x and the three different ITO/ZnO samples - SP, A-ED and B-ED - are shown in Figure 6.1. All three ITO/ZnO substrates (Figure 6.1a) and TiO_x (Figure 6.1b) show good transparency in the visible part of the spectrum with little deviation from bare ITO, where the P3HT:PCBM blend film absorbs best. This suggests that the deposition of the TMO layer is unlikely to be detrimental to device performance due to any undesirable light absorption at these thicknesses.

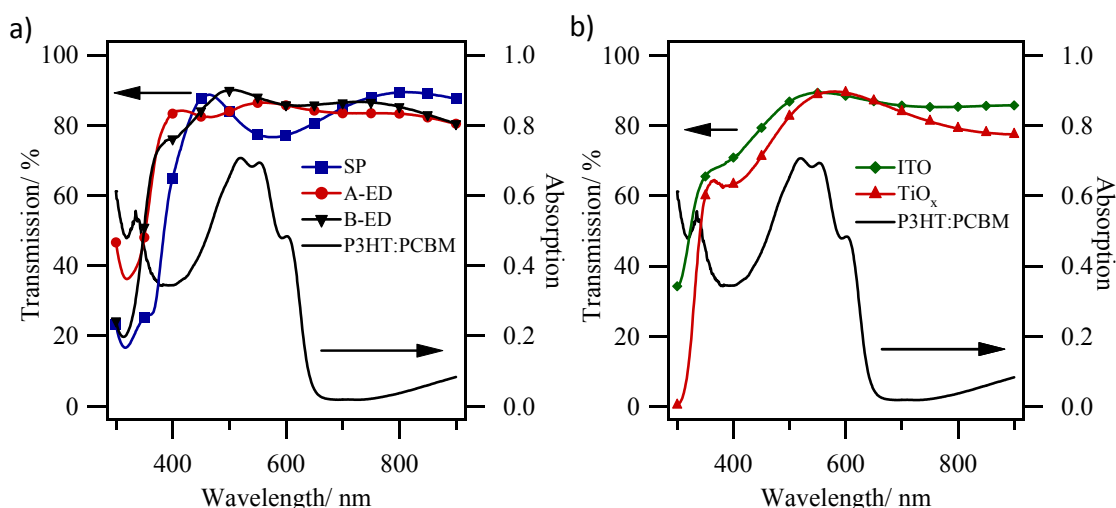


Figure 6.1 Transmission spectra a) various ZnO films deposited on ITO: SP, A-ED and B-ED and b) TiO_x (3000 rpm) in comparison to the absorption spectrum of the P3HT:PCBM film.

6.3.2 Morphology

The morphological properties of the three types of ZnO and TiO_x films are shown in Figure 6.2, where FE-SEM and AFM images for SP (a), A-ED (b), B-ED (c) and TiO_x (d) substrates are presented including their corresponding AFM height cross-section profiles.

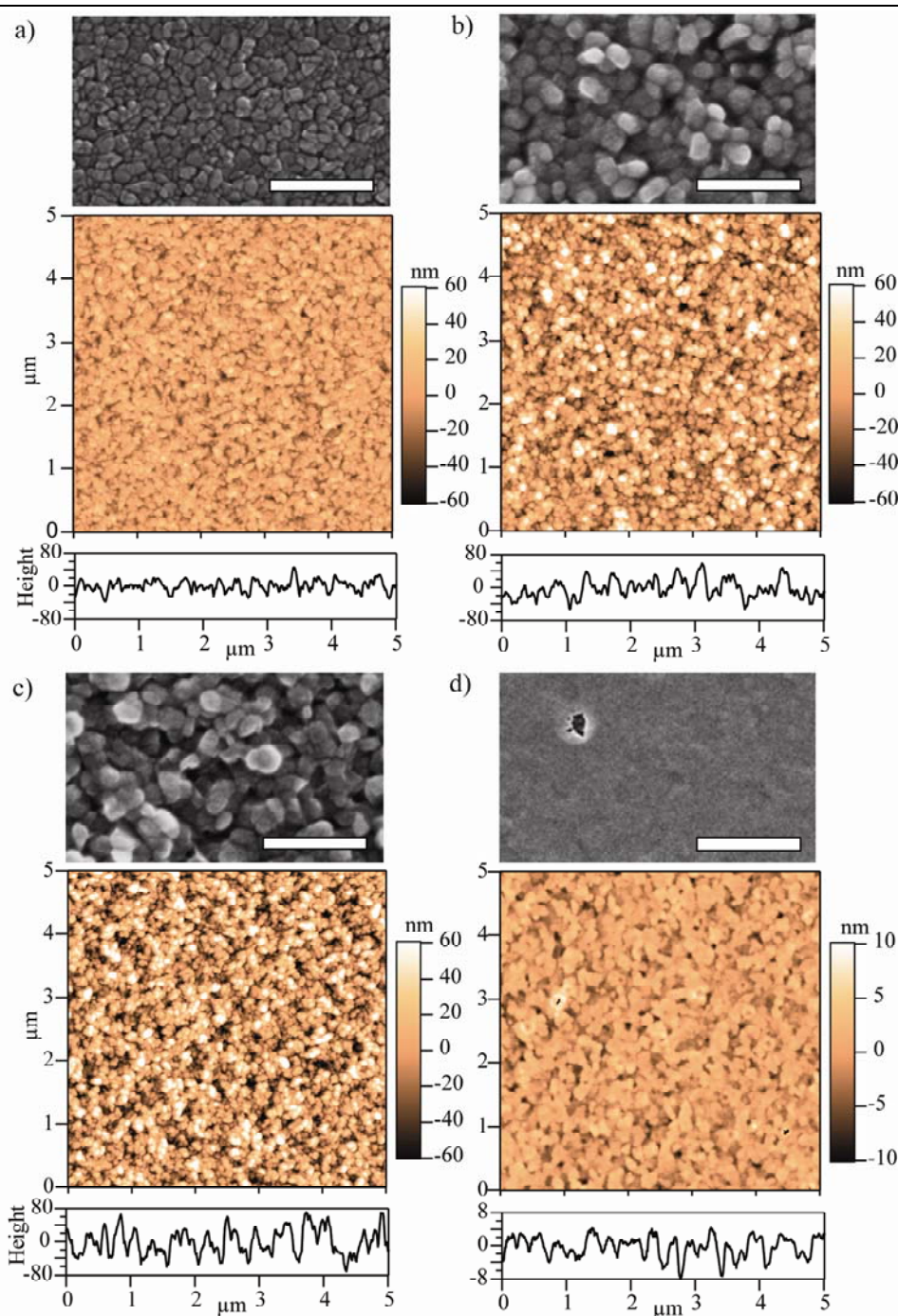


Figure 6.2 Top view FE-SEM and AFM images of the ZnO and TiO_x films: a) SP, b) A-ED, c) B-ED and d) TiO_x, respectively. The images in d) also show the hole inhomogeneities in the TiO_x thin film. Representative AFM height cross-section profiles are also provided. The scale bar in the SEM images is 500 nm in length.

It is evident how the ZnO film roughness increases in going from the SP sample with a surface roughness value R_q of 12.7 nm, to electrochemical deposition with R_q values of 23.7 nm and 27.9 nm for the A-ED and B-ED samples respectively. The SEM images in Figures 6.2b and 6.2c also highlight the different morphologies of the two electrochemically deposited ZnO layers from the SP sample in Figures 6.2a. TiO_x films on the other hand are very smooth with an R_q value of only 2.3 nm compared to 4.4 nm for bare ITO. Most of the TiO_x film is very dense and evens out the ITO surface. The film shows occasional film inhomogeneities such as holes of less than 100 nm in diameter reaching all the way through the film to the ITO substrate which can clearly be seen in Figure 6d. The holes originate from tiny gas bubbles in the wet gel formed during the spin-coating process. A change in roughness from a sintered thin film with an R_q of 2.3 nm to a film without heat treatment with an R_q of only 1.2 nm could be observed. This change hints towards nanocrystal formation in the film although no larger features could be seen in AFM images.

6.3.3 XRD

Additional characterisation of the ZnO films was provided by XRD measurements. The preferential orientation of the films was estimated by calculating the texture coefficients (TC) using Equation 6.1:

$$TC(hkl) = \frac{I(hkl)}{I_0(hkl)} / \frac{1}{n} \sum \frac{I(hkl)}{I_0(hkl)} \quad (\text{Equ. 6.1})$$

$TC(hkl)$ is the texture coefficient of the specific (hkl) plane, $I(hkl)$ is the measured intensity, $I_0(hkl)$ is the relative intensity factor given in the Joint Committee on Powder Diffraction Standards (JCPDS) data, and n is the number of reflections or peaks considered. XRD patterns of the SP, A-ED and B-ED ZnO films are shown in Figure 6.3a. If the films do not show a preferential crystal orientation in the considered direction, $TC(hkl)$ is close to one. For films with a preferential crystal orientation of the grains, $TC(hkl)$ is greater than one. The main diffraction peaks in the XRD pattern have been

fitted with a Gaussian curve to calculate $TC(hkl)$. Figure 6.3b shows the different crystal plane orientations of a ZnO wurtzite-type structure. ZnO crystallises in a wurtzite structure with polar and non-polar faces and the crystal has a polar hexagonal c-axis. A Zn^{2+} ion is surrounded by four O^{2-} ions in a tetrahedral configuration and vice versa.^[115]

The three XRD patterns present strikingly different features in the region centred around $2\theta = 36^\circ$. The corresponding TC values for the ZnO peaks are summarised in Table 6.1. The SP and A-ED films appear to have a more pronounced preferential orientation for the (002) plane ($TC = 4.47$ and 5.56 respectively) than the B-ED type, which has an in-plane (100) preferential orientation ($TC = 2.10$). The polar (002) surface can be either Zn^{2+} or O^{2-} terminated depending on the substrate polarity, growth environment and terminating surface residues such as hydroxyl and hydrocarbon groups. (100) and (110) are non-polar surfaces based on charge neutral Zn-O dimers.^[292] These differences can lead to different affinities with the polymer blend at the inorganic-organic interface and help provide a qualitative explanation for the different performances of the OPV devices fabricated using the three different types of substrates (section 6.3.4).

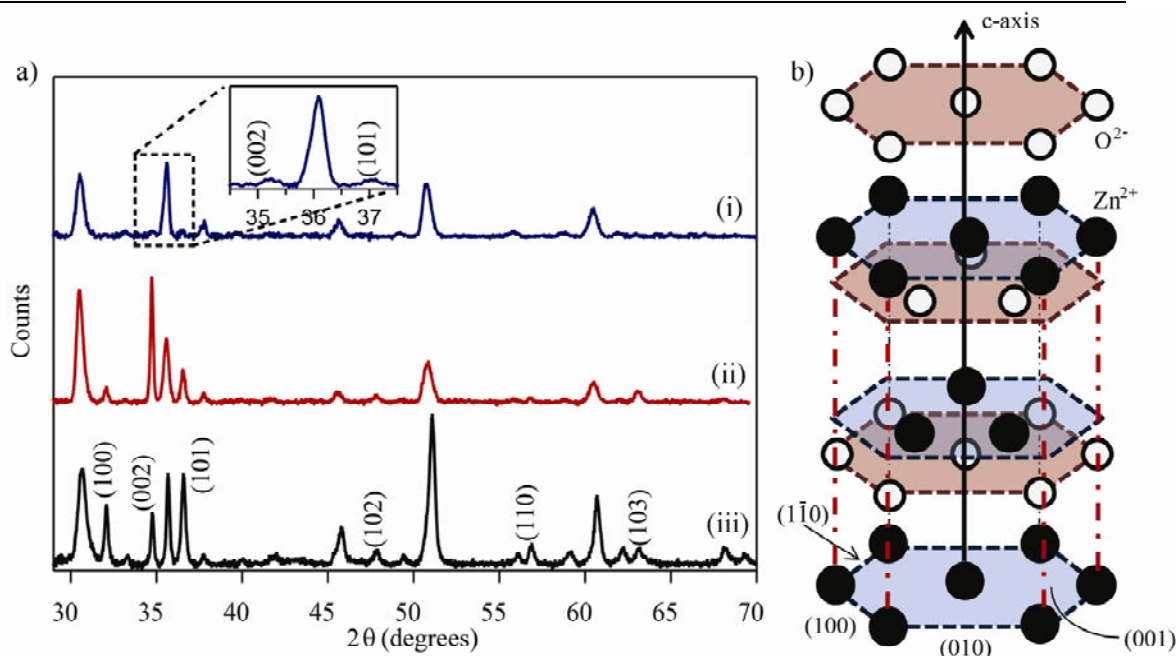


Figure 6.3 XRD patterns of the ZnO films: (i) SP, (ii) A-ED and (iii) B-ED. The inset shows a magnified view of the diffraction pattern (i) between $35\text{--}38^\circ$ obtained with a higher counting time. The ZnO peaks have been indexed using Miller indices (hkl). All other peaks correspond to ITO. b) ZnO wurtzite-type crystal structure.

Table 6.1 TC values for deposited ZnO thin films highlighting the effect of different deposition conditions on the crystal plane orientation using the Miller indices (hkl) respectively.

(hkl)	TC_{SP}	TC_{A-ED}	TC_{B-ED}
(100)	-	0.42	2.10
(002)	4.47	5.56	0.94
(101)	1.52	0.52	1.39
(102)	-	0.71	0.52
(110)	-	0.04	1.23
(103)	-	1.27	0.72
(200)	-	0.00	0.17
(112)	-	0.48	0.98
(201)	-	0.00	0.96

XRD measurements on TiO_x films did not show any characteristic diffraction peaks which could mean that the films were either amorphous or the films were too thin (<50 nm) to detect a distinct signal. The spun precursor gel hydrolyses in air to form a TiO_x network at room temperature. Only sintering above 450 °C leads to anatase or rutile crystal phases. Although the films were sintered at 450 °C (hot plate setting) the films can be assumed to be at least partially amorphous and no distinct anatase phase has been developed. Despite the surface roughening upon sintering no distinct surface or crystal features could be observed. Studies by Kim *et al.* showed good electron mobility of $1.7 \times 10^{-4} \text{ cm}^2 \text{ V}^{-1} \text{ s}^{-1}$ for amorphous TiO_x from sol-gel process sintered at only 150 °C.^[105]

6.3.4 OPV device performance

A schematic of the basic regular and inverted OPV device architectures including electronic energy level diagrams is shown in Figure 6.4. In the regular structure MoO_x and WO_x are replacing PEDOT:PSS, and BCP is inserted as an exciton blocking layer. In the inverted structure ZnO and TiO_x are placed on top of the bottom electrode and MoO_x and WO_x cover the top of the BHJ layer.

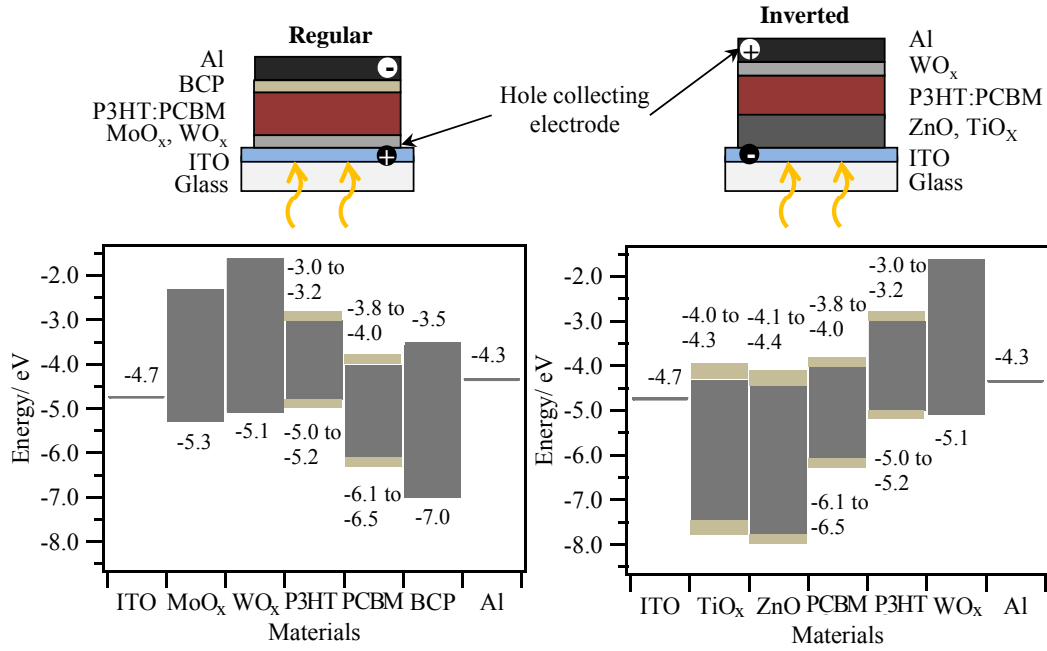


Figure 6.4 Schematic of a regular and an inverted device architecture with the corresponding electronic energy level diagrams below. The light grey bars indicate the range of the reported energy values.

6.3.4.1 TiO_x interlayer thickness optimisation

Figure 6.5 shows the J - V curves of inverted BHJ devices with varying TiO_x interlayer thickness, d , based on an ITO/TiO_x (d nm)/P3HT:PCBM/WO_x/Al architecture. Different film thicknesses were fabricated by varying the spin speed during film deposition of the precursor sol which indirectly relates to film thickness (as shown in the inset of Figure 6.5a).

Spin speeds from 2000 up to 5000 rpm were applied leading to film thicknesses between 43 nm for low speeds down to 20 nm for high speeds. All fabricated devices show good diode behaviour with similar device performance for layers between 29 nm and 43 nm. Only the thinnest TiO_x layer of 20 nm thickness has a reduced J_{SC} which then affects its PCE . An optimum performance was achieved with a 37 nm thick interlayer with a V_{OC} of 0.53 V, a J_{SC} of 10.48 mA cm⁻², a FF of 0.53 and a PCE of 3.12 %. This performance is in good agreement with other reported values of 2.6 %.^[125] The trend is illustrated in Figure 6.5b. The reduction in J_{SC} for thin interlayers can be attributed to current leakage through defects at a partially mixed ITO/TiO_x interface where P3HT and

PCBM are both in contact with ITO. For thicker layers than 37 nm the J_{SC} decreases slightly due to a reduced transmission and increased R_s which both correlate with increasing film thickness.

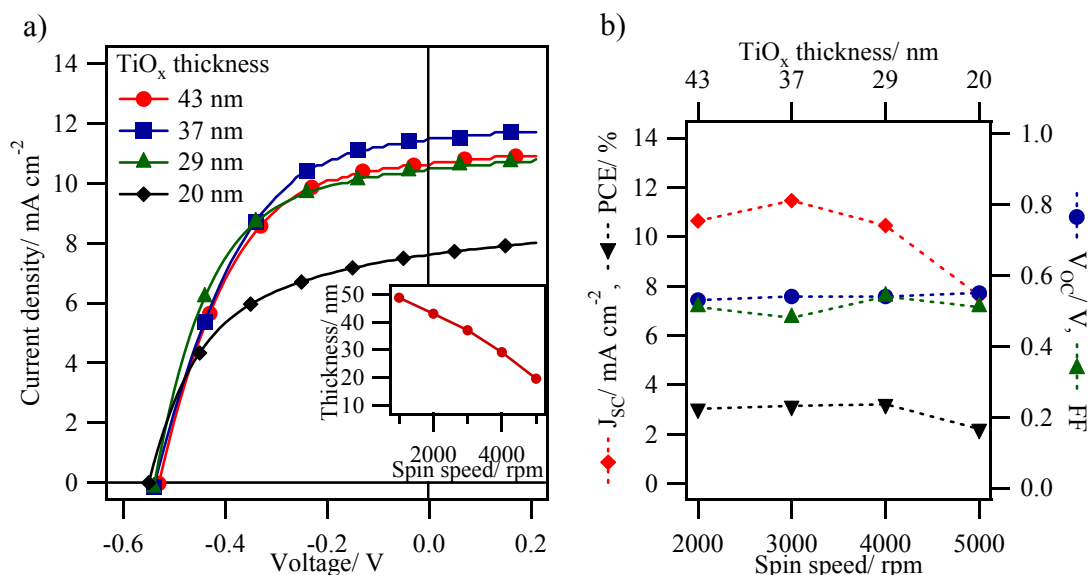


Figure 6.5 J - V curves under 1 sun illumination of inverted OPV devices (ITO/ TiO_x (d nm)/P3HT:PCBM/ WO_x /Al) with different TiO_x interlayer thicknesses d . The inset shows a plot of TiO_x thickness against spin-speed. b) Summarising performance plot of inverted BHJ devices employing different TiO_x interlayer thicknesses.

6.3.4.2 ZnO interlayer devices and comparison of their performance

ZnO interlayers of the three different types; SP, A-ED and B-ED were incorporated in complete inverted BHJ OPV devices following an ITO/ZnO/P3HT:PCBM/ WO_x /Al device structure.

Due to the dramatically increased TMO interlayer film roughness the fabricated devices had to be checked for complete blend infiltration and sufficient surface coverage in order to avoid current leakage through pinholes in the TMO structures. A cross-section of a typical device was prepared by FIB milling before examination by TEM. A protective layer of Pt is deposited onto the surface of the area of interest prior to milling to minimize the damage to the subsurface.

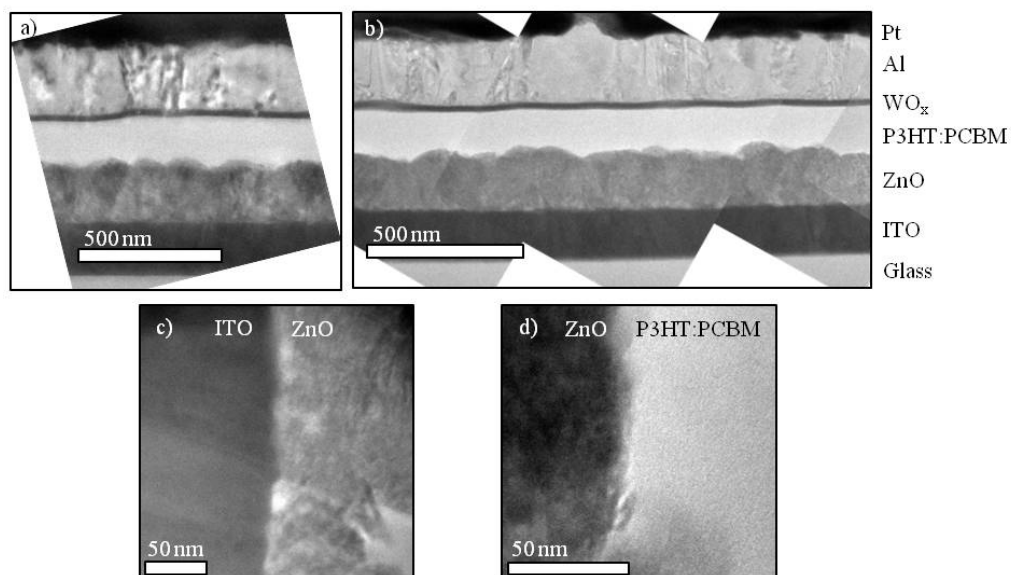


Figure 6.6 Bright field TEM cross-sections of a BHJ OPV device grown on a) the A-ED and b) the B-ED substrate. High-resolution TEM images of different interfaces in the BHJ device (A-ED): c) ITO/ZnO and d) ZnO/P3HT:PCBM.

The montage of bright field TEM images of A-ED and B-ED presented in Figure 6.6 shows that a high quality layered structure has been formed over large areas with relatively sharp interfaces. It is interesting to note that the roughness at the ZnO/blend interface is consistent with the plan view AFM measurements, and that deposition of the blend results in planarisation of the surface before subsequent WO_x deposition. The high resolution interface images in Figure 6.6c-d also prove the completeness of the subsequent layers which are free of any visible voids or defects.

The J - V performance for the different inverted devices based on ZnO and TiO_x interlayers and the regular reference devices are shown in Figure 6.7 with key device parameters summarised in Table 6.2. When the SP ZnO interlayer is used, the devices provide a V_{OC} of 0.48 V, a FF of 0.53, a J_{SC} of 10.03 mA cm^{-2} and a PCE of 2.56 %. This is a significant improvement with respect to the inverted reference device grown without a ZnO layer that gives a V_{OC} of 0.41 V, a FF of 0.50, a J_{SC} of 8.91 mA cm^{-2} and a PCE of 1.76 %, and also gives improved overall performance consistency. Such behaviour highlights the need for the TMO interlayer to achieve considerably higher and more reproducible performance. The inverted devices containing different electrodeposited

ZnO interlayers result in even better performance with a V_{OC} of 0.53 V and a FF of 0.52 for the A-ED device, and a V_{OC} of 0.55 V and a remarkably high FF of 0.66 for the B-ED device. The J_{SC} for the A-ED device was 9.26 mA cm^{-2} , a value slightly lower than that obtained for the devices containing SP (10.03 mA cm^{-2}) and B-ED (10.68 mA cm^{-2}) ZnO with 140 nm blend thickness. The optimised B-ED based device with a 173 nm P3HT:PCBM layer shows a comparable V_{OC} of 0.54 V and FF of 0.65 to the 140 nm B-ED device but a larger J_{SC} of 13.45 mA cm^{-2} and a resulting remarkable (average) PCE of 4.81 % with a maximum of 4.91 %. This is one of the highest reported PCE s for an inverted OPV BHJ device. The efficiency increase originates from the improved light harvesting of the thicker organic active layer.

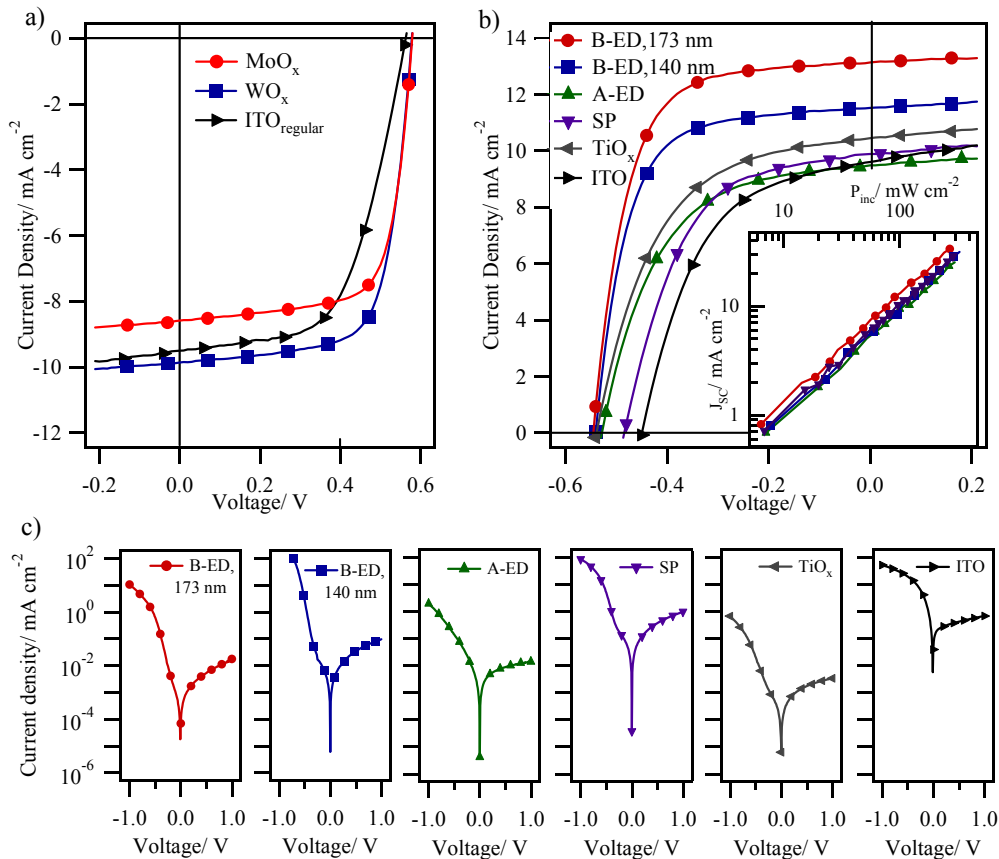


Figure 6.7 J - V curves under 1 sun illumination of a) regular OPV devices and b) inverted OPV devices (ITO/ZnO or $\text{TiO}_x/\text{P3HT:PCBM}/\text{WO}_x/\text{Al}$) with TiO_x and different types of ZnO interlayers including B-ED with 173 nm and 140 nm thick P3HT:PCBM layers, A-ED, SP and bare ITO as a reference. The inset shows a log-log plot of J_{SC} against illumination intensity (P_{inc}) for the device with the TiO_x and A-ED interlayer with 140 nm and the B-ED interlayer with 140 nm and 173 nm thick P3HT:PCBM layers respectively. c) J - V curves under dark condition for all the different inverted devices.

In contrast to the devices incorporating different ZnO interlayers, the device performance of an optimised TiO_x based device shows a similar V_{OC} and FF to A-ED leading to a PCE of 3.12 %.

Regular devices employing either an ITO/MoO_x or ITO/WO_x bottom electrode reached a slightly higher V_{OC} of 0.58 V and an excellent FF of 0.70 compared to the inverted devices as well as a J_{SC} of 8.39 mA cm⁻² and 9.74 mA cm⁻² and a PCE of 3.59 % and 4.15 % respectively. The regular ITO reference device outperforms the inverted ITO reference device with a better V_{OC} of 0.55 V, a J_{SC} of 9.40 mA cm⁻², a FF of 0.54 and a PCE of 2.75 % but is significantly lower in performance and less consistent than those devices containing MoO_x and WO_x interlayers. This highlights the importance and the effect of the hole extracting TMO interlayers in a device with similar effects reported for small molecule based OPVs.^[124, 148]

Table 6.2 Summary of device performance for inverted OPVs based on the ITO/ZnO or TiO_x/P3HT:PCBM/WO_x/Al structure. It also includes the performance summary of inverted and regular reference OPVs. The PCE is quoted as an average value with the highest performance measured in brackets. All devices are labelled with respect to their bottom electrode.

Device structure	V_{OC} [V]	J_{SC} [mA cm ⁻²]	FF	PCE [%]
Inverted architecture				
A-ED, 140 nm P3HT:PCBM	0.53±0.02	9.26±0.77	0.52±0.03	2.55±0.33 (3.26)
B-ED, 140 nm P3HT:PCBM	0.55±0.01	10.68±0.59	0.66±0.01	4.00±0.17 (4.24)
B-ED, 173 nm P3HT:PCBM	0.54±0.01	13.45±0.52	0.65±0.01	4.81±0.13 (4.91)
SP, 140 nm P3HT:PCBM	0.48±0.01	10.03±0.10	0.53±0.01	2.56±0.09 (2.64)
TiO _x , 140 nm P3HT:PCBM	0.53±0.01	10.48±0.09	0.53±0.01	3.12±0.07 (3.21)
ITO, 140 nm P3HT:PCBM	0.41±0.07	8.91±1.59	0.50±0.03	1.76±0.51 (2.23)
Regular architecture				
MoO _x , 140 nm P3HT:PCBM	0.58±0.01	8.39±0.28	0.70±0.01	3.59±0.17 (3.71)
WO _x , 140 nm P3HT:PCBM	0.58±0.01	9.74±0.17	0.70±0.01	4.15±0.05 (4.18)
ITO, 140 nm P3HT:PCBM	0.55±0.01	9.40±0.16	0.54±0.06	2.75±0.43 (3.05)

The general trend of improvement in OPV performance for inverted structures, including the increase in V_{OC} , FF and J_{SC} compared to devices without the TiO_x or ZnO layer, can be partly explained by a more efficient electron extraction mechanism by the TiO_x and ZnO interlayer as a consequence of the high electron mobility in TMOs and better energy alignment of the TMO CB and the PCBM LUMO.^[281]

The energy level alignment between the conduction band of ZnO (-4.1 to -4.4 eV)^[84] and TiO_x (-4.0 to -4.3 eV)^[86, 105] with the LUMO of the PCBM acceptor (-3.8 eV to -4.0 eV)^[86, 105] provides an energy level cascade towards the electron collecting electrode with a more favourable extraction into ITO (-4.7 eV) than when using ITO on its own (see Figure 6.4).^[121, 147] A simple ITO/PCBM contact has an energy mismatch of about 0.7 to 0.9 eV which is clearly non-ohmic leading to losses in V_{OC} due to V_{OC} being dominated by the electrode workfunction rather than the effective band gap. The formation of an ohmic-like contact at the ZnO /blend interface leads to an electrode pinning close to the PCBM LUMO as well as a band bending effect which helps to improve charge extraction.^[80]

Specific differences in J - V performance between the devices containing SP, A-ED and B-ED interlayer based devices most likely originate from the differences in crystal structure of the films. The XRD results suggest a significant difference in the ZnO crystal structure for B-ED films, showing a much less distinct preferential crystal alignment than the well expressed (002) crystal orientation for SP and A-ED (see Table 6.1). As the workfunction of the material within a single crystal varies due to anisotropic density of state distributions for different crystal plane vectors, it is assumed that a more favourable overall workfunction, i.e. closer to the LUMO of the PCBM, is exposed at the ZnO /P3HT:PCBM interface in B-ED devices compared to the preferential polar (002) orientation in SP and A-ED interlayers. This results in an improved ohmic contact leading to a higher J_{SC} and overall device performance. It suggests that highly oriented structures might not be the most suitable ones for efficient electron extraction at the inorganic-organic interface. Furthermore, the FF of SP and A-ED based devices with the preferential polar (002) orientation is reduced by almost 20 % compared to the ones incorporating B-ED with a slight preferential orientation for non-polar surfaces, which could suggest an anisotropic resistivity of the crystals in the film.

In addition to the improved electron extraction characteristics associated with use of the ZnO and TiO_x layer, these TMOs also serve as efficient hole blocking layers providing an energy barrier for hole extraction from the HOMO of the PCBM (-6.1 eV to -6.5 eV) to the ZnO and TiO_x VB (between -7.5 eV and -8.0 eV), as shown in Figure 6.4.^[293] This effect is also reflected in a reduced dark current under reverse bias and an improved V_{OC} which was seen for all devices incorporating a ZnO or TiO_x interlayer except the SP type (see Figure 6.7c).^[293-295] The interlayer also leads to reduced current leakage through an increased R_{SH} and compensates the slight increase in R_S through the additional interlayer.^[280] A possibility to explain the anomaly of the SP interlayer could be the presence of defect states in the bulk structure allowing hole transport through the layer.

Further support for efficient electron extraction and hole blocking by the ZnO and TiO_x interlayers is provided by the light intensity studies shown in the inset of Figure 6.7b. The linear fit of the bi-logarithmic plot of incident light intensity, P_{inc} , against J_{SC} , results in a power-law coefficient γ of 0.97 for A-ED devices, 0.99 for B-ED (140 nm and 173 nm) devices and 0.98 for TiO_x devices, consistent with very low bimolecular recombination.^[296, 297] Even at high light intensities (3 suns) the J - V performance is consistently good. The results for B-ED devices (140 nm and 173 nm) suggest that charge extraction remains very efficient despite the thicker active layer for the optimised device.

Similar to MoO_x and WO_x in regular devices, the ZnO and TiO_x interlayers also provide a more homogenous conducting layer on top of the ITO electrode bridging the inactive or dead spots which prevent efficient charge collection.^[131] Both contributions are reflected in the steep increase in FF from 0.44 without ZnO to 0.66 for B-ED based devices and reduced variation in J_{SC} . For the devices incorporating TiO_x and SP the FF can be reduced by the heat treatment of the sample during or after TMO deposition up to high temperatures of 400 °C and 450°C, respectively which can lead to ITO damage and reduces its conductivity.

From a morphological perspective, an improvement in J_{SC} for ZnO based devices would be expected with an increasing ZnO surface roughness (R_q values of 12.7 nm to 23.7 nm and 27.9 nm for the SP, A-ED and B-ED samples respectively), providing a

larger extraction interface and a more penetrating electrode into the P3HT:PCBM bulk-heterojunction, thus reducing long distance free charge transport. However, no evidence was found to confirm such a direct dependence of R_q and J_{SC} for ZnO based devices. This was further confirmed by the TiO_x based devices showing a comparable J_{SC} despite exposing a very smooth surface ($R_q = 2.3$ nm). Treat *et al.* reported a similar phenomenon for nanopatterned TiO_x interlayers in inverted BHJ where the patterning influence on blend morphology and composition dominated the device behaviour over pure electrode geometry effects.^[298]

D/A phase separation is a crucial factor for efficient BHJ devices which occurs during film deposition, film drying and annealing. Surface morphology and wettability can have a significant impact on the phase separation of the P3HT:PCBM blend influencing vertical (into P3HT richer and PCBM richer layers) as well as bulk phase separation (into larger or smaller domains).^[36, 37, 299, 300] Bulliard *et al.* report an increase in J_{SC} by varying the surface wettability of the ZnO interlayer by employing SAMs whilst keeping the workfunction constant using surface-directed phase separation.^[301, 302] A similar effect could be expected from different crystal phases of polar or non-polar nature found in the different ZnO interlayers. Depending on the phase exposed it can lead to at least local changes in phase separation. In the presented devices the more randomly oriented ZnO film (B-ED) achieves a better performance with a J_{SC} and FF which is somehow inversely proportional to the TC of the (002) plane and could indicate a favourable blend formation on the interface compared to polar surfaces.

For the top electrode the inverted devices are fabricated with a WO_x interlayer that enhances hole extraction towards the Al electrode. Although a workfunction mismatch between P3HT and Al as well as an unfavourable Fermi-level alignment under short-circuit conditions between ITO and Al in the inverted device architecture are assumed, the introduction of the TiO_x , ZnO and WO_x interlayers successfully compensates for these energy alignment problems. This highlights the important role of the TMO sandwich which dominates the contact workfunction and establishes a suitable built-in field to extract charges efficiently. Additionally, the use of WO_x avoids the need for expensive high workfunction metals such as Au or Pd as top metal electrodes.^[125, 303]

The choice of WO_x was further confirmed by the data obtained from the regular devices employing MoO_x and WO_x as a suitable hole extraction layer on the bottom electrode. The J_{SC} of the WO_x and ITO reference device are higher than that of the MoO_x device due to the MoO_x providing a barrier to charge extraction (Figure 6.7a). Hancox *et al.* reported the importance of energy level alignment for a series of small molecules with different HOMO energy levels leading to either enhanced or hindered charge extraction.^[124] Nevertheless, both WO_x and MoO_x based devices clearly show the advantages of a charge extracting TMO interlayer with a much higher PCE and a FF of 0.70 compared to 0.54 for the ITO reference and a much lower variation in performance. Inverted devices further benefit from TMO layers on top of the organic material preventing it from damage during metal electrode deposition.^[304]

6.3.4.3 EQE and operational stability measurements

As a complementary measurement EQE studies carried out on the B-ED devices revealed a very high photon-to-free-charge conversion efficiency of 74.1 % at 508 nm. The normalised EQE profile from 400 to 700 nm reproduces very well the shape of the absorption spectrum of the blend (Figure 6.8a). Again, the rise to such high conversion efficiencies can be qualitatively explained by invoking an improved charge collection mechanism, and consequently a better charge collection efficiency, which is supported by the measured high FF of 0.66.

Stability measurements of the B-ED (140 nm) based and ITO reference devices over continuous 40 hour illumination at 100 mW cm^{-2} under N_2 atmosphere are shown in Figure 6.8c-f. Very little degradation of all key OPV parameters occurs in the B-ED device in comparison to the reference device. The V_{OC} decreased by only 1.7 % for the B-ED device and 34.4 % for the ITO reference device, the J_{SC} by 8.4 % and 20.2 %, and the FF by 8.8 % and 23.5 %, resulting in an overall decline in PCE of 19.3 % and 60.3 % from the original performance of the two devices. For the B-ED device this degradation occurred primarily in the first few hours of illumination. The degradation is more drastic for the reference device showing a more continuous process with particular impact on the V_{OC} .

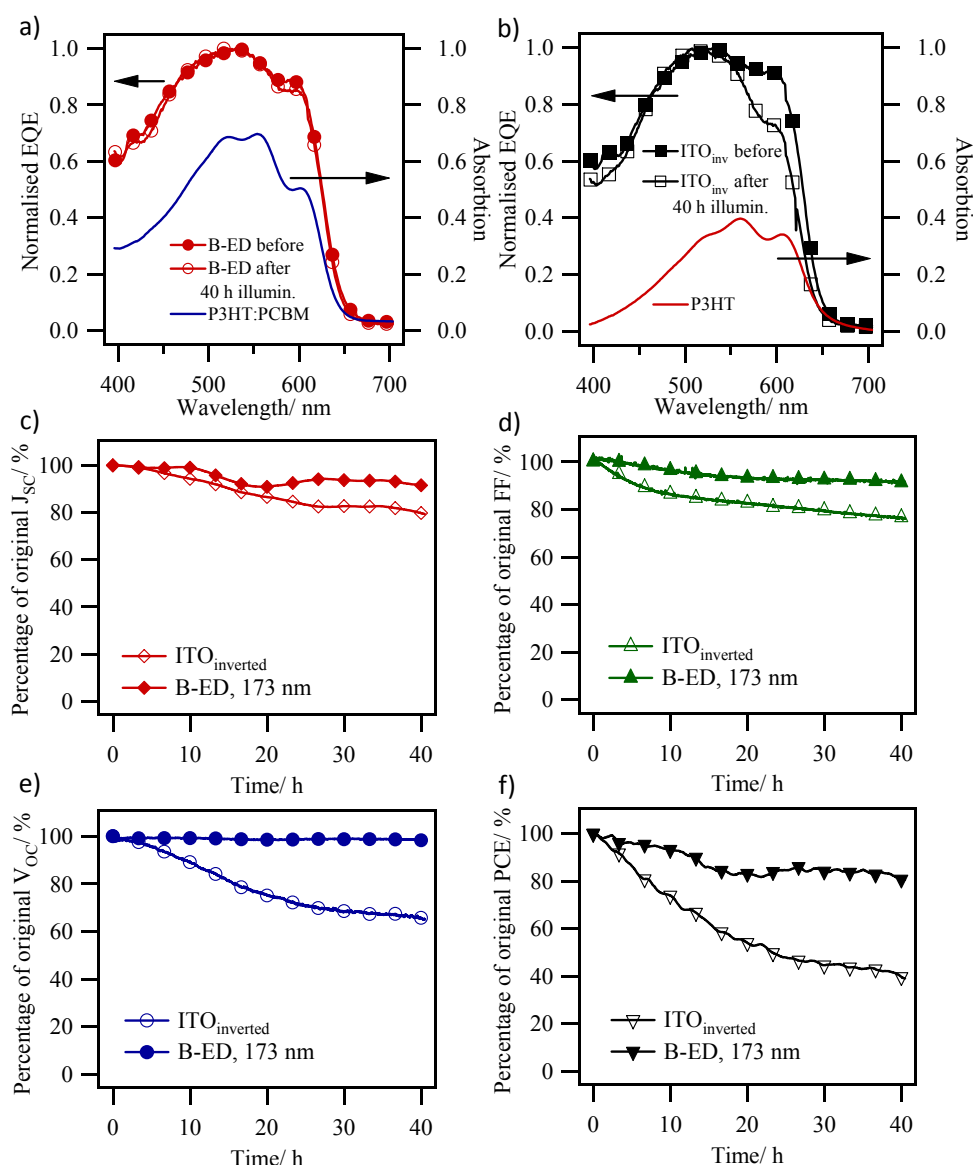


Figure 6.8 Normalised EQE before and after 40 hour constant illumination under N_2 atmosphere for the inverse OPV device fabricated a) with the B-ED interlayer and b) the reference on bare ITO. A comparison of the normalised EQE to a thin film UV/vis electronic absorption spectrum of a) P3HT:PCBM and b) P3HT is also shown. Plots of c) J_{sc} , d) FF , e) V_{oc} and f) PCE as a function of illumination time during continuous light exposure for 40 hours at 100 mW cm^{-2} under N_2 atmosphere for the B-ED and ITO reference device.

The normalised EQE in Figure 6.8a and 6.8b shows a decline in EQE at around 600 nm for the device without ZnO, attributed to P3HT degradation. There is no observable change in EQE profile after the same period of continuous illumination for the device fabricated on B-ED.

The improved device stability with the ZnO and WO_x interlayers is believed to be due to the chemically stable TMO layer sandwich protecting the polymer blend from direct contact with either electrode, i.e. ITO and Al. It is known that fullerenes can react with alkali metals (K₃C₆₀) and a similar reaction is proposed with Al.^[224, 305] Furthermore, the interface of the organic photoactive layer with low workfunction metal electrodes has generally been identified as vulnerable point for the fabrication of OPV devices with long operational life time.^[224] Direct contact of the blend to ITO is known to lead device degradation through various processes including diffusion of oxygen and electrode material into the active layer.^[306, 307]

Illumination can accelerate the oxidation process of the photoactive components resulting in a reduced photocurrent and charge transport which also leads to a lower V_{OC} due to charge build-up interfering with the device built-in field. A specific mechanism is believed to be oxygen activation with UV irradiation which is significantly reduced by the ZnO interlayer with a possible impact on P3HT degradation.^[224] It has to be noted that the process is not well understood and different mechanisms are proposed.^[308, 309]

6.3.5 Conclusions

The introduction of a ZnO or TiO_x interlayer between ITO and the photoactive polymer blend layer in inverted polymer blend BHJ OPV devices significantly improves the device performance compared to devices based on bare ITO. Notably it provides efficient electron extraction based on the formation of an ohmic contact at the ITO/PCBM interface, but also has the ability to successfully block holes. Inverted BHJ OPV devices have the advantages of favourable vertical blend phase segregation of the deposited film with the PCBM rich phase on the bottom electrode, and the use of inexpensive, inert metal oxide interlayers for efficient charge extraction and improved energy level alignment at the interfaces. Optimised device structures employing a B-ED interlayer based on electrochemically deposited ZnO with a WO_x interlayer on the opposite electrode achieved a remarkable maximum *PCE* of up to 4.91 %, an *EQE* of 74 %, as well as good operational device stability based on the TMO sandwich structure. Especially for ZnO interlayers, film roughness and preferred crystal orientation of the

grains embedded in the film seem to have a great influence on the device performance. Electrodeposition of ZnO in particular is shown to be a very promising thin film growth technique for electrode modification providing good control over layer thickness, nano and micro thin film morphology, as well as crystal orientation for favourable charge extraction and surface structure modification. This deposition technique has several important advantages over other more common ZnO and TiO_x thin film growth processes, with considerable potential for scalability to large areas.

Chapter 7: Planar inorganic/organic hybrid devices

This chapter covers the development and optimisation of inorganic/organic hybrid OPV devices with inverted architectures employing TMOs such as ZnO and TiO_x as electron acceptor material which substitutes commonly used fullerenes. Apart from the polymeric donor P3HT, a new device concept based on small molecules such as SubPc is successfully demonstrated proving a working hybrid A/D interface concept. The thin films and device characterisation involves comprehensive techniques such as UV/vis, AFM as well as *J-V* and *EQE* measurements to develop a deeper understanding of the hybrid A/D interface. Additional studies compare TiO_x/SubPc inverted hybrids to regular SubPc/C₆₀ devices using *EQE* to confirm sufficient exciton dissociation at the hybrid interface.

7.1 Introduction

7.1.1 Background of TMO/organic hybrid OPVs

There have been developments in replacing the fullerene with TMOs such as ZnO and TiO_x as electron acceptors, with polymer donors, to develop hybrid inorganic/organic A/D heterojunctions with the potential of improved device stability and electron mobility (see also section 1.4.3).^[117, 152] Inorganic acceptor materials based on TMOs do not contribute to the device photocurrent because of their transparency in the visible range. Energy alignment problems and polymer crystallinity disorder at the A/D interface are the main causes for the low performance, although improvements can be made by interface engineering through insertion of SAMs between the TMO and P3HT.^[153, 310]

The substitution of the polymer by different donor materials such as small molecule organic semiconductors offers an alternative means of improving the

performance of hybrid OPV devices. Surprisingly, there have been few reports of the use of these types of materials in a proper A/D hybrid cell, the exception being the demonstration of CuPc as a sensitiser in a ZnO/CuPc/P3HT device.^[311]

A new type of inverted planar hybrid OPV device is based on the small molecule organic semiconductor SubPc (molecular structure see Figure 1.7d in Chapter 1) in combination with a TiO_x acceptor layer. SubPc has been utilised successfully by a number of groups in conventional D/A OPV cells.^[99, 101, 312] It has a longer L_D than P3HT, typically a few tens of nanometres compared to <10 nm for P3HT, as well as a high absorption coefficient and improved light harvesting at longer wavelengths. Films can be deposited in a highly controlled way using OMBD. The molecule SubPc also provides the basis for different substituted and functionalised derivatives where the energy levels of the molecule can be shifted to larger HOMO and LUMO energy levels by intelligent halogenation.^[100]

7.1.2 Aim

The aim of this chapter is to develop inverted planar hybrid OPV devices employing organic materials such as polymeric P3HT and small molecular SubPc as electron donors and inorganic TMOs such as TiO_x and ZnO as acceptors. The films and devices are characterised and compared in structure, morphology and OPV device performance using UV/vis electron absorption spectroscopy, AFM, SEM, J - V device analysis and EQE . A particular focus of the work is on the novel TiO_x/SubPc hybrid device type, which was further optimised. The TiO_x/SubPc hybrids are also compared to regular fullerene based SubPc/C₆₀ devices to develop a deeper understanding of the inverted hybrid A/D interface and differences between the two OPV device systems. In a further step the hybrid device stability is assessed in different atmospheres under illumination to characterise the influence of UV light exposure on the device stability. The development of such a planar hybrid device serves as a model system to explore the possibility of TMO based 3D open-cellular nanostructures from nanosphere templating for hybrids as demonstrated for organic composite OPVs in Chapters 5.

7.2 Experimental

All devices were fabricated on ITO-coated glass substrates. The titanium oxide precursor solution based on titanium isopropoxide was prepared as described in section 2.1.3.2. The solution was spin-coated onto ITO substrates at 3000 rpm for 1 min followed by drying at room temperature for 30 min and calcination in air at 450°C for 120 minutes. The ZnO film was prepared by spray pyrolysis (SP) as described in Chapter 6.

P3HT was spin-coated on TMO samples from a solution of 10 mg mL⁻¹ in dichlorobenzene at 1000 rpm. SubPc, MoO_x, WO_x, C₆₀ and Al were vacuum evaporated onto either prepared ZnO, TiO_x or bare ITO substrates using an OMBD system with film thicknesses of 14 nm to 34 nm for SubPc, 5 nm for MoO_x, 10 nm for WO_x, 40 nm for C₆₀ and approximately 100 nm for Al respectively. Al electrodes were deposited *in-situ* through a shadow mask defining the active area to 0.16 cm².

J-V measurements of OPV devices were carried out in a sealed sample holder under nitrogen atmosphere. Operational stability measurements for extended testing times of up to 1 hour of constant light exposure were carried out with and without an optical filter blocking UV light, with a transmission window of about 90 % in the visible range starting sharp at 400 nm. Further device analysis involved *EQE* measurements. Thin film analysis included UV/vis absorption spectroscopy and morphology studies performed by AFM.

7.3 Results and discussion

7.3.1 Electronic absorption and transmission

The sol-gel process allows to fabricate very thin TiO_x films of about 30 nm in thickness which demonstrate good transparency in the visible range of the spectrum (90% transmittance at 600 nm) as can be seen in Figure 7.1. The ZnO (SP) film of 50-70 nm in thickness shows a similar transparency window but has a reduced transparency at 600 nm of about 80 % which overlaps with the P3HT and the SubPc absorption spectra and could therefore compromise the OPV photocurrent performance. With an absorption spectrum onset at ~360 nm ZnO acts partially as a UV light filter which may protect the

photoactive materials such as SubPc and P3HT from damage.^[116] For TiO_x the onset is around 310 nm which provides a slightly larger absorption window for P3HT and SubPc but also allows more UV light penetration.

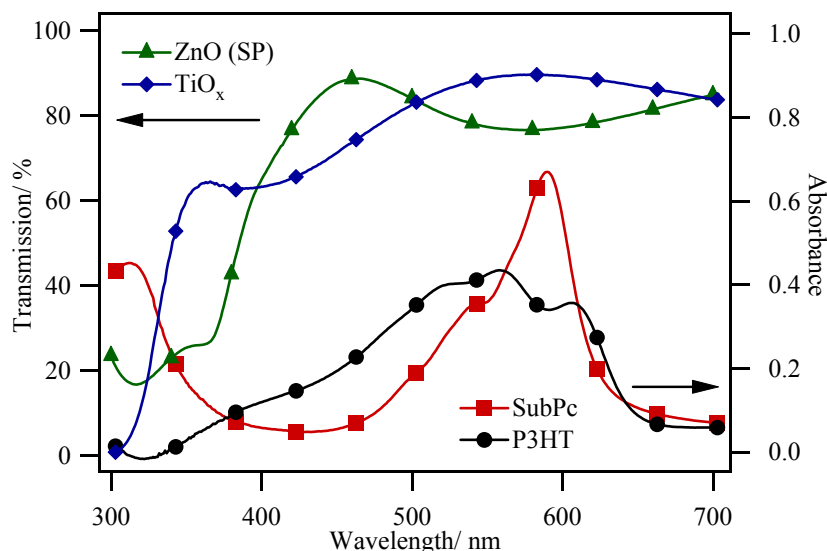


Figure 7.1 Transmission spectra of a ZnO film from spray pyrolysis (SP) and TiO_x film from sol-gel process deposited on ITO in comparison to the absorption spectra of a P3HT and a SubPc thin film.

7.3.2 Morphology

The AFM images in Figure 7.2 show TiO_x thin films in different stages of the thin film and device fabrication process as well as bare ITO for comparison. The R_q roughness value of the TiO_x thin film increases from 1.2 nm to 2.3 nm with calcination of the film at 450 °C. The surface only shows a minor smoothening upon SubPc deposition with an R_q of 2.2 nm. The small holes in the TiO_x film are defects which originate from the initial sol spinning process as they appear already in the untreated spun film. The holes are narrow but probably penetrate the entire film. A possible cause can be tiny gas bubbles in the initially applied sol film. The holes increase in size with temperature treatment and are also present in the SubPc film which follows closely the underlying TiO_x film morphology. Such pin holes can lead to a disturbed A/D interface and current leakage due to direct contact of the organic layer to the ITO.

Overall the low R_q of 2.3 nm is an improvement over the typical roughness of bare ITO electrodes ($R_q \sim 4.4$ nm). The TiO_x acceptor layer therefore provides a smooth surface for subsequent deposition by OMBD of the planar SubPc donor layer or spin-coated P3HT.

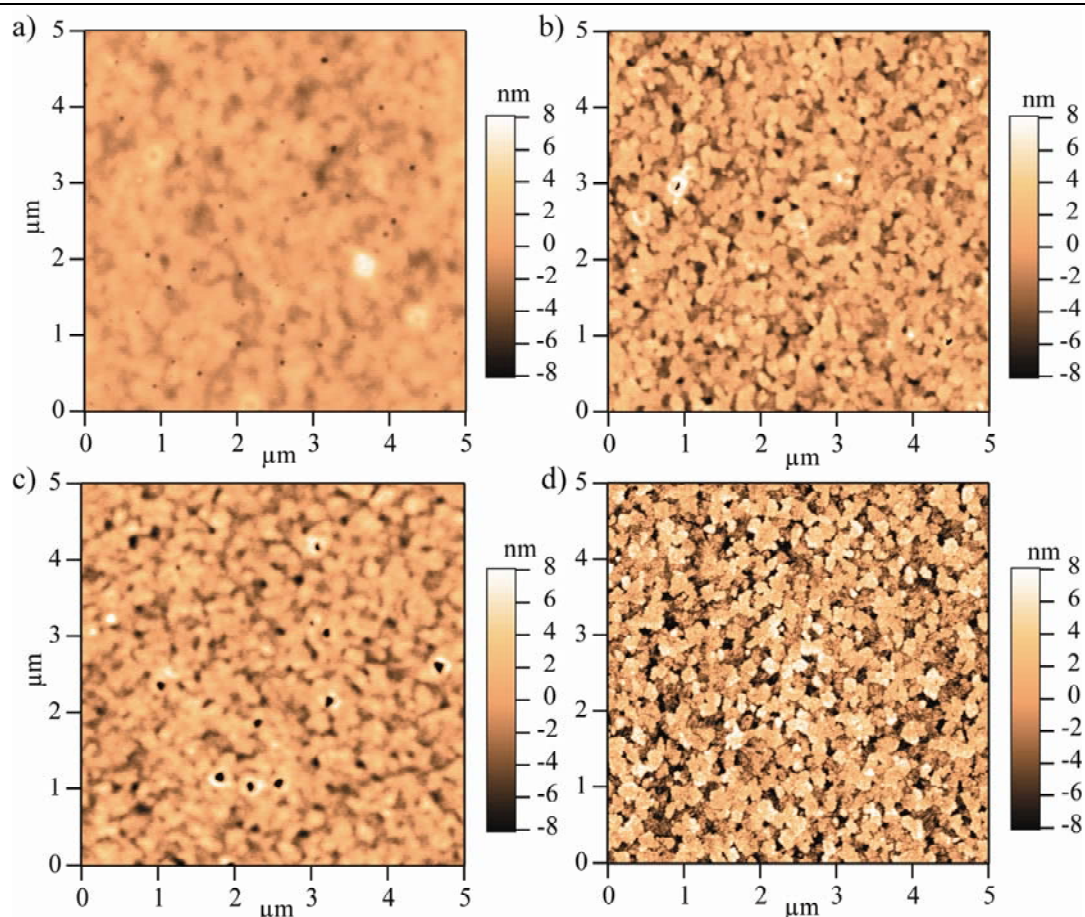


Figure 7.2 Top view AFM images of TiO_x films in different stages of the film and device fabrication process: TiO_x a) before and b) after calcination at 450 °C, c) covered by a SubPc thin film (32 nm) and d) bare ITO as a comparison.

As already shown in Chapter 6 the ZnO film fabricated from spray pyrolysis (SP) is much rougher with R_q values of 12.7 nm. It is most likely that such a high R_q roughness value coupled with only 28 nm of vacuum deposited SubPc would lead to a disturbed A/D interface. This is the reason why ZnO/SubPc devices were not considered for

fabrication in this study, but are subject to further work. Further data including SEM and XRD of TiO_x and ZnO thin films are shown and discussed in Chapter 6.

7.3.3 OPV device performance

Figure 7.3 shows schematics of both inverted hybrid and regular OPV devices including their energy level diagram. The inverted hybrids are based on either ITO/TMO/P3HT/ WO_x (10 nm)/Al employing both TiO_x in device (A) and ZnO in device (B) as an electron acceptor or ITO/ TiO_x /SubPc (d nm)/ MoO_x (5 nm)/Al with varying SubPc film thickness d . The SubPc based devices have film thicknesses d of 14 nm for device (C), 20 nm for device (D), 28 nm for device (E), 30 nm for device (F), 32 nm for device (G) and 34 nm for device (H). The control device (N) does not employ any TiO_x to emphasise the role of TMOs as efficient electron acceptors: ITO/SubPc (28 nm)/ MoO_x (5 nm)/Al. The layer thicknesses of MoO_x (5 nm) and WO_x (10 nm) were adapted from Chapter 6.^[121, 124]

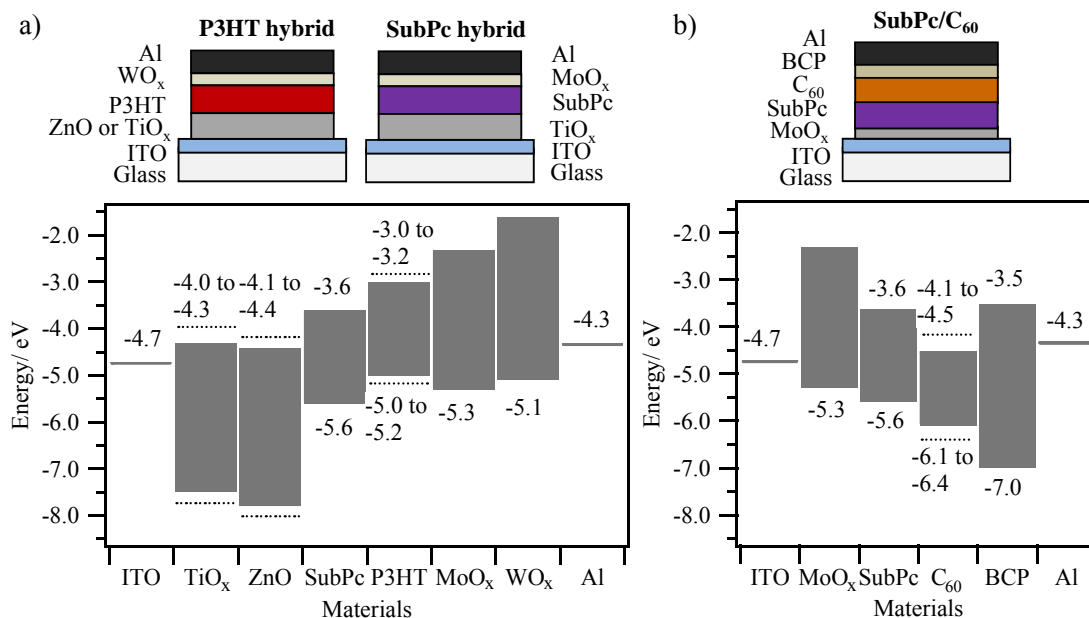


Figure 7.3 Schematic of a) inverted hybrid OPV device architectures employing P3HT and SubPc as an electron donor as well as b) a regular fullerene based OPV device architecture with the corresponding electronic energy level diagrams below. The dotted lines in the energy level diagrams indicate the range of the literature values.

The regular OPV devices follow a commonly used ITO/MoO_x/SubPc (*d* nm)/C₆₀/BCP/Al device structure with *d* being 14 nm and 28 nm thick for device (O) and (P) respectively. Devices (O) and (P) both serve as references as a comparison to TiO_x/SubPc hybrid devices in order to highlight similarities and differences of the two different device types.

Figure 7.4 shows the *J-V* curves of planar inverted hybrid P3HT and SubPc devices under illumination demonstrating the two hybrid systems which are considered and compared in this study. The P3HT devices (A) and (B) in Figure 7.4a show a considerable device performance difference between ZnO and TiO_x based hybrids. With a *J*_{SC} of 0.35 mA cm⁻² and 0.91 mA cm⁻², a *V*_{OC} of 0.29 V and 0.43 V, a *FF* of 0.40 and 0.55 as well as a *PCE* of 0.04 % and 0.22 % for P3HT devices (A) and (B), the TiO_x based device (B) demonstrates a much better performance than the ZnO based device (A).

Figure 7.4b shows the *J-V* curves of planar inverted hybrid OPV devices of device (E) with an optimised SubPc layer thickness of 28 nm and reference device (N). With a *J*_{SC} of 1.75 mA cm⁻², *V*_{OC} of 0.56 V, a *FF* of 0.40 and a *PCE* of 0.40 %, the device with the TiO_x acceptor (E) outperforms significantly the reference device (N), which only shows a *J*_{SC} of 0.50 mA cm⁻², a *V*_{OC} of 0.44 V, a *FF* of 0.26 and a *PCE* of 0.06 %.

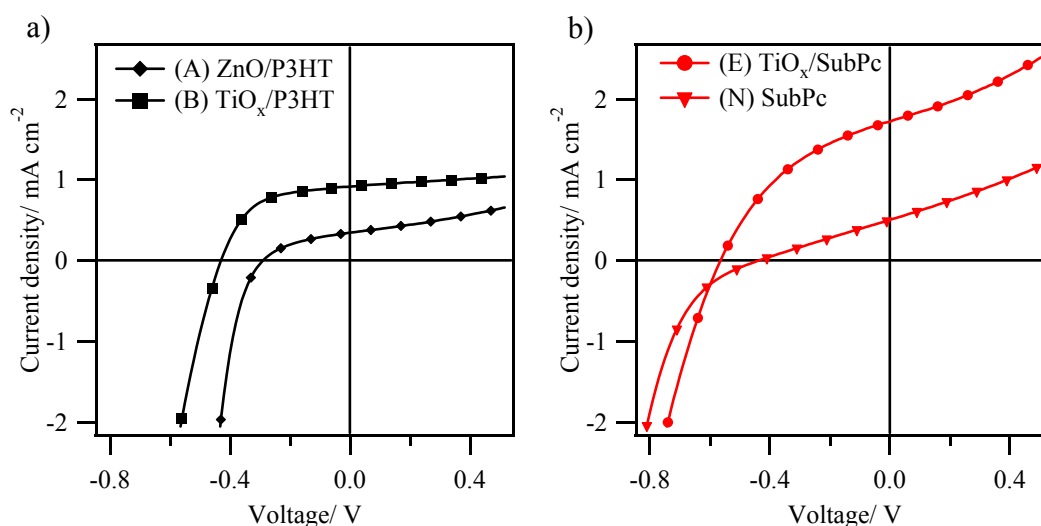


Figure 7.4 *J-V* curves under 1 sun illumination of inverted hybrid OPV devices based on a) TMO/P3HT devices (A) and (B) as well as b) TiO_x/SubPc device (E) and SubPc reference device (N).

The film thickness optimisation trends and J - V curves of SubPc are shown in Figure 7.5. The general trend of the J_{SC} starts at 0.92 mA cm^{-2} for device (C) with a steady increase towards device (E) where it peaks with 1.75 mA cm^{-2} followed by a steep decrease in current performance towards 0.76 mA cm^{-2} for device (H). The V_{OC} reveals a tendency to increase from 0.52 V for device (C) to 0.70 V and 0.68 V for devices (G) and (H) with minor fluctuations in between. The FF was found to be 0.32 for device (C) with an increase to a steady value between 0.36 to 0.40 for devices (D) to (G) and a drop to 0.25 for device (H). The same trend as found for J_{SC} is seen for the PCE with 0.16% for device (C), an increase towards device (E) with 0.40% and steep drop towards device (H) with a PCE of only 0.14% . Overall a 28 nm SubPc layer as employed in device (E) was found to be the optimum thickness which was used for any further studies. All data of devices (A) to (H) and (N) to (P) are summarised in Table 7.1.

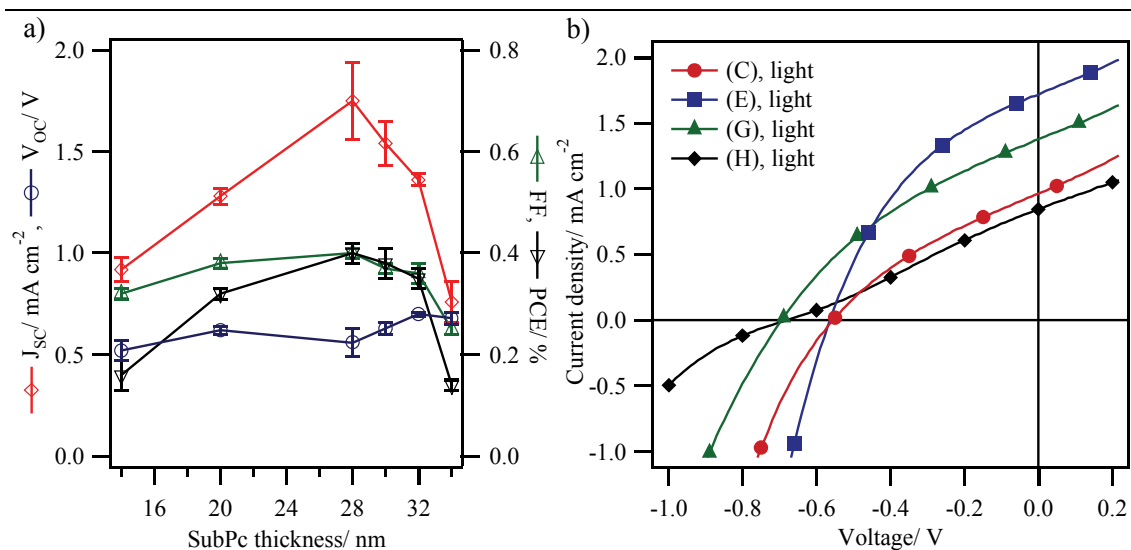


Figure 7.5 a) Summary of performance parameters for devices (C) to (H), including J_{SC} , V_{OC} , FF and PCE , with varying SubPc layer thickness d . b) J - V curves under 1 sun illumination of inverted SubPc hybrid OPV devices (ITO/TiO_x/SubPc (d nm)/MoO_x/Al) with different SubPc layer thicknesses d .

Table 7.1 Summary of device performance for inverted hybrid devices including devices (A) and (B) (ITO/TMO/P3HT/WO_x/Al) employing both TiO_x and ZnO, devices (C) to (H) (ITO/TiO_x/SubPc (*d* nm)/MoO_x/Al) with varying SubPc film thickness *d*, SubPc reference device (N) and regular fullerene devices (O) and (P).

Device	V_{OC} [V]	J_{SC} [mA cm ⁻²]	FF	PCE [%]
(A) ZnO (SP)/P3HT	0.29	0.35	0.40	0.04
(B) TiO _x /P3HT	0.43	0.91	0.55	0.22
(C) TiO _x /SubPc (14 nm)	0.52	0.92	0.32	0.16
(D) TiO _x /SubPc (20 nm)	0.62	1.28	0.38	0.32
(E) TiO _x /SubPc (28 nm)	0.56	1.75	0.40	0.40
(F) TiO _x /SubPc (30 nm)	0.63	1.54	0.37	0.38
(G) TiO _x /SubPc (32 nm)	0.70	1.36	0.36	0.35
(H) TiO _x /SubPc (34 nm)	0.68	0.76	0.25	0.14
(N) SubPc (28 nm)	0.44	0.50	0.26	0.06
(O) SubPc (14 nm)/C ₆₀	1.12	4.53	0.43	2.18
(P) SubPc (28 nm)/C ₆₀	1.14	4.00	0.26	1.21

The difference in performance of the two P3HT based hybrid devices (A) and (B) employing both inorganic electron acceptor materials, ZnO and TiO_x, can be attributed to different factors. In both cases a sufficient energy level offset between the LUMO of P3HT and the CB of TiO_x and ZnO of >1.1 eV at the A/D interface provides the potential energy to overcome the exciton binding energy as can be seen in Figure 7.3 a. The energy offset between the P3HT HOMO and the TMO CB, which to a first approximation limits the maximum achievable V_{OC} , is about 0.1 eV larger for the TiO_x/P3HT interface and is reflected in the collected V_{OC} data. The FF for device (A) is lower due to the very rough ZnO surface where pinholes cause a lower R_{SH} and result in current leakage. This is also reflected in the shape of the J - V curve of device (A) under positive bias (Figure 7.4 a). Despite the pinholes in the TiO_x layer (see AFM images in Figure 7.2) the solution processed P3HT smoothens the defects and leads to a higher FF for device (B). One of

the biggest differences between the two types of device is the J_{SC} , which is significantly higher for TiO_x based device (B) compared to device (A). Although it could be assumed that a film with a significantly higher R_q roughness value, i.e. a built-in nanostructured interface, as in device (A) would lead to a higher J_{SC} compared to a very smooth interface in device (B), the opposite was found. For polymer based hybrid OPVs energy alignment mismatch between donor and acceptor as well as polymer crystallinity disorder at the A/D interface are believed to be the main causes for the low performance.^[153] A recent study revealed that the P3HT crystallinity shows chain disorder in close proximity (<6 nm) to the ZnO surface due to unfavourable surface bonding chemistry of sulphur and zinc leading to amorphous P3HT with low PV performance.^[313] By decoupling the two interface materials P3HT and ZnO through selective SAM insertion the problem can be tackled, which leads to device performance improvements with a particular increase in J_{SC} .^[310] It is assumed that such a specific surface phenomenon does not occur for TiO_x which can therefore provide a better interface to enable the vital P3HT crystallisation at the A/D interface which is reflected in the higher J_{SC} in this experiment.

In the TiO_x based device (E) P3HT is exchanged by the small molecule SubPc. This leads to a doubling of the *PCE* performance based on a significantly improved J_{SC} compared to device (B) and demonstrates the potential of SubPc as an alternative hybrid donor. A second comparison of device (E) to reference device (N) without TiO_x (Figure 7.3 b) shows clearly the suitability of TiO_x as an inorganic electron acceptor in these hybrid cells. In fact, device (E) provides an almost seven-fold increase in performance compared to (N), which is a simple Schottky-like SubPc reference device. This result undoubtedly demonstrates the significant potential of SubPc as a viable small molecule electron donor material in combination with TiO_x in a hybrid OPV device. The results for device (E) also demonstrate that TiO_x /SubPc hybrids are comparable to the best performing TMO/polymer hybrid devices, with significantly better currents than the majority of planar and even nanostructured hybrids reported in the literature.^[140, 141, 153, 314]

SubPc layer thickness optimisation experiments showed that with increasing SubPc thickness from 14 nm in device (C) to 34 nm in device (H) the J_{SC} peaks at 28 nm for device (E). The trend shape of the current development with a steady increase towards

the optimum thickness followed by a steep drop for thicker layers supports the argument of a device limitation by L_D of SubPc for thicker layers (Figure 7.5 a). With additional SubPc thickness from 14 nm to 28 nm the J_{SC} shows a nearly linear increase in J_{SC} which is consistent with known estimates of L_D at the higher end of the reported range. L_D is generally thought to be approximately 8 nm to 28 nm depending on the literature.^[67, 68] The trend of J_{SC} is also reflected in the summarising PCE with a similar trend line. For this type of device, a remarkable J_{SC} of 1.75 mA cm^{-2} and the resulting PCE of 0.40 % for the optimised device (E), based on the new organic small molecule donor SubPc, state a great performance for a planar hybrid OPV device, significantly outperforming the P3HT based hybrid device (B).

The suitability of the TiO_x /SubPc combination is also confirmed by the energy levels between the LUMO of SubPc at -3.6 eV with the CB of TiO_x at between -4.0 eV and -4.3 eV, which provides an energy offset of 0.6 eV to 0.9 eV at the A/D interface. This energy difference is high enough to overcome the exciton binding energy and leads to efficient exciton dissociation (see Figure 7.3a). The relatively deep SubPc HOMO at -5.6 eV compared to P3HT also results in a higher V_{OC} than for similar devices employing P3HT as the donor, which has a higher HOMO at -5.0 eV to -5.2 eV. In addition to their good electron mobility, TiO_x and ZnO act as efficient hole blocking layers due to their very deep valence bands which are located between ca. -7.5 eV and -8.0 eV.^[293] At the opposite side of the device, where the Al hole collecting top electrode is located, the MoO_x interlayer acts both as a hole extractor, due to its good energy level alignment with the SubPc HOMO, and also protects the sensitive organic SubPc layer from damage during deposition of the Al electrode. Similarly, WO_x with a 0.2 eV lower CB than MoO_x is used on top of P3HT to provide a better match to the P3HT HOMO at -5.0 eV.

7.3.4 EQE and device structure comparison

Figure 7.6 shows a comparison of the EQE spectra of device (E) with a maximum of 20.1 % and device (N) with a maximum of 4.8 % at approximately 588 nm and also the EQE spectra of the two fullerene based regular OPV devices (O), employing a SubPc

layer of 14 nm, with a maximum of 27.7 % at 584 nm and (P), employing a SubPc layer of 28 nm, with a maximum of 19.9 % at 572 nm for OPV device type comparison.

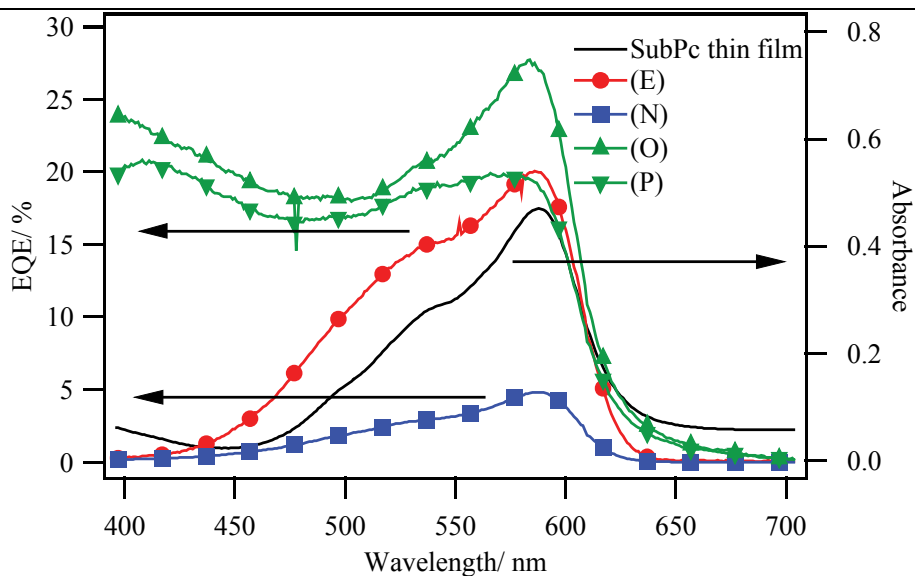


Figure 7.6 EQE spectra of inverted hybrid OPV device (E) and the reference device (N), as well as the EQE of fullerene based devices (O) and (P) with a SubPc layer thickness of 14 nm and 28 nm respectively. It also shows a comparison of the EQE to a thin film UV/vis electronic absorption spectrum of a SubPc thin film.

The EQE of device (E) is similar to some reported values for SubPc/F₁₆CuPc,^[110] and matches the SubPc contribution towards the EQE of the fullerene based device (P) with an equivalent SubPc layer thickness, but is lower than a well optimised SubPc/C₆₀ device (O). When compared to the reference device (N) the more than four-fold increase in EQE and more than three-fold increase in J_{SC} of device (E) is high enough to confidently discard a purely Schottky-like behaviour, indicating TiO_x as an efficient electron acceptor. Both hybrid device EQEs match the thin film UV/vis absorption spectrum of SubPc suggesting that the SubPc layer is the dominant contributor to the photocurrent. The EQE of the fullerene based devices have their maxima in the same spectral range as the SubPc but additionally reveal a high EQE response at lower wavelengths matching the C₆₀ absorption, and therefore show higher current contribution. In SubPc/C₆₀ both components significantly contribute to the photocurrent leading to J_{SC} values of 4.53 mA cm⁻² and 4.00 mA cm⁻² for devices (O) and (P) respectively (see Table

7.1). The D/A interface provides ideal energy offsets for exceptionally high V_{OC} values above 1.1 V as can be seen in the energy level diagram in Figure 7.3b. For SubPc/C₆₀ devices with regular device architecture the SubPc thickness in device (O) was found to give the highest EQE and current contribution at only 14 nm. Although (P) provides the double SubPc layer thickness for increased absorption, the actual J_{SC} contribution in the EQE is significantly reduced. This behaviour could be explained by a compromise between absorption, L_D and film resistance assuming a relatively short L_D . However, when compared to inverted TiO_x/SubPc hybrid devices the optimum is shifted to thicker SubPc layers generating the highest currents. A possible explanation for this different behaviour is the fundamental change in device architecture from regular to inverted devices which changes the cell geometry including the position of the SubPc layer with the highest exciton density in relation to the D/A and A/D interface respectively. In a regular SubPc/C₆₀ device L_D has a larger influence on the device performance because the majority of excitons is generated close to the ITO and the SubPc film thickness sets the average travelling distance for excitons within the donor layer to the D/A interface. In a TiO_x/SubPc device the majority of excitons created by the incoming photons are generated in close proximity to the A/D interface which makes this type of device less dependent on L_D . Thicker layers may still contribute to the photocurrent but do not increase the average exciton travel path for the majority of created excitons.

7.3.5 Device stability

Figures 7.7a-d show the change of key J - V characteristics during an operational lifetime study of SubPc hybrid device (E) under continuous light exposure for 1 hour at 100 mW cm⁻². A summary of device performance changes under constant illumination for device (E) in nitrogen atmosphere comparing the impact of an optical UV filter with cut-off at 400 nm can be found in Table 7.2.

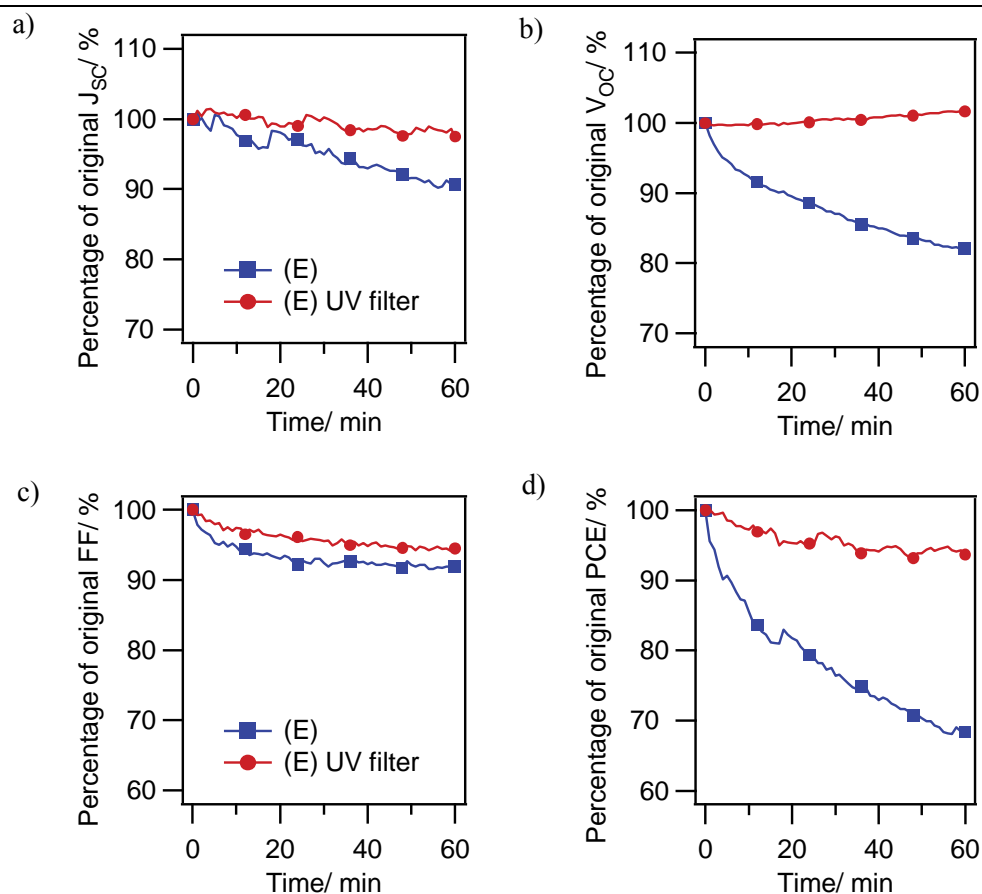


Figure 7.7 a-d) Plots of key device characteristics as a function of time for device (E) during continuous light exposure for 1 hour at 100 mW cm^{-2} under N_2 atmosphere with and without a UV filter in the incident beam.

Table 7.2 Summary of percentage device performance changes under constant illumination at 100 mW cm^{-2} for 1 hour and 4 hours under nitrogen atmosphere comparing the impact of an optical UV filter with cut-off at 400 nm for ITO/ TiO_x /SubPc device (E).

Device (E)	V_{OC} [%]	J_{SC} [%]	FF [%]	PCE [%]
In N_2 , 1h	-18.0	-9.4	-8.0	-31.7
In N_2 , UV-filter, 1h	-1.6	-2.5	-5.5	-6.3
In N_2 , UV-filter, 4h	-6.4	-8.8	-8.3	-11.1

There is a significant performance loss in V_{OC} when exposed to the entire solar spectrum and this results in a PCE drop of about 30 %. By using an optical UV filter the V_{OC} remains very stable resulting in significantly reduced PCE degradation of about 6 %, which mainly occurs in the first 20 min. A steady performance for longer exposure times is seen with only 11 % PCE reduction over 4 hours as shown in Table 7.2.

A possible explanation for the reduction in V_{OC} is a shift in the electronic energy level offset, i.e. a lowering of the TiO_x CB. Schmidt *et al.* found that under UV light irradiation the workfunction of TiO_x and TiO_2 changed due to desorption of oxygen species, showing a shift from higher to lower work functions as much as 0.46 eV.^[315] This shift moves the Fermi level of TiO_x closer to its CB whilst keeping the Fermi level alignment with SubPc. This results in a deeper TiO_x CB in comparison to the SubPc HOMO and therefore leads to a reduction of the V_{OC} , which is determined by the donor HOMO-acceptor CB energy gap. This workfunction change is successfully prevented by the UV filter. The FF and J_{SC} are only slightly affected by the degradation which is most likely due to donor oxidation. TiO_2 is known to photogenerate superoxide radical anions from bound oxygen which can oxidise the organic material.^[316, 317] The UV filter also protects the device from this effect and justifies the trade-off for a slightly compensated photocurrent.

To compare, Hancox *et al.* studied the operational stability of regular SubPc/ C_{60} devices with and without a MoO_x interlayer which showed a reduction in PCE of 10 %, with stable V_{OC} , and 50 % respectively after one hour of constant illumination under N_2 .^[124] For these tests no UV filter was applied. EQE studies showed that MoO_x prevented the SubPc donor from degradation but showed little effect on the prevention of C_{60} degradation. The stability improvement in both cases, for the regular MoO_x /SubPc/ C_{60} device as well as the hybrid TiO_x /SubPc/ MoO_x device, is likely to arise from the TMO interlayer which decouples the organic layer from the ITO blocking off oxygen and electrode material diffusion into the active layer.^[223-225] The oxidation of the photoactive components can be accelerated by illumination and ultimately leads to a reduced photocurrent, and charge transport reduction resulting in a lower V_{OC} .^[224] However, photo-oxidation of C_{60} occurs regardless of the presence of protecting interlayer which is accounted for in hybrid devices. Moreover, the hybrid cells are

equipped with a very stable TMO sandwich creating a good encapsulation around the photoactive layer which leads to a slightly improved stability over SubPc/C₆₀ devices with MoO_x and a remarkable enhancement in stability over SubPc/C₆₀ devices without MoO_x.

7.4 Conclusion

It has been demonstrated that the small molecule organic semiconductor, SubPc, is a good donor material for hybrid OPV devices fabricated with a TiO_x electron acceptor. The new hybrid compatible electron donor material significantly exceeds the device performance of the fabricated P3HT based hybrids in this work.

The low device performance of TMO/P3HT based hybrid OPVs can partly be explained by energy alignment problems between donor and acceptor. More importantly, polymer disorder at the A/D interface could be the main cause for the low performance.

For an optimised SubPc (28 nm) device a remarkable J_{SC} of 1.75 mA cm⁻² and a *PCE* of 0.40 % was achieved, placing the TiO_x/SubPc system in direct competition with state-of-the-art TMO/polymer planar and nanostructured hybrid devices. When comparing to a SubPc reference device without TiO_x the generated current drops to a J_{SC} of only 0.50 mA cm⁻² which highlights the role of the TMO as an efficient electron acceptor material. Moreover, SubPc is a good hybrid electron donor because it has a relatively long L_D and good light absorption properties and possesses well controllable processability by vacuum deposition. Due to its energy level structure a sufficiently high energy band gap is provided at the TiO_x/SubPc A/D heterojunction for efficient exciton dissociation which does not compromise the high V_{OC} given due to the deeper lying SubPc HOMO. Operational stability studies show a good stability for TiO_x/SubPc devices in N₂ when an optical UV filter is applied which prevents mainly the V_{OC} from degradation due to workfunction changes of TiO_x upon UV exposure.

The comparison of TiO_x/SubPc inverted hybrids to regular SubPc/C₆₀ devices with focus on the *EQE* analysis show a similar *EQE* of SubPc in both device types which confirms sufficient exciton dissociation at the A/D hybrid interface and charge generation. This clearly shows the potential of this new small molecule based hybrid

interface. However, it becomes clear that the TMOs do not contribute to the photocurrent where C_{60} provides a significant part which explains the much higher J_{SC} and PCE for regular SubPc/ C_{60} devices. In order to increase the J_{SC} and consequently the PCE of TMO hybrids further optimisation efforts need to be in nanostructured hybrid interfaces to provide larger interfaces without compromising either exciton diffusion or charge transport, which could be achieved by nanosphere templating as demonstrated in Chapter 5.

The TiO_x /SubPc devices also suggest that the use of small molecule organic semiconductors with high quality TMO films represents a good opportunity to produce new types of hybrid OPV cells with the promise of reproducible, large area processing and low cost manufacture.

Chapter 8: Conclusions and further work

8.1 Conclusions

In OPV devices different interfaces have a crucial influence on the device behaviour, including the D/A and electrode/photoactive layer interfaces. These interfaces can be modified and controlled by structural engineering and selective material choice.

By developing and applying controlled nanoengineering methods the interface structure can be shaped and optimised. Furthermore, a deeper understanding of a structure/function relationship can help to improve the methods to achieve a higher device performance. The main approaches to interface structuring and modification, as well as alternative choices of materials in this thesis can be split into three sections:

- D/A interface nanostructuring for enhanced exciton diffusion without compromising absorption or charge collection.
- Electrode contact interface modification by inserting TMO interlayers for enhanced charge extraction through energy level tuning and structure/morphology optimisation.
- Hybrid OPVs employing TMOs as an alternative to fullerene based acceptor materials, which combine advantages from both organic and inorganic material classes.

8.1.1 Nanosphere synthesis

Nanospheres free of surfactants and of small radius in the range of the L_D of appropriate organic semiconductors are needed for nanosphere templating. Using radical initiated surfactant-free emulsion polymerisation, PS nanospheres with small, i.e. <100 nm sphere diameter and good monodispersity ($PDI < 0.05$) were synthesised. The synthesis was first carried out in a round-bottom flask to screen size and polydispersity

controlling parameters. Due to better temperature and stirring control it was shifted to a reactor for later experiments.

In round-bottom flask based reactions concentrations of styrene and both types of initiator, anionic KPS and cationic AMPAD, were varied leading to monodisperse particles of between 80 nm to 120 nm in diameter, suitable for nanosphere templating. By using O₂ quenching of the reaction far below full conversion, the particle diameter was reduced to 54 nm, but suffers from very low solid particle content.

In a second set of experiments in the reactor a cationic system was studied using the NaSS co-monomer concentration as a size control. With increasing NaSS concentration the PDI increased and the particle diameter decreased showing the expected opposite trend. Monodisperse latexes from 550 nm to about 90 nm in particle diameter suitable for templating were obtained from NaSS concentrations of ≤ 1.25 % of the monomer weight. Particles as small as 53 nm but with much larger size distribution were achieved from NaSS concentrations between 1.5-2.0 % showing clearly the limit of this approach for monodisperse particles.

8.1.2 Planar heterojunction devices

Planar heterojunction OPV devices employing C₆₀ and small molecule TSCuPc and polymeric PTEBS electron donors processable from aqueous solution have been fabricated and characterised. TSCuPc demonstrates *PCEs* of up to 0.32 % and a *V_{OC}* of almost 0.6 V compared to 0.46 V for regular CuPc. The TSCuPc layer thickness was optimised to 8 nm. The improved *V_{OC}* and solubility in water arises from the sulfonic acid group substituents which have a significant influence on film formation and OPV device behaviour. *EQE* measurements showed almost no current contribution from TSCuPc, instead only providing a favourable heterojunction for exciton dissociation from the acceptor. Furthermore, an assumed short *L_D* of <10 nm, charge transport imbalance, increased *R_S* for thicker layers and a grainy film surface morphology limit the device performance of TSCuPc based OPV cells.

Optimised PTEBS based devices reached *PCEs* of 0.90 %. Similar to TSCuPc, the side chains of PTEBS are modified with a charged functional group, which impacts

the polymer film formation and chain alignment. PTEBS shows only little contribution to the photocurrent leaving it in a similar position as TSCuPc. Optimised PTEBS devices reach the highest performance with very thin films <5 nm, which suggests a limitation due to a short L_D <10 nm but also a limited charge carrier mobility causing a charge transport imbalance within the device.

Thin film characterisation combined with J - V analysis allows to develop a deeper understanding of the relation between thin film morphology, material characteristics and the impact on OPV device behaviour which is employed for further interpretation of the 3D interpenetrating nanostructured D-A composite thin films and devices based on TSCuPc and PTEBS.

8.1.3 3D interdigitated organic D-A composite structures and OPV devices

The fabrication of controlled 3D ordered highly interpenetrating organic D-A composite OPV devices with sub-100 nm features is a multistep process: direct co-deposition of PS templates and appropriate donor material, template removal, acceptor material infiltration and completion of the full device.

The developed co-deposition is based on convective self-assembly followed by selective template removal using hot solvent vapour treatment. The method proves to be very promising for the fabrication of 3D open-cellular highly interconnected thin films of tunable sub-100 nm pore size. Nanospheres with diameters between 35-96 nm were employed to template both donor materials, small molecule based TSCuPc and polymeric PTEBS. 3D open-cellular TSCuPc films showed larger cracks dividing the film into distinct domains. PTEBS based films presented very low and localised crack defects providing a much better film structure for composite device fabrication. With films templated from nanospheres as small as 35 nm, porous structures with low template packing order were produced with only limited use for device fabrication. D-A composite films from open-cellular structure infiltration was achieved from different infiltration methods, with PCBM solution drop-casting followed by controlled drying being the most successful one. TSCuPc-PCBM and PTEBS-PCBM composite films were implemented

in complete OPV devices and tested under 1 sun illumination. TSCuPc based devices showed a very low device performance due to the large crack defects. PTEBS-PCBM composite devices from 96 nm and 78 nm templates achieved a *PCE* of 0.11 % and 0.08 % respectively which are comparable with a solution processed reference device. The consistent V_{OC} and FF indicate an in-tact composite D-A structure. The expected J_{SC} improvement over the planar reference due to enhanced exciton diffusion efficiency was not found. A likely explanation for this behaviour is the presence of photocurrent inactive film domains caused by remaining interface contaminating residues, film defects as well as variations in film quality and thickness. It is further assumed that the complexity and conditions of such a multistep fabrication process greatly compromise the advantages of the nanoengineered large active area interpenetrating composite devices. Overall, the fabrication method shows a new approach towards 3D interdigitated organic D-A composite OPV devices and presents a model system towards a proof of concept which has to our knowledge not been reported in the literature.

8.1.4 Transition metal oxide (TMO) interlayers

A substantial increase in device performance in solution processed inverted BHJ OPV devices is demonstrated by introducing a ZnO or TiO_x interlayer between the electron collecting bottom electrode and the photoactive blend of P3HT and PCBM. The structure and morphology of the dense, planar ZnO layers was controlled either by electrodeposition or spray pyrolysis techniques. The TiO_x thin films were sol-gel processed resulting in thin and very smooth interlayers. Metal oxide sandwich OPV devices based on the photoactive blend on an electrodeposited ZnO interlayer with a non-polar (100) preferential crystal orientation, and using a WO_x interlayer on the opposite electrode, resulted in a remarkable increase in *PCE* with a value of 4.91 % under AM1.5 illumination and a maximum *EQE* of 74 % at 508 nm. The devices reported set a new benchmark in performance for inverted architectures which are comparable to those achieved by regular devices.

Optimised devices employing TiO_x achieved a *PCE* of up to 3.21 % with a lower *FF* and J_{SC} compared to ZnO based B-ED but still much improved performance compared to an ITO based inverted reference device.

Electrodeposition of the ZnO at low temperature proved to be the most promising method for forming the ZnO interlayers, allowing the highest control of film structure and morphology, as well as leading to significantly improved device efficiency and stability.

8.1.5 Planar inorganic/organic hybrid devices

The small molecule organic semiconductor SubPc is a promising candidate as a donor material for the fabrication of inverted planar hybrid OPV devices using a TMO such as TiO_x as the electron acceptor material to substitute fullerenes. The TiO_x /SubPc cells demonstrate performance characteristics comparable to the best-reported planar and nanostructured TMO/polymer hybrid cells and outperform TMO/P3HT based hybrid devices presented in this work. For an optimised planar hybrid device a relatively high J_{SC} of 1.75 mA cm^{-2} and a maximum *EQE* of 20 % leads to a *PCE* of 0.40 % under AM1.5 solar illumination. The more than four-fold increase in the *EQE* and more than three-fold increase in J_{SC} of the TiO_x /SubPc(28 nm) device compared to that of the SubPc reference without TiO_x acceptor further confirms the difference between the hybrid cell with a working A/D heterojunction and the Schottky-like reference cell with an ineffective exciton dissociation process.

The comparison of TiO_x /SubPc inverted hybrids to regular SubPc/ C_{60} devices shows a similar *EQE* of SubPc in both device types which confirms sufficient exciton dissociation at the A/D hybrid interface and charge generation. This clearly shows the potential of this new small molecule based hybrid interface. In addition, the effect of UV irradiation on the stability of the TiO_x /SubPc cells is also demonstrated showing a clear improvement in stability when a UV filter is applied.

8.2 Further work

The presented multistep fabrication process for 3D interdigitated organic D-A composite structures led to the first successful devices of its kind. However, there is scope of improvement in the fabrication process including nanosphere synthesis, convective self-assembly, sphere removal process and second infiltration step. Although templating from 96 nm and 78 nm diameter spheres, with the radius in good range of L_D of fullerenes, was already achieved, the total device thickness approaches a few hundred nanometres for <10 layers. The use of even smaller particles would allow much thinner composite cells with an increased surface area and smaller features for more efficient exciton dissociation, but also requires the synthesis of such small particles.

Surfactant-free emulsion polymerisation of PS nanospheres already allowed the synthesis of monodisperse particles of about 80 nm in diameter with high solid content at full conversion. A possible way of synthesising even smaller spheres using styrene and NaSS co-monomer without surfactants is a continuous monomer feed to maintain good monodispersity.^[194] Furthermore, centrifugation could be employed for latexes to narrow the size distribution improving the monodispersity.

Although convective self-assembly allows co-deposition of spheres and filling donor material the change in concentration during the deposition process greatly affects the uniformity and controllability of the composite film thickness. Alternative co-deposition techniques could involve methods such as spin-coating although highly ordered domains might be hard to achieve.

A change of donor materials away from water-soluble PTEBS and TSCuPc is difficult because it would ask for a complete change of solvent and therefore D/A material system as well as a different template material. Other considerations would involve templating from non-sacrificial spheres or particles such as polythiophene spheres or inorganic semiconductor TMO nanospheres. Furthermore, the method of template-assisted nanostructuring is greatly applicable to sol-gel processed inorganic semiconducting materials such as ZnO and TiO_x to fabricate 3D open-cellular thin films with great application in hybrid OPVs following the same concept.

In order to further confirm the interpenetrating D-A composite structure “pseudo tomography” employing FIB/SEM could be very helpful to get a better understanding of the bulk structure and grade of internal domain network of composite structures templated from sub-100 nm sphere templates as it has been done for large spheres >200 nm.^[203] Due to the size of the features and the low contrast difference between the two organic compounds a high-resolution FEG-SEM coupled with a FIB would be required in order to carry out such a task.

In order to gain more details and further understanding of the energy level alignment of the TMO interlayer contacts, ultraviolet photoelectron spectroscopy (UPS) and X-Ray photoelectron spectroscopy (XPS) would allow to determine the exact VB and Fermi level positions as well as the CBs from the band gaps with estimations of the doping levels for the different types of ZnO and TiO_x. The measurement of these thin film characteristics could help to further distinguish between the films with different preferential crystal orientation and would allow to tailor the layer fabrication from electrodeposition towards even closer contact alignment.

In further experiments the TMO interlayers could be tested with other types of polymers and fullerene derivatives of matching LUMOs to achieve an even higher *PCE* as P3HT:PCBM was selected purely as a well understood model system which is reaching its limit at about 5 % for optimised regular devices.^[44]

With the introduction of SubPc as an example of a small molecule donor material for A/D hybrid OPVs many potential materials with similar HOMO and LUMO energy levels, longer L_D and good absorption behaviour could be used, including other phthalocyanines and SubPc derivatives in particular. Furthermore, solution processing of SubPc or more soluble derivatives could be very promising to achieve an even higher J_{SC} when processed as a blend with TMO nanoparticles or as a filling material of the suggested TMO 3D open-cellular nanostructures.^[155]

References

- [1] N. Armaroli, V. Balzani, *Angewandte Chemie International Edition*, 2007, 46, 52.
- [2] G. Boyle, A. Gary, *Renewable Energy*, Oxford University Press, 2004.
- [3] M. Z. Jacobson, *Energy & Environmental Science*, 2009, 2, 148.
- [4] M. Z. Jacobson, M. A. Delucchi, *Science*, 2009, 301, 58.
- [5] P. V. Kamat, *Journal of Physical Chemistry C*, 2007, 111, 2834.
- [6] R. F. Service, *Science*, 2005, 309, 548.
- [7] D. M. Chapin, C. S. Fuller, G. L. Pearson, *Journal of Applied Physics*, 1954, 25, 676.
- [8] M. A. Green, K. Emery, Y. Hishikawa, W. Warta, *Progress in Photovoltaics: Research and Applications*, 2010, 18, 346.
- [9] L. Kazmerski, www.nrel.gov/pv/thin_film/, 20/10/2010.
- [10] P. L. Ong, I. A. Levitsky, *Energies*, 2010, 3, 313.
- [11] B. Kippelen, J. L. Bredas, *Energy & Environmental Science*, 2009, 2, 251.
- [12] B. Oregan, M. Gratzel, *Nature*, 1991, 353, 737.
- [13] M. Graetzel, *Nature*, 2001, 414, 338.
- [14] M. Graetzel, *Accounts of Chemical Research*, 2009, 42, 1788.
- [15] J. Simon, J. J. Andre, *Molecular Semiconductors*, Springer-Verlag Berlin, 1985.
- [16] D. L. Morel, A. K. Ghosh, T. Feng, E. L. Stogryn, P. E. Purwin, R. F. Shaw, C. Fishman, *Applied Physics Letters*, 1978, 32, 495.
- [17] C. W. Tang, *Applied Physics Letters*, 1986, 48, 183.
- [18] H. W. Kroto, J. R. Heath, S. C. O'Brien, R. F. Curl, R. E. Smalley, *Nature*, 1985, 318, 162.
- [19] M. S. Dresselhaus, G. Dresselhaus, *Annual Review of Materials Science*, 1995, 25, 487.
- [20] P. J. Sullivan, Department of Chemistry, Imperial College London, London, 2006.
- [21] P. J. Sullivan, T. S. Jones, *Organic Electronics*, 2008, 9, 656.
- [22] L. M. Torres-Martinez, C. Sanchez-Trinidad, V. Rodriguez-Gonzalez, S. W. Lee, R. Gomez, *Research on Chemical Intermediates*, 2010, 36, 5.
- [23] D. Wynands, M. Levichkova, K. Leo, C. Uhrich, G. Schwartz, D. Hildebrandt, M. Pfeiffer, M. Riede, *Applied Physics Letters*, 2010, 97, 073503.
- [24] T. Stubinger, W. Brutting, *Journal of Applied Physics*, 2001, 90, 3632.
- [25] S. Yoo, *Applied Physics Letters*, 2004, 85, 5427.
- [26] P. Peumans, A. Yakimov, S. R. Forrest, *Journal of Applied Physics*, 2003, 93, 3693.
- [27] B. P. Rand, J. Genoe, P. Heremans, J. Poortmans, *Progress in Photovoltaics*, 2007, 15, 659.
- [28] T. Ameri, G. Dennler, C. Lungenschmied, C. J. Brabec, *Energy & Environmental Science*, 2009, 2, 347.
- [29] J. Gilot, M. M. Wienk, R. A. J. Janssen, *Applied Physics Letters*, 2007, 90, 143512.
- [30] D. Cheyns, B. P. Rand, P. Heremans, *Applied Physics Letters*, 2010, 97, 033301.
- [31] M. Riede, K. Leo, www.heliatek.com, 20/10/2010.
- [32] S. Sista, M. H. Park, Z. R. Hong, Y. Wu, J. H. Hou, W. L. Kwan, G. Li, Y. Yang, *Advanced Materials*, 2010, 22, 380.

-
- [33] J. Y. Kim, K. Lee, N. E. Coates, D. Moses, T. Q. Nguyen, M. Dante, A. J. Heeger, *Science*, 2007, 317, 222.
- [34] G. Yu, J. Gao, J. C. Hummelen, F. Wudl, A. J. Heeger, *Science*, 1995, 270, 1789.
- [35] W. L. Ma, C. Y. Yang, X. Gong, K. Lee, A. J. Heeger, *Advanced Functional Materials*, 2005, 15, 1617.
- [36] C. Muller, T. A. M. Ferenczi, M. Campoy-Quiles, J. M. Frost, D. D. C. Bradley, P. Smith, N. Stingelin-Stutzmann, J. Nelson, *Advanced Materials*, 2008, 20, 3510.
- [37] M. Campoy-Quiles, T. Ferenczi, T. Agostinelli, P. G. Etchegoin, Y. Kim, T. D. Anthopoulos, P. N. Stavrinou, D. D. C. Bradley, J. Nelson, *Nature Materials*, 2008, 7, 158.
- [38] S. S. van Bavel, M. Barenklau, G. de With, H. Hoppe, J. Loos, *Advanced Functional Materials*, 2010, 20, 1458.
- [39] N. S. Sariciftci, L. Smilowitz, A. J. Heeger, F. Wudl, *Science*, 1992, 258, 1474.
- [40] B. C. Thompson, J. M. J. Frechet, *Angewandte Chemie International Edition*, 2008, 47, 58.
- [41] G. Dennler, M. C. Scharber, C. J. Brabec, *Advanced Materials*, 2009, 21, 1323.
- [42] C. J. Brabec, S. Gowrisanker, J. J. M. Halls, D. Laird, S. J. Jia, S. P. Williams, *Advanced Materials*, 2010, 22, 3839.
- [43] Q. D. Zheng, B. J. Jung, J. Sun, H. E. Katz, *Journal of the American Chemical Society*, 2010, 132, 5394.
- [44] H. Y. Chen, J. H. Hou, S. Q. Zhang, Y. Y. Liang, G. W. Yang, Y. Yang, L. P. Yu, Y. Wu, G. Li, *Nature Photonics*, 2009, 3, 649.
- [45] S. H. Park, A. Roy, S. Beaupre, S. Cho, N. Coates, J. S. Moon, D. Moses, M. Leclerc, K. Lee, A. J. Heeger, *Nature Photonics*, 2009, 3, 297.
- [46] Y. Y. Liang, Z. Xu, J. B. Xia, S. T. Tsai, Y. Wu, G. Li, C. Ray, L. P. Yu, *Advanced Materials*, 2010, 22, 135.
- [47] M. Hiramoto, H. Fujiwara, M. Yokoyama, *Applied Physics Letters*, 1991, 58, 1062.
- [48] P. J. Sullivan, S. Heutz, S. M. Schultes, T. S. Jones, *Applied Physics Letters*, 2004, 84, 1210.
- [49] S. Heutz, P. J. Sullivan, B. M. Sanderson, S. M. Schultes, T. S. Jones, *Solar Energy Materials and Solar Cells*, 2004, 83, 229.
- [50] J. G. Xue, B. P. Rand, S. Uchida, S. R. Forrest, *Advanced Materials*, 2005, 17, 66.
- [51] T. D. Nielsen, C. Cruickshank, S. Foged, J. Thorsen, F. C. Krebs, *Solar Energy Materials and Solar Cells*, 2010, 94, 1553.
- [52] J. Nelson, *The Physics of Solar Cells*, Imperial College Press, London, 2003.
- [53] P. Wuerfel, U. Wuerfel, *Physics of Solar Cells: From Basic Principles to Advanced Concepts*, Wiley-VCH Verlag GmbH & Co KGaA, Weinheim, 2009.
- [54] P. Heremans, D. Cheyns, B. P. Rand, *Accounts of Chemical Research*, 2009, 42, 1740.
- [55] A. W. Hains, Z. Liang, M. A. Woodhouse, B. A. Gregg, *Chemical Reviews*, 2010, 110, 6689.
- [56] B. P. Rand, D. P. Burk, S. R. Forrest, *Physical Review B*, 2007, 75, 115327.
- [57] M. Riede, T. Mueller, W. Tress, R. Schueppel, K. Leo, *Nanotechnology*, 2008, 19, 424001.
- [58] J. L. Bredas, J. E. Norton, J. Cornil, V. Coropceanu, *Accounts of Chemical Research*, 2009, 42, 1691.
-

-
- [59] C. W. Schlenker, M. E. Thompson, *Chemical Communications*, 2011, 47, 3702.
- [60] A. J. Heeger, *Chemical Society Reviews*, 2010, 39, 2354.
- [61] B. A. Gregg, M. C. Hanna, *Journal of Applied Physics*, 2003, 93, 3605.
- [62] G. D. Scholes, G. Rumbles, *Nature Materials*, 2006, 5, 683.
- [63] G. D. Scholes, *Advanced Functional Materials*, 2008, 18, 1157.
- [64] I. G. Hill, A. Kahn, Z. G. Soos, R. A. Pascal, *Chemical Physics Letters*, 2000, 327, 181.
- [65] M. Knupfer, *Applied Physics a-Materials Science & Processing*, 2003, 77, 623.
- [66] S. E. Gledhill, B. Scott, B. A. Gregg, *Journal of Materials Research*, 2005, 20, 3167.
- [67] W. A. Luhman, R. J. Holmes, *Advanced Functional Materials*, 2011, 21, 764.
- [68] H. Gommans, S. Schols, A. Kadashchuk, P. Heremans, S. C. J. Meskers, *Journal of Physical Chemistry C*, 2009, 113, 2974.
- [69] P. W. M. Blom, V. D. Mihailetschi, L. J. A. Koster, D. E. Markov, *Advanced Materials*, 2007, 19, 1551.
- [70] T. M. Clarke, J. R. Durrant, *Chemical Reviews*, 2010, 110, 6736.
- [71] C. Deibel, T. Strobel, V. Dyakonov, *Advanced Materials*, 2010, 22, 4097.
- [72] P. A. van Hal, R. A. J. Janssen, G. Lanzani, G. Cerullo, M. Zavelani-Rossi, S. De Silvestri, *Chemical Physics Letters*, 2001, 345, 33.
- [73] T. Offermans, S. C. J. Meskers, R. A. J. Janssen, *Chemical Physics*, 2005, 308, 125.
- [74] H. Ohkita, S. Cook, Y. Astuti, W. Duffy, S. Tierney, W. Zhang, M. Heeney, I. McCulloch, J. Nelson, D. D. C. Bradley, J. R. Durrant, *Journal of the American Chemical Society*, 2008, 130, 3030.
- [75] R. Schueppel, K. Schmidt, C. Uhrich, K. Schulze, D. Wynands, J. L. Bredas, E. Brier, E. Reinold, H. B. Bu, P. Baeuerle, B. Maennig, M. Pfeiffer, K. Leo, *Physical Review B*, 2008, 77, 085311.
- [76] D. Cheyns, J. Poortmans, P. Heremans, C. Deibel, S. Verlaak, B. P. Rand, J. Genoe, *Physical Review B*, 2008, 77, 165332.
- [77] W. J. Potscavage, A. Sharma, B. Kippelen, *Accounts of Chemical Research*, 2009, 42, 1758.
- [78] M. C. Scharber, D. Wuhlbacher, M. Koppe, P. Denk, C. Waldauf, A. J. Heeger, C. L. Brabec, *Advanced Materials*, 2006, 18, 789.
- [79] W. Tress, A. Petrich, M. Hummert, M. Hein, K. Leo, M. Riede, *Applied Physics Letters*, 2011, 98, 063301.
- [80] V. D. Mihailetschi, P. W. M. Blom, J. C. Hummelen, M. T. Rispens, *Journal of Applied Physics*, 2003, 94, 6849.
- [81] S. Khodabakhsh, B. M. Sanderson, J. Nelson, T. S. Jones, *Advanced Functional Materials*, 2006, 16, 95.
- [82] S. A. DiBenedetto, A. Facchetti, M. A. Ratner, T. J. Marks, *Advanced Materials*, 2009, 21, 1407.
- [83] C. Donley, D. Dunphy, D. Paine, C. Carter, K. Nebesny, P. Lee, D. Alloway, N. R. Armstrong, *Langmuir*, 2002, 18, 450.
- [84] L. M. Chen, Z. Xu, Z. R. Hong, Y. Yang, *Journal of Materials Chemistry*, 2010, 20, 2575.
- [85] R. Steim, F. R. Kogler, C. J. Brabec, *Journal of Materials Chemistry*, 2010, 20, 2499.
- [86] L. M. Chen, Z. R. Hong, G. Li, Y. Yang, *Advanced Materials*, 2009, 21, 1434.
-

-
- [87] K. S. Liao, S. D. Yambem, A. Haldar, N. J. Alley, S. A. Curran, *Energies*, 2010, 3, 1212.
- [88] C. C. Leznoff, A. B. P. Lever, *Phthalocyanines: Properties and Applications*, VCH Publishers, Inc., New York, 1989.
- [89] S. H. Liu, W. C. M. Wang, A. L. Briseno, S. C. E. Mannsfeld, Z. N. Bao, *Advanced Materials*, 2009, 21, 1217.
- [90] M. V. Martinez-Diaz, G. de la Torre, T. Torres, *Chemical Communications*, 2010, 46, 7090.
- [91] D. Hohnholz, S. Steinbrecher, M. Hanack, *Journal of Molecular Structure*, 2000, 521, 231.
- [92] G. de la Torre, C. G. Claessens, T. Torres, *Chemical Communications*, 2007, 2000.
- [93] M. Knupfer, H. Peisert, *Phys Status Solidi A*, 2004, 201, 1055.
- [94] R. A. Hatton, N. P. Blanchard, A. J. Miller, S. R. P. Silva, *Physica E-Low-Dimensional Systems & Nanostructures*, 2007, 37, 124.
- [95] Y. S. Hsiao, W. T. Whang, S. C. Suen, J. Y. Shiu, C. P. Chen, *Nanotechnology*, 2008, 19, 415603.
- [96] O. Berger, W. J. Fischer, B. Adolphi, S. Tierbach, V. Melev, J. Schreiber, *Journal of Materials Science-Materials in Electronics*, 2000, 11, 331.
- [97] A. Meller, A. Ossko, *Monatshefte fuer Chemie*, 1972, 103, 150.
- [98] C. G. Claessens, D. Gonzalez-Rodriguez, T. Torres, *Chemical Reviews*, 2002, 102, 835.
- [99] K. L. Mutolo, E. I. Mayo, B. P. Rand, S. R. Forrest, M. E. Thompson, *Journal of the American Chemical Society*, 2006, 128, 8108.
- [100] H. Gommans, T. Aernouts, B. Verreet, P. Heremans, A. Medina, C. G. Claessens, T. Torres, *Advanced Functional Materials*, 2009, 19, 3435.
- [101] H. Gommans, D. Cheyns, T. Aernouts, C. Girotto, J. Poortmans, P. Heremans, *Advanced Functional Materials*, 2007, 17, 2653.
- [102] J. J. M. Halls, C. A. Walsh, N. C. Greenham, E. A. Marseglia, R. H. Friend, S. C. Moratti, A. B. Holmes, *Nature*, 1995, 376, 498.
- [103] Z. Bao, A. Dodabalapur, A. J. Lovinger, *Applied Physics Letters*, 1996, 69, 4108.
- [104] G. Li, C. W. Chu, V. Shrotriya, J. Huang, Y. Yang, *Applied Physics Letters*, 2006, 88, 253503.
- [105] J. Y. Kim, S. H. Kim, H. H. Lee, K. Lee, W. L. Ma, X. Gong, A. J. Heeger, *Advanced Materials*, 2006, 18, 572.
- [106] H. Sirringhaus, N. Tessler, R. H. Friend, *Science*, 1998, 280, 1741.
- [107] F. Tran-Van, M. Carrier, C. Chevrot, *Synthetic Metals*, 2004, 142, 251.
- [108] A. Hamed, Y. Y. Sun, Y. K. Tao, R. L. Meng, P. H. Hor, *Physical Review B*, 1993, 47, 10873.
- [109] T. Asakawa, et al., *Japanese Journal of Applied Physics*, 1995, 34(4A), 1958.
- [110] J. L. Yang, S. Schumann, R. A. Hatton, T. S. Jones, *Organic Electronics*, 2010, 11, 1399.
- [111] H. Ajie, *The Journal of Physical Chemistry* 1990, 94, 8630.
- [112] W. Kratschmer, L. D. Lamb, K. Fostiropoulos, D. R. Huffman, *Nature*, 1990, 347, 354.
- [113] T. B. Singh, N. Marjanovic, G. J. Matt, S. Gunes, N. S. Sariciftci, A. M. Ramil, A. Andreev, H. Sitter, R. Schwodiauer, S. Bauer, *Organic Electronics*, 2005, 6, 105.
-

-
- [114] X. Chen, S. S. Mao, *Chemical Reviews*, 2007, 107, 2891.
- [115] C. Klingshirn, *ChemPhysChem*, 2007, 8, 782.
- [116] A. B. Djuricic, Y. H. Leung, *Small*, 2006, 2, 944.
- [117] M. Skompska, *Synthetic Metals*, 2010, 160, 1.
- [118] C. Waldauf, M. Morana, P. Denk, P. Schilinsky, K. Coakley, S. A. Choulis, C. J. Brabec, *Applied Physics Letters*, 2006, 89, 233517.
- [119] M. S. White, D. C. Olson, S. E. Shaheen, N. Kopidakis, D. S. Ginley, *Applied Physics Letters*, 2006, 89, 143517.
- [120] V. Shrotriya, G. Li, Y. Yao, C. W. Chu, Y. Yang, *Applied Physics Letters*, 2006, 88, 073508.
- [121] S. Han, W. S. Shin, M. Seo, D. Gupta, S. J. Moon, S. Yoo, *Organic Electronics*, 2009, 10, 791.
- [122] M. Kroger, S. Hamwi, J. Meyer, T. Riedl, W. Kowalsky, A. Kahn, *Applied physics letters*, 2009, 95, 123301.
- [123] D. Cahen, A. Kahn, *Advanced Materials*, 2003, 15, 271.
- [124] I. Hancox, P. Sullivan, K. V. Chauhan, N. Beaumont, L. A. Rochford, R. A. Hatton, T. S. Jones, *Organic Electronics*, 2010, 11, 2019.
- [125] C. Tao, S. P. Ruan, X. D. Zhang, G. H. Xie, L. Shen, X. Z. Kong, W. Dong, C. X. Liu, W. Y. Chen, *Applied Physics Letters*, 2008, 93, 193307.
- [126] K. Kanai, K. Koizumi, S. Ouchi, Y. Tsukamoto, K. Sakanoue, Y. Ouchi, K. Seki, *Organic Electronics*, 2010, 11, 188.
- [127] M. Ichikawa, J. Amagai, Y. Horiba, T. Koyama, Y. Taniguchi, *Journal of Applied Physics*, 2003, 94, 7796.
- [128] P. Peumans, S. R. Forrest, *Applied Physics Letters*, 2001, 79, 126.
- [129] H. Gommans, B. Verreet, B. P. Rand, R. Muller, J. Poortmans, P. Heremans, J. Genoe, *Advanced Functional Materials*, 2008, 18, 3686.
- [130] M. Y. Chan, C. S. Lee, S. L. Lai, M. K. Fung, F. L. Wong, H. Y. Sun, K. M. Lau, S. T. Lee, *Journal of Applied Physics*, 2006, 100, 094506.
- [131] N. R. Armstrong, P. A. Veneman, E. Ratcliff, D. Placencia, M. Brumbach, *Accounts of Chemical Research*, 2009, 42, 1748.
- [132] F. Yang, S. R. Forrest, *ACS Nano*, 2008, 2, 1022.
- [133] N. Haberkorn, M. C. Lechmann, B. H. Sohn, K. Char, J. S. Gutmann, P. Theato, *Macromolecular Rapid Communications*, 2009, 30, 1146.
- [134] P. K. Watkins, A. B. Walker, G. L. B. Verschoor, *Nano Letters*, 2005, 5, 1814.
- [135] P. Peumans, S. Uchida, S. R. Forrest, *Nature*, 2003, 425, 158.
- [136] T. Erb, U. Zhokhavets, G. Gobsch, S. Raleva, B. Stuhn, P. Schilinsky, C. Waldauf, C. J. Brabec, *Advanced Functional Materials*, 2005, 15, 1193.
- [137] B. Walker, A. B. Tomayo, X. D. Dang, P. Zalar, J. H. Seo, A. Garcia, M. Tantiwiwat, T. Q. Nguyen, *Advanced Functional Materials*, 2009, 19, 3063.
- [138] X. Yang, J. Loos, *Macromolecules*, 2007, 40, 1353.
- [139] S. Günes, H. Neugebauer, N. S. Sariciftci, *Chemical Reviews*, 2007, 107, 1324.
- [140] A. M. Peiro, P. Ravirajan, K. Govender, D. S. Boyle, P. O'Brien, D. D. C. Bradley, J. Nelson, J. R. Durrant, *Journal of Materials Chemistry*, 2006, 16, 2088.
- [141] D. C. Olson, Y. J. Lee, M. S. White, N. Kopidakis, S. E. Shaheen, D. S. Ginley, J. A. Voigt, J. W. P. Hsu, *Journal of Physical Chemistry C*, 2007, 111, 16640.
-

-
- [142] Y. J. Lee, M. T. Lloyd, D. C. Olson, R. K. Grubbs, P. Lu, R. J. Davis, J. A. Voigt, J. W. P. Hsu, *Journal of Physical Chemistry C*, 2009, 113, 15778.
- [143] N. Haberkorn, J. S. Gutmann, P. Theato, *ACS Nano*, 2009, 3, 1415.
- [144] R. A. Segalman, B. McCulloch, S. Kirmayer, J. J. Urban, *Macromolecules*, 2009, 42, 9205.
- [145] R. Micheletto, H. Fukuda, M. Ohtsu, *Langmuir*, 1995, 11, 3333.
- [146] D. J. Norris, Y. A. Vlasov, *Advanced Materials*, 2001, 13, 371.
- [147] M. D. Irwin, B. Buchholz, A. W. Hains, R. P. H. Chang, T. J. Marks, *Proceedings of the National Academy of Science of the United States of America*, 2008, 105, 2783.
- [148] I. Hancox, K. V. Chauhan, P. Sullivan, R. A. Hatton, A. Moshar, C. P. A. Mulcahy, T. S. Jones, *Energy & Environmental Science*, 2010, 3, 107.
- [149] A. Roy, S. H. Park, S. Cowan, M. H. Tong, S. N. Cho, K. Lee, A. J. Heeger, *Applied Physics Letters*, 2009, 95, 013302.
- [150] N. Sekine, C. H. Chou, W. L. Kwan, Y. Yang, *Organic Electronics*, 2009, 10, 1473.
- [151] J. Boucle, S. Chyla, M. S. P. Shaffer, J. R. Durrant, D. D. C. Bradley, J. Nelson, *Advanced Functional Materials*, 2008, 18, 622.
- [152] S. Guenes, N. S. Sariciftci, *Inorganica Chimica Acta*, 2008, 361, 581.
- [153] J. Boucle, P. Ravirajan, J. Nelson, *Journal of Materials Chemistry*, 2007, 17, 3141.
- [154] C. C. Oey, A. B. Djurisic, H. Wang, K. K. Y. Man, W. K. Chan, M. H. Xie, Y. H. Leung, A. Pandey, J. M. Nunzi, P. C. Chui, *Nanotechnology*, 2006, 17, 706.
- [155] S. D. Oosterhout, M. M. Wienk, S. S. van Bavel, R. Thiedmann, L. J. A. Koster, J. Gilot, J. Loos, V. Schmidt, R. A. J. Janssen, *Nature Materials*, 2009, 8, 818.
- [156] R. F. Salzman, J. Xue, B. P. Rand, A. Alexander, M. E. Thompson, S. R. Forrest, *Organic Electronics*, 2005, 6, 242.
- [157] S. Peulon, D. Lincot, *Advanced Materials*, 1996, 8, 166.
- [158] T. Pauporte, D. Lincot, *Journal of the Electrochemical Society*, 2001, 148, C310.
- [159] M. Izaki, T. Omi, *Applied Physics Letters*, 1996, 68, 2439.
- [160] T. Yoshida, D. Komatsu, N. Shimokawa, H. Minoura, *Thin Solid Films*, 2004, 451, 166.
- [161] B. N. Illy, C. A. Cruickshank, S. Schumann, R. Da Campo, T. S. Jones, S. Heutz, M. A. McLachlan, D. W. McComb, D. J. Riley, M. P. Ryan, *Journal of Materials Chemistry*, 2011, submitted.
- [162] G. Adamopoulos, A. Bashir, W. P. Gillin, S. Georgakopoulos, M. Shkunov, M. A. Baklar, N. Stingelin, D. D. C. Bradley, T. D. Anthopoulos, *Advanced Functional Materials*, 2011, 21, 525.
- [163] S. R. Forrest, *Chemical Reviews*, 1997, 97, 1793.
- [164] S. Kowarik, A. Gerlach, F. Schreiber, *Journal of Physics: Condensed Matter*, 2008, 20, 18, 184005.
- [165] R. Gutzler, W. M. Heckl, M. Lackinger, *Review of Scientific Instruments*, 2010, 81, 1, 015108.
- [166] M. Campione, M. Cartotti, E. Pinotti, A. Sassella, A. Borghesi, *Journal of Vacuum Science & Technology A*, 2004, 22, 482.
- [167] G. Binnig, H. Rohrer, *Reviews of Modern Physics*, 1987, 59, 615.
- [168] G. Binnig, H. Rohrer, *Reviews of Modern Physics*, 1999, 71, S324.
- [169] G. Binnig, C. F. Quate, C. Gerber, *Phys Rev Lett* 1986, 56, 930.
- [170] Y. Seo, W. Jhe, *Reports on Progress in Physics*, 2008, 71, 1, 016101.
-

-
- [171] R. A. Oliver, Report on Progress in Physics, 2008, 71, 7, 076501.
- [172] C. Manos, B. Tompkins, MFP-3D Atomic Force Microscope, Asylum Research Inc., 2008.
- [173] P. J. Goodhew, J. Humphreys, R. Beanland, Electron Microscopy and Analysis, Taylor & Francis, London, 2001.
- [174] S. R. Wenham, M. A. Green, M. E. Watt, R. Corkish, Applied Photovoltaics, Earthscan, Sterling, 2007.
- [175] V. Shrotriya, G. Li, Y. Yao, T. Moriarty, K. Emery, Y. Yang, Advanced Functional Materials, 2006, 16, 2016.
- [176] Y. N. Xia, B. Gates, Y. D. Yin, Y. Lu, Advanced Materials, 2000, 12, 693.
- [177] W. Qun, F. Shoukuan, Y. Tongyin, Progress in Polymer Science, 1994, 19, 703.
- [178] S. C. Thickett, M. Gaborieau, R. G. Gilbert, Macromolecules, 2007, 40, 4710.
- [179] K. Tauer, H. F. Hernandez, S. Kozempel, O. Lazareva, P. Nazaran, Macromolecular Symposia, 2007, 259, 253.
- [180] G. Lichti, R. G. Gilbert, D. H. Napper, Journal of Polymer Science Part A: Polymer Chemistry, 1983, 21, 269.
- [181] D. F. Wood, B. C. Y. Whang, D. H. Napper, R. G. Gilbert, G. Lichti, Journal of Polymer Science Part A: Polymer Chemistry, 1983, 21, 985.
- [182] E. M. Coen, R. G. Gilbert, B. R. Morrison, H. Leube, S. Peach, Polymer, 1998, 39, 7099.
- [183] S. C. Thickett, R. G. Gilbert, Polymer, 2007, 48, 6965.
- [184] M. C. Wilkinson, J. Hearn, P. A. Steward, Advances in Colloid and Interface Science, 1999, 81, 77.
- [185] A. R. Goodall, M. C. Wilkinson, J. Hearn, Journal of Polymer Science Part A: Polymer Chemistry, 1977, 15, 2193.
- [186] J. W. Goodwin, J. Hearn, C. C. Ho, R. H. Ottewill, Colloid and Polymer Science, 1974, 252, 464.
- [187] D. Munro, A. R. Goodall, M. C. Wilkinson, K. Randle, J. Hearn, Journal of Colloid and Interface Science, 1979, 68, 1.
- [188] P. Jiang, J. F. Bertone, K. S. Hwang, V. L. Colvin, Chemistry of Materials, 1999, 11, 2132.
- [189] M. A. McLachlan, N. P. Johnson, R. De La Rue, D. W. McComb, Journal of Materials Chemistry, 2005, 15, 369.
- [190] F. Zhang, L. Cao, W. T. Yang, Macromolecular Chemistry and Physics, 2010, 211, 744.
- [191] Z. Q. Song, G. W. Poehlein, Journal of Polymer Science Part A: Polymer Chemistry, 1990, 28, 2359.
- [192] G. T. D. Shouldice, G. A. Vandezande, A. Rudin, European Polymer Journal, 1994, 30, 179.
- [193] J. H. Kim, M. Chainey, M. S. Elaasser, J. W. Vanderhoff, Journal of Polymer Science Part A: Polymer Chemistry, 1992, 30, 171.
- [194] X. J. Xu, K. S. Siow, M. K. Wong, L. M. Gan, Journal of Polymer Science Part A: Polymer Chemistry, 2001, 39, 1634.
- [195] Malvern, Zetasizer Nano, User Manual, Malvern Instruments Ltd., Malvern, 2009.
- [196] M. A. McLachlan, N. P. Johnson, R. M. De La Rue, D. W. McComb, Journal of Materials Chemistry, 2004, 14, 144.
-

-
- [197] K. Tauer, H. Hernandez, S. Kozempel, O. Lazareva, P. Nazaran, *Colloid and Polymer Science*, 2008, 286, 499.
- [198] D. Qiu, T. Cosgrove, A. M. Howe, *Macromolecular Chemistry and Physics*, 2005, 206, 2233.
- [199] M. S. D. Juang, I. M. Krieger, *Journal of Polymer Science Part A: Polymer Chemistry*, 1976, 14, 2089.
- [200] M. T. Lloyd, J. E. Anthony, G. G. Malliaras, *Materials Today*, 2007, 10, 34.
- [201] R. A. Hatton, N. P. Blanchard, V. Stolojan, A. J. Miller, S. R. P. Silva, *Langmuir*, 2007, 23, 6424.
- [202] M. A. McLachlan, D. W. McComb, S. Berhanu, T. S. Jones, *Journal of Materials Chemistry*, 2007, 17, 3773.
- [203] S. Berhanu, F. Tariq, T. Jones, D. W. McComb, *Journal of Materials Chemistry*, 2010, 20, 8005.
- [204] M. R. Detty, S. L. Gibson, S. J. Wagner, *Journal of Medicinal Chemistry*, 2004, 47, 3897.
- [205] P. Bertoncello, M. Peruffo, *Colloids and Surfaces A: Physicochemical and Engineering Aspects*, 2008, 321, 106.
- [206] J. Locklin, K. Shinbo, K. Onishi, F. Kaneko, Z. N. Bao, R. C. Advincula, *Chemistry of Materials*, 2003, 15, 1404.
- [207] R. A. Hatton, A. J. Miller, S. R. P. Silva, *Journal of Materials Chemistry*, 2008, 18, 1183.
- [208] H. Benten, N. Kudo, H. Ohkita, S. Ito, *Thin Solid Films*, 2009, 517, 2016.
- [209] S. Schumann, S. A. F. Bon, R. A. Hatton, T. S. Jones, *Chemical Communications*, 2009, 6478.
- [210] S. Berhanu, M. A. McLachlan, D. W. McComb, T. S. Jones, *Organic Photovoltaics IX*, 2008, 7052, H521.
- [211] J. K. Mwaura, M. R. Pinto, D. Witker, N. Ananthakrishnan, K. S. Schanze, J. R. Reynolds, *Langmuir*, 2005, 21, 10119.
- [212] Q. Q. Qiao, L. Y. Su, J. Beck, J. T. McLeskey, *Journal of Applied Physics*, 2005, 98, 094906.
- [213] Q. Q. Qiao, J. T. Mcleskey, *Applied Physics Letters*, 2005, 86, 153501.
- [214] A. J. Miller, R. A. Hatton, S. R. P. Silva, *Applied Physics Letters*, 2006, 89, 123115.
- [215] P. Sullivan, T. S. Jones, A. J. Ferguson, S. Heutz, *Applied Physics Letters*, 2007, 91, 233114.
- [216] V. Chauhan, R. A. Hatton, P. Sullivan, T. S. Jones, S. W. Cho, L. Piper, A. deMasi, K. Smith, *Journal of Materials Chemistry*, 2010, 20, 1173.
- [217] L. G. Yang, H. Z. Chen, M. Wang, *Thin Solid Films*, 2008, 516, 7701.
- [218] Y. Terao, H. Sasabe, C. Adachi, *Applied Physics Letters* 2007, 90, 103515.
- [219] P. J. Brown, D. S. Thomas, A. Kohler, J. S. Wilson, J. S. Kim, C. M. Ramsdale, H. Sirringhaus, R. H. Friend, *Physical Review B*, 2003, 67, 064203.
- [220] G. Li, V. Shrotriya, Y. Yao, J. S. Huang, Y. Yang, *Journal of Materials Chemistry*, 2007, 17, 3126.
- [221] J. H. Yang, A. Garcia, T. Q. Nguyen, *Applied Physics Letters*, 2007, 90, 103514.
- [222] C. Uhrich, D. Wynands, S. Olthof, M. K. Riede, K. Leo, S. Sonntag, B. Maennig, M. Pfeiffer, *Journal of Applied Physics*, 2008, 104, 043107.
-

-
- [223] J. C. Scott, J. H. Kaufman, P. J. Brock, R. DiPietro, J. Salem, J. A. Goitia, *Journal of Applied Physics*, 1996, 79, 2745.
- [224] M. Jorgensen, K. Norrman, F. C. Krebs, *Solar Energy Materials and Solar Cells*, 2008, 92, 686.
- [225] F. C. Krebs, K. Norrman, *Progress in Photovoltaics*, 2007, 15, 697.
- [226] H. Fudouzi, Y. N. Xia, *Langmuir*, 2003, 19, 9653.
- [227] H. Fudouzi, Y. N. Xia, *Advanced Materials*, 2003, 15, 892.
- [228] C. I. Aguirre, E. Reguera, A. Stein, *Advanced Functional Materials*, 2010, 20, 2565.
- [229] E. Yablonovitch, T. Gmitter, J. P. Harbison, R. Bhat, *Applied Physics Letters* 1987, 51, 2222.
- [230] S. John, *Physical Review Letters*, 1987, 58, 2486.
- [231] N. R. Thomson, M. A. McLachlan, C. L. Bower, D. W. McComb, *Langmuir*, 2009, 25, 11344.
- [232] J. Ge, Y. Yin, *Angewandte Chemie International Edition*, 2011, 50, 1492.
- [233] B. T. Holland, C. F. Blanford, A. Stein, *Science*, 1998, 281, 538.
- [234] N. P. Johnson, D. W. McComb, A. Richel, B. M. Treble, R. M. De la Rue, *Synthetic Metals*, 2001, 116, 469.
- [235] D. Tonti, M. J. Torralvo, E. Enciso, I. Sobrados, J. Sanz, *Chemistry of Materials*, 2008, 20, 4783.
- [236] J. H. Zhang, B. Yang, *Advanced Functional Materials*, 2010, 20, 3411.
- [237] S. K. Yang, W. P. Cai, L. C. Kong, Y. Lei, *Advanced Functional Materials*, 2010, 20, 2527.
- [238] C. F. Blanford, H. W. Yan, R. C. Schroden, M. Al-Daous, A. Stein, *Advanced Materials*, 2001, 13, 401.
- [239] R. C. Schroden, M. Al-Daous, C. F. Blanford, A. Stein, *Chemistry of Materials*, 2002, 14, 3305.
- [240] P. D. Yang, T. Deng, D. Y. Zhao, P. Y. Feng, D. Pine, B. F. Chmelka, G. M. Whitesides, G. D. Stucky, *Science*, 1998, 282, 2244.
- [241] T. V. Teperik, F. J. G. de Abajo, A. G. Borisov, M. Abdelsalam, P. N. Bartlett, Y. Sugawara, J. J. Baumberg, *Nature Photonics*, 2008, 2, 299.
- [242] C. Sanchez, C. Boissiere, D. Grosso, C. Laberty, L. Nicole, *Chemistry of Materials*, 2008, 20, 682.
- [243] W. T. Dong, H. Bongard, B. Tesche, F. Marlow, *Advanced Materials*, 2002, 14, 1457.
- [244] I. G. Yu, Y. J. Kim, H. J. Kim, C. Lee, W. I. Lee, *Journal of Materials Chemistry*, 2011, 21, 532.
- [245] J. A. Xu, B. F. Yang, M. Wu, Z. P. Fu, Y. Lv, Y. X. Zhao, *Journal of Physical Chemistry C*, 2010, 114, 15251.
- [246] S. Guldin, S. Hüttner, M. Kolle, M. E. Welland, P. Müller-Buschbaum, R. H. Friend, U. Steiner, N. Tétreault, *Nano Letters*, 2010, 10, 2303.
- [247] D. J. Norris, E. G. Arlinghaus, L. L. Meng, R. Heiny, L. E. Scriven, *Advanced Materials*, 2004, 16, 1393.
- [248] Q. Li, U. Jonas, X. S. Zhao, M. Kappl, *Asia-Pacific Journal of Chemical Engineering*, 2008, 3, 255.
-

-
- [249] M. Bardosova, M. E. Pemble, I. M. Povey, R. H. Tredgold, *Advanced Materials*, 2010, 22, 3104.
- [250] S. Pillai, A. G. Hemmersam, R. Mukhopadhyay, R. L. Meyer, S. M. Moghimi, F. Besenbacher, P. Kingshott, *Nanotechnology*, 2009, 20, 025604.
- [251] N. D. Denkov, O. D. Velev, P. A. Kralchevsky, I. B. Ivanov, H. Yoshimura, K. Nagayama, *Nature*, 1993, 361, 26.
- [252] A. S. Dimitrov, C. D. Dushkin, H. Yoshimura, K. Nagayama, *Langmuir*, 1994, 10, 432.
- [253] A. S. Dimitrov, K. Nagayama, *Langmuir*, 1996, 12, 1303.
- [254] P. A. Kralchevsky, K. Nagayama, *Langmuir*, 1994, 10, 23.
- [255] A. Imhof, D. J. Pine, *Nature*, 1997, 389, 948.
- [256] J. Wang, S. Ahl, Q. Li, M. Kreiter, T. Neumann, K. Burkert, W. Knoll, U. Jonas, *Journal of Materials Chemistry*, 2008, 18, 981.
- [257] L. K. Wang, X. S. Zhao, *Journal of Physical Chemistry C*, 2007, 111, 8538.
- [258] G. Guillaud, J. Simon, J. P. Germain, *Coordination Chemistry Reviews*, 1998, 178, 1433.
- [259] T. Cassagneau, F. Caruso, *Advanced Materials*, 2002, 14, 34.
- [260] D. Y. Wang, F. Caruso, *Advanced Materials*, 2001, 13, 350.
- [261] Y. F. Zhou, M. Eck, M. Kruger, *Energy & Environmental Science*, 2010, 3, 1851.
- [262] E. S. Kwak, W. Lee, N. G. Park, J. Kim, H. Lee, *Advanced Functional Materials*, 2009, 19, 1093.
- [263] Y. J. Kim, M. H. Lee, H. J. Kim, G. Lim, Y. S. Choi, N. G. Park, K. Kim, W. I. Lee, *Advanced Materials*, 2009, 21, 3668.
- [264] A. Mihi, M. E. Calvo, J. A. Anta, H. Miguez, *Journal of Physical Chemistry C*, 2008, 112, 13.
- [265] K. M. Coakley, M. D. McGehee, *Applied Physics Letters*, 2003, 83, 3380.
- [266] H. J. Snaith, G. L. Whiting, B. Q. Sun, N. C. Greenham, W. T. S. Huck, R. H. Friend, *Nano Letters*, 2005, 5, 1653.
- [267] G. L. Whiting, H. J. Snaith, S. Khodabakhsh, J. W. Andreasen, D. Breiby, M. M. Nielsen, N. C. Greenham, P. H. Friend, W. T. S. Huck, *Nano Letters*, 2006, 6, 573.
- [268] D. M. Nanditha, M. Dissanayake, A. A. D. T. Adikaari, R. J. Curry, R. A. Hatton, S. R. P. Silva, *Applied Physics Letters*, 2007, 90, 253502.
- [269] D. Cheyns, K. Vasseur, C. Rolin, J. Genoe, J. Poortmans, P. Heremans, *Nanotechnology*, 2008, 19, 424016.
- [270] X. M. He, F. Gao, G. L. Tu, D. Hasko, S. Huttner, U. Steiner, N. C. Greenham, R. H. Friend, W. T. S. Huck, *Nano Letters*, 2010, 10, 1302.
- [271] W. Wiedemann, L. Sims, A. Abdellah, A. Exner, R. Meier, K. P. Musselman, J. L. MacManus-Driscoll, P. Muller-Buschbaum, G. Scarpa, P. Lugli, L. Schmidt-Mende, *Applied Physics Letters*, 2010, 96, 263109.
- [272] C. Groves, R. A. Marsh, N. C. Greenham, *Journal of Chemical Physics*, 2008, 129, 11, 114903.
- [273] L. K. Teh, N. K. Tan, C. C. Wong, S. Li, *Applied Physics A: Materials Science & Processing*, 2005, 81, 1399.
- [274] E. R. Dufresne, D. J. Stark, N. A. Greenblatt, J. X. Cheng, J. W. Hutchinson, L. Mahadevan, D. A. Weitz, *Langmuir*, 2006, 22, 7144.
- [275] K. D. Danov, B. Pouligny, P. A. Kralchevsky, *Langmuir*, 2001, 17, 6599.
-

-
- [276] E. L. Ratcliff, P. A. Lee, N. R. Armstrong, *Journal of Materials Chemistry*, 2010, 20, 2672.
- [277] K. Kawano, R. Pacios, D. Poplavskyy, J. Nelson, D. D. C. Bradley, J. R. Durrant, *Solar Energy Materials and Solar Cells*, 2006, 90, 3520.
- [278] K. Norrman, M. V. Madsen, S. A. Gevorgyan, F. C. Krebs, *Journal of the American Chemical Society*, 2010, 132, 16883.
- [279] E. D. Gomez, Y. L. Loo, *Journal of Materials Chemistry*, 2010, 20, 6604.
- [280] R. Steim, S. A. Choulis, P. Schilinsky, C. J. Brabec, *Applied Physics Letters*, 2008, 92, 093303.
- [281] T. B. Yang, W. Z. Cai, D. H. Qin, E. G. Wang, L. F. Lan, X. Gong, J. B. Peng, Y. Cao, *Journal of Physical Chemistry C*, 2010, 114, 6849.
- [282] X. H. Ju, W. Feng, K. C. Varutt, T. S. Hori, A. H. Fujii, M. N. Ozaki, *Nanotechnology*, 2008, 19, 435706.
- [283] T. Trindade, J. D. P. Dejesus, P. O'Brien, *Journal of Materials Chemistry*, 1994, 4, 1611.
- [284] S. W. Liu, C. C. Lee, C. F. Lin, J. C. Huang, C. T. Chen, J. H. Lee, *Journal of Materials Chemistry*, 2010, 20, 7800.
- [285] J. C. Wang, W. T. Weng, M. Y. Tsai, M. K. Lee, S. F. Horng, T. P. Perng, C. C. Kei, C. C. Yu, H. F. Meng, *Journal of Materials Chemistry*, 2010, 20, 862.
- [286] K. Takanezawa, K. Tajima, K. Hashimoto, *Applied Physics Letters*, 2008, 93, 063308.
- [287] C. H. Hsieh, Y. J. Cheng, P. J. Li, C. H. Chen, M. Dubosc, R. M. Liang, C. S. Hsu, *Journal of the American Chemical Society*, 2010, 132, 4887.
- [288] M. Glatthaar, M. Niggemann, B. Zimmermann, P. Lewer, M. Riede, A. Hinsch, J. Luther, *Thin Solid Films*, 2005, 491, 298.
- [289] I. Gonzalez-Valls, M. Lira-Cantu, *Energy & Environmental Science*, 2009, 2, 19.
- [290] E. A. Meulenkaamp, *Journal of Physical Chemistry B*, 1998, 102, 5566.
- [291] S. Yamabi, H. Imai, *Chemistry of Materials*, 2002, 14, 609.
- [292] A. Wander, N. M. Harrison, *Surface Science*, 2000, 457, 342.
- [293] J. H. Lee, S. Cho, A. Roy, H. T. Jung, A. J. Heeger, *Applied Physics Letters*, 2010, 96, 163303.
- [294] K. Vandewal, K. Tvingstedt, A. Gadisa, O. Inganas, J. V. Manca, *Nature Materials*, 2009, 8, 904.
- [295] N. Li, B. E. Lassiter, R. R. Lunt, G. Wei, S. R. Forrest, *Applied Physics Letters*, 2009, 94, 023307.
- [296] P. Schilinsky, C. Waldauf, C. J. Brabec, *Applied Physics Letters*, 2002, 81, 3885.
- [297] I. Riedel, J. Parisi, V. Dyakonov, L. Lutsen, D. Vanderzande, J. C. Hummelen, *Advanced Functional Materials*, 2004, 14, 38.
- [298] N. D. Treat, L. M. Campos, M. D. Dimitriou, B. W. Ma, M. L. Chabinyc, C. J. Hawker, *Advanced Materials*, 2010, 22, 4982.
- [299] Z. Xu, L. M. Chen, G. W. Yang, C. H. Huang, J. H. Hou, Y. Wu, G. Li, C. S. Hsu, Y. Yang, *Advanced Functional Materials*, 2009, 19, 1227.
- [300] A. M. Ballantyne, T. A. M. Ferenczi, M. Campoy-Quiles, T. M. Clarke, A. Maurano, K. H. Wong, W. M. Zhang, N. Stingelin-Stutzmann, J. S. Kim, D. D. C. Bradley, J. R. Durrant, I. McCulloch, M. Heeney, J. Nelson, S. Tierney, W. Duffy, C. Mueller, P. Smith, *Macromolecules*, 2010, 43, 1169.
-

- [301] K. H. Yim, Z. J. Zheng, R. H. Friend, W. T. S. Huck, J. S. Kim, *Advanced Functional Materials*, 2008, 18, 2897.
- [302] X. Bulliard, S.-G. Ihn, S. Yun, Y. Kim, D. Choi, J.-Y. Choi, M. Kim, M. Sim, J.-H. Park, W. Choi, K. Cho, *Advanced Functional Materials*, 2010, 20, 4381.
- [303] C. Tao, S. P. Ruan, G. H. Xie, X. Z. Kong, L. Shen, F. X. Meng, C. X. Liu, X. D. Zhang, W. Dong, W. Y. Chen, *Applied Physics Letters*, 2009, 94, 043311.
- [304] H. Schmidt, H. Flugge, T. Winkler, T. Bulow, T. Riedl, W. Kowalsky, *Applied Physics Letters*, 2009, 94, 243302.
- [305] C. Melzer, V. V. Krasnikov, G. Hadziioannou, *Applied Physics Letters*, 2003, 82, 3101.
- [306] A. R. Schlatmann, D. W. Floet, A. Hilberer, F. Garten, P. J. M. Smulders, T. M. Klapwijk, G. Hadziioannou, *Applied Physics Letters*, 1996, 69, 1764.
- [307] W. Z. Cai, X. Gong, Y. Cao, *Solar Energy Materials and Solar Cells*, 2010, 94, 114.
- [308] M. S. A. Abdou, F. P. Orfino, Y. Son, S. Holdcroft, *Journal of the American Chemical Society*, 1997, 119, 4518.
- [309] M. Manceau, A. Rivaton, J. L. Gardette, *Macromolecular Rapid Communications*, 2008, 29, 1823.
- [310] Y. Vaynzof, D. Kabra, L. H. Zhao, P. K. H. Ho, A. T. S. Wee, R. H. Friend, *Applied Physics Letters*, 2010, 97, 033309.
- [311] L. Shen, G. H. Zhu, W. B. Guo, C. Tao, X. D. Zhang, C. X. Liu, W. Y. Chen, S. P. Ruan, Z. C. Zhong, *Applied Physics Letters*, 2008, 92, 073307.
- [312] L. J. Pegg, S. Schumann, R. A. Hatton, *ACS Nano*, 2010, 4, 5671.
- [313] J. W. P. Hsu, M. T. Lloyd, *MRS Bulletin*, 2010, 35, 422.
- [314] P. Ravirajan, A. M. Peiro, M. K. Nazeeruddin, M. Graetzel, D. D. C. Bradley, J. R. Durrant, J. Nelson, *Journal of Physical Chemistry B*, 2006, 110, 7635.
- [315] H. Schmidt, K. Zilberberg, S. Schmale, H. Flugge, T. Riedl, W. Kowalsky, *Applied Physics Letters*, 2010, 96, 243305.
- [316] A. M. Peiro, C. Colombo, G. Doyle, J. Nelson, A. Mills, J. R. Durrant, *Journal of Physical Chemistry B*, 2006, 110, 23255.
- [317] A. Mills, G. Doyle, A. M. Peiro, J. Durrant, *Journal of Photochemistry and Photobiology A: Chemistry*, 2006, 177, 328.